UNIVERSIDAD AUTÓNOMA DE MADRID
Facultad de Ciencias
Departamento de Física Teórica

A study of the dynamics of isolated-photon plus jet production in pp collisions at $\sqrt{s} = 7$ TeV with the ATLAS detector

Submitted in partial fullfilment of the requirements
for the degree 'Doctor en Ciencias Físicas' by

Josu Cantero García
Supervisors : Claudia Glasman and Juan Terrón

14/01/2013

UNIVERSIDAD AUTÓNOMA DE MADRID
Facultad de Ciencias
Departamento de Física Teórica

Estudio de la dinámica de la producción asociada de un fotón aislado y un jet en colisiones pp a $\sqrt{s} = 7$ TeV con el detector ATLAS

Entregado como requisito parcial del título
de 'Doctor en Ciencias Físicas' por

Josu Cantero García
Directores de tesis : Claudia Glasman and Juan Terrón

14/01/2013

Doktore-tesi hau nire familiari eskaintzen diot

Contents

Chapter 1

Introduction

The production of prompt photons in association with jets in proton-proton collisions provides a testing ground of perturbative QCD (pQCD) in a cleaner environment than jet production since the photon originates directly from the hard interaction and does not undergo hadronisation. At LHC, the process $pp \rightarrow \gamma$ jet X proceeds via two production mechanisms: direct photon, in which the photon originates in the hard process, and fragmentation photons, in which the photon is produced in the fragmentation of a coloured high transverse momentum, P_T, parton [1].

The study of angular correlations between the photon and the jet can be used to test pQCD at large hard-scattering scales and over a wide range of the parton momentum fraction x to understand the dynamics of the hard-scattering processes and to constrain the photon fragmentation contribution. Since the dominant production mechanism in pp collisions at LHC is through the $qg \rightarrow q\gamma$ process, the measurement of prompt-photon plus jet cross sections can help to constrain the gluon density in the proton. In addition, this type of events provides one of the main backgrounds in searches for Higgs boson decaying into a photon pair.

The dynamics of the underlying processes in $2 \rightarrow 2$ hard scattering can be investigated using the variable θ^*, $\cos\theta^* \equiv \tanh(\Delta Y/2)$, where ΔY is the difference in rapidity of the two final-state particles, which coincides with the scattering angle in the dijet centre-of-mass system and whose distribution is sensitive to the spin of the exchanged particle. The dominant subprocess for dijet events in pp collisions at LHC proceeds via t-channel gluon exchange and so the differential cross section behaves as $(1 - |\cos\theta^*|)^{-2}$ when $|\cos\theta^*| \rightarrow 1$. The fragmentation contribution to prompt-photon plus jet production is expected to display the same behaviour. On the other hand, the direct-photon contribution is expected to exhibit a different behaviour, namely $(1 - |\cos\theta^*|)^{-1}$ when $|\cos\theta^*| \rightarrow 1$, due to the dominance

of t-channel quark exchange. As a result, a measurement of the cross section for prompt-photon plus jet production as a function of $|\cos\theta^*|$ provides a handle on the relative contributions of the direct-photon and fragmentation components as well as the possibility to test the dominance of t-channel quark exchange.

The production of inclusive isolated photons in pp collisions has been studied previously with the ATLAS detector [2, 3]. This thesis presents studies of isolated-photon plus jet production in pp collisions at $\sqrt{s} = 7$ TeV with the ATLAS detector at the LHC using an integrated luminosity of 37.1 pb^{-1}. The goals are the studies of the kinematics and dynamics of the isolated-photon plus jet system through the measurement of the differential cross sections as functions of the leading photon transverse energy ($E^{\gamma}_{T,\mathrm{lead}}$), the leading jet transverse momentum ($P^{\mathrm{jet}}_{T,\mathrm{lead}}$) and rapidity $|Y^{\mathrm{jet}}_{\mathrm{lead}}|$), the difference in azimuthal angle between the photon and the jet ($\Delta\phi^{\gamma-\mathrm{jet}}$), the photon-jet invariant mass ($M^{\gamma-\mathrm{jet}}$) and[1] $\cos\theta^{\gamma-\mathrm{jet}}$. The photon is required to be isolated, with a transverse energy around its direction below 4 GeV. The jets are defined using the anti-k_T jet algorithm [5] with radius $R = 0.6$. The measurements are performed in the phase-space region of $E^{\gamma}_{T,\mathrm{lead}} > 45$ GeV, $|\eta^{\gamma}_{\mathrm{lead}}| <2.37$ (excluding the region of $1.37< |\eta^{\gamma}_{\mathrm{lead}}| <1.52$), $P^{\mathrm{jet}}_{T,\mathrm{lead}} > 40$ GeV, $|Y^{\mathrm{jet}}_{\mathrm{lead}}| < | 2.37$ and $\Delta R^2_{\gamma-\mathrm{jet}} = (\eta^{\gamma}_{\mathrm{lead}} - \eta^{\mathrm{jet}}_{\mathrm{lead}})^2 + (\phi^{\gamma}_{\mathrm{lead}} - \phi^{\mathrm{jet}}_{\mathrm{lead}})^2 > 1$. The measurements of the $d\sigma/dM^{\gamma-\mathrm{jet}}$ and $d\sigma/d|\cos\theta^{\gamma-\mathrm{jet}}|$ cross sections are performed for $|\eta^{\mathrm{jet}}_{\mathrm{lead}} + Y^{\mathrm{jet}}_{\mathrm{lead}} < |$ 2.37, $|\cos\theta^{\gamma-\mathrm{jet}}| < 0.83$ and $M^{\gamma-\mathrm{jet}} > 161$ GeV. Next-to-leading-order (NLO) QCD calculations are compared to the measurements.

[1] The variable θ^* is referred to as $\theta^{\gamma-\mathrm{jet}}$ here and henceforth.

Chapter 2

Experimental setup

Some fundamental aspects of the LHC accelerator as well as a detailed description of the ATLAS detector are explained in this chapter. The LHC is a proton-proton accelerator designed to run at high energies and luminosities. ATLAS is a multipurpose detector designed to observe the new phenomena expected at the TeV scale.

2.1 The LHC accelerator

The Large Hadron Collider (LHC) is a two-ring-superconducting-hadron accelerator and collider installed in the existing 26.7 km tunnel that was constructed between 1984 and 1989 for the CERN LEP machine (see Fig. 2.1).

The LHC design depends on some basic principles linked with the latest technology for particle acceleration. Being a particle-particle collider, there are two rings with counter-rotating beams, unlike particle-antiparticle colliders that can have both beams sharing the same phase space in a single ring. A proton machine such as the LHC does not have synchrotron radiation problems as in the case of electron-positron machine and could ideally, have longer arcs and shorter straight sections for the same circumference [6–8].

The main motivation for the LHC was to reveal physics beyond the Standard Model with centre-of-mass collision energies of up to 14 TeV and with high luminosities. The number of events per second generated in the LHC collisions is given by:

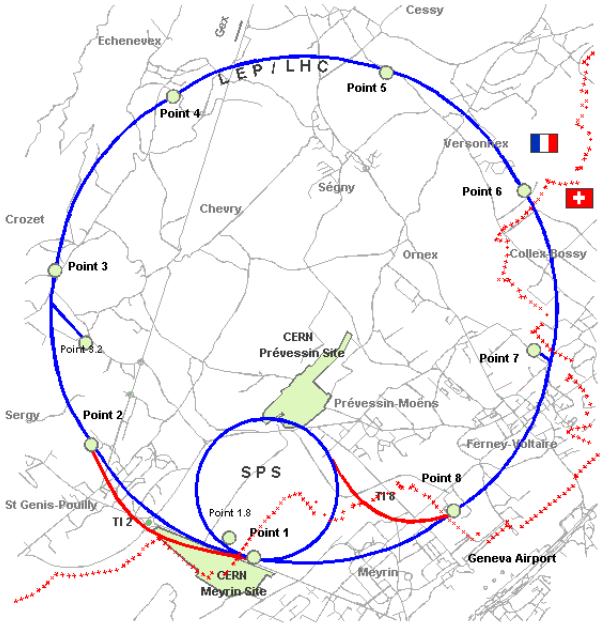

Figure 2.1: The Large Hadron Collider (LHC)

.

$$N_{\text{event}} = \mathcal{L} \cdot \sigma_{\text{event}} \ , \tag{2.1}$$

where σ_{event} is the cross section for the process under study and $\mathcal{L}$ is the machine luminosity. The machine luminosity depends only on the beam parameters and can be written, for a Gaussian beam distribution as:

$$\mathcal{L} = \frac{N_b^2 n_b f_{\text{rev}} \gamma_r}{4\pi\epsilon_n \beta^*} F \ , \tag{2.2}$$

where N_b is the number of particles per bunch, n_b is the number of bunches per beam, f_{rev} is the revolution frequency, γ_r is the relativistic gamma factor, ϵ_n is the normalised transverse beam emittance, β^* is the beta function at the collision point and F is the geometric luminosity reduction factor due to the crossing angle at the interaction point (IP), given by;

$$F = (1 + (\frac{\theta_c \sigma_z}{2\sigma^*})^2)^{-1/2} \ . \tag{2.3}$$

In Eq. 2.3, θ_c is the full crossing angle at the IP, σ_z is the RMS bunch length and σ^* the transverse RMS beam size at the IP. In this equation, circular beams, with

$\sigma_z \ll \beta$, and equal beam parameter for both beams are assumed. The exploration of rare events in LHC collisions requires high beam energies and intensities.

The LHC provides proton-proton collisions to two high-luminosity multipurpose experiments, ATLAS and CMS. There are also two low-luminosity experiments: LHCb, designed to study mainly b-quark physics, and TOTEM, designed to study very-forward physics. In addition to proton beams, the LHC is also operated with heavy-ion (Pb) beams. The LHC has one dedicated heavy-ion experiment, ALICE. Figure 2.2 shows the location of the different experiments in the LHC ring.

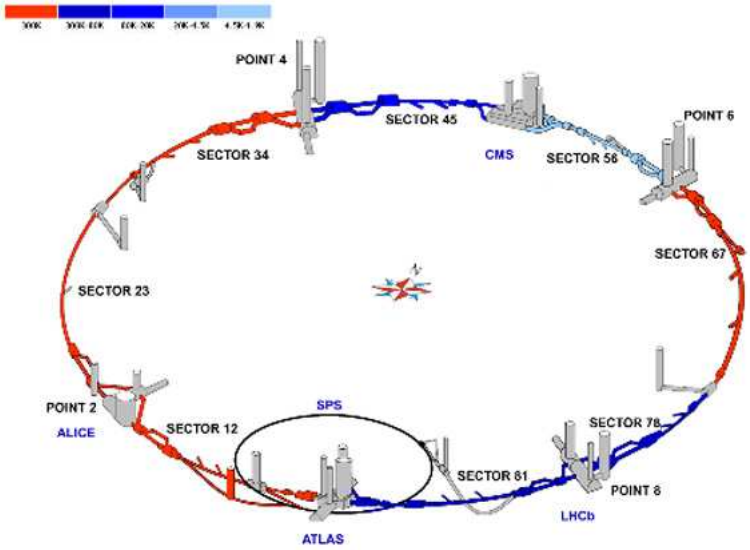

Figure 2.2: ATLAS, CMS, ALICE and LHCb detectors location in the LHC ring.

2.1.1 Luminosity lifetime

The luminosity in the LHC is not constant over a physics run, but decays due to the degradation of intensities and emittance of the circulating beams. The main cause of the luminosity decay during nominal LHC operation is the beam loss from collisions. The initial decay time of the bunch intensity, due to this effect, is,

$$\tau_{\text{nuclear}} = \frac{N_{\text{tot},0}}{\mathcal{L}\sigma_{\text{tot}}k} \ , \tag{2.4}$$

where $N_{\text{tot},0}$ is the initial beam intensity, $\mathcal{L}$ is the initial luminosity, σ_{tot} is the total cross section and k is the number of IPs. Assuming an initial peak luminosity of

$\mathcal{L} = 10^{34}\text{cm}^{-2}\text{s}^{-1}$ and two high-luminosity experiments, the above expression yields an initial decay time of τ= 44.85 h. Equation 2.4 results in the following decay of the beam intensity and luminosity as functions of time

$$N_{\text{tot}}(t) = \frac{N_{\text{tot},0}}{1 + t/\tau_{\text{nuclear}}} \text{ and} \tag{2.5}$$

$$\mathcal{L}(t) = \frac{\mathcal{L}_0}{(1 + t/\tau_{\text{nuclear}})^2}. \tag{2.6}$$

The time required to reach $1/e$ of the initial luminosity is given by

$$t_{1/e} = (\sqrt{(}e) - 1)\tau \ , \tag{2.7}$$

yielding a luminosity decay time of $\tau_{\text{nuclear},1/e} = 29$ h.

Taking into account contributions coming from scattering of particles on residual gas and intra-beam scattering effects (IBS), the net luminosity lifetime can be estimated, approximating further decay by an exponential process, as

$$\frac{1}{\tau_L} = \frac{1}{\tau_{\text{IBS}}} + \frac{2}{\tau_{\text{restgas}}} + \frac{1}{\tau_{\text{nuclear,1/e}}}. \tag{2.8}$$

Assuming an IBS time constant of 80 h and a rest gas time constant of 100 h, together with the above nuclear decay time, a net estimate of the luminosity lifetime of

$$\tau_L = 14.9\text{h} \tag{2.9}$$

is obtained.

2.2 ATLAS detector

ATLAS (**A** **T**oroidal **L**HC Apparatu**S**) is a multipurpose detector. Requirements for the ATLAS detector system have been defined using a set of processes covering much of the new phenomena expected to be observed at the TeV scale.

The high luminosity and increased cross sections at the LHC enable searches for new phenomena as well as high-precision tests of QCD, electroweak interactions and flavour physics. However, such a high luminosity, with an inelastic proton-proton cross section of ∼80 mb, presents a serious experimental difficulty as it implies that

every candidate event for new physics will, on average, be accompanied by ∼23 inelastic events per bunch crossing.

Viewed in this context, these benchmark physics goals can be turned into a set of general requirements for the LHC detectors:

- due to the experimental conditions at the LHC, the detectors require fast, radiation-hard electronics and sensor elements. In addition, high detector granularity is needed to handle the particle fluxes and to reduce the influence of overlapping events;
- large acceptance in pseudorapidity[1] (η) with almost full ϕ coverage is required;
- very good electromagnetic (EM) and hadronic calorimetry. This is essential for electron or positron[2] and photon identification and kinematical variable measurements, and for accurate measurements of the jet transverse energy and missing transverse energy (E_T^{miss}). These measurements form the basis of many physics studies;
- good muon identification and momentum resolution over a wide range of momenta and the ability to determine unambiguously the charge of high p_T muons are fundamental requirements;
- high-efficient triggers for low transverse-momentum objects with sufficient background rejection is a requirement to achieve an acceptable trigger rate for most physics processes of interest.

The ATLAS detector layout is shown in Fig. 2.3 and its main performance goals are listed in Table 2.1. The dimensions of the detector are 25 m height and 44 m in length. The overall weight of the detector is approximately 7000 tonnes.

The ATLAS detector is nominally forward-backward symmetric with respect to the interaction point. The magnet configuration comprises a thin superconducting solenoid surrounding the inner-detector cavity and three large superconducting toroids (one barrel and two end-caps) arranged with and eight-fold azimuthal symmetry around the calorimeters. This fundamental choice has driven the design of

[1]The ATLAS reference system is a Cartesian right-handed coordinate system, with the nominal collision point at the origin. The anticlockwise beam direction defines the positive z-axis, while the positive x-axis is defined as pointing from the collision point to the centre of the LHC ring and the positive y-axis points upwards. The azimutal angle ϕ is measured around the beam axis, and the polar angle θ is measured with respect to the z-axis. Pseudorapidity is defined as $\eta = -\ln \tan(\theta/2)$ and transverse energy is defined as $E_T = E\sin\theta$.

[2]In the following, the term electron will refer to electron or positron, unless otherwise stated.

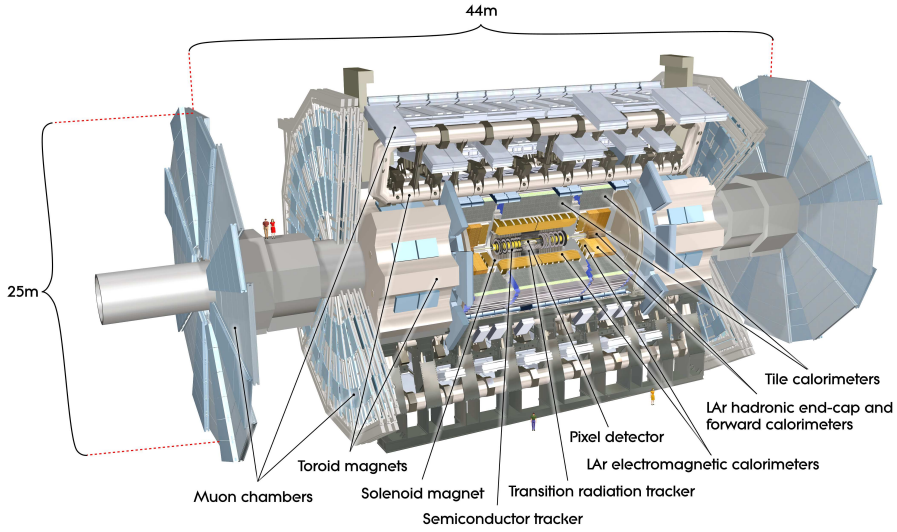

Figure 2.3: Cut-away view of the ATLAS detector.

the rest of the detector.

ATLAS is composed of three main subdetectors:

- the inner detector, immersed in a 2 T solenoidal field. Pattern recognition, momentum and vertex measurements and electron identification are achieved resulting from a combination of discrete, high-resolution semiconductor pixel and strip detectors in the inner part of the tracking volume and straw-tube tracking detectors with the capability to generate and detect transition radiation in its outer part;

- the high granularity liquid-argon (LAr) electromagnetic sampling calorimeter, with excellent performance in terms of energy and position resolution. The LAr covers the range $|\eta| < 3.2$. The hadronic calorimeter, in the range $|\eta| < 1.7$, is provided by a scintillator-tile calorimeter, which is separated into a large barrel and two smaller extended barrel cylinders, each one on either side of the central barrel. In the end-caps ($|\eta| > 1.5$), LAr technology is also used for the hadronic calorimeters, matching the outer $|\eta|$ limits of end-cap electromagnetic calorimeters. The LAr forward calorimeters provide both electromagnetic and hadronic energy measurements and extend the coverage to $|\eta| = 4.9$;

- the muon spectrometer surrounding the calorimeter. The air-core toroid system, with a long barrel and two inserted end-cap magnets, generates strong bending power in a large volume within a light and open structure. Multiple-scattering effects are thereby minimised and excellent muon momentum reso-

lution is achieved with three layers of high-precision tracking chambers. The muon instrumentation includes trigger chambers with timing resolution of order of ≈1.5-4 ns. The muon spectrometer defines the overall dimensions of the ATLAS detector.

2.2.1 Tracking

The ATLAS Inner Detector (ID) was designed to provide hermetic and robust pattern recognition, excellent momentum resolution and both primary-and secondary vertex measurements for charged tracks above a given p_T threshold (nominally 0.5 GeV within the range $|\eta| < 2.5$) [9].

The ID provides tracking measurements in a range matched by the precision measurements of the electromagnetic calorimeter (see section 2.2.2). The electron identification capabilities are enhanced by the detection of transition-radiation photons. The semiconductor trackers also allow impact parameter measurements and vertexing for heavy-flavour and τ-lepton tagging. The secondary-vertex measurements performance is enhanced by the innermost layer of pixels, at a radius of about 5 cm.

Approximately 1000 particles are expected to emerge from the collision point every 25 ns within $|\eta| < 2.5$, creating a very large track density in the detector. The ID achieves high-precision measurements of the momentum and vertex position. The ID also provides electron identification over $|\eta| < 2.0$ and a wide range of energies (between 0.5 GeV and 150 GeV). The layout of the ID is illustrated in Fig. 2.4.

The ID is immersed in a 2 T magnetic field generated by the central solenoid, which extends over a length of 5.3 m with a diameter of 2.5 m. The ID consists of three independent but complementary sub-detectors. The envelopes of each sub-

Detector component	**Required resolution**	**η coverage**
Tracking	σ_{p_T}/p_T =0.05% ⊕ 1%	±2.5
EM calorimetry	σ_E/E =10%/$\sqrt{E}$ ⊕ 0.7%	±3.2
Hadronic calorimeters (jets)		
barrel and end-cap	σ_E/E =50%/$\sqrt{E}$ ⊕ 3%	±3.2
forward	σ_E/E =100%/$\sqrt{E}$ ⊕ 10%	3.1< $\|\eta\|$ <4.9
Muon spectrometer	σ_{p_T}/p_T =10% at p_T = 1 TeV	±2.7

Table 2.1: General performance goals of the ATLAS detector. The units for E and p_T are in GeV.

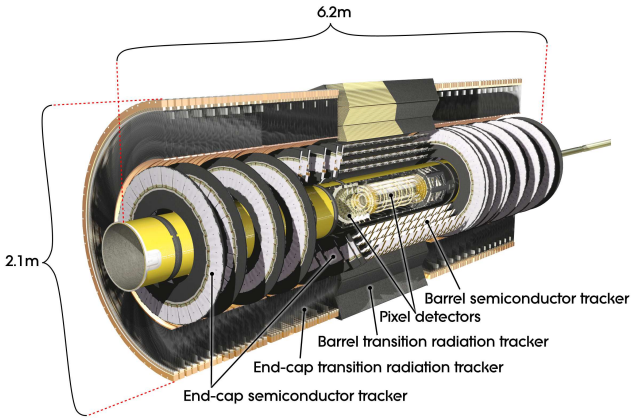

Figure 2.4: Cut-away view of the ATLAS inner detector

.

detector are listed in Table 2.2.

Item		**Radial extension (mm)**	**Length (mm)**
Overall ID envelope		$0 < R < 1150$	$0 < \|z\| < 3512$
Beam-pipe		$29 < R < 36$	
Pixel	Overall envelope	$45.5 < R < 242$	$0 < \|z\| < 3092$
3 cylindrical layers	Sensitive barrel	$50.5 < R < 122.5$	$0 < \|z\| < 400.5$
2×3 disks	Sensitive end-cap	$88.8 < R < 149.6$	$495 < \|z\| < 650$
SCT	Overall envelope	$255 < R < 549$(barrel)	$0 < \|z\| < 805$
		$251 < R < 610$(end-cap)	$810 < \|z\| < 2797$
4 cylindrical layers	Sensitive barrel	$299 < R < 514$	$0 < \|z\| < 749$
2×9 disks	Sensitive end-cap	$275 < R < 560$	$839 < \|z\| < 2735$
TRT	Overall envelope	$554 < R < 1082$(barrel)	$0 < \|z\| < 780$
		$617 < R < 1106$(end-cap)	$827 < \|z\| < 2744$
73 straw planes	Sensitive barrel	$563 < R < 1066$	$0 < \|z\| < 712$
160 straw planes	Sensitive end-cap	$644 < R < 1004$	$848 < \|z\| < 2710$

Table 2.2: Main parameters of the inner-detector system.

At inner radii, high-resolution pattern recognition capabilities are available using discrete space-points from silicon pixel layers and stereo pairs of silicon microstrip (SCT) layers. At larger radii, the transition radiation tracker (TRT) comprises many layers of gaseous straw tube elements interleaved with transition radiation material. With an average of 36 hits per track, the TRT provides continuous tracking to enhance the pattern recognition and improve the momentum resolution for $|\eta| < 2$ and

electron identification complementary to that of the calorimeter over a wide range of energies.

The highest granularity in the ID is found around the vertex region and is achieved using silicon pixel detectors. The pixel layers are segmented in $R-\phi$ and z with typically three pixel layers crossed typically by each track. All pixel sensors are identical and have a minimum pixel size in $R-\phi \times z$ of 50×400 μm^2. The intrinsic accuracies in the barrel are 10 μm for $R-\phi$ and 115 μm for z; in the disks, placed transversally to the simmetry axis of the silicon pixel detector barrel, are 10 μm for $R-\phi$ and 115 μm for R. The pixel detector has ≈80.4 million readout channels.

For the SCT, eight strip layers (four space points) are crossed by each track. In the barrel region, this detector uses small-angle (40 mrad) stereo strips to measure both coordinates, with one set of strips in each layer parallel to the beam direction, measuring $R-\phi$. They consist of two 6.4 cm long daisy-chained sensors with a strip pitch of 80 μm. In the end-cap region, the detectors have a set of strips running radially and a set of stereo strips at an angle of 40 mrad. The mean pitch of the strips is also ≈80 μm. The intrinsic accuracies per module in the barrel are 17 μm for $R-\phi$ and 580 μm for z and in the disk are 17 μm for $R-\phi$ and 580 μm for R. The total number of readout channels in the SCT is ≈6.3 million.

A large number of hits (typically 36 per track) is provided by the 4 mm diameter xenon-based gas mixture straw tubes of the TRT, which enables track-following up to $|\eta| = 2.0$. The TRT only provides $R-\phi$ information, for which it has an intrinsic accuracy of 130 μm per straw. In the barrel region, the straws are parallel to the beam axis and are 144 cm long, with their wires divided into two halves, approximately at η=0. In the end-cap region, the 37 cm long straws are arranged radially in wheels. The total number of TRT readout channels is ≈351.000.

A charged track going through the ID is represented in Fig. 2.5. The track traverses successively the beryllium beam-pipe, the three cylindrical silicon-pixel layers with individual sensor elements of 50×400 μm^2, the four cylindrical double layers (one axial and one with a stereo angle of 40 mrad) of barrel silicon-microstrip sensors of pitch 80 μm, and approximately 36 axial straws of 4 mm diameter contained in the barrel transition-radiation tracker modules within their support structure.

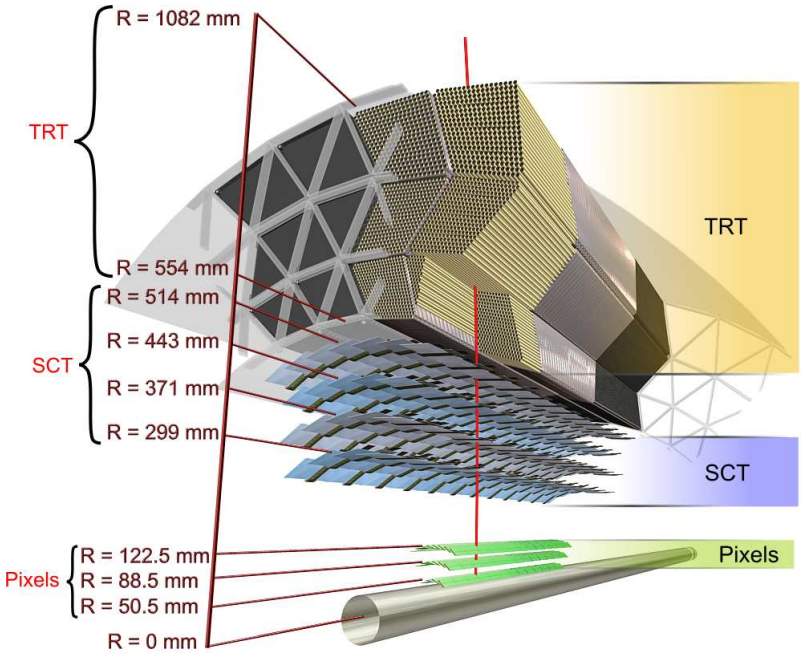

Figure 2.5: Drawing showing the sensor and structural elements traversed by a charged track of 10 GeV p_T in the barrel inner detector (η=0.3).

2.2.2 Calorimetry

A view of the sampling calorimeters is presented in Fig. 2.6. The pseudorapidity coverage, granularity and segmentation in depth of the calorimeters are summarised in Table 2.3.

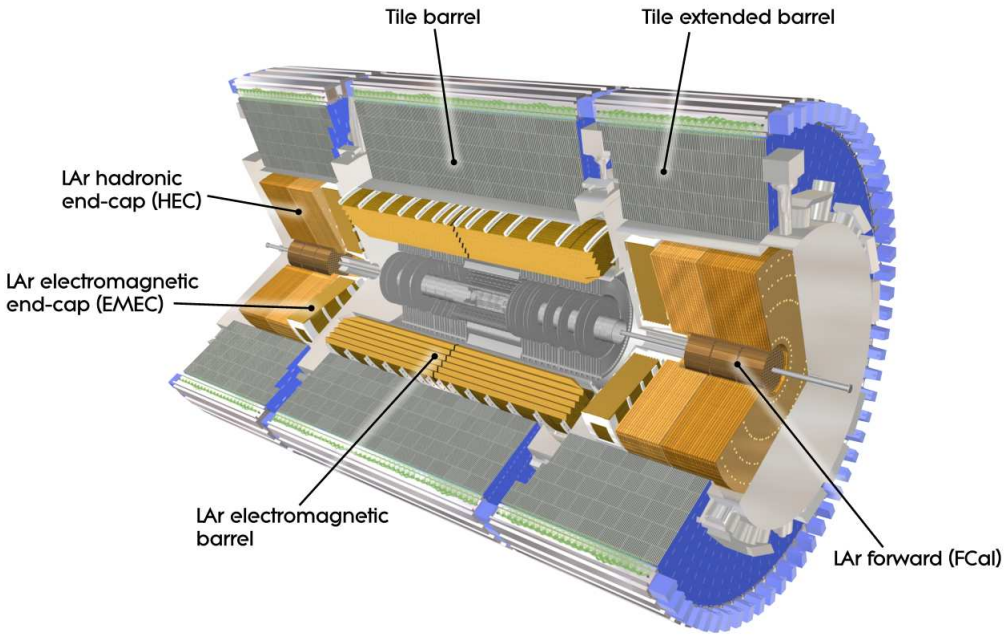

Figure 2.6: Cut-away view of the ATLAS calorimeter system.

These calorimeters cover the range $|\eta|$ <4.9. Different techniques, suited to the widely varying requirements of the physics processes of interest and of the radiation environment over this large $|\eta|$ range, are used [10].

Within the $|\eta|$ region matched to the inner detector, the fine granularity of the EM calorimeter is ideally suited for precision measurements of electrons and photons. The coarser granularity of the rest of the calorimeter is sufficient to satisfy the physics requirements for jet reconstruction and E_T^{miss} measurements.

The ATLAS calorimeters consist of various sampling detectors with full ϕ-symmetry and coverage around the beam axis. The calorimeters closest to the beam-line are housed in three cryostats, one barrel and two end-caps. The barrel cryostat contains the electromagnetic barrel calorimeter, whereas the two end-cap cryostat each contain an electromagnetic end-cap calorimeter (EMEC), a hadronic end-cap calorimeter (HEC), located behind the EMEC, and a forward calorimeter (FCal) to cover

the region closest to the beam. All these calorimeters use liquid argon as the active detector medium; liquid argon has been chosen for its intrinsic linear behavior, its stability of response over time and its intrinsic radiation-hardness.

Calorimeters must provide good containment for electromagnetic and hadronic showers and must also limit punch-through into the muon system. Hence, calorimeter depth is an important design consideration. The total thickness of the EM calorimeter is > 22 radiation lengths (X_0) in the barrel and > 24 X_0 in the end-caps. The $\approx$9.7 interaction lengths (λ) of active calorimeter in the barrel (10 λ in the end-caps) are adequate to provide good resolution for high-energy jets. The total thickness, including 1.3 λ from the outer support, is 11 λ at $\eta = 0$ and has been shown both by measurements and simulations to be sufficient to reduce punch-through well below the irreducible level of prompt or decay muons. Together with the large $|\eta|$ coverage, this thickness also ensures a good E_T^{miss} measurement, which is important for many new physics signatures.

LAr electromagnetic calorimeter

The EM calorimeter is divided into a barrel part ($|\eta| < 1.475$) and two end-cap components ($1.375 < |\eta| < 3.2$), each housed in its own cryostat. The position of the central solenoid in front of the EM calorimeter demands optimisation of the material to achieve the desired calorimeter performance. As a consequence, the central solenoid and the LAr calorimeter share a common vacuum vessel, thereby eliminating two vacuum walls. The barrel calorimeter consists of two identical half-barrels, separated by a small gap (4 mm) at $z = 0$. Each end-cap calorimeter is mechanically divided into two coaxial wheels: an outer wheel covering the region $1.375 < |\eta| < 2.5$ and an inner wheel covering the region $2.5 < |\eta| < 3.2$.

The EM calorimeter is a lead-LAr detector with accordion-shaped kapton electrodes and lead absorber plates over its full coverage. The accordion geometry provides ϕ symmetry without azimuthal cracks. The lead thickness in the absorber plates has been optimised as a function of η in terms of EM calorimeter performance in energy resolution. Over the region devoted to precision physics ($|\eta| < 2.5$), the EM calorimeter is segmented in three sections in depth. For the end-cap inner wheel, the calorimeter is segmented in two sections in depth and has a coarser lateral granularity than for the rest of the acceptance.

In the region of $|\eta| < 1.8$, a presampler detector is used to correct for the energy

lost by electrons and photons upstream of the calorimeter. The presampler consists of an active LAr layer of thickness 1.1 cm (0.5 cm) in the barrel (end-cap) region.

The LAr calorimeter has a fine segmentation in both the lateral, $\eta \times \phi = 0.003 \times 0.1$, 0.025×0.025, 0.05×0.025, respectively, in front, middle and back compartments assisted by a pre-sampler in front of the calorimeter and longitudinal directions.

Hadronic calorimeters

The hadronic calorimeters of the ATLAS detector are: the tile calorimeter, the liquid-argon hadronic end-cap calorimeter (HEC) and the liquid-argon forward calorimeter (FCal).

Tile calorimeter

The Tile is a sampling calorimeter using steel as the absorber and scintillating tiles as the active material. It is placed directly outside the EM calorimeter envelope. The barrel covers the region $|\eta| < 1$ and the two extended barrels cover the range $0.8 < |\eta| < 1.7$. The barrel and extended barrels are divided azimuthally into 64 modules. Radially, the tile calorimeter extends from an inner radius of 2.28 m to an outer radius of 4.25 m. It is segmented in depth in three layers, $\approx$1.5, 4.1 and 1.8 λ thick for the barrel and 1.5, 2.6 and 3.3 λ for the extended barrel. The total detector thickness at the outer edge of the tile-instrumented region is 9.7 λ at $\eta = 0$. Two sides of the scintillating tiles are read out by wavelength-shifting fibres into two separate photon multiplier tubes. In pseudorapidity, the readout cells built by grouping fibres into the photon multipliers are pseudo-projective towards the interaction region.

LAr hadronic end-cap calorimeter

The Hadronic End-cap Calorimeter (HEC) consists of two independent wheels per end-cap, located directly behind the end-cap electromagnetic calorimeter and sharing the same LAr cryostats (see Fig. 2.7). The outer radius of the cylindrical cryostat vessel is 2.25 m and the length of the cryostat is 3.17 m. To reduce the drop in material density at the transition between the end-cap and the forward calorimeter (around $|\eta| = 3.1$), the HEC extends out to $|\eta| = 3.2$, thereby overlapping with the forward calorimeter. Similarly, the HEC η range also overlaps slightly with the tile calorimeter ($|\eta| < 1.7$) by extending up to $|\eta| = 1.5$. Each wheel is built from 32 identical wedge-shaped modules, assembled with fixtures at the periphery and at

the central bore. Each wheel is divided into two segments in depth, with a total of four layers per end-cap. The wheels closest to the interaction point are built from 25 mm parallel copper plates, while those further away use 50 mm copper plates. The outer radius of the copper plates is 2.03 m, while the inner radius is 0.475 m, except in the overlap region with the forward calorimeter where this radius becomes 0.372. The copper plates are interleaved with 8.5 mm LAr gaps, providing the active medium for this sampling calorimeter.

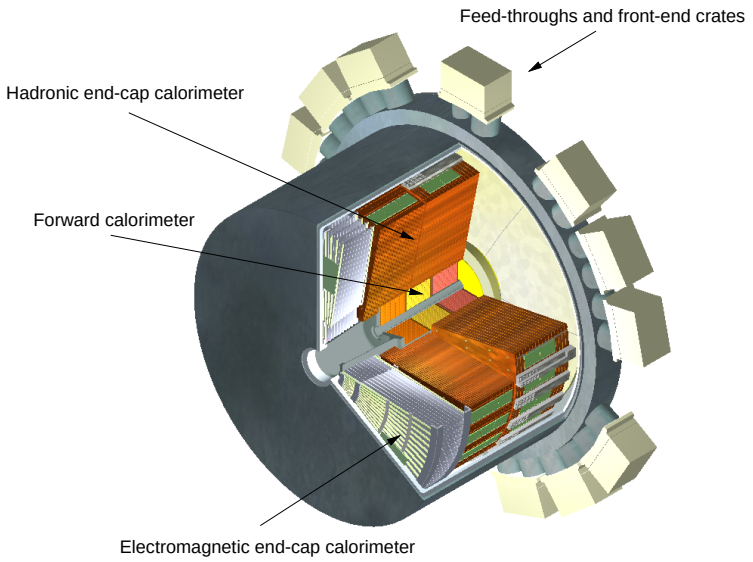

Figure 2.7: Cut-away view of an end-cap cryostat showing the positions of the three end-cap calorimeters.

LAr forward calorimeter

The Forward Calorimeter (FCal) is integrated into the end-cap cryostats, as this provides clear benefits in terms of uniformity of the calorimetric coverage as well as reduced radiation background levels in the muon spectrometer. To reduce the amount of neutron albedo in the inner detector cavity, the front face of the FCal is recessed by about 1.2 m with respect to the EM calorimeter front face. This severely limits the depth of the calorimeters and therefore calls for a high-density design. The FCal is $\approx$10 λ deep, and consists of three modules in each end-cap: the first, made of copper, is optimised for electromagnetic measurements, while the other two, made of tungsten, measure predominantly the energy of hadronic interactions. Each module consists of a metal matrix, with regularly spaced longitudinal channels filled with the electrode structure consisting of concentric rods and tubes parallel to the beam axis. The LAr in the gap between the rod and the tube is the

sensitive medium. This geometry allows for excellent control of the gaps, which are as small as 0.25 mm in the first section, in order to avoid problems due to ion buildup.

2.2.3 Muon spectrometer

The muon spectrometer forms the outer part of the ATLAS detector. It is designed to detect charged particles exiting the barrel and end-cap calorimeters and to measure their momentum in the pseudorapidity range $|\eta|$ <2.7. It is also designed to trigger on these particles in the region $|\eta|$ <2.4. It is based on the magnetic deflection of muon tracks in the large superconducting air-core toroid magnets, instrumented with separate trigger and high-precision tracking chambers [11]. The conceptual layout of the muon spectrometer is shown in Fig. 2.8.

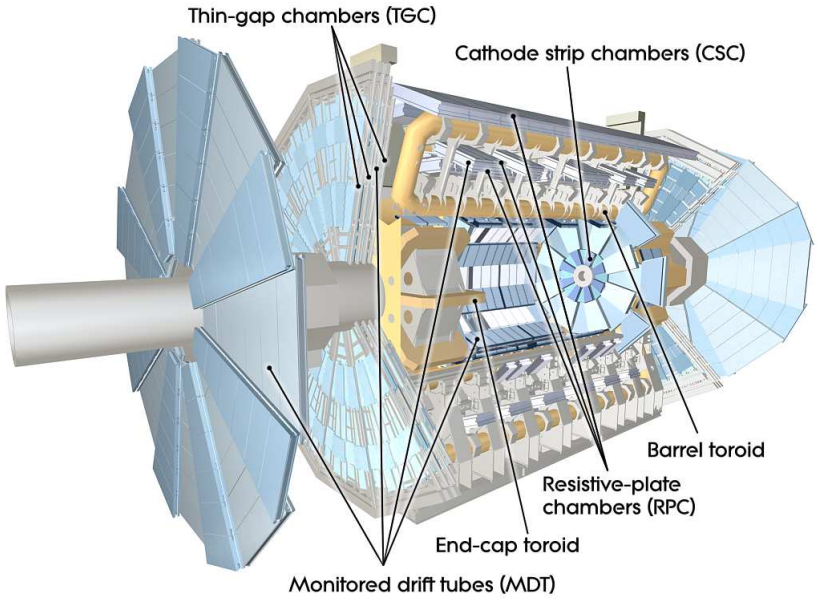

Figure 2.8: Cut-away view of the ATLAS muon system

In the range $|\eta|$ <1.4, magnetic bending is provided by the large barrel toroid. The barrel toroid provides 1.5 to 5.5 Tm of bending power in the pseudorapidity range 0< $|\eta|$ <1.4. For 1.6< $|\eta|$ <2.7, muon tracks are bent by two smaller end-cap magnets inserted into both ends of the barrel toroid. The end-cap toroids provide ≈1 to 7.5 Tm in the region 1.6< $|\eta|$ <2.7. For 1.4< $|\eta|$ <1.6, usually referred to as the transition region, magnetic deflections are provided by a combination of barrel and end-cap fields. This magnet configuration provides a field which is mostly orthogonal to the muon trajectories, while minimising the degradation of resolution due to multiple scattering. The anticipated high level of particle flux has had a ma-

jor impact on the choice and design of the spectrometer instrumentation, affecting performance parameters such as rate capability, granularity, ageing properties and radiation hardness.

	barrel		**endcap**	
EM calorimeter				
Number of layers and $\|\eta\|$ coverage				
Presampler	1	η <1.52	1	1.5< $\|\eta\|$ <1.8
Calorimeter	3	$\|\eta\|$ <1.35	2	1.375< $\|\eta\|$ <1.5
	2	1.35< $\|\eta\|$ <1.475	3	1.5< $\|\eta\|$ <2.5
			2	2.5< $\|\eta\|$ <3.2
Granularity $\Delta\eta \times \Delta\phi$ versus $\|\eta\|$				
Presampler	0.025×0.1	η <1.52	0.025×0.1	1.5< $\|\eta\|$ <1.8
Calorimeter 1st layer	0.025/8×0.1	$\|\eta\|$ <1.40	0.050×0.1	1.375< $\|\eta\|$ <1.425
	0.025×0.025	1.40< $\|\eta\|$ <1.475	0.025×0.1	1.425< $\|\eta\|$ <1.5
			0.025/8×0.1	1.5< $\|\eta\|$ <1.8
			0.025/6×0.1	1.8< $\|\eta\|$ <2.0
			0.025/4×0.1	2.0< $\|\eta\|$ <2.4
			0.025×0.1	2.4< $\|\eta\|$ <2.5
			0.1×0.1	2.5< $\|\eta\|$ <3.2
Calorimeter 2st layer	0.025×0.025	$\|\eta\|$ <1.40	0.050×0.025	1.375< $\|\eta\|$ <1.425
	0.075×0.025	1.40< $\|\eta\|$ <1.475	0.025×0.025	1.425< $\|\eta\|$ <2.5
			0.1×0.1	2.5< $\|\eta\|$ <3.2
Calorimeter 3rd layer	0.050×0.025	$\|\eta\|$ <1.35	0.050×0.025	1.5< $\|\eta\|$ <2.5
Number of readout channels				
Presampler	7808		1536(both sides)	
Calorimeter	101760		62208(both sides)	
LAr hadronic end-cap				
$\|\eta\|$coverage			1.5< $\|\eta\|$ <3.2	
Number of layers			4	
Granularity $\Delta\eta \times \Delta\phi$			0.1×0.1	1.5< $\|\eta\|$ <2.5
			0.2×0.2	2.5< $\|\eta\|$ <3.2
Readout channels			5632 (both sides)	
LAr forward calorimeter				
$\|\eta\|$coverage			3.1< $\|\eta\|$ <4.9	
Number of layers			3	
Granularity $\Delta\eta \times \Delta\phi$ (cm)			FCal1: 3.0×2.6	3.15< $\|\eta\|$ <4.30
			FCal1: ≈four times finer	3.10< $\|\eta\|$ <3.15
				4.30< $\|\eta\|$ <4.83
			FCal2: 3.3×4.2	3.24< $\|\eta\|$ <4.50
			FCal2: ∼four times finer	3.20< $\|\eta\|$ <3.24
				4.50< $\|\eta\|$ <4.81
			FCal3: 5.4×4.7	3.32< $\|\eta\|$ <4.60
			FCal3: ∼four times finer	3.29< $\|\eta\|$ <3.32
				4.60< $\|\eta\|$ <4.75
Redout channels			3524	
Scintillator tile calorimeter				
	Barrel		Extended barrel	
$\|\eta\|$ coverage	$\|\eta\|$ <1.0		0.8< $\|\eta\|$ <1.7	
Number of layers	3		3	
Granularity $\Delta\eta \times \Delta\phi$	0.1×0.1		0.1×0.1	
Last layer	0.2×0.1		0.2×0.1	
Readout channels	5760		4092 (both sides)	

Table 2.3: Main parameters of the calorimetry system.

Monitored drift tubes	**MDT**
-Coverage	$\|\eta\|$ <2.7 (innermost layer: $\|\eta <$ |2.0
-Number of chambers	1088(1150)
-Number of channels	339000(354000)
-Function	Precision tracking
Cathode strip chambers	**CSC**
-Coverage	2.0< $\|\eta\|$ <2.7
-Number of chambers	32
-Number of channels	31000
-Function	Precision tracking
Resistive plate chambers	**RPC**
-Coverage	$\|\eta\|$ <1.05
-Number of chambers	544(606)
-Number of channels	359000(373000)
-Function	Triggering, second coordinate
Thin gap chambers	**TGC**
-Coverage	1.05< $\|\eta\|$ <2.7 (2.4 for triggering)
-Number of chambers	3588
-Number of channels	318000
-Function	Triggering, second coordinate

Table 2.4: Main parameters of the muon spectrometer. Numbers in brackets for MDT's and the RPC's refer to the final configuration of the detector in 2009.

The precision momentum measurement is performed by the Monitored Drift Tube chambers (MDT's), which combine high-measurement accuracy, predictability of mechanical deformations and simplicity of construction. They cover the pseudo-rapidity range $|\eta| < 2.7$, except in the innermost end-cap layer where their coverage is limited to $|\eta| < 2.0$. These chambers consist of three to eight layers of drift tubes, operated at an absolute pressure of 3 bar and achieve an average resolution of 80 μm per tube, or about 35 μm per chamber.

In the forward region ($2< |\eta| <2.7$), Cathode-Strip Chambers (CSC) are used in the innermost tracking layer due to their higher rate capability and time resolution. The CSC are multi-wire proportional chambers with cathode planes segmented into strips in orthogonal directions. This allows both coordinates to be measured from the induced-charge distribution. The resolution of a chamber is 40 μm in the bending plane for η and about 5 mm in the transverse plane for ϕ.

The precision-tracking chambers have been complemented by a system of fast trigger chambers capable of delivering track information within a few tens of nanoseconds after the passage of a particle. In the barrel region ($|\eta| <1.05$), Resistive Plate Chambers (RPC) were selected for this purpose, while in the end-cap ($1.05< |\eta| <2.4$) Thin Gap Chambers (TGC) were chosen. The design goal was to keep these contributions low enough for reliable beam-crossing identification with $\geq 99\%$ probability. Both chamber types deliver signals with a spread of 15-25 ns, thus providing the ability to tag the beam crossing. The trigger chambers measure both coordinates of the track, one in the bending plane and one in the non-bending plane. The main parameters of the muon chambers are listed in Table 2.4.

2.2.4 Forward detectors

Three smaller detector systems cover the ATLAS forward region. The main function of the first two systems is to determine the luminosity delivered to ATLAS. Ordered according to their distance from the interaction point, as shown in Fig. 2.9, the first system is a Cerenkov detector called LUCID (Luminosity measurement using Cherenkov Integrating Detector). LUCID is the main relative luminosity monitor in ATLAS, located at a distance of $\pm$17 m from the interaction point. It detects inelastic *pp* scattering in the forward direction.

The second system is the Zero-Degree Calorimeter (ZDC), located at a distance of $\pm$140 m from the interaction point. This corresponds to the location where the LHC beam-pipe is divided into two separate pipes. The ZDC's primary purpose is to

detect forward neutrons in heavy-ion collisions. The ZDC modules consist of layers of alternating quartz rods and tungsten plates which measure particles at $|\eta| \geq 8.2$.

The most remote detector is the absolute luminosity detector ALFA (Absolute Luminosity For ATLAS). It detects inelastic pp scattering in the forward direction and is the main online relative-luminosity monitor for ATLAS. It consists of scintillating fiber trackers located inside Roman pots which are designed to approach as close as 1 mm to the beam.

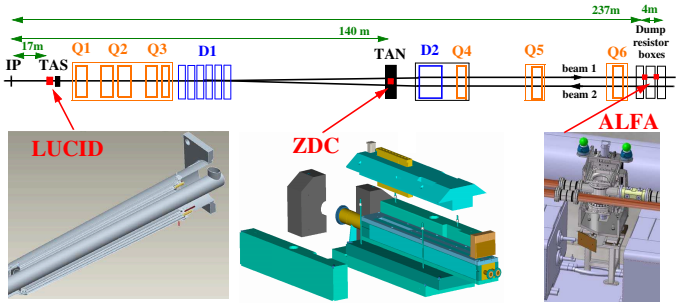

Figure 2.9: Placement of the forward detectors along the beam-line around the ATLAS interaction point.

2.2.5 Trigger system

The trigger system has three distinct levels: Level-1 (L1), Level-2 and the Event Filter (EF). Each trigger level refines the decisions made at the previous level and, where necessary, applies additional selection criteria. The L2 and EF together form the High-Level Trigger (HLT). The L1 trigger is implemented using custom-made electronics, while the HLT is almost entirely based on commercially available computers and networking hardware [12].

L1 trigger

The L1 trigger searches for signatures from high-p_T muons, electrons/photons, jets and τ-leptons decaying into hadrons. It also selects events with large E_T^{miss} and large total transverse energy. The L1 trigger uses reduced-granularity information from a subset of detectors: RPC and TGC for high-p_T muons, and all the calorimeter subsystems for electromagnetic clusters, jets, τ-leptons, E_T^{miss} and large total transverse energy. The maximum L1 accept rate which the detector readout systems can handle is 75 kHz (upgradeable to 100kHz) and the L1 decision must reach the front-end

electronics within 2.5 μs after the bunch-crossing with which it is associated. The flow of the L1 trigger is shown in Fig. 2.10.

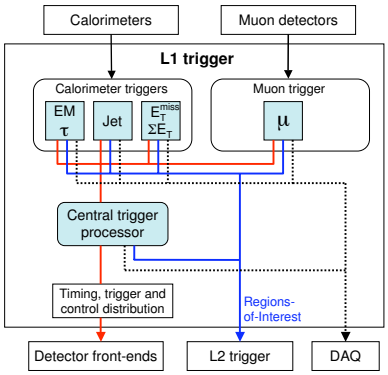

Figure 2.10: Block diagram of the L1 trigger. The overall L1 accept decision is made by the central trigger processor, taking input from calorimeter and muon trigger results. The paths to the detector front-ends, L2 trigger and data acquisition system are shown from left to right in red, blue and black, respectively.

The L1 Calorimeter Trigger

The L1 Calorimeter Trigger (L1Calo) aims to identify high-E_T objects such as electrons and photons, jets and τ-leptons decaying into hadrons, as well as events with large E_T^{miss} and large total transverse energy. For the electron/photon and τ triggers, isolation can be required. Isolation implies that the energetic particle must have a minimum angular separation from any significant energy deposit in the same trigger.

L1Calo is a pipelined digital system designed to work about 7000 analogue trigger towers of reduced granularity (0.1×0.1 in $\Delta\eta \times \Delta\phi$ innermost parts, but larger at higher $|\eta|$) from the electromagnetic and hadronic calorimeters. The L1Calo system is located off-detector. Its architecture consists of three main subsystems. The pre-processor digitises the analogue input signals, then uses a digital filter to associate them with specific bunch crossings. The data are then transmitted to both the Cluster Processor (CP) and Jet/Energy-sum Processor (JEP) subsystems in parallel. The CP subsystem identifies electron/photon and τ-lepton candidates with E_T above the corresponding programmable threshold and satisfying, if required, certain isolation criteria.

The cluster processor module

The electron/photon trigger algorithm [12], shown in Fig. 2.11, identifies 2×2 clusters of trigger towers in which at least one of the four possible two-tower sum (1×2 or 2×1) of nearest-neighbour electromagnetic towers exceeds a predefined threshold. Isolation-veto thresholds are set for the 12-tower surrounding ring in the electromagnetic calorimeter, as well as for the 2×2 hadronic-tower core sum behind the cluster and the 12-tower hadronic ring around it. All these thresholds are programmable.

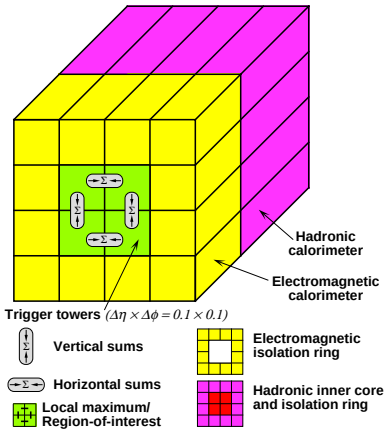

Figure 2.11: Electron/photon trigger algorithm, as described in the text.

High-energy clusters generally have looser isolation criteria to maximise the efficiency for possible low-rate exotic signal processes, while lower-energy clusters have stricter isolation criteria in order to minimise the rates, at the expense of a limited loss of signal.

This algorithm is run over all possible 4×4 windows, which means that the windows overlap and slide by steps of 0.1 in both η and ϕ. Thus, an electron/photon cluster can satisfy the algorithm in two or more neighbouring windows. Multiple-counting of clusters is avoided by requiring the sum of the four central electromagnetic plus the sum of the four central hadronic towers to be a local maximum with respect to its eight nearest overlapping neighbour. To avoid problems in comparing digital sums with identical values, four of the eight comparisons are "greater than" while the other four are "greater than or equal to", as shown in Fig 2.12. The location of this 2×2 local maximum also defines the coordinates of the electron/photon Region of Interest (RoI).

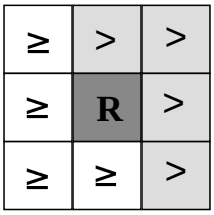

Figure 2.12: E_T local-maximum test for a cluster/RoI candidate. The η-axis runs from left to right and the ϕ-axis from bottom to top. The symbol R refers to the candidate 2×2 region being tested.

The L2 and EF triggers

The L2 trigger is seeded by RoIs. These are regions of the detector where the L1 trigger has identified possible trigger objects within the event. The L2 trigger uses RoI information on coordinates, energy and type of signature to limit the amount of data which must be transferred from the detector readout. The L2 trigger reduces the event ratio to below 3.5 kHz, with an average event processing time of approximately 40 ms.

The EF uses offline analysis procedures on fully-built events to further select events down to a rate which can be recorded for subsequent offline analysis. It reduces the event rate to ≈200 Hz, with an average event processing time of ≈4 seconds.

Chapter 3

Theoretical framework

In this chapter, the most relevant aspects of the theoretical framework underlying the work presented here are reviewed, such as

- the parton model and the QCD-improved parton model;
- short-time interactions and ultraviolet and final-state divergences;
- long-time interactions, PDFs and initial-state divergences;
- characteristics of prompt-photon production;
- jet algorithms.

The theoretical context of the discussions included in this chapter refers to hadron-hadron collisions. However, to simplify and take into account only the most relevant aspects, the final- and initial-state divergences are explained in the context of $e^+e^- \to q\bar{q}$ and $ep \to e + X$ processes. The final part of this chapter is dedicated to jet algorithms and prompt-photon production in hadron-hadron collisions, where concepts such as photon fragmentation functions, next-to-leading order corrections to prompt-photon production, differences between prompt- and isolated-prompt production, guidelines of jet algorithms and next-to-leading order calculations are discussed in detail.

3.1 The parton model

In the parton model [13], hadrons are considered as extended objects made up of point-like constituents (partons) held together by their mutual interactions. These partons can be identified with the quarks and gluons.

The underlying process of a hadron-hadron collision is considered as the elastic scattering between point-like partons inside the hadrons (see Fig. 3.1), which are considered to be free during the short time of the interaction. The total cross section for a generic deeply inelastic scattering of two hadrons can be written as

$$\sigma = \int dx_1 f_{q_1/h_A}(x_1) \int dx_2 f_{q_2/h_B}(x_2)\ \hat{\sigma}(x_1, x_2, \hat{s}), \quad \hat{s} = x_1 x_2 s\ , \tag{3.1}$$

where $\hat{\sigma}$ is the cross section of the parton underlying process, x_1 (x_2) is the momentum fraction of parton q_1 (q_2) with respect to the colliding hadron h_A (h_B), $\hat{s}$ is the invariant mass of the parton-parton collision and f_{q_1/h_A} (f_{q_2/h_B}) is the parton distribution function (PDF) of parton q_1 (q_2) inside hadron h_A (h_B).

The $f_{q/h}(x)\ dx$ represents the probability of finding a parton q inside hadron h with a momentum fraction between x and $x + dx$. The PDF is universal, which means it is independent of the process.

In hadron-hadron interactions, the magnitudes of the momenta of the colliding partons are not necessarily equal. It is necessary, in general, to do a boost along the colliding axis to get to the parton-parton centre-of-mass frame. For this reason, it is useful to use a variable that transforms simply under boosts. This is the motivation for using the rapidity y. For two colliding partons along the z axis, the y of a final-state particle with energy E and momentum p_z is defined as

$$y = \frac{1}{2}\ln\Big(\frac{E + p_z}{E - p_z}\Big)\ , \tag{3.2}$$

which transforms under a boost ω along the z axis as

$$y \to y + \omega. \tag{3.3}$$

In Eq. 3.1, σ is factorised into a part which describes the hard interaction at partonic level, $\hat{\sigma}(x_1, x_2, \hat{s})$, and the PDF which describes the long time-scale dynamics of a parton inside the hadron [14]. Therefore, Eq. 3.1 states that the total cross section at hadronic level can be expressed as the convolution of the PDFs with the hard process cross section.
In a hadron-hadron scattering at high energy and momentum transfer, the interaction is Lorentz contracted in the direction of the collision and the internal interactions of partons are time dilated. As the centre-of-mass energy increases, the lifetime of any virtual partonic state is lengthened, while the time it takes the parton from the other hadron to traverse the hadron is shortened. When the time of the traversing parton is much shorter than the internal interaction time of the partons,

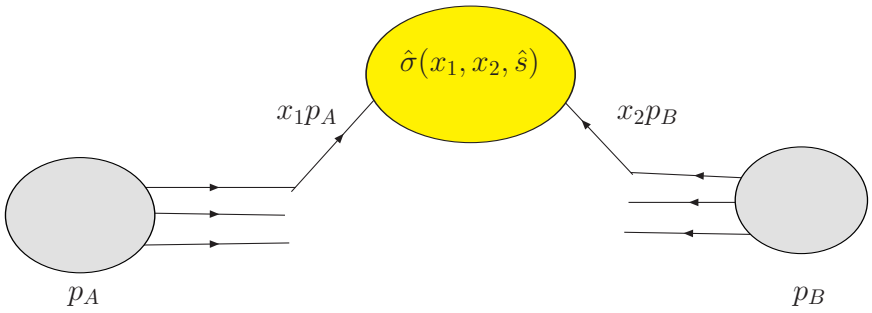

Figure 3.1: Schematic representation for a generic deeply inelastic scattering of two hadrons.

the hadron will be in a single virtual state characterised by a definite number of partons during the entire time the interacting parton takes to cross it. Since the partons do not interact during this time, each one may be thought of as carrying a definite fraction x of the hadron momentum in the centre-of-mass frame. In this sense, a parton-parton hard interaction with definite momentum is produced. In addition, when the momentum transfer is very high, the virtual particle which mediates parton-parton scattering cannot travel very far. Then, if the density of partons is not too high, there is only interaction between single partons. Besides, the interactions of the partons between themselves which occur before and after the hard scattering (long-time scales interactions), with time scales much bigger than the time scale of the hard scattering, do not interfere with the hard interaction between partons (short-time scales interactions). For all these reasons, factorisation of the total cross section for a given hard process becomes a good approximation.

Generally, $\hat{\sigma}(x_1, x_2, \hat{s})$ is calculable by first principles in quantum field theory. However, the PDFs are not calculable due to the low-energy regime of the parton dynamics inside the hadrons and the non-perturbative character of the interaction. They have to be determined using data.

3.2 The QCD-improved parton model

Quantum chromodynamics (QCD) [15] is the theory of the strong interactions. It is formulated in terms of elementary fields: quarks, antiquarks and gluons, whose interactions obey the principles of a relativistic quantum field theory (QFT), with a non-abelian gauge invariance based on the group SU(3). Quarks and antiquarks are particles with spin-1/2 which interact via the exchange of spin-1 gluons.

One of the fundamental differences between QCD and quantum electrodynamics (QED), is that the gauge particles of QCD (gluons) can interact with each other, unlike photons. This fact is due to the non-abelian character of the QCD gauge symmetry group. The leading order Feynman diagrams of the processes $q\bar{q} \to g$, $gg \to g$ and $q \to gq$ are shown in Fig. 3.2.

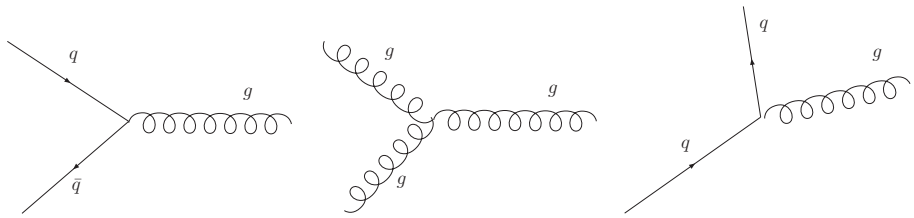

Figure 3.2: LO Feynman diagrams of the process (a) $q\bar{q} \to g$, (b) $gg \to g$ and (c) $q \to gq$.

The most fundamental principle of QCD is that hadronic matter is made out of quarks [16]. The idea of quarks arose from the need to have a physical manifestation of the SU(3) group of flavour [$SU(3)_f$] observed in the spectrum of the lowest-mass mesons and baryons. The properties of the six known quarks are shown in Table 3.1.

Quark	**Charge**	**Mass**	**Baryon Number**	**Isospin**
u	$+\frac{2}{3}$	$\sim$ 4 MeV	$\frac{1}{3}$	$+\frac{1}{2}$
d	$-\frac{1}{3}$	$\sim$ 7 MeV	$\frac{1}{3}$	$-\frac{1}{2}$
c	$+\frac{2}{3}$	$\sim$ 1.5 GeV	$\frac{1}{3}$	0
s	$-\frac{1}{3}$	$\sim$ 135 MeV	$\frac{1}{3}$	0
t	$+\frac{2}{3}$	$\sim$ 175 GeV	$\frac{1}{3}$	0
b	$-\frac{1}{3}$	$\sim$ 5 GeV	$\frac{1}{3}$	0

Table 3.1: The properties of the six types of quarks.

In this model, baryons are formed by three quarks (or antiquarks) and mesons by quark-antiquark pairs. They are the so-called valence quarks. The importance of the valence quarks is that they determine the charge and flavour of the hadron. For example, a proton is made out of uud quarks (two quarks of type *up* and one quark of type *down*) and a pion (π^+) is composed by $u\bar{d}$ (one quark of type *up* and one antiquark of type *down*). However, the internal structure of hadrons cannot be explained in such simple terms. Due to the dynamics and the interactions between quarks, gluons can be radiated by the valence quarks and then they can split into

quark-antiquark pairs. Therefore, there is a probability of finding gluons and quarks with flavours different than those of the valence quarks inside the hadron. This kind of quarks are called sea quarks. As a result, hadrons are considered to be composed of quarks, antiquarks and gluons.

Fig. 3.3 shows a recent parametrisation of the parton momentum fraction (x) times the proton PDF ($f_{q/p}(x)$) as a function of x [17]. It can be observed that the valence quarks have predominantely higher x values, whereas gluons and sea quarks have lower x values.

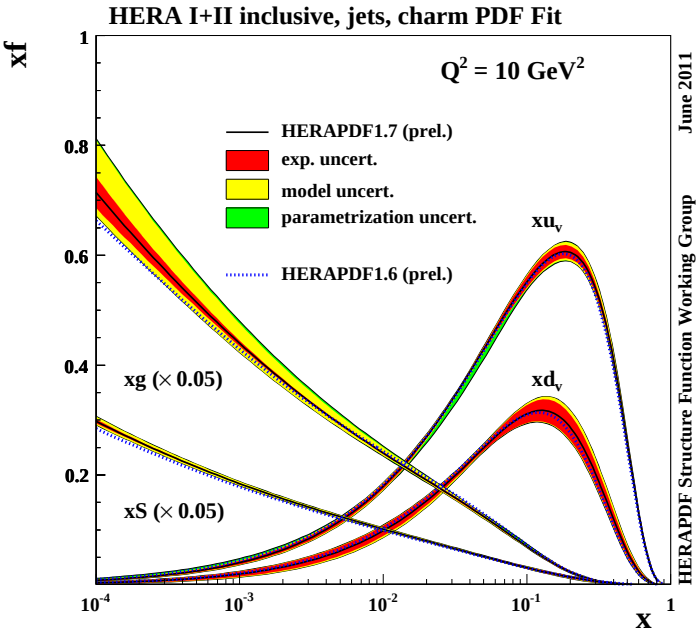

Figure 3.3: $xf_{q/p}(x)$ as a function of x for the proton. The u_v and d_v are the PDF of valence quarks, S is the PDF of the sea quarks and g the PDF of the gluon.

3.2.1 Short-time scale interactions

As discussed in Section 3.1, $\hat{\sigma}(x_1, x_2, \hat{s})$ represents the partonic-level hard interaction. Normally, this cross section can be calculated using perturbation theory and the corresponding Feynman diagrams. The application of Feynman diagrams to carry out computations in perturbation theory is extremely convenient. It provides a very useful bookkeeping technique to account for all contributions to a process at a given order in the coupling constant of the theory. The number of diagrams

contributing to a process grows very fast with the order in perturbation theory and the integrals that appear when calculating loop diagrams also get very complicated. Generally, the cross section $\hat{\sigma}$ can be expressed as

$$\hat{\sigma} = \hat{\sigma}^{(0)} + \alpha \cdot \hat{\sigma}^{(1)} + \alpha^2 \cdot \hat{\sigma}^{(2)} + ..., \tag{3.4}$$

where $\hat{\sigma}^0$ is the contribution of $\hat{\sigma}$ at leading order (LO), $\hat{\sigma}^1$ is the contribution at next-to-leading order (NLO) and α is the coupling constant of the theory [1], for example, α_s in the case of QCD. It turns out that at higher orders the terms of the expansion, calculated according to the standard Feynman rules, come out formally infinite. These infinities are related to the appearance of loops and result from the integration over the unconstrained loop momenta. Integrating over the loop momenta, two basic kinds of divergences are encountered

- ultraviolet divergences (UV), coming from integration over large values of the loop momenta. The UV divergences are dealt with using the renormalisation method;
- mass divergences, coming from integration over the region of small virtualities. These small virtualities appear in two different situations:
  - for vanishingly small energy and momentum of the virtual particles. These so-called infrared (IR) divergences occur for massless particles;
  - whenever two of the three particles, for example, in the QCD vertex qgq become parallel to each other. These singularities are called collinear divergences.

The mass divergences are related to the behaviour of gauge theories at large distances (long times), in contrast to the UV divergences, which come from short distances.

Ultraviolet divergences

As explained before, some divergences result from the integration over large values of the loop momenta. These divergences are dealt with using a renormalisation method. The renormalisation procedure is not only a technique for removing unpleasant UV infinities, but also the way for obtaining an effective description of quantum phenomena.

[1] A value $\alpha << 1$ is needed for the application of perturbation theory to be valid.

Loop integrals in Feynman diagrams get large contributions from momenta much larger than Q, where Q is the typical scale of the hard process. That is, there are large contributions from interactions that happen on time scales much smaller than $t_Q = 1/Q$. For an ultraviolet cut-off M that is much larger than Q, it is possible to calculate the effect of fluctuations with $1/M < \Delta t$ up to some order of perturbation theory. There is a remarkable theorem [18] which states that the effect of the fluctuations ($\Delta t < 1/M$) are not particularly small, but they can be absorbed into changes in the couplings of the theory (α_s), changes in the masses of the theory (m_q) and adjustments to the normalisation of the field operators (Z_ψ). The procedure to absorb very short-time physics into a few parameters is called renormalisation.

There are several schemes available for renormalisation: minimal subtraction scheme (MS), $\overline{\text{MS}}$ scheme, on-shell scheme, etc. Each of them involves the introduction of some scale parameter, μ_R, that is not intrinsic to the theory but gives the order of the renormalisation scale. One interpretation of μ_R is that the physics of time scales $\Delta t \ll 1/\mu_R$ is removed from the perturbative calculation. The effect of the small-time physics is accounted for by adjusting the values of $\alpha_s = \alpha_s(\mu_R)$, $m_q = m_q(\mu_R)$ and $Z_\psi = Z_\psi(\mu_R)$.

As μ_R is an arbitrary parameter, the observables can not depend on the value of μ_R. Therefore, shifts in the observables due to variations of μ_R should cancel order by order in perturbation theory by changes in the coupling constant, mass and the normalisation of the field operators. The relation between changes in the renormalisation of the scale μ_R and the corresponding shifts in α_s, m_q and Z_ψ are described in terms of the Callan-Symanzik equation [19].

For a dimensionless physical observable R, which depends on the coupling constant α_s and on the energy scale Q, the calculation of R as a perturbation series in the coupling constant α_s, a renormalisation procedure is needed to remove the UV divergences. As explained before, the renormalisation procedure introduces a mass scale μ_R. Due to the fact that R is a dimensionless observable, after renormalisation, it must depend on the ratio Q^2/μ^2. Mathematically, the μ_R independence of R may be expressed by

$$\mu_R^2 \frac{d}{d\mu_R^2} R(Q^2/\mu^2, \alpha_s) = \left(\mu_R^2 \frac{\partial}{\partial \mu_R^2} + \beta(\alpha_s) \frac{\partial}{\partial \alpha_s} \right) R(Q^2/\mu^2, \alpha_s) = 0 \ . \tag{3.5}$$

The solution of this first-order partial differential equation is $R = R(1, \alpha_s(Q^2/\mu^2))$, where

$$\mu^2 \frac{\partial \alpha_s(Q^2/\mu^2)}{\partial \mu^2} = \beta(\alpha_s(Q^2/\mu^2)) \ . \tag{3.6}$$

The dimensionless $\beta(\alpha_s(Q^2/\mu^2))$ function is the so-called β function and it is related to the shifts in the coupling constant. The scale dependence on R enters through the running of the coupling constant $\alpha_s(Q^2/\mu^2)$.

The β function in QCD

In QCD, the perturbative expansion to the β function is given by

$$\beta(\alpha_s) = -b\alpha_s^2 + O(\alpha_s^3) \ , \tag{3.7}$$

where

$$b = \frac{33 - 2n_f}{12\pi} \tag{3.8}$$

and n_f is the number of active light flavours. The solution of Eq. 3.6 with the β function expressed as in Eq. 3.7 is

$$\alpha_s(Q^2) = \frac{\alpha_s(\mu_R^2)}{1 + \alpha_s(\mu_R^2)bt}, \qquad t = \ln\frac{Q^2}{\mu_R^2} \ . \tag{3.9}$$

This gives the relation between $\alpha_s(Q^2)$ and $\alpha_s(\mu_R)$, if both are in the perturbative regime. Equation 3.9 shows that as t become large, the running coupling $\alpha_s(Q^2)$ decreases. This is the property of asymptotic freedom. The sign of b is crucial. The coupling constant would increase as a function of t with an opposite sign of b, as it happens with the QED coupling constant. Figure 3.4 shows the evolution of α_s as a function of Q [20].

The increasing behaviour of α_s at lower scales is another interesting aspect of Eq. 3.9 which can explain why quarks and gluons are bound inside hadrons. At a certain energy, $\alpha_s > 1$, giving rise to a break down of the perturbation theory. The energy at which $\alpha_s \sim 1$ defines $\Lambda_{\rm QCD}$. This parameter represents a fundamental energy scale parameter, which appears in the theory entirely due to the renormalisation procedure. This phenomenon is called dimensional transmutation and is typical for theories with dimensionless coupling constants as QCD. The value of $\Lambda_{\rm QCD}$ depends on the adopted renormalisation scheme, being $100 \lesssim \Lambda_{\rm QCD} \lesssim 400$ MeV for the $\overline{\rm MS}$ scheme.

Asymptotic freedom implies that QCD acts like a weakly interacting theory for short time scales. It is true that quarks and gluons are strongly bound inside hadrons, but this strong binding is the result of weak forces acting collectively over a long time.

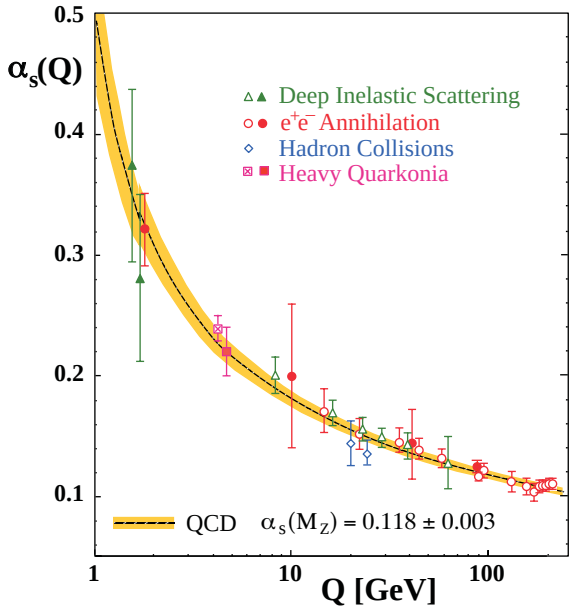

Figure 3.4: Evolution of the QCD coupling constant (α_s) as a function of Q. The line is the QCD prediction and the points are data from various experiments.

Final-state infrared and collinear divergences

There are two kinds of final-state infrared and collinear divergences in a QCD calculation:

- divergences coming from terms due to the radiation of a real parton by a final-state particle (real terms);
- divergences coming from terms due to loops of virtual partons (virtual terms).

The real and virtual terms have to be taken into account in the calculation of the cross section. The notable fact is that divergences due to the virtual terms are canceled by the divergences obtained in the calculation of the real terms. As an example, the production of a quark-antiquark pair by colliding an electron and a positron is considered. The Feynman diagram for the LO contribution is shown in Fig. 3.5. Fig. 3.6 shows the NLO virtual contributions to $e^+e^- \to q\bar{q}$ whereas the NLO real contributions to $e^+e^- \to q\bar{q}$ are shown in Fig. 3.7.

The inclusion of virtual-gluon (Fig. 3.6) emissions cures the mass singularity. A quark can radiate a virtual gluon, which eventually recombines with the parent quark (Fig. 3.6(b) or (c)), or with an accompanying antiquark, as shown in Fig. 3.6(a), producing a real $q\bar{q}$ pair in the final state. In both cases, the virtual gluon can be arbitrarily close to its mass-shell and thus propagate to arbitrary large distances. Integration over the loop of Fig. 3.6, therefore, also leads to mass singularities.

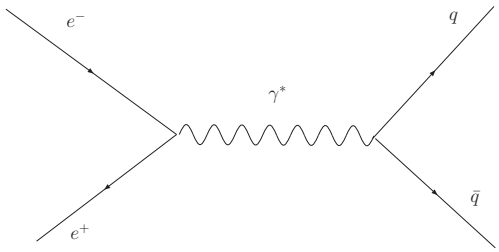

Figure 3.5: LO Feynman diagrams for the process $e^+e^- \to q\bar{q}$.

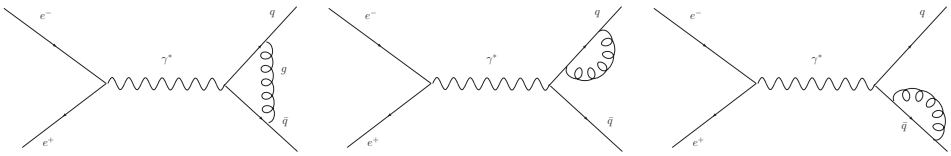

(a) (b) (c)

Figure 3.6: Feynman diagrams for the NLO virtual corrections to the process $e^+e^- \to q\bar{q}$.

It is evident that the interference term (σ_{virtual}) between LO (Fig. 3.5) and the loop diagrams (Fig. 3.6) is of the same order α_s as the square of the diagram in Fig. 3.7 (σ_{real}). The crucial observation is the following: the infinity due to the mass divergence of the virtual correction to $\sigma(e^+e^- \to q\bar{q})$ cancels exactly the infinity coming from the integral over the real gluon emission. So, if the real and virtual-gluon emission cross sections are considered,

$$\sigma_{\text{tot}} = \sigma_{\text{real}} + \sigma_{\text{virtual}}, \tag{3.10}$$

a finite result for the total cross section (σ_{tot}) is obtained. Therefore, σ_{tot} is insensitive to long-time physics.

The mass divergences resulting from the gluon radiation of initial-state quarks are dealt with in a different way. This is explained in detail in the next section.

3.2.2 Long-time scale interaction: PDFs

In the parton model, the PDFs are independent of the scale of the process, having only a dependence on the transverse momentum fraction of the parton, x. As discussed before, hadrons are formed by quarks, antiquarks and gluons. They are dynamical objects which interact with each other varying their hadron momentum fraction. To preserve the factorisation property of the cross section (Eq. 3.1), a factorisation scale μ_F is introduced to separate the interactions between the quarks,

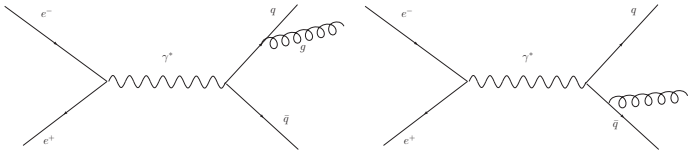

(a) (b)

Figure 3.7: Feynman diagrams for the NLO real corrections to the process $e^+e^- \to q\bar{q}$.

antiquarks and gluons inside the hadron from the short-time-scale hard interaction.

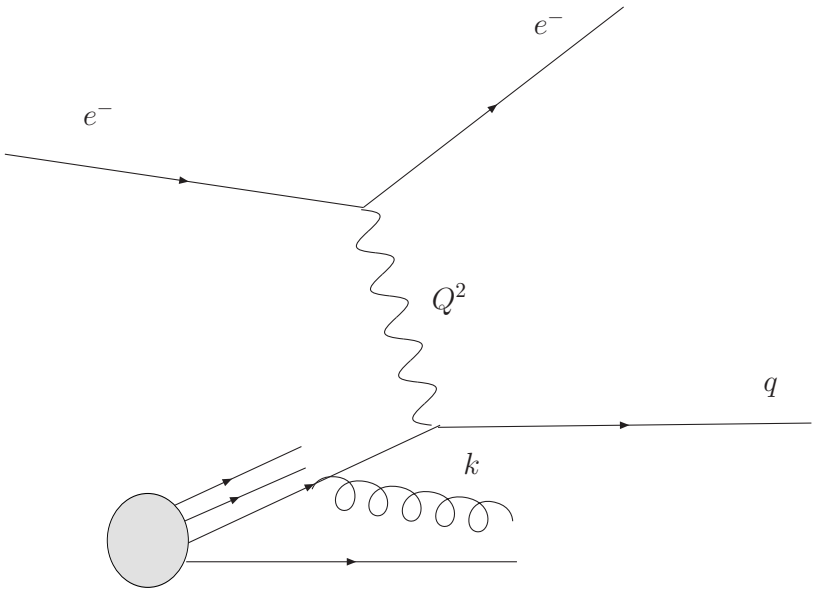

Figure 3.8: Interaction at parton level between a proton and an electron. A gluon with momentum k is emitted by the quark. The momentum transfer between the quark and the electron is Q^2.

An interaction with a high momentum transfer Q^2 between a quark inside a proton and an electron is shown in Fig. 3.8. The total cross section for this process can be written as

$$\sigma = \int dx \; f_{q/p}(x) \; \hat{\sigma}, \tag{3.11}$$

where $f_{q/p}$ is the quark PDF and $\hat{\sigma}$ is the cross section of the hard process. Let us consider the case where there is gluon emission by the quark before the interaction with the electron. Such emission, with $k^2 \sim \Lambda_{QCD}$, is part of $f_{q/p}(x)$, while a gluon emission with $k^2 \sim Q^2$ is part of $\hat{\sigma}$. When calculating the diagram in Fig. 3.8, an integration over k is performed. The contribution from $k^2 < \mu_F^2$ is counted as part of the higher-order contribution to $f_{q/p}$, convoluted with the lowest-order hard

scattering function $\hat{\sigma}$ for deep inelastic scattering with a quark. The contribution from $k^2 > \mu_F^2$ counts as part of the higher-order contribution to $\hat{\sigma}$ convoluted with an uncorrected parton distribution. A consequence of this is that both $\hat{\sigma}$ and $f_{q/p}(x)$ depend on μ_F.

Since the introduction of this scale is an artifact to separate the long time-scale term from the calculable short time-scale term, the cross section cannot depend on μ_F. Thus, $d\sigma/d\mu_F = 0$ must be satisfied to the accuracy of the perturbative calculation used. It is rather common to set $\mu_F = Q$. The μ_F scale is also used to renormalise collinear singularities of the partonic emission.

Initial-state infrared and collinear divergences

In the emission of a gluon by the initial quarks, there are two kind of divergences:

- *infrared divergences*: divergences in the calculation when the energy of the emitted gluon tends to zero;
- *collinear divergences*: divergences in the calculation when the emitted gluon is collinear to the quark.

Unlike gluon emission from final-state partons, the collinear divergences are not cancelled by the virtual-term contributions. Therefore, as for the renormalisation of the coupling constant (see Section 3.2.1), the PDF is regarded as an unmeasurable, bare distribution. The collinear singularities are absorbed into this bare distribution at a factorisation scale μ_F, which plays a similar role to the renormalisation scale.

Since a scale μ_F is introduced in the definition of the parton distributions to define their renormalisation, there is a renormalisation group equation, extracted from the fact that the total cross section must be independent of μ_F, that gives the μ_F dependence of the parton distribution function,

$$\frac{d}{d\ln\mu_F} f_{a/h}(x,\mu_F) = \sum_b \int_x^1 \frac{d\xi}{\xi}\; P_{ab}(x/\xi, \alpha_s(\mu_F))\; f_{b/h}(\xi,\mu_F)\;. \tag{3.12}$$

This is variously known as the evolution equation, the Altarelli-Parisi equation [22] or the DGLAP (Dokshitzer-Gribov-Lipatov-Altarelli-Parisi) [23, 24] equation. In Eq. 3.12, $f_{a/h}$ is the PDF of parton a in hadron h, P_{ab} is the splitting function, which is related to the probability of emission of parton a by parton b, and $f_{b/h}$ is the PDF of parton b in hadron h. For example, the evolution of an up quark

($a = u$) can involve a gluon ($b = g$) through the element P_{ug} that describes gluon splitting into a $\bar{u}u$ pair.

Equation 3.12 is illustrated in Fig. 3.9. When the factorisation scale μ_F is changed, the change in the probability to find a parton with momentum fraction x and flavor a is proportional to the probability to find such a parton with large transverse momentum. The way to obtain a parton with large transverse momentum is for a parton carrying momentum fraction ξ and much smaller transverse momentum to split into partons carrying large transverse momenta, including the desired parton. This splitting probability, integrated over the transverse momentum ranges, is the kernel P_{ab}.

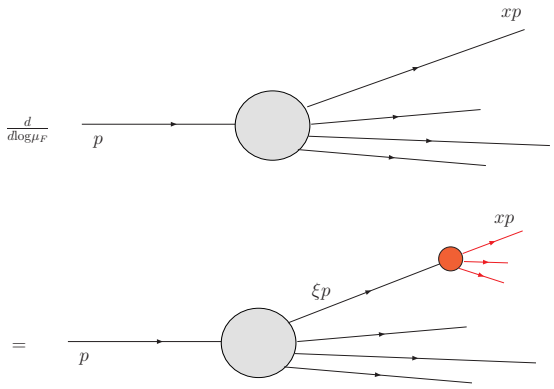

Figure 3.9: The renormalisation group equation for the parton distribution functions.

The kernel P in Eq. 3.12 has a perturbative expansion,

$$P_{ab}(x/\xi, \alpha_s(\mu_F)) = P_{ab}^{(1)}(x/\xi)\Big(\frac{\alpha_s(\mu_F)}{\pi}\Big) \; + \; P_{ab}^{(2)}(x/\xi)\Big(\frac{\alpha_s(\mu_F)}{\pi}\Big)^2 \, , \tag{3.13}$$

where $P_{ab}^{(1)}$ and $P_{ab}^{(2)}$ represent the splitting functions at LO and NLO. Figure 3.10 shows the LO Feynman diagrams for the calculation of the P_{gq}, P_{qq}, P_{qg} and P_{gg} splitting functions.

3.3 Theory of prompt-photon production

In this section the main mechanism for prompt-photon production at the LHC is discussed. In proton-proton collisions a high-p_T prompt photon can be produced via two possible mechanisms:

- direct photon (DP) process: the photon takes part directly in the hard subprocess and it is most likely to be well separated from any hadronic activity;

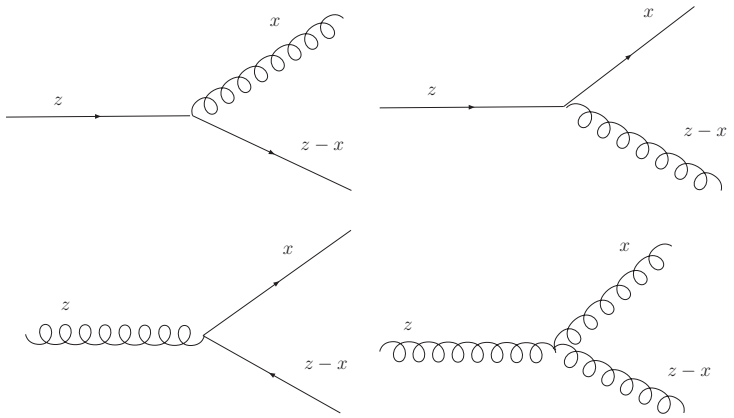

Figure 3.10: The processes related to the LO QCD splitting functions. Each splitting function $P_{ab}(x/z)$ gives the probability that a parton of type b converts into a parton of type a, carrying a fraction x/z of the momentum parton b.

- fragmentation (F) process: the photon results from the collinear fragmentation of a parton produced with large transverse momentum and it is most probably accompanied by hadrons.

The LO contribution to DP production is given by the Born-level processes q (or $\bar{q}$)$g \to \gamma q$ (or $\bar{q}$) ("QCD Compton process") and $q\bar{q} \to g\gamma$ ("annihilation process"). The cross section for DP production at LO is $O(\alpha\alpha_s)$ (see Fig. 3.11).

In the LO contribution of the fragmentation type (sometimes called "bremsstrahlung contribution"), the photon arises from the collinear fragmentation of a hard parton produced in a short-distance subprocess. The production of a hard parton is given by Born-level processes such as $qq \to qq$, $gq \to gq$, $gg \to q\bar{q}$, etc (see Fig. 3.12). At LO, the production cross section of these processes is $O(\alpha_s^2)$. The photon-fragmentation contribution appears when a final-state quark-photon collinear singularity occurs in the calculation of the contribution from the subprocess $gq \to g\gamma q$. At higher orders, final-state multiple collinear singularities appear in any subprocess where a high-p_T parton (quark or gluon) undergoes a cascade of successive collinear splittings ending up with a quark-photon splitting. According to the factorisation theorem [25], these singularities are factorised to all orders in α_s accordingly and absorbed into quark and gluon fragmentation functions of the photon, $D_q^\gamma(z, \mu_f)$ and $D_g^\gamma(z, \mu_f)$, where z is the relative fraction of the fragmenting-parton momentum taken by the photon. These fragmentation functions are defined in a certain factorisation scheme at a factorisation scale μ_f chosen to be of the order of the hard scale of the process. When the fragmentation scale μ_f is large with respect to $O(1)$ GeV, these functions behave

roughly as $\alpha/\alpha_s(\mu_f)$, and, as a result, the photon-fragmentation contribution is of the same order $O(\alpha\alpha_s)$ as the Born-level terms in the direct mechanism.

The LO Feynman diagrams for DP and F production are presented in Figs. 3.11 and 3.12, respectively. At LO, the final state for a DP or F process is formed by a γ and a high-p_T parton. Therefore, the topology of the event, from the experimental point of view, is described by a γ + jet final state (see Section 3.4). From a topological point of view, when a "direct" photon is produced, it is most probable that it will be separated from any hadronic activity, whereas a photon from "fragmentation" is most probably accompanied by hadrons, except when the photon carries away most of the momentum of the fragmenting parton. These fragmentation configurations are rare and atypical and they are not suppressed by isolation criteria.

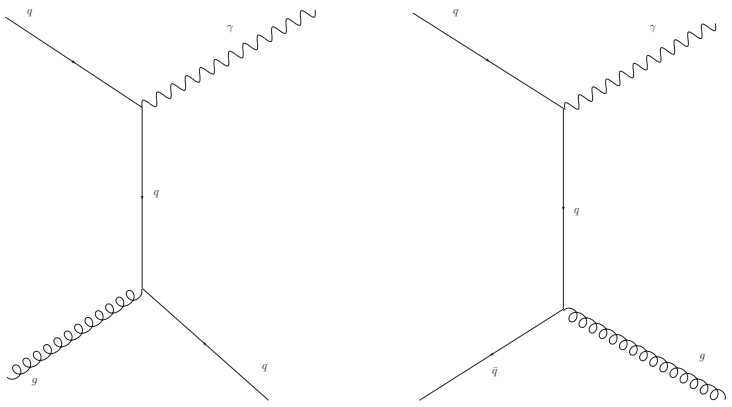

Figure 3.11: LO Feynman diagrams for the direct-photon processes (a) $qg \to \gamma q$ and (b) $q\bar{q} \to g\gamma$.

The LO hadronic differential cross section, denoted by $d\sigma^{\rm LO}/dp_T^\gamma$ for a process $pp \to \gamma + \text{jet} + X$, is given by the sum of the "fragmentation" and "direct" contributions. It can be written as

$$\frac{d\sigma^{\rm LO}}{dp_T^\gamma} = \frac{d\hat{\sigma}^{\rm LO,\gamma}}{dp_T^\gamma}(p_T^\gamma, \mu_F) + \sum_a \int_0^1 \frac{dz}{z}\, \frac{d\hat{\sigma}^{\rm LO,a}}{dp_T^\gamma}(p_T^\gamma/z, \mu_F, \mu_f)\; D_a^{\rm LO,\gamma}(z, \mu_f)\;, \quad (3.14)$$

where $\frac{d\hat{\sigma}^{\rm LO,a}}{dp_T^\gamma}$ and $\frac{d\hat{\sigma}^{\rm LO,\gamma}}{dp_T^\gamma}$ are the corresponding "partonic" cross sections convoluted with the parton distribution functions.

$$\frac{d\hat{\sigma}^{\rm LO,\gamma}}{dp_T^\gamma} = \sum_{i,j} \int_0^1 dx_1 \int_0^1 dx_2\; f_{i/\rm p}(x_1, \mu_F)\; f_{j/\rm p}(x_2, \mu_F)\; \frac{d\bar{\sigma}^{i+j\to\gamma+k}}{dp_T^\gamma}(x_1, x_2, p_T^\gamma, \mu_F) \quad (3.15)$$

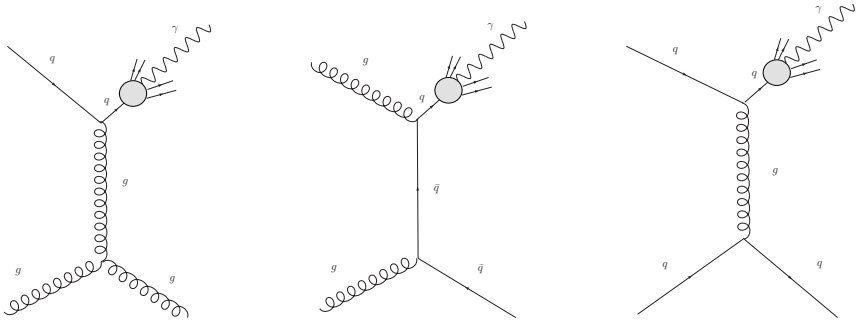

(a) (b) (c)

Figure 3.12: LO Feynman diagrams for the fragmentation processes (a) $qg \to q\gamma(q)$, (b) $gg \to \bar{q}\gamma(q)$ and (c) $qq \to q\gamma(q)$.

$$\frac{d\hat{\sigma}^{\mathrm{LO},a}}{dp_T^\gamma} = \sum_{i,j} \int_0^1 dx_1 \int_0^1 dx_2 \; f_{i/\mathrm{p}}(x_1,\mu_F) \; f_{j/\mathrm{p}}(x_2,\mu_F) \; \frac{d\bar{\sigma}^{i+j\to a+k}}{dp_T^\gamma}(x_1,x_2,p_T^\gamma/z,\mu_F), \tag{3.16}$$

where $\frac{d\hat{\sigma}^{\mathrm{LO},a}}{dp_T^\gamma}$ is the production differential cross section of a parton a ($a = q, \bar{q}, g$) in the hard collision; $D_a^{\mathrm{LO},\gamma}$ is the fragmentation function of the parton a into a photon (see Fig. 3.12) and μ_F is the factorisation scale of the initial-state partons.

Equation 3.14 states that at large values of p_T, the short-distance dynamics is perturbatively computable in terms of partonic cross sections, while the dominant non-perturbative phenomena can be factorised into the parton densities of the colliding hadrons and the fragmentation function of the final-state photon. Owing to the inclusiveness of the process, all the remaining non-perturbative effects have the form $(Q_0/p_T^\gamma)^p$, with $p \geq 0$. These terms are not indicated on the right-hand side of 3.14, since they are negligible as long as p_T^γ is much larger than the typical hadronic scale, $Q_0 \sim O(1\ \mathrm{GeV})$.

The direct contribution $\frac{d\hat{\sigma}^{\mathrm{LO},\gamma}}{dp_T^\gamma}$ does not contain any fragmentation function and it is independent of the factorisation scale μ_f of the photon fragmentation function. It corresponds to the point-like coupling of the large-p_T photon to a quark produced in the hard subprocess (see Fig. 3.11). At LO, the theoretical calculations of DP and F processes converge. Therefore, both process can be considered independently. This is no longer true if higher orders are taken into account. In NLO calculations, the final-state infrared and collinear divergences are only cancelled when both processes are considered simultaneously (see Section 3.3.1), so that DP and F processes separately have no longer a physical meaning.

3.3.1 Next-to-leading-order QCD calculations

The distinction between the two mechanisms (F) and (DP) has no physical meaning beyond LO. From a theoretical point of view, the distinction is defined by an arbitrary choice. It follows from the necessity of factorising the final-state collinear singularities and absorbing them into the fragmentation functions. This factorisation requires the introduction of an arbitrary fragmentation scale μ_f, which is an unphysical parameter. It relies on an arbitrary choice of the factorisation scheme, which defines the finite part of the higher-order corrections that is absorbed in the fragmentation functions together with the singularities; the remaining finite part is then included in the higher-order contributions to the partonic cross sections. Feynman diagrams for the NLO contributions of DP and F processes are shown in Fig 3.13.

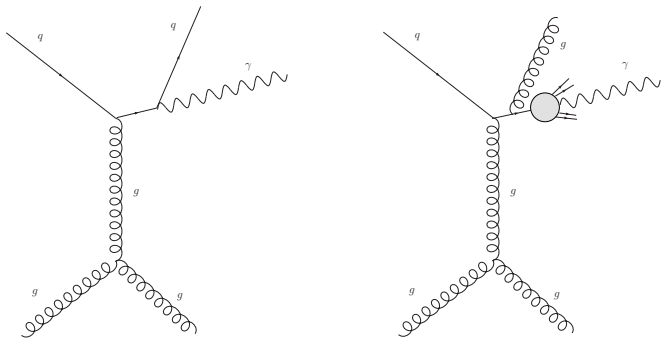

(a) (b)

Figure 3.13: Feynman diagrams for (a) the NLO direct-photon process $qg \to \gamma qg$ and (b) the NLO fragmentation process $qg \to gg\gamma(q)$.

In general, taking into account higher-order calculations, Eq. 3.14 can be written as

$$\frac{d\sigma}{dp_T^\gamma} = \frac{d\hat{\sigma}^\gamma}{dp_T^\gamma}(p_T^\gamma, \mu_F, \mu_R, \mu_f) + \sum_a \int_0^1 \frac{dz}{z} \frac{d\hat{\sigma}^a}{dp_T^\gamma}(p_T^\gamma/z, \mu_F, \mu_R, \mu_f)\ D_a^\gamma(z, \mu_f)\ . \quad (3.17)$$

The cross sections $\frac{d\hat{\sigma}^\gamma}{dp_T^\gamma}$ and $\frac{d\hat{\sigma}^a}{dp_T^\gamma}$ are known up to NLO in α_s,

$$\frac{d\hat{\sigma}^\gamma}{dp_T^\gamma} = \left(\frac{\alpha_s(\mu_R)}{\pi}\right) \frac{d\hat{\sigma}^\gamma_{\text{born}}}{dp_T^\gamma}(p_T^\gamma, \mu_F) + \left(\frac{\alpha_s(\mu_R)}{\pi}\right)^2 \frac{d\hat{\sigma}^\gamma_{\text{HO}}}{dp_T^\gamma}(p_T^\gamma, \mu_F, \mu_R, \mu_f) \quad (3.18)$$

$$\frac{d\hat{\sigma}^a}{dp_T^\gamma} = \left(\frac{\alpha_s(\mu_R)}{\pi}\right)^2 \frac{d\hat{\sigma}^a_{\text{born}}}{dp_T^\gamma}(p_T^\gamma, \mu_F) + \left(\frac{\alpha_s(\mu_R)}{\pi}\right)^3 \frac{d\hat{\sigma}^a_{\text{HO}}}{dp_T^\gamma}(p_T^\gamma, \mu_F, \mu_R, \mu_f)\ . \quad (3.19)$$

The expressions of $\frac{d\hat{\sigma}_{\text{HO}}}{dp_T^\gamma}$ and $\frac{d\hat{\sigma}_{\text{born}}}{dp_T^\gamma}$ for the direct and fragmentation contributions can be found in refs. [26] and [27], respectively. They depend on μ_f, μ_F and on the renormalisation scale μ_R.

3.3.2 Calculations for isolated-photon production

Strictly speaking, inclusive measurements of photons cannot be performed in collider experiments. To suppress the overwhelming background of secondary photons coming from the decays of hadrons, mainly π^0, η, etc., isolation criteria on the photon candidates must be applied. A widely used calorimetric criterium, which has the virtue to be implementable also at the partonic level [2], is the so-called "cone criterium": in a cone around the direction of the photon defined in rapidity η and azimuth angle ϕ by

$$(\eta - \eta^\gamma)^2 + (\phi - \phi^\gamma)^2 \leq R^2 \ , \tag{3.20}$$

the accompanying hadronic transverse energy, $E_{T,\mathrm{had}}$, is required to be less than some finite amount,

$$E_{T,\mathrm{had}} \leq E_{T,\mathrm{max}} \ , \tag{3.21}$$

R and $E_{T,\mathrm{max}}$ are specified by each experiment; $E_{T,\mathrm{max}}$ is given either as a fixed value or as a fixed fraction ϵ_h of p_T^γ.

The cross section for producing such isolated photons depends on the isolation parameters R and $E_{T,\mathrm{max}}$. The isolation criteria enforce additional phase-space restrictions. This implies that the cross section is no longer fully inclusive over the hadronic final state and, hence, that the factorised expression 3.14 is no longer necessarily valid [28–31].

Any isolation criteria applied to the photon is thus specified in terms of a function,

$$F^{(n+1)}_{\mathrm{isolation}}(p_A, p_B; p_\gamma; p_1, ...p_{n+1}), \tag{3.22}$$

where p_A and p_B are the initial partons and $p_1, ...p_{n+1}$ are the momentum of the final-state partons; the subscript "isolation" denotes the dependence on the isolation parameters. Factorisation is recovered provided $F_{\mathrm{isolation}}$ fulfills the following requirements:

i) infrared safety:

$$F^{(n+1)}_{\mathrm{isolation}}(p_A, p_B; p_\gamma; p_1, ...p_i, ...p_{n+1}) \overset{p_i \to 0}{\to} F^{(n)}_{\mathrm{isolation}}(p_A, p_B; p_\gamma; p_1, ...p_{n+1}); \tag{3.23}$$

ii) collinear safety:

$$F^{(n+1)}_{\mathrm{isolation}}(p_A, p_B; p_\gamma; p_1, ...p_i, p_j, ...p_{n+1}) \overset{p_i || p_j}{\to} F^{(n)}_{\mathrm{isolation}}(p_A, p_B; p_\gamma; p_1, ...p_i + p_j, ...p_{n+1}); \tag{3.24}$$

[2] Vetoes on charged tracks around the direction of the photon are also used experimentally, however they cannot be accounted for in a partonic calculation. A detailed description of the final state including full hadronisation would be required.

iii) final-state collinear factorisability:

$$F^{(n+1)}_{\rm isolation}(p_A, p_B; p_\gamma; p_1, ...p_i...p_{n+1}) \overset{p_i||p_\gamma}{\to} F^{(n)}_{\rm isolation}(p_A, p_B; p_\gamma + p_i; p_1, ...p_{n+1}); \tag{3.25}$$

iv) initial-state collinear factorisability:

$$F^{(n+1)}_{\rm isolation}(p_A, p_B; p_\gamma; p_1, ...p_i...p_{n+1}) \overset{p_i||p_A}{\to} F^{(n)}_{\rm isolation}(p_A - p_i, p_B; p_\gamma; p_1, ...p_{n+1}). \tag{3.26}$$

The requirement of *i*) infrared safety means that the cross section is insensitive to the momenta of arbitrary soft particles. The requirement of *ii*) collinear safety implies that, when some final-state particles are produced collinearly, the cross section depends on their total momentum rather than on the momentum of each of them. The property *iii*) guarantees that all the long-distance phenomena related to the low momentum fragmentation of the photon can be absorbed and factorised in the universal fragmentation function $D^\gamma_a(z;\mu_f)$. It has been proven [31, 32] that the cross section fulfills the factorisation property and is finite to all orders in perturbation theory for non-zero R and $E_{T,\rm max}$.

The isolation cut reduces the fragmentation contribution, although it does not suppress it completely. If z is the transverse momentum fraction taken by the photon of the final-state parton, the transverse momentum of the parton produced after fragmentation is given by

$$p^p_T = \frac{1-z}{z} p^\gamma_T \ . \tag{3.27}$$

Taking into account the isolation condition of Eq. 3.21, fragmentation photons survive provided that

$$z \geq \left(1 + \frac{E_{T,\rm max}}{p^\gamma_T}\right)^{-1} \tag{3.28}$$

or $z \geq (1+\epsilon_h)^{-1}$ if a fixed fraction ϵ_h of the p^γ_T is taken as $E_{T,\rm max}$. At LHC energies, the mean value $< z >$ for non-isolated photons from fragmentation is 0.6 or less [33], whereas typically $(1+\epsilon_h)^{-1} \geq$ 0.8-0.9, so that fragmentation is quite suppressed by the isolation requirements.

Due to the isolation requirements, the theoretical cross-section calculation depends on the values of R and $E_{T,\rm max}$. The value of $E_{T,\rm max}$ has to be non-zero otherwise the calculation of the cross section in perturbative QCD is infrared (IR) divergent in the DP contribution, since it involves a term $\sim \alpha_s R^2 \log(p_T/E_{T,\rm max})$.

In practice, no IR sensitivity appears down to fairly low values of $E_{T,\max} \sim 1$ GeV due to the smallness of $\alpha_s R^2$. Another source of trouble for the NLO calculation is caused by the use of too small a cone size, where the collinear sensitivity would require all-order resummation of large log R terms: the NLO calculation might not be reliable for $R \leq 0.3$ [32].

As discussed in Section 3.3.1, the isolated-photon cross section measured experimentally cannot be identified with the direct cross section calculated at the Born level without any contribution from fragmentation processes. In addition to the fragmentation piece left over ($z \geq (1+\epsilon_h)^{-1}$), higher-order terms originating from the non-collinear fragmentation processes contribute to the isolated-photon cross section. Such terms are important in some kinematical regions as they correspond to new hard processes, not allowed at the lowest order.

3.4 Jet algorithms

Reconstruction of the topology of the final-state partons is possible in terms of jets by using jet algorithms with analogous implementation in experiment and theory. The jet algorithm must ensure a close correspondence between jets and the final-state partons. There is no universal jet algorithm for the hadronic final state in all topologies of interest. For measurements of the inclusive-jet cross sections, wider jets are typically preferred to capture the hard-scattering parton kinematics, including possible small-angle gluon radiation, whereas to reconstruct W bosons decaying into two quarks, narrower jets would be preferred. On the experimental side, the common feature of a jet algorithm is that it must not depend strongly on the presence of soft final-state particles or particles produced after the decays of hadrons. On the theoretical side, the major guidelines of a jet algorithm are:

- **infrared safety:** the presence of additional soft particles between two particles belonging to the same jet should not affect the recombination of these two particles into a jet. In the same sense, the absence of additional particles between these two should not disturb the correct reconstruction of the jet. Generally, any soft particle should not affect the number of jets produced;

- **collinear safety:** a jet should be reconstructed independently of the fact that a certain amount of transverse momentum is carried by one particle or if the particle splits into two collinear particles;

- **input-object independence:** the same jet topology should be reconstructed independently at parton, particle or detector level.

From the experimental point of view, the particles mentioned in these theoretical guidelines can, up to a point, be replaced by four-momentum type objects reconstructed from detector signals.

There are two different methods to reconstruct jets from the final-state particles: cluster- and cone-type algorithms. Cluster algorithms, such as k_T [34] or anti-k_T [35] are based of sequential recombination of particles. Cone algorithms, such as the seedless infrared-safe cone jet algorithm [36] (SISCone) are based on a maximisation of the energy density within a cone of fixed size, together with a split-merge step that disentangles overlapping stable cones.

Recently [37], tools have been developed to support the debate with analytical calculations of the contrasting properties of boundaries of jets within different algorithms. One of the main results is that all known infrared- and collinear-safe (IRC) algorithms have the property that soft radiation can provoke irregularities in the boundaries of the final state. This is the case even for the SISCone algorithm. Therefore, IRC-safe algorithms, in general, can be described as having a "soft-adaptable" boundary. It is not clear whether it is better to have regular ("soft-resilient") or less regular ("soft-adaptable") jets. Regularity implies a certain rigidity in the ability of a jet algorithm to adapt a jet to the successive branching nature of QCD radiation. On the other hand, the knowledge of the typical shape of jets is often quoted as facilitating experimental calibration of jets and soft-resilience can simplify certain theoretical calculations, as well as eliminate some parts of the momentum-resolution loss caused by underlying-event and pile-up contamination (see Chapter 4).

In hadronic interactions, jets are usually defined using the transverse-energy flow in the rapidity (y)-azimuth (ϕ) plane. The transverse-energy flow with respect to the colliding axis ensures Lorentz invariance under longitudinal boosts.

In recombination algorithms, distances d_{ij} between a pair of objects (i, j) (e.g. final-state partons, final-state hadrons or energy deposits in the calorimeter) and distances between the object i and the beam (B) $d_{iB} = E_{T,i}^2$ are introduced. The distance d_{ij} is defined as

$$d_{ij} = \min(E_{T,i}^2, E_{T,j}^2)\frac{\Delta_{ij}^2}{R^2}, \tag{3.29}$$

where R is the usual radius parameter, $\Delta_{ij}^2 = (y_i - y_j)^2 + (\phi_i - \phi_j)^2$ and $E_{T,i}$, y_i and ϕ_i are respectively the transverse momentum, rapidity and azimuth of object i. The (inclusive) clustering proceeds by identifying the smallest distance and if it is a d_{ij} recombining entities i and j, while if it is d_{iB} calling i a jet and removing it from the list of entities. Then, the distances are recalculated and the procedure repeated until no entities are left.

An extension relative to the k_T and Cambridge/Aachen [39] algorithms lies in the definition of the distances:

$$d_{ij} = \min(E_{T,i}^{2p}, E_{T,j}^{2p}) \frac{\Delta_{ij}^2}{R^2} \tag{3.30}$$

and

$$d_{iB} = E_{T,i}^{2p}. \tag{3.31}$$

For p=1, the inclusive k_T algorithm is recovered. It can be shown in general that for $p > 0$ the behavior of the jet algorithm with respect to soft radiation is rather similar to that observed for the k_T algorithm, because what matters is the ordering between particles and for finite Δ this is maintained for all positive values of p. The case of p=0 is special and it corresponds to the inclusive Cambridge/Aachen algorithm. Negative values of p lead to a different behaviour of the jet algorithm with respect to soft radiation; the jets exhibit resilience to soft radiation. The case of p=-1 corresponds to the anti-k_T jet-clustering algorithm.

For the measurements presented in this analysis, the anti-k_T algorithm with $R = 0.6$, as implemented in the FastJet program [38] was used to reconstruct jets.

3.4.1 The anti-k_T jet algorithm

The functionality of the anti-k_T algorithm can be understood by considering an event with a few well-separated hard particles with transverse energies E_{T1}, E_{T2} ..., and many soft particles. The $d_{1i} = \min(1/E_{T1}^2, 1/E_{Ti}^2)\Delta_{1i}^2/R^2$ between a hard particle 1 and a soft particle is exclusively determined by the transverse energy of the hard particle and the Δ_{1i} separation. The d_{ij} between similarly separated soft particles will instead be much larger. Therefore, soft particles will tend to cluster with hard ones long before they cluster between themselves. If a hard particle has no hard neighbours within a distance $2R$, then it will simply accumulate all the soft particles within a circle of radius R, resulting in a perfectly conical jet.

If another particle 2 is present such that $R < \Delta_{12} < 2R$, then there will be two hard jets. It is not possible for both to be perfectly conical. If $E_{T1} \gg E_{T2}$ then jet 1 will be conical and jet 2 will be partly conical, since it will miss the part overlapping with jet 1. If $E_{T1} = E_{T2}$, neither jet will be conical and the overlapping part will simply be divided by a straight line equally between the two. For a general situation $E_{T1} \sim E_{T2}$, the boundary between them will be defined by $\Delta_{1b}/E_{T1} = \Delta_{2b}/E_{T2}$.

If $\Delta_{12} < R$, particles 1 and 2 will cluster to form a single jet. If $E_{T1} \gg E_{T2}$, the jet will be conical centered on E_{T1}. For $E_{T1} \sim E_{T2}$, the shape will be the union of cones (radius$< R$) around each hard particle plus a cone (of radius R) centered on the final jet.

As explained before, hard particles modify the shape of the jet instead of the soft particles. Therefore, the jet boundary in this algorithm is resilient with respect to soft radiation, but flexible with respect to hard radiation. The behavior of different jet algorithms is shown in Fig 3.14.

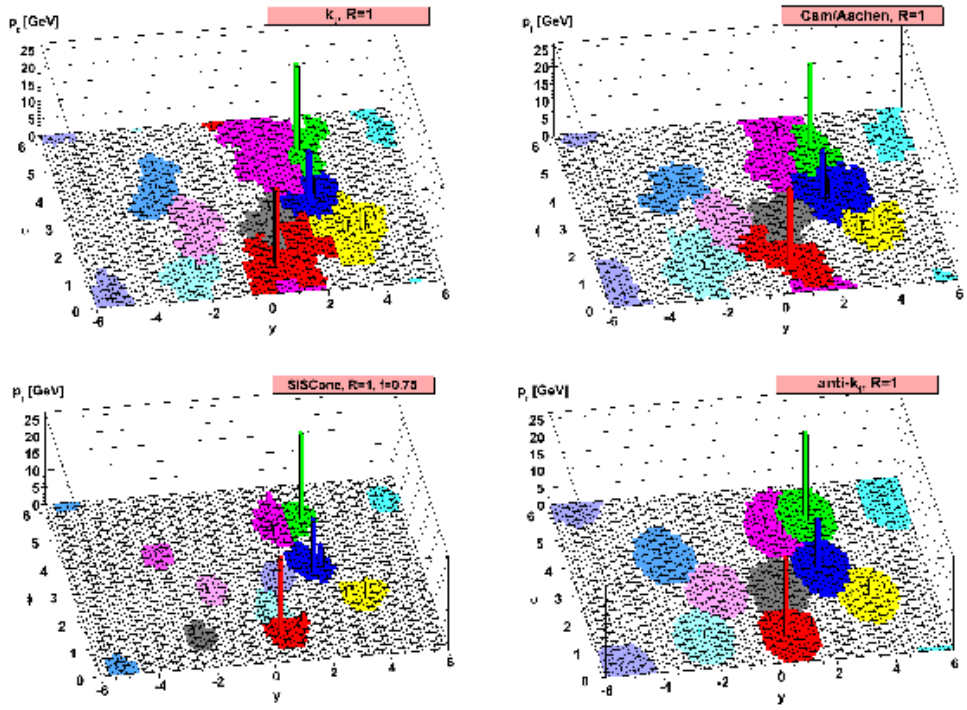

Figure 3.14: A sample parton-level event illustration of the "active" catchment areas of the resulting hard jets for different jet algorithms.

3.4.2 Recombination schemes

When combining particles during the clustering procedure, it has to be specified how to combine the momenta. The simplest procedure (E-scheme) adds the four-vectors. The E-scheme was used in this analysis for the recombination procedure. However, other schemes can be used, such as:

- p_T scheme;
- p_T^2 scheme;
- E_T scheme;
- E_T^2 scheme.

These schemes incorporate a "preprocessing" stage to make the initial momenta massless (rescaling the energy to be equal to the 3-momentum for the p_T and p_T^2 scheme, rescaling the 3-momentum to be equal to the energy in the E_T and E_T^2 schemes). Then for all schemes the recombination p_r of p_i and p_j is a massless 4-vector satisfying

$$p_{T,r} = p_{T,i} + p_{T,j} \ , \tag{3.32}$$

$$\phi_r = (w_i\phi_i + w_j\phi_j)/(w_i + w_j) \ , \tag{3.33}$$

$$y_r = (w_i y_i + w_j y_j)/(w_i + w_j), \tag{3.34}$$

where w_i is $p_{T,i}$ for the p_T and E_T schemes, and is $p_{T,i}^2$ for the p_T^2 and E_T^2 schemes.

3.5 Calculations for isolated-prompt photon plus jet production

In the case of isolated-prompt photon production, the theoretical cross-section calculation depends on the isolation requirements, such as $E_T^{\max}$ and the isolation radius R. If a jet is taken into account in the final state, the isolated-prompt photon + jet theoretical calculation also depends on the jet-finder parameters, such as the jet algorithm, jet radius R and recombination scheme.

Normally, some requirements are imposed to the final-state jet, such as $p_T^{\text{jet}} > p_T^{\text{cut}}$ and $|y^{\text{jet}}| < y^{\text{cut}}$. These criteria, as in the case of the isolation criteria, enforce phase-space restrictions. These phase-space restrictions make the cross section less inclusive over the hadronic final state, possibly violating the factorisation theorem. To ensure the validity of the cross-section factorisation property, the jet algorithm

must fulfill analogue requirements to those listed in Section 3.3.2.

As it was explained in the previous section, recombination-based jet algorithms, such as the anti-k_T, are infrared and collinear safe at all orders of perturbation theory, so that the factorisation property is guaranteed for such jet algorithms.

3.6 Fixed-order calculations

In practice, due to the difficulty of calculating theoretical predictions at high orders, the calculations are done up to a certain order in perturbation theory. The truncation of the perturbative series has implications. As explained in the previous section, the physical observables must be independent of the μ_F, μ_R and μ_f scales, which were introduced to make the theoretical prediction finite. This is no longer true if not all orders are considered. The production cross section for the Higgs boson as a function of the renormalisation scale is shown in Fig. 3.15 [21]. It is observed that the dependence of the Higgs boson production cross section depends less on the scale as higher-order terms are added to the theoretical calculation.

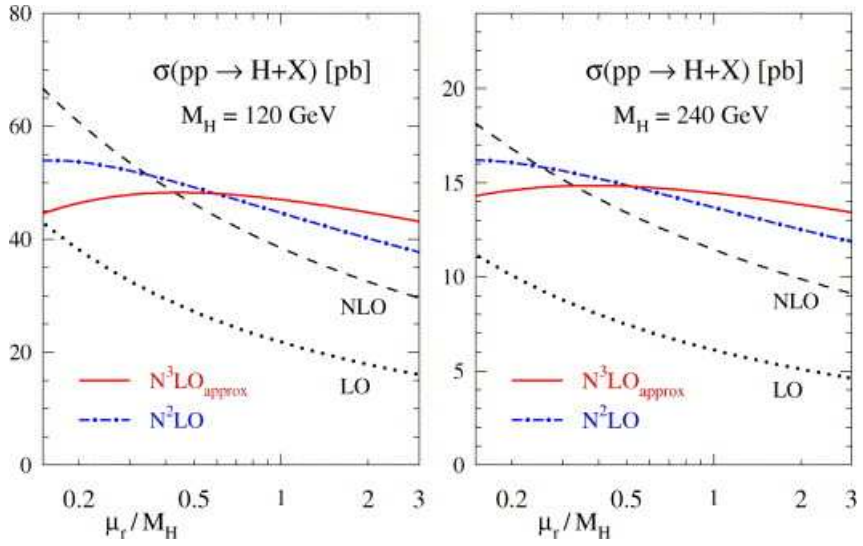

Figure 3.15: The production cross section of the Higgs boson as a function of μ_R/M_H.

Considering the cross section of the hard process ($\hat{\sigma}$) as the observable, the dependence of $\hat{\sigma}$ on the μ_F, μ_R and μ_f scales at fixed order usually is $(\ln\frac{\mu^2}{Q^2})^n$, where μ^2 can be any of the three scales, n some power which depends on the perturbation-theory order and Q the scale of the hard process. By chosing a value of $\mu = Q$,

the magnitude of the terms depending on the scales is reduced. For that reason, $\mu_R = \mu_F = \mu_f = Q$ is used.

3.7 Next-to-leading-order QCD predictions

The NLO QCD ($O(\alpha_s^2\alpha)$) calculations used in the analysis presented here were computed using the program JETPHOX [32]. This program is a general purpose cross-section integrator of Monte Carlo type, designed to calculate both single-photon inclusive and photon-jet inclusive cross sections and related correlations, accounting easily for any kind of experimental cut (e.g. on kinematics, isolation) implementable at the partonic level. The JETPHOX program includes a full NLO QCD calculation of both the DP and F contributions to the cross section. The calculations are based on a combination of the phase-space slicing [40] and the subtraction [41] methods to treat the soft and collinear singular parts of the perturbative matrix elements.

For the calculations presented here, the number of flavours was set to five. The μ_R, μ_F and μ_f scales were chosen to be $\mu_R = \mu_F = \mu_f = E_T^\gamma$. The strong coupling constant was calculated at two loops with $\Lambda_{\overline{\rm MS}} = 226$ MeV, corresponding to $\alpha_s(M_Z)$= 0.118. The calculations were performed using the CTEQ6.6 [42] set of proton PDFs and the BFG set II NLO photon fragmentation function [43].

The calculations were performed using a parton-level isolation cut, which required a total transverse energy below 4 GeV from the partons inside a cone of radius $R = 0.4$ around the photon direction. The anti-k_T algorithm was applied to the partons in the events generated by this program to compute the cross-section predictions.

The NLO QCD calculations predict one photon and one or two jets in the final state. The events generated by the NLO QCD calculations were selected with the following requirements:

- $E_T^\gamma > 45$ GeV, $|\eta^\gamma| < 2.37$ (excluding the $1.37 < |\eta^\gamma| < 1.52$ region) and an isolation requirement of $E_T^{\rm max} = 4$ GeV using a cone radius of 0.4;
- jets with $P_T^{\rm jet} > 40$ GeV and $\Delta R^{\gamma-{\rm jet}} = \sqrt{(\eta^\gamma - \eta^{\rm jet})^2 + (\phi^\gamma - \phi^{\rm jet})^2} > 1.0$, where $\eta^{\rm jet}$ ($\phi^{\rm jet}$) is the jet pseudorapidity (azimuthal angle);
- an event is selected if the rapidity of the jet with the largest transverse momentum fulfills $|Y_{\rm lead}^{\rm jet}| < 2.37$.

Figure 3.16 shows the predicted differential cross sections as functions of E_T^{γ}, $P_{T,\mathrm{lead}}^{\mathrm{jet}}$, $|Y_{\mathrm{lead}}^{\mathrm{jet}}|$, the difference in azimuthal angle between the photon and the leading jet ($\Delta\phi^{\gamma-\mathrm{jet}}$), the invariant mass of the photon-jet system ($M^{\gamma-\mathrm{jet}}$) and the variable $|\cos\,\theta^{\gamma-\mathrm{jet}}|$ (see below) based on the CTEQ6.6, MSTW2008nlo [44] and CTEQ10 [45] sets of proton PDFs. The variable $\cos\,\theta^{\gamma-\mathrm{jet}}$ approximates the cosine of the polar angle between the photon and the z-axis in the centre-of-mass system ($\theta_{\mathrm{CM}}^{\gamma-\mathrm{jet}}$) and is defined as

$$\cos\,\theta^{\gamma-\mathrm{jet}} = \tanh\Big(\frac{Y_{\mathrm{lead}}^{\mathrm{jet}} - \eta_{\mathrm{lead}}^{\gamma}}{2}\Big)\ . \tag{3.35}$$

This observable, which makes use only of the rapidities, gives a better handle on $\theta_{\mathrm{CM}}^{\gamma-\mathrm{jet}}$ since its counterpart at detector level is not affected by the relatively large uncertainties associated to the measurement of the jet energy. For the differential cross sections as functions of $M^{\gamma-\mathrm{jet}}$ and $|\cos\,\theta^{\gamma-\mathrm{jet}}|$, the following additional cuts are imposed: $|\eta_{\mathrm{lead}}^{\gamma} + Y_{\mathrm{lead}}^{\mathrm{jet}}|$ <2.37, $|\cos\,\theta^{\gamma-\mathrm{jet}}| < 0.83$ and $M^{\gamma-\mathrm{jet}} > 161$ GeV.

For each observable, the shape of these three calculations is similar. The predictions based on CTEQ6.6 and CTEQ10 have similar normalisation and the one based on MSTW2008nlo is $\approx 5\%$ higher than that of CTEQ6.6.

It should be noted that for the $\Delta\phi^{\gamma-\mathrm{jet}}$ distribution, the cross section is zero for $\Delta\phi^{\gamma-\mathrm{jet}} < \frac{\pi}{2}$ since the photon and the leading jet cannot be in the same hemisphere in the transverse plane.

3.8 Comparison between LO and NLO QCD calculations

To gain insight into the interpretation of the NLO QCD results, LO QCD calculations of the direct-photon and fragmentation contributions to the cross section as well as their sum were made. The LO and NLO QCD calculations are compared in Fig. 3.17. It is observed that the ratio LO/NLO does not show a strong dependence with $E_{T,\mathrm{lead}}^{\gamma}$, $|Y_{\mathrm{lead}}^{\mathrm{jet}}|$ and $M^{\gamma-\mathrm{jet}}$; it exhibits a strong dependence with $P_{T,\mathrm{lead}}^{\mathrm{jet}}$ and $|\cos\,\theta^{\gamma-\mathrm{jet}}|$. The fragmentation contribution is observed to decrease as a function of $E_{T,\mathrm{lead}}^{\gamma}$, $P_{T,\mathrm{lead}}^{\mathrm{jet}}$ and $M^{\gamma-\mathrm{jet}}$ and is approximately constant as a function of $|Y_{\mathrm{lead}}^{\mathrm{jet}}|$. However, it increases as a function of $|\cos\,\theta^{\gamma-\mathrm{jet}}|$ from 2% up to 16%. Therefore, the regions at low $E_{T,\mathrm{lead}}^{\gamma}$, $P_{T,\mathrm{lead}}^{\mathrm{jet}}$ and $M^{\gamma-\mathrm{jet}}$ as well as large $|\cos\,\theta^{\gamma-\mathrm{jet}}|$ are expected to be particularly sensitive to the fragmentation contribution.

The shapes of the differential cross sections for the direct-photon and fragmentation contributions at LO QCD are compared in Fig. 3.18. The largest difference is observed in the differential cross section as a function of $|\cos\,\theta^{\gamma-\mathrm{jet}}|$, with the contribution from fragmentation showing a steeper increase as $|\cos\,\theta^{\gamma-\mathrm{jet}}| \to 1$ than that of direct-photon processes. This different behavior is due to the different spin of the exchanged particle dominating each of the processes: a quark in the case of direct processes and a gluon in the case of fragmentation processes. Therefore, the distribution in $|\cos\,\theta^{\gamma-\mathrm{jet}}|$ is particularly useful to study the dynamics underlying the hard process and the relative contributions of direct processes and fragmentation.

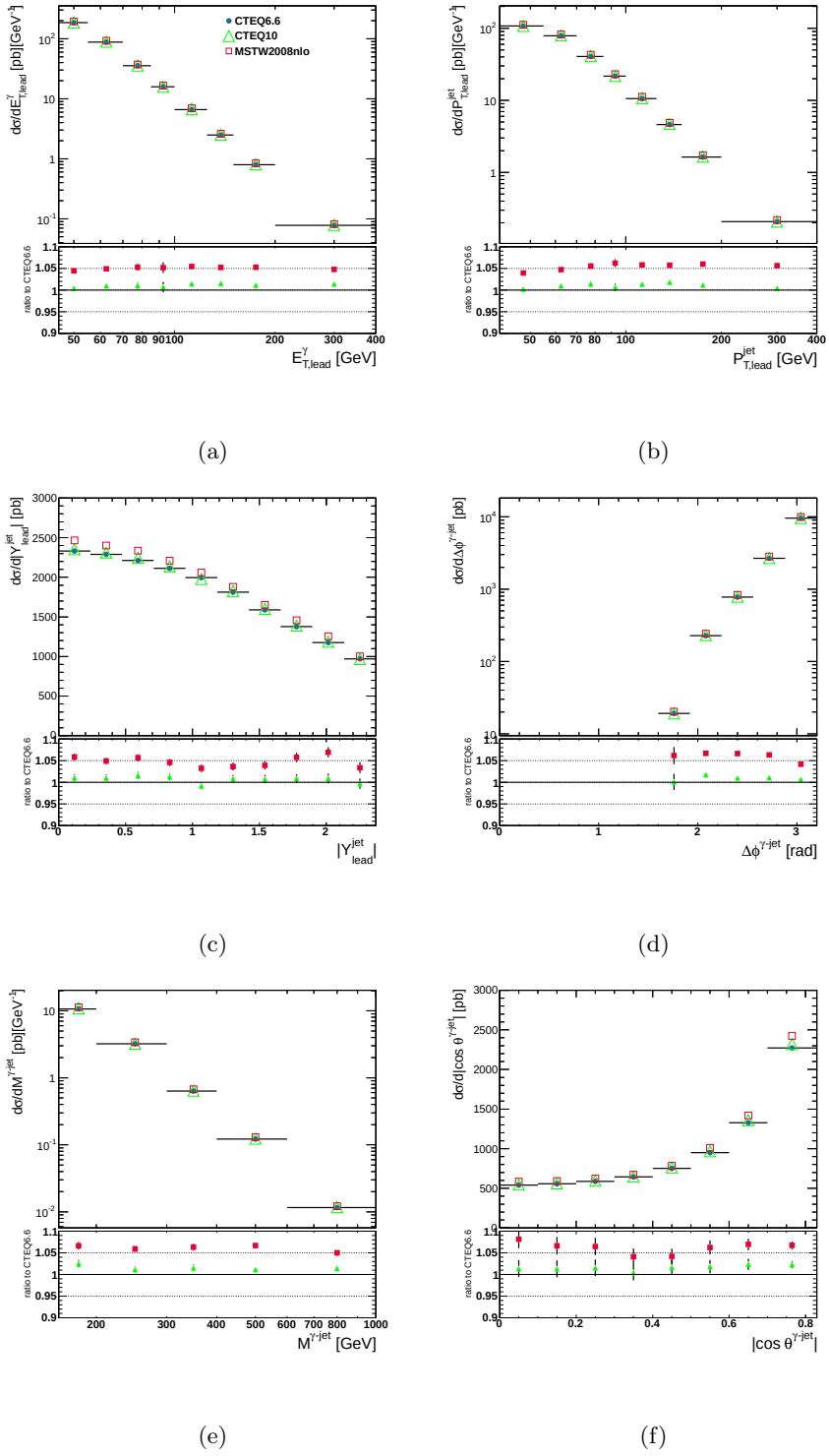

Figure 3.16: Predicted NLO QCD differential cross sections based on different proton PDFs as functions of (a)$E^{\gamma}_{T,\mathrm{lead}}$, (b) $P^{\mathrm{jet}}_{T,\mathrm{lead}}$, (c) $|Y^{\mathrm{jet}}_{\mathrm{lead}}|$, (d) $\Delta\phi^{\gamma-\mathrm{jet}}$, (e) $M^{\gamma-\mathrm{jet}}$ and (f) $|\cos\,\theta^{\gamma-\mathrm{jet}}|$.

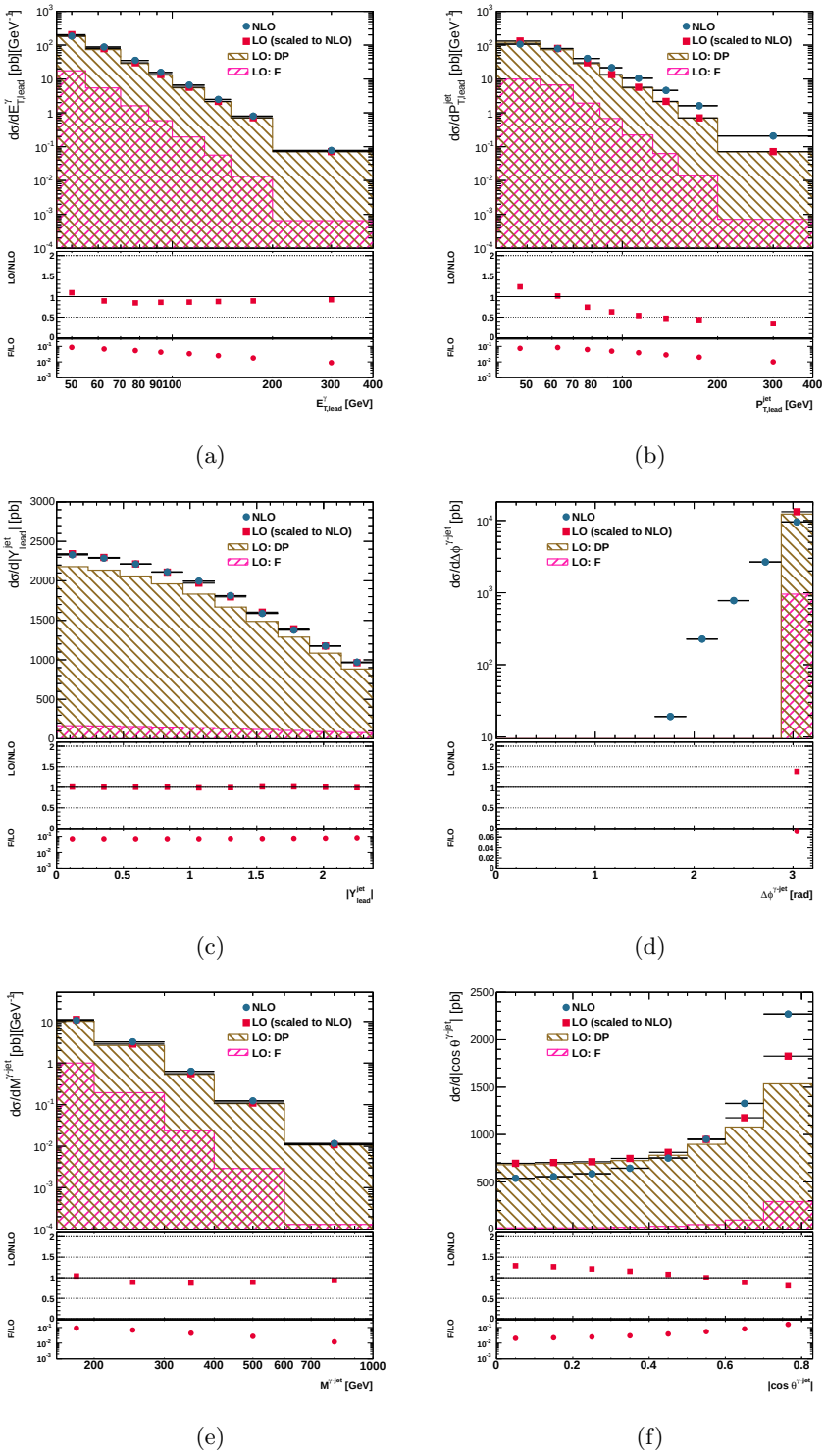

Figure 3.17: The NLO QCD predicted differential cross section for isolated-photon plus jet production as a function of (a) $E^{\gamma}_{T,\mathrm{lead}}$, (b) $P^{\mathrm{jet}}_{T,\mathrm{lead}}$, (c) $|Y^{\mathrm{jet}}_{\mathrm{lead}}|$, (d) $\Delta\phi^{\gamma-\mathrm{jet}}$, (e) $M^{\gamma-\mathrm{jet}}$ and (f) $|\cos\theta^{\gamma-\mathrm{jet}}|$. The LO QCD calculations scaled to the NLO integrated cross section (squares), together with the direct-photon (right-hatched histogram) and fragmentation (left-hatched histogram) components are also shown. The lower parts of the figure shows the ratio of the LO to the NLO QCD calculation (squares) and the fragmentation component to the full LO calculation (dots).

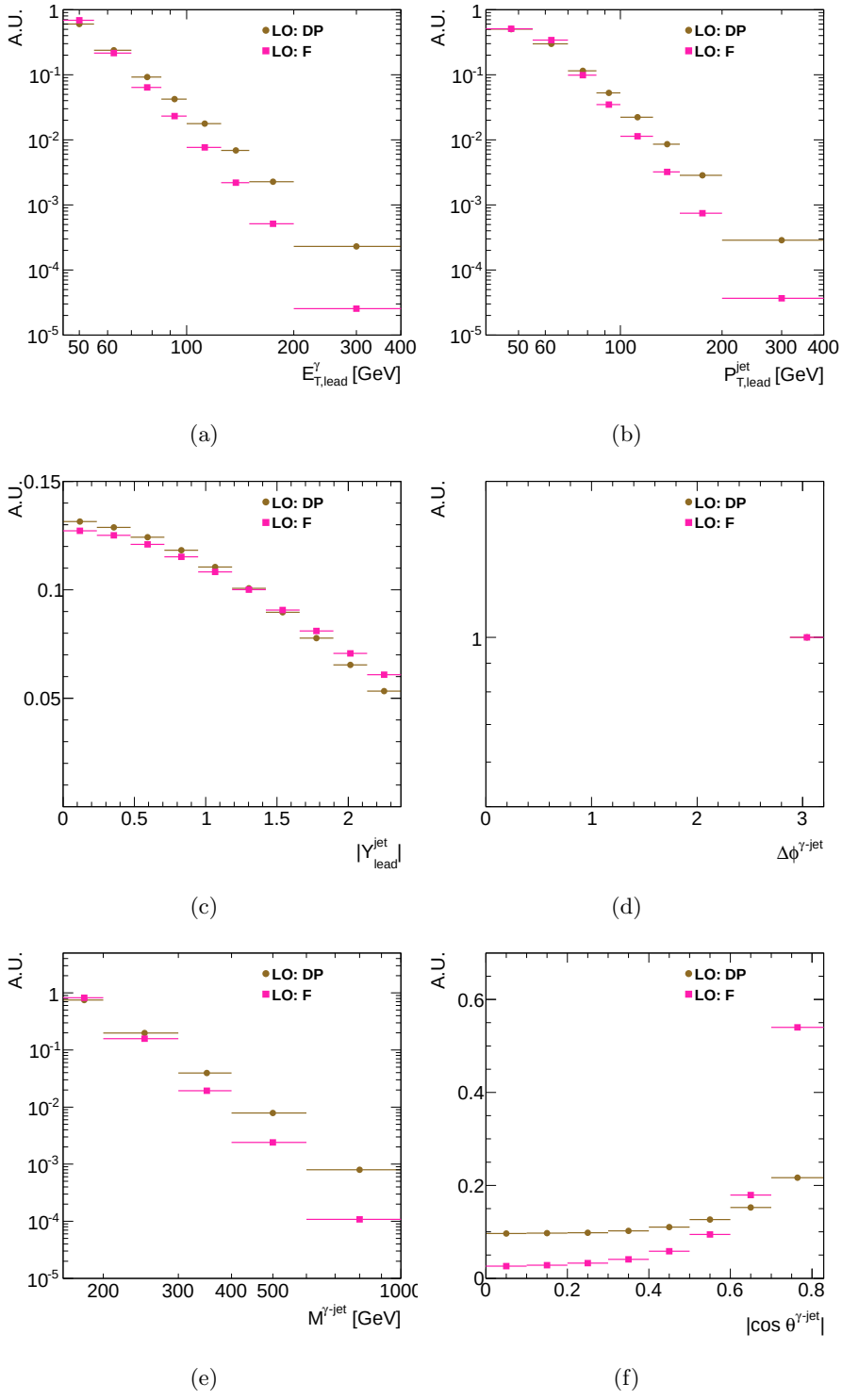

Figure 3.18: The direct-photon (dots) and fragmentation (squares) components of the LO QCD predicted differential cross section for isolated-photon plus jet production as a function of (a) $E^{\gamma}_{T,\mathrm{lead}}$, (b) $P^{\mathrm{jet}}_{T,\mathrm{lead}}$, (c) $|Y^{\mathrm{jet}}_{\mathrm{lead}}|$, (d) $\Delta\phi^{\gamma-\mathrm{jet}}$, (e) $M^{\gamma-\mathrm{jet}}$ and (f) $|\cos\,\theta^{\gamma-\mathrm{jet}}|$. Both calculations have been normalised to unit area.

Chapter 4

Monte Carlo simulations

The main aspects of Monte Carlo (MC) event generators are discussed in this chapter, such as:

- elementary hard subprocess generation;
- initial- and final-state parton shower;
- electromagnetic final-state radiation;
- multiple scattering;
- hadronisation.

The simulation of direct- and fragmentation-photon processes by Monte Carlo event generators are also discussed. In addition, the differential cross section for direct-photon and fragmentation-photon production estimated with the Monte Carlo event generators are presented. To compare the events generated by Monte Carlo programs with data, a final detector-simulation stage as well as a good simulation of pile-up effects are crucial. In the last part of this chapter, the generalities of detector and pile-up simulations are discussed.

4.1 Monte Carlo event generators

A Monte Carlo event generator simulates events aleatory weighted with a statistical distribution derived from the cross section of the process. The objective is to generate events as detailed as could be observed by a perfect detector. This is not done in one step, but rather by "factorising" the full problem into a number of components, each of which can be handled with reasonable accuracy. If the full problem is too complicated to be solved in one step, it may be possible to subdivide it into smaller

tasks of more manageable proportions. In the actual generation procedure, most steps therefore involve the branching of one object into two, or at least into a very small number, with the daughters free to branch in their turn.

As the name indicates, the output of an event generator should be in the form of "events" with the same average behaviour and the same fluctuations as the data. In the data, fluctuations arise from the quantum mechanics character of the underlying theory. In generators, Monte Carlo techniques are used to select all relevant variables according to the desired probability distributions and, thereby, ensure (quasi-)randomness in the final events. Clearly, some loss of information is entailed: quantum mechanics is based on amplitudes, not probabilities. However, only very rarely do (known) interference phenomena appear that cannot be cast in a probabilistic language.

An event generator can be used in many different ways. The five main applications are the following:

- to give physicists an estimate of the kind of events expected to be found and at what rates;
- as a help in the planning of a new detector, so that detector performance is optimised, within other constraints, for the study of interesting physics scenarios;
- as a tool for devising the analysis strategies that should be used on data, so that signal-to-background conditions are optimised;
- as a method for estimating detector acceptance corrections that have to be applied to raw data to extract the "true" physics signal;
- as a convenient framework within which to interpret the observed phenomena in terms of a more fundamental underlying theory.

All these applications make the event-generator approach the most powerful tool to gain a detailed and realistic understanding of physics at the LHC.

For the description of a typical high-energy event, an event generator should contain a simulation of several physics aspects. The processes involved can be divided into a number of stages corresponding to increasing time and distance scales:

- initially, two beam particles are coming in towards each other. Each particle is characterised by a set of PDFs, which defines the partonic substructure in terms of flavour composition and energy sharing;

- one shower-initiator parton from each particle beam starts off a sequence of branchings, such as $q \to qg$, which builds up an initial-state shower;
- one incoming parton from each of the two showers undergoes a hard scattering process; then, a number of outgoing partons (or other elementary particles such as leptons, electroweak bosons, etc) are produced. In general, this is computed at leading order in perturbation theory. The nature of this process determines the main characteristics of the event;
- the outgoing partons may branch, to build up final-state showers;
- the outgoing particles, if charged, can create electromagnetic showers;
- in addition to the hard scattering process considered above, further semihard interactions may occur between the other partons in the two incoming hadrons;
- the beam remnants left behind may have an internal structure and a net colour charge relates them to the rest of the final state. At this stage, the event is made up of partons. This stage, before the hadronisation process, is called the partonic-level of the MC;
- when the momentum scales of the outgoing partons are low enough, the hadronisation stage takes place. The QCD confinement mechanism ensures that the outgoing quarks and gluons are not observed, but instead fragment into colour-neutral hadrons;
- many of the produced hadrons are unstable and decay to more stable particles. The final particles make up the so-called hadron level of the MC.

The main differences between Monte Carlo generators are in the modelling of the initial- and final-state radiation, hadronisation and underlying event. In the following sections, these stages are discussed in detail as well as the differences between Monte Carlo generators, mainly, PYTHIA [46] and HERWIG [47].

4.1.1 Initial- and final-state radiation

In every process that contains coloured objects in the initial or final state, gluon and/or photon radiation may give large corrections to the overall topology of the events. As the available energies increase, hard emission of this kind is increasingly important, relative to fragmentation, in determining the event structure.

There exist two traditional approaches to the modelling of perturbative corrections. One is the matrix-element method, in which Feynman diagrams are calculated order by order. In principle, this is the correct approach, which takes into account exact kinematics and the full interference and helicity structure. The only problem is that calculations become increasingly difficult at higher orders, particularly for loop graphs. This perturbative expansion is better behaved at high-energy scales, owing to the running of α_s.

The second method is the parton-shower approach. In this method, an arbitrary number of branchings of one parton into two may be performed, to yield a description of multijet events, with no explicit upper limit on the number of partons involved. In practice, parton-shower programs may be matched to first-order matrix elements to describe hard-gluon emission. Nevertheless, the shower description is not always optimal such as for absolute α_s determinations.

The two approaches are complementary. Because of its simplicity and flexibility, the parton-shower option is often the first choice, while the full higher-order matrix elements one is mainly used for α_s determinations, angular distributions of jets, triple-gluon vertex studies, etc.

Parton showers

The separation of radiation into initial- and final-state showers is arbitrary, but very convenient. In general, the assignment of radiation to a given mother parton is a good aproximation for an emission close to the direction of motion of that parton, but not for the wide-angle emission in between two jets, where interference terms are expected to be important.

In both initial- and final-state showers, the structure is given in terms of branchings $a \to bc$, specifically $e \to e\gamma$, $q \to qg$, $q \to q\gamma$ and $g \to q\bar{q}$. Each of these processes is characterised by a splitting kernel $P_{a\to bc}(z)$. The branching rate is proportional to the integral $\int P_{a\to bc}(z)dz$. The z value picked for a branching describes the energy sharing, with daughter b taking a fraction z and daughter c the remaining 1-z of the energy of the mother. Once formed, the daughters b and c may in turn branch, and so on.

Each parton is characterised by some virtuality scale Q^2, which gives an approximate sense of time ordering to the cascade. Different definitions of Q^2 are possible. In the initial-state or in final-state showers Q^2 values can gradually increase or de-

crease depending on the definition of Q^2. The shower evolution is cut off at some lower (Q_0) or maximum value ($Q_{\max}$).

In the PYTHIA Monte Carlo event generator, initial-state radiation is space-like. This means that, in the sequence of branchings $a \to bc$ that lead up from the shower initiator to the hard interaction, particles a and b have $m^2 = E^2 - p^2 < 0$. The "side branch" particle c, which does not participate in the hard scattering, may be on the mass shell or have a time-like virtuality. To first approximation, the evolution of the space-like main branch is characterised by a p_T-ordered shower algorithm, where the evolution variable $Q^2 = -p_T^2 = -(1-z)m^2$ is required to be strictly increasing along the shower. In contrast, final-state radiation is time-like; i.e. partons have $m^2 = E^2 - p^2 \geq 0$. Starting from some maximum scale $Q^2_{\max}$, an original parton is evolved downwards in Q^2 until a branching occurs. The selected Q^2 value defines the p_T of the branching.

In the HERWIG Monte Carlo generator program, the parton-shower emissions are angular ordered. For a sequence of branchings $a \to bc$, the evolution variables are given by $Q^2 = 2E_a^2(1-cos\theta_{bc})$, where θ_{bc} is the angle between the b and c partons. For small angles, $Q \approx E_a\theta_{bc}$. When a branching occurs, the daughter partons b and c, with momentum fractions z and 1-z, respectively, have their starting evolution scales set to zQ and (1-z)Q, respectively, where $zQ \approx E_b\theta_{bc}$ and (1-z)$Q \approx E_c\theta_{bc}$. In this way, the maximum opening angle of any subsequent branching is θ_{bc}, thereby implementing angular ordering. For initial-state showers, by backward evolution, away from the hard process, the angle between the mother of the branching and its final-state daughter parton must decrease.

4.1.2 Hadronisation

In the hadronisation process, partons are combined to form hadrons. The QCD perturbation theory, formulated in terms of quarks and gluons, is valid only at short distances. At long distances, QCD becomes strongly interacting and perturbation theory breaks down. In this confinement regime, the coloured partons are transformed into colourless hadrons, a process called either hadronisation or fragmentation.

The hadronisation process is not understood from first principles, starting from the QCD lagrangian. Therefore, a number of different phenomenological models have been developed to treat this regime. Three main schools are usually distinguished: string fragmentation (SF), independent fragmentation (IF) and cluster

fragmentation (CF), but many variants and hybrids exist. None of these models can lay claim to being "correct", although some may be better founded than others. The best that can be aimed for is internal consistency, a good description of existing data and a somewhat predictive power for properties not yet studied or results at higher energies. The SF and CF models are discussed in detail in the following sections.

After hadronisation, many hadrons are unstable. The final stage of a Monte Carlo event generator is the hadron decay. After hadron decay, the event is completely characterised in terms of the final-state particles.

String fragmentation model

The string fragmentation model is also known as the "Lund string model" [48]. This is the default for all PYTHIA applications. All current models are of a probabilistic and iterative nature. This means that the fragmentation process as a whole is described in terms of one or a few simple underlying branchings of the type $jet \rightarrow\ hadron\ +\ remainder - jet$ or $string \rightarrow\ hadron\ +\ remainder - string$. At each branching, probabilistic rules are given for the production of new flavours and for the sharing of energy and momentum between the products.

Lattice QCD studies lend support to a linear confinement picture: in the absence of dynamical quarks, the energy stored in the colour-dipole field between a charge and an anticharge increases linearly with the separation between charges, if the short-distance Coulomb term is neglected. This is quite different from the behaviour in QED and is related to the presence of the triple-gluon vertex in QCD.

The assumption of linear confinement provides the starting point for the string model. As the q and $\bar{q}$ move apart from their common production vertex, the physical picture is that of a colour flux tube being stretched between the q and the $\bar{q}$. The transverse dimensions of the tube are of typical hadronic sizes, roughly 1 fm. If the tube is assumed to be uniform along its length, this automatically leads to a confinement picture with a linearly rising potencial. As the q and $\bar{q}$ move apart, the potencial energy stored in the string increases and the string may break by the production of a new $q'\bar{q}'$ pair, so that the system splits into two colour-singlet systems, $q\bar{q}'$ and $q'\bar{q}$. If the invariant mass of either of these string pieces is large enough, further breaks may occur. In the Lund string model, the string break-up process is assumed to proceed until only on-mass-shell hadrons remain, each hadron corre-

sponding to a small piece of string with a quark in one and an antiquark in the other.

To generate the quark-antiquark pairs $q'\bar{q}'$ which lead to string break-ups, the Lund model invokes the idea of quantum mechanical tunnelling. This leads to a flavour-independent Gaussian spectrum for the p_T of $q'\bar{q}'$ pairs. Since the string is assumed to have no transverse excitations, this p_T is locally compensated between the quark and the antiquark of the pair. The total p_T of a hadron is made up out of the p_T contributions from the quark and antiquark that together form the hadron. Some contribution of very soft perturbative gluon emission may also effectively be included in this description.

Cluster fragmentation model

The colour preconfinement property of the angular-ordered parton shower is used as the basis of the cluster model [49], which is used in HERWIG to model the hadronisation. This model has the properties that it is local in the colour of the partons and independent of both the hard process and the centre-of-mass energy of the collision.

The first step of the cluster hadronisation model is to non-perturbatively split the gluons left at the end of the parton shower into quark-antiquark pairs. Since at the end of the HERWIG shower the gluons are given their constituent mass, it is essential that this mass is heavier than twice the constituent mass of the lightest quark. The gluon is allowed to decay into any of the accessible quark flavours with a probability given by the available phase space for the decay.

The gluon decays isotropically and, following this isotropic decay, the event only contains colour connected (di)quarks and anti-(di)quarks. The colour singlets formed by these colour connected parton pairs are combined into clusters with the momentum given by the sum of the momenta of the constituent partons. The principle of colour-preconfinement states that the mass distribution of these clusters is independent of the hard-scattering process and its centre-of-mass energy. Thus, due to the fact that the cluster mass spectrum is both universal and peaked at low masses, the clusters can be regarded as highly excited hadron resonances and decayed, according to phase space, into the observed hadrons. There is, however, a small fraction of clusters that are too heavy for this to be a reasonable approach. These heavy clusters are therefore first split into lighter clusters before they decay.

The final step of the cluster hadronisation model is the decay of the cluster into

a pair of hadrons. For a cluster of a given flavour a quark-antiquark or diquark-antidiquark pair is extracted from the vacuum and a pair of hadrons with flavours $(q_1, \bar{q})$ and $(q, \bar{q}_2)$ formed. The hadrons are selected from all the possible hadrons with the appropiate flavour based on the available phase space, spin and flavour of the hadrons.

Hadron decay

A large fraction of the particles produced by hadronisation are unstable and subsequently decay into the observable stable ones. The definition of an unstable hadron is, to some extent, ambiguous. In a real collision, hadrons can interact with the detector material before decaying. Therefore, from the detector point of view, these hadrons are considered as stable particles. In the ATLAS Monte Carlo tune, a hadron is considered stable if its lifetime is longer than 10 ps.

The normal hadron decay treatment uses a set of look up tables where branching ratios and decay modes are stored. It encompasses all hadrons made out of d, u, s, c and b quarks and also leptons. All particles are included with their proper mass distributions and decay properties. Normally, the decay products are hadrons, leptons and photons.

4.1.3 Beam remmant and underlying event

Until now, a hadron-hadron collision was considered as a single parton-parton interaction. In this case, the initial-state radiation algorithm reconstructs one shower initiator in each beam. This initiator only takes some fraction of the total beam energy, leaving behind a beam remnant which takes the rest. For a proton beam, the remnant is colour-connected to the hard interaction and forms part of the same fragmenting system.

The parton-shower initiator usually has a primordial transverse momentum (k_T), required at least by the uncertainty principle by the proton size. This primordial k_T is selected according to some suitable distribution. The magnitude of k_T can increase to typically $p_T^{\min} \sim 1.5 - 2.5$ GeV due to additional interactions. These interactions arise because the interacting parton from one beam scatters against several different partons from the other beam. Therefore, the recoil, assumed to be taken up by the beam remnant, can be significant. This is called a “minimum-bias” interaction.

In a typical "minimum-bias" interaction, one or a few scatterings at scales around or a bit above $p_T^{\min}$ are expected. In a high-p_T event, additional scatterings at the $p_T^{\min}$ scale can also occur. This is called the underlying event (UE).

Due to the poor understanding of the underlying event mechanism, Monte Carlo generators usually have different tunes for generation of such process. The differences concern the level of detail in the generation of scatterings after the first one, the model that describes how the scatterings are intercorrelated in flavour, colour and momentum space, etc.

4.2 Monte Carlo simulations of prompt-photon processes

Samples of MC events were generated to study the characteristics of signal and background events. The MC samples were also used to determine the response of the detector to jets of hadrons and the correction factors necessary to obtain the hadron-level jet cross section. In addition, these samples were used to estimate hadronisation corrections to the NLO QCD calculations.

The MC programs PYTHIA 6.4.21 [50] and HERWIG 6.5 [51] were used to generate the simulated events. In both generators, the partonic processes are simulated using leading order matrix elements, with the inclusion of initial- and final-state parton showers (see Section 4.1.1). Fragmentation into hadrons was performed using the Lund string model in the case of PYTHIA, and a cluster model in the case of HERWIG, as explained in Section 4.1.2. The modified leading order MRST2007 [52] PDFs were used to parameterise the proton structure. Both samples include a simulation of the underlying event, via a multiple-parton interaction model (see Section 4.1.3) in the case of PYTHIA and via the JIMMY package [53] in the case of HERWIG. The event generator parameters were set according to the "ATLAS-MC10" tune [54].

The signal sample generated using PYTHIA includes leading-order photon plus jet events from both direct-photon process (the hard subprocess $qg \to q\gamma$ and $q\bar{q} \to g\gamma$; the box-diagram hard subprocess $gg \to g\gamma$ is part of the next-to-next-to-leading order (NNLO) cross section and gives a negligible contribution to the total cross section compared to the other two subprocesses) and photon bremsstrahlung coming from electromagnetic final-state radiation of one of the two final state partons of the leading-order QCD dijet process, called fragmentation process. The

HERWIG signal sample was obtained from the luminosity-weighted mixture of the samples containing direct-photon plus jet events only and bremsstrahlung-photon plus jet events only. The signal samples are listed in Table 4.1.

Process	σ **(pb)**	**Filter type**	**Filter threshold (GeV)**	**Filter efficiency**	**Events in ntuples**	**Equivalent luminosity** (pb^{-1})	**Generator**
QCD	5.491E+7	1 prompt γ	35	3.22E-4	995551	5.63E+1	PYTHIA
QCD	3.168E+6	1 prompt γ	70	4.73E-4	997426	6.66E+2	PYTHIA
QCD	1.077E+5	1 prompt γ	140	8.42E-4	994458	1.10E+4	PYTHIA
QCD	4.403E+7	1 prompt γ	35	1.38E-4	987492	1.63E+2	HERWIG
QCD	2.550E+6	1 prompt γ	70	1.64E-4	943342	2.26E+3	HERWIG
QCD	8.735E+4	1 prompt γ	140	2.41E-4	983110	4.66E+4	HERWIG
γ-jet	1.478E+4	1 prompt γ	35	6.02E-1	1819353	2.04E+2	HERWIG
γ-jet	1.284E+3	1 prompt γ	70	6.51E-1	997449	1.19E+3	HERWIG
γ-jet	6.980E+1	1 prompt γ	140	7.75E-1	999109	1.85E+4	HERWIG

Table 4.1: Signal Monte Carlo samples. The QCD PYTHIA samples contain both direct and bremsstrahlung γ+jet events, while the QCD HERWIG samples contain only the bremsstrahlung component. Both the QCD PYTHIA and HERWIG samples include also QCD background events, which are filtered away after event generation.

The background from diphoton events was estimated using the PYTHIA MC sample, as the ratio between diphoton and isolated-photon plus jet events, and found to be negligible [55, 56].

A contribution of QCD processes to the background is expected from "fake" photon candidates (typically from π^0 and η decays). The QCD background was simulated using the dijet samples of PYTHIA and HERWIG listed in Table 4.2. The transverse momentum of the hard scattering products was required to be greater than at least 15 GeV and the generated event was fully simulated if it contained at least one truth-particle jet with transverse energy above a certain threshold (at least 17 GeV).

Process	σ **(pb)**	**Filter type**	**Filter threshold (GeV)**	**Filter efficiency**	**Events in ntuples**	**Equivalent luminosity** (pb^{-1})	**Generator**
QCD	1.147E+9	1 jet	17	7.41E-2	9981031	1.17E+1	PYTHIA
QCD	5.497E+7	1 jet	35	1.41E-1	4992260	6.42E+1	PYTHIA
QCD	3.167E+6	1 jet	70	2.05E-1	998167	1.54E+0	PYTHIA
QCD	9.162+8	1 jet	17	8.14E-2	9979038	1.34E+1	HERWIG
QCD	4.396E+7	1 jet	35	1.44E-1	4965322	7.86E+1	HERWIG
QCD	2.550E+6	1 jet	70	1.93E-1	999199	2.03E+0	HERWIG

Table 4.2: Background Monte Carlo samples.

4.3 Results at hadron level for prompt-photon+jet production

The sample of isolated-photon plus jet events at hadron level (HL) was selected applying the following criteria:

- the photon-candidate selection is based on the particle data group identification (pdgID). For a MC generated photon the value of the pdgID is equal to 22 (pdgID$_\gamma$ =22). The photon-candidate selection criteria are:

  - events in which the photon with highest transverse momentum (leading photon) with $E^{\gamma}_{T,\mathrm{HL}} > 45$ GeV and $|\eta^{\gamma}_{\mathrm{HL}}| < 2.37$ (excluding the region $1.37< |\eta^{\gamma}_{\mathrm{HL}}| <1.52$) were selected;

  - the isolation transverse energy, $E^{\mathrm{iso}}_{T,\mathrm{HL}}$, was required to be below 4 GeV. The $E^{\mathrm{iso}}_{T,\mathrm{HL}}$ variable was reconstructed by using final-state particles in the MC simulations, excluding muons and neutrinos. To reduce the uncertainties from underlying-event modelling, $E^{\mathrm{iso}}_{T,\mathrm{HL}}$ was corrected using the so-called "jet-area method" [57] applied to final-state particles excluding muons and neutrinos;

- jets were reconstructed from the final-state particles, including the preselected photon, muons and neutrinos, using the anti-k_T algorithm with radius R=0.6. The jet four-momenta were computed from the jet constituents based in the recombination E-scheme (see Chapter 3). The selection criteria applied to the jets are:

  - events with at least one jet candidate of $P^{\mathrm{jet}}_{T,\mathrm{HL}} > 40$ GeV and $R^{\gamma-\mathrm{jet}} = \sqrt{(\eta^{\gamma}_{\mathrm{HL}} - \eta^{\mathrm{jet}}_{\mathrm{HL}})^2 + (\phi^{\gamma}_{\mathrm{HL}} - \phi^{\mathrm{jet}}_{\mathrm{HL}})^2} >1$ were selected. In events with multiple

jets satisfying these requirements, the jet with highest transverse momentum (leading jet) was retained for further study;

- the leading jet rapidity was required to be in the region $|Y^{\rm jet}_{\rm lead,HL}| < 2.37$.

For the measurements of the $M^{\gamma-{\rm jet}}_{\rm HL}$ and $|\cos\theta^{\gamma-{\rm jet}}_{\rm HL}|$ cross section, additional cuts were imposed (see Chapter 6). Figures 4.1, 4.2 and 4.3 show the predictions of the normalised differential cross sections as functions of $E^{\gamma}_{T,\rm lead,HL}$, $P^{\rm jet}_{T,\rm lead,HL}$, $|Y^{\rm jet}_{\rm lead,HL}|$, $\Delta\phi^{\gamma-{\rm jet}}_{HL} = \phi^{\gamma}_{\rm HL} - \phi^{\rm jet}_{\rm HL}$, invariant mass of the photon and jet system ($M^{\gamma-{\rm jet}}_{HL}$) and $|\cos\,\theta^{\gamma-{\rm jet}}_{HL}| = |\tanh(\frac{Y^{\gamma}_{\rm HL}-Y^{\rm jet}_{\rm HL}}{2})|$ for DP, F and DP+F processes by PYTHIA and HERWIG.

The predictions by PYTHIA and HERWIG for the DP process are very similar for the six variables studied, as shown in Fig. 4.1. However, PYTHIA and HERWIG give different predictions for the F process, as shown in Fig. 4.2. PYTHIA and HERWIG differ in the modelling of the initial- and final-state QED radiation, as explained in Section 4.1.1. Therefore, differences between PYTHIA and HERWIG for the F process are expected. The leading photon produced in a DP process is more energetic than the one produced in a F process, as observed in the tail of the normalised differential cross section as functions of $E^{\gamma}_{T,\rm lead,HL}$ (see Figs. 4.1 and 4.2). A fragmentation photon usually takes a small p_T fraction of one of the two final-state partons of the leading order QCD dijet process; therefore, due to the condition of $E^{\gamma}_{T,\rm HL} > 45$ GeV, the p_T of the leading jet for a F process is higher, as shown in Figs. 4.1(b) and 4.2(b). There are also differences in the shape of the normalised differential cross section as a function of $|\cos\,\theta^{\gamma-{\rm jet}}_{HL}|$, due to spin differences of the dominant exchanged particle in the two processes (see Figs. 4.1(f) and 4.2 (f)).

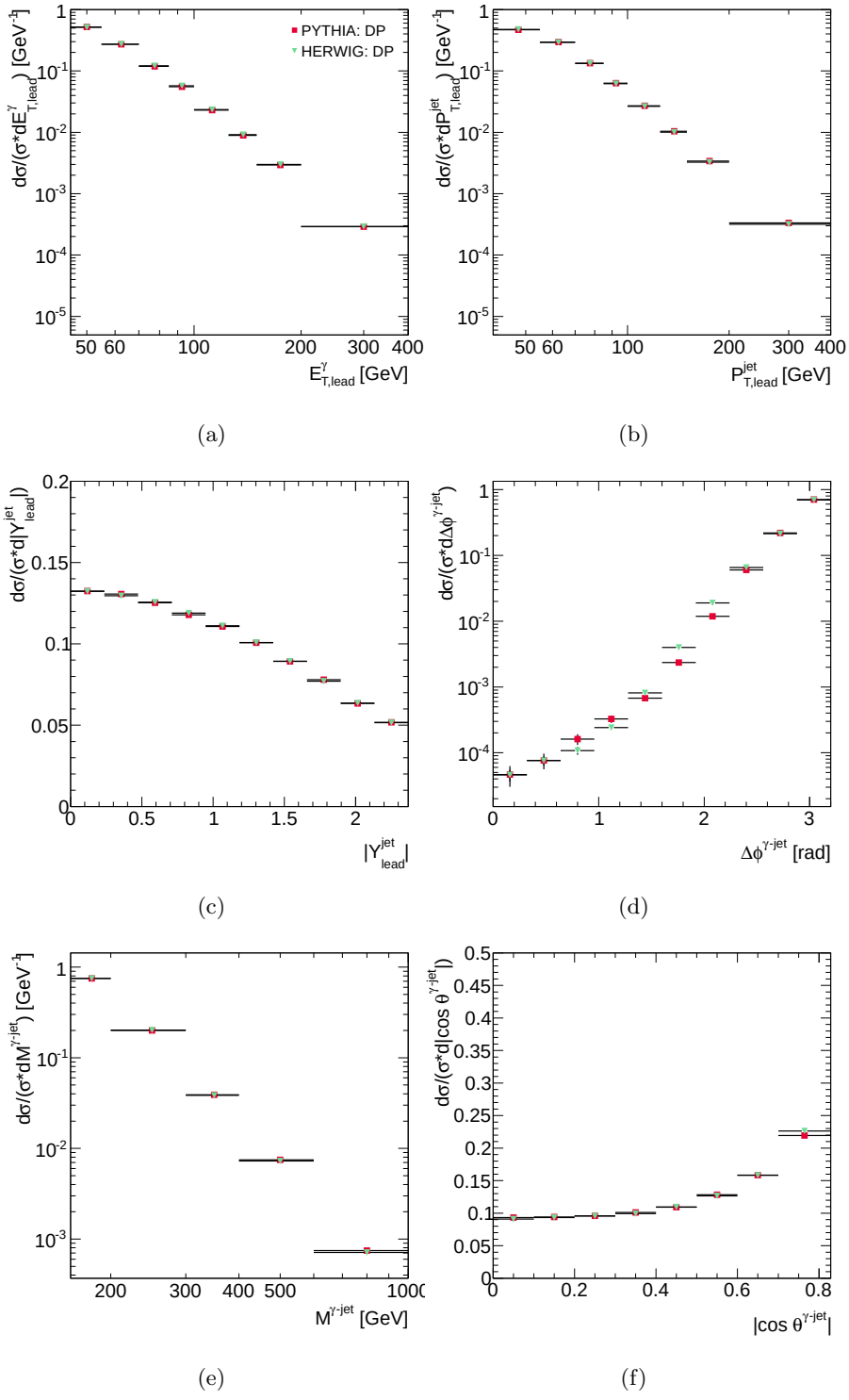

Figure 4.1: Hadron-level predictions of the normalised differential cross section by PYTHIA (squares) and by HERWIG (triangles) for photon plus jet production through direct-photon processes as a function of (a) $E^{\gamma}_{T,\mathrm{lead,HL}}$, (b) $P^{\mathrm{jet}}_{T,\mathrm{lead,HL}}$, (c) $|Y^{\mathrm{jet}}_{\mathrm{lead,HL}}|$, (d) $\Delta\phi^{\gamma-\mathrm{jet}}_{HL}$, (e) $M^{\gamma-\mathrm{jet}}_{HL}$ and (f) $|\cos\theta^{\gamma-\mathrm{jet}}_{HL}|$.

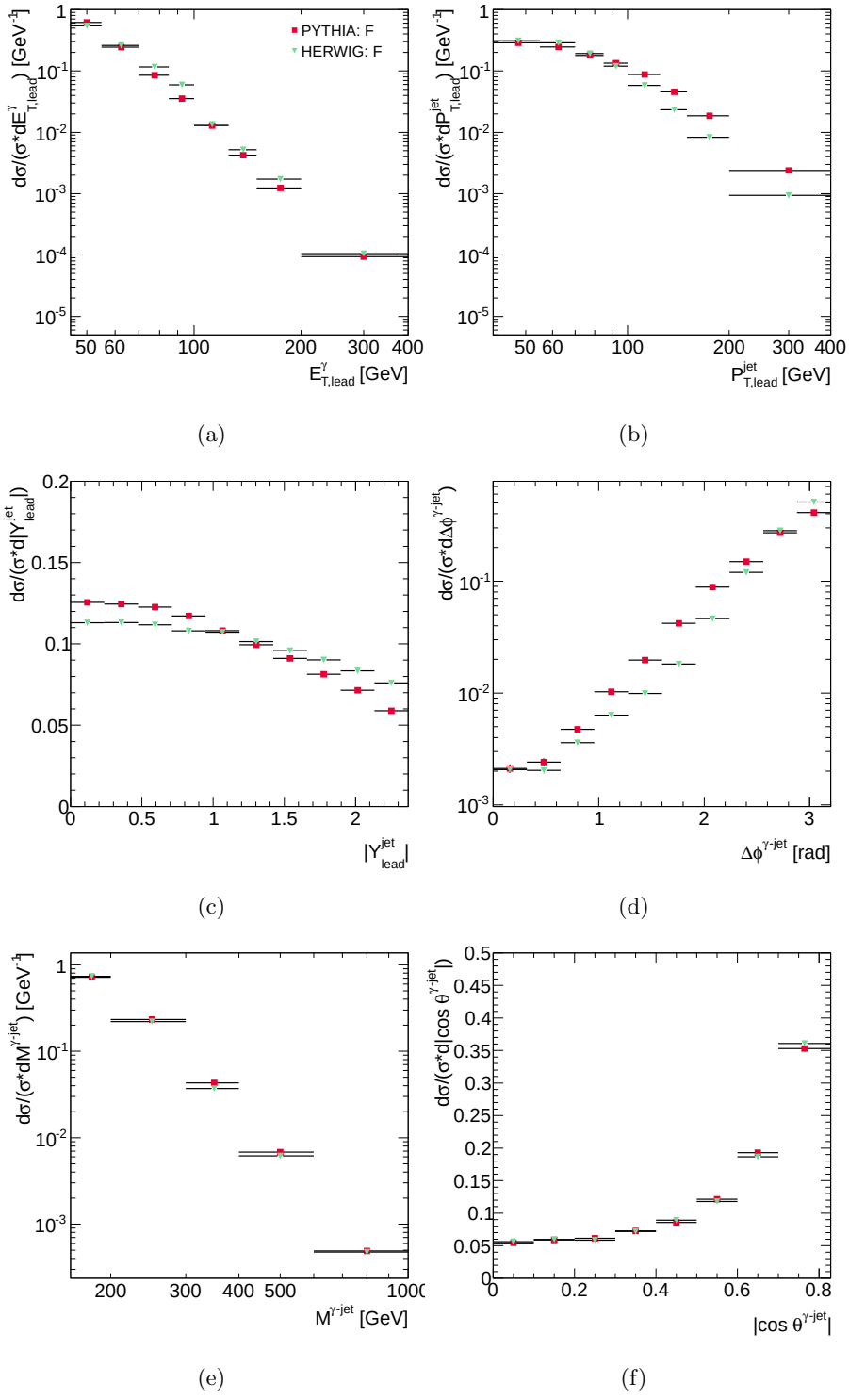

Figure 4.2: Hadron-level predictions of the normalised differential cross section by PYTHIA (squares) and by HERWIG (triangles) for photon plus jet production through fragmentation processes as a function of (a) $E^{\gamma}_{T,\mathrm{lead,HL}}$, (b) $P^{\mathrm{jet}}_{T,\mathrm{lead,HL}}$, (c) $|Y^{\mathrm{jet}}_{\mathrm{lead,HL}}|$, (d) $\Delta\phi^{\gamma-\mathrm{jet}}_{HL}$, (e) $M^{\gamma-\mathrm{jet}}_{HL}$ and (f) $|\cos\theta^{\gamma-\mathrm{jet}}_{HL}|$.

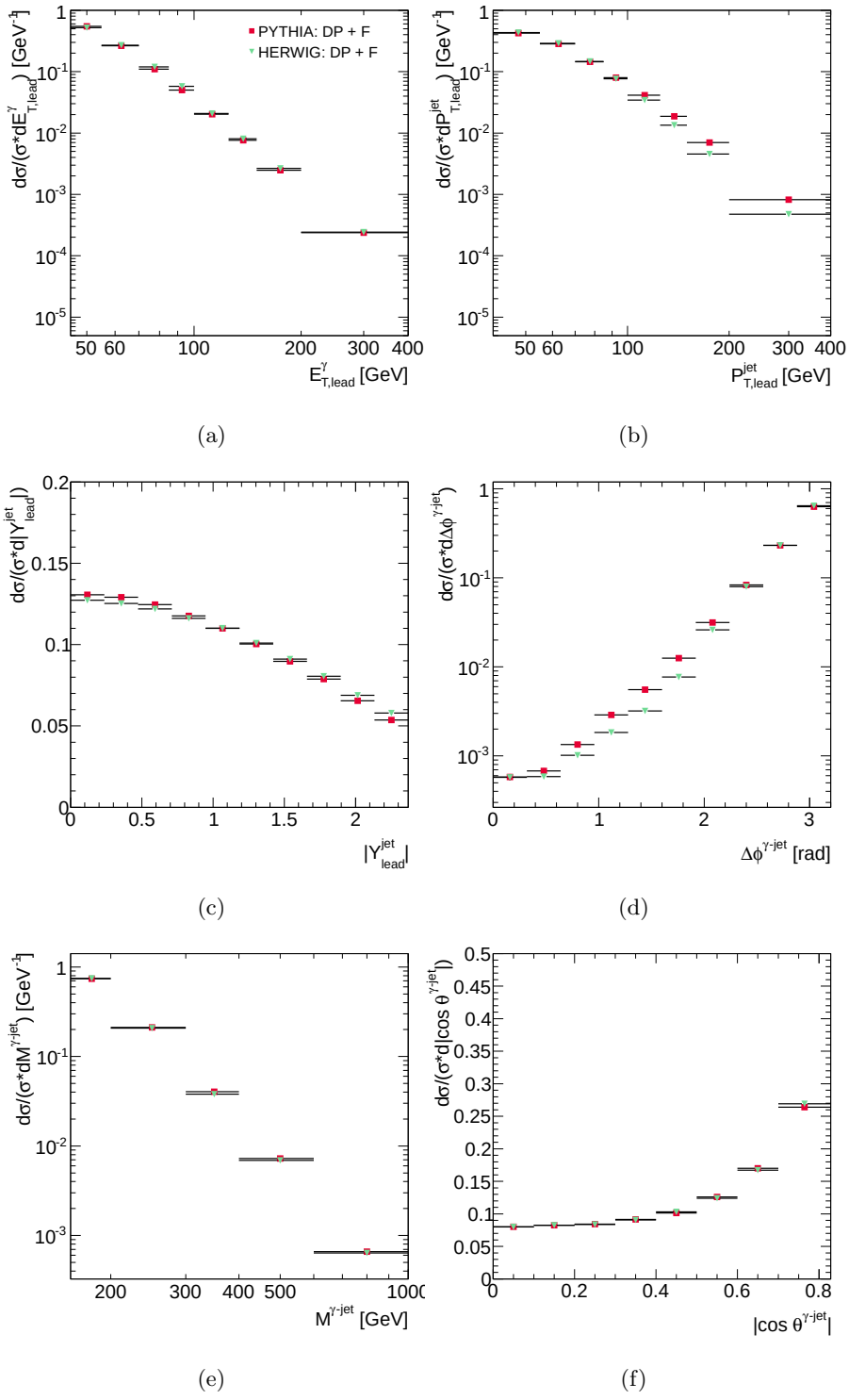

Figure 4.3: Hadron-level predictions of the normalised differential cross section by PYTHIA (squares) and by HERWIG (triangles) for photon plus jet production through direct-photon and fragmentation processes as a function of (a) $E^{\gamma}_{T,\mathrm{lead,HL}}$, (b) $P^{\mathrm{jet}}_{T,\mathrm{lead,HL}}$, (c) $|Y^{\mathrm{jet}}_{\mathrm{lead,HL}}|$, (d) $\Delta\phi^{\gamma-\mathrm{jet}}_{HL}$, (e) $M^{\gamma-\mathrm{jet}}_{HL}$ and (f) $|\cos\theta^{\gamma-\mathrm{jet}}_{HL}|$.

4.4 Results at parton level for prompt-photon+jet production

The Monte Carlo parton level (PL) was defined as the partons generated by the MC generator (PYTHIA or HERWIG) before hadronisation and excluding those from the underlying event. The selection cuts applied at this level are similar to those at hadron level. The differences in the parton-level selection are:

- the photon isolation variable ($E_{T,\mathrm{PL}}^{\mathrm{iso}}$) was reconstructed with partons instead of hadrons and the underlying-event correction was not performed;
- jets were reconstructed from partons instead of hadrons.

Figures 4.4, 4.5 and 4.6 show the predicted normalised differential cross sections as functions of $E_{T,\mathrm{lead,PL}}^{\gamma}$, $P_{T,\mathrm{lead,PL}}^{\mathrm{jet}}$, $|Y_{\mathrm{lead,PL}}^{\mathrm{jet}}|$, $\Delta\phi_{PL}^{\gamma-\mathrm{jet}}$, $M_{PL}^{\gamma-\mathrm{jet}}$ and $|\cos\theta_{PL}^{\gamma-\mathrm{jet}}|$ for the DP, F and DP+F processes by PYTHIA and HERWIG.

The MC generator parton-level distributions exhibit the same properties discussed in Section 4.3, as shown in Figs. 4.1 to 4.6. This is a consequence of the hypothesis of local hadron-parton duality (LHPD) [58, 59], in which it is assumed that the flow of momentum and quantum numbers at the hadron level is already established at the parton level, so that the effect of hadronisation is only to smear the energy configuration at the parton level.

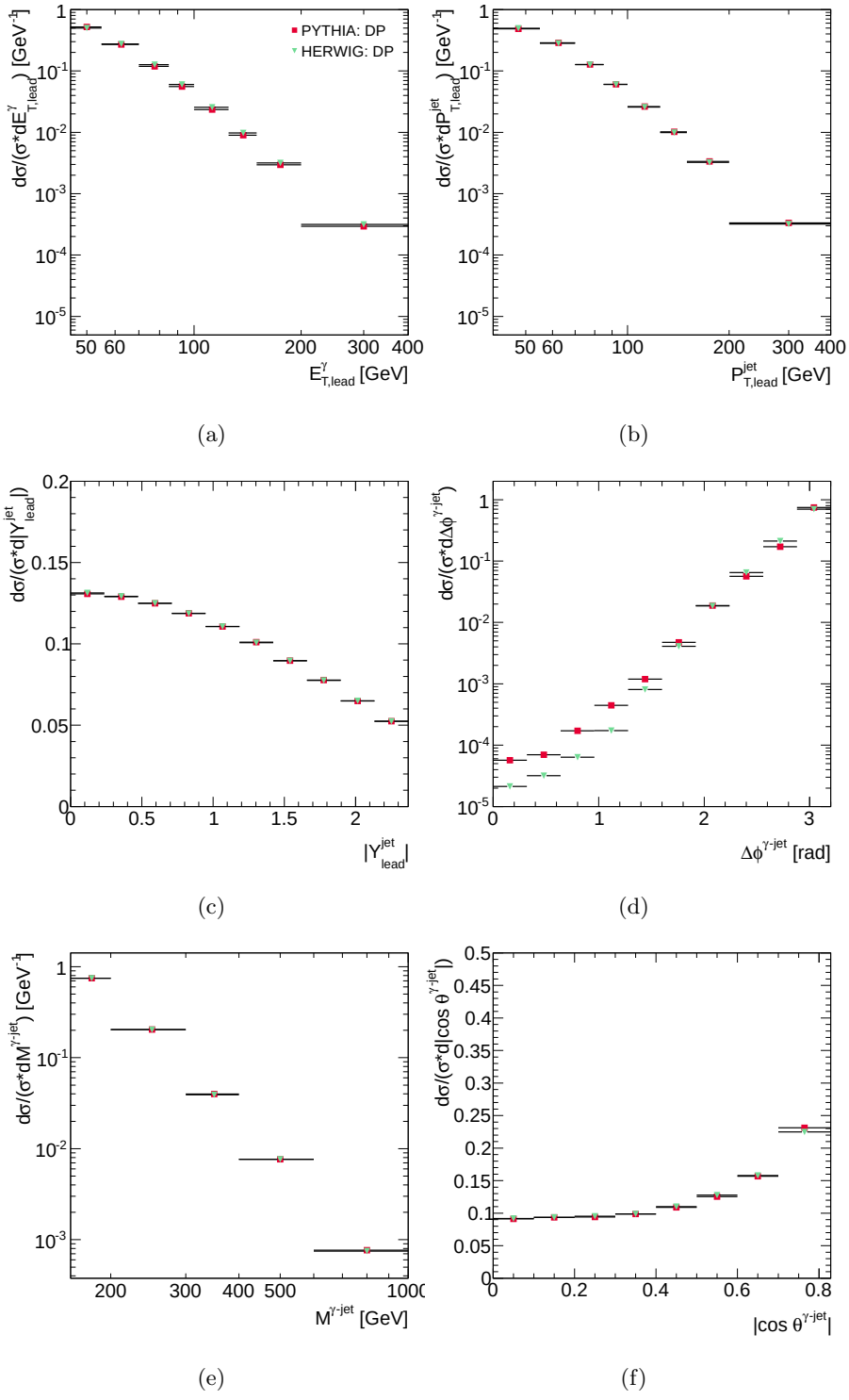

Figure 4.4: Parton-level predictions of the normalised differential cross section by PYTHIA (squares) and by HERWIG (triangles) for photon plus jet production through direct-photon processes as a function of (a) $E^{\gamma}_{T,\mathrm{lead,PL}}$, (b) $P^{\mathrm{jet}}_{T,\mathrm{lead,PL}}$, (c) $|Y^{\mathrm{jet}}_{\mathrm{lead,PL}}|$, (d) $\Delta\phi^{\gamma-\mathrm{jet}}_{PL}$, (e) $M^{\gamma-\mathrm{jet}}_{PL}$ and (f) $|\cos\theta^{\gamma-\mathrm{jet}}_{PL}|$.

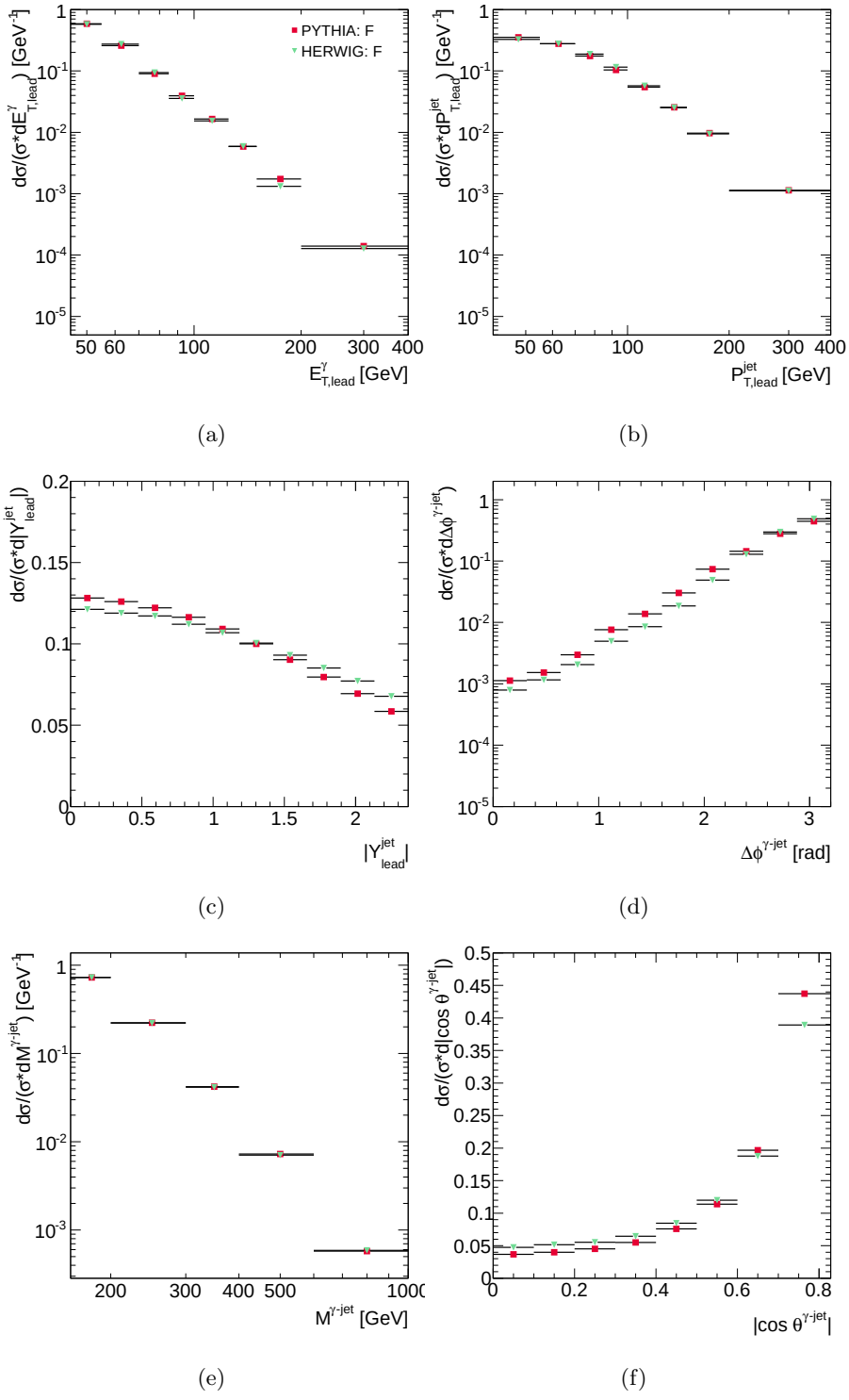

(a) (b) (c) (d) (e) (f)

Figure 4.5: Parton-level predictions of the normalised differential cross section by PYTHIA (squares) and by HERWIG (triangles) for photon plus jet production through fragmentation processes as a function of (a) $E^{\gamma}_{T,\mathrm{lead,PL}}$, (b) $P^{\mathrm{jet}}_{T,\mathrm{lead,PL}}$, (c) $|Y^{\mathrm{jet}}_{\mathrm{lead,PL}}|$, (d) $\Delta\phi^{\gamma-\mathrm{jet}}_{PL}$, (e) $M^{\gamma-\mathrm{jet}}_{PL}$ and (f) $|\cos\theta^{\gamma-\mathrm{jet}}_{PL}|$.

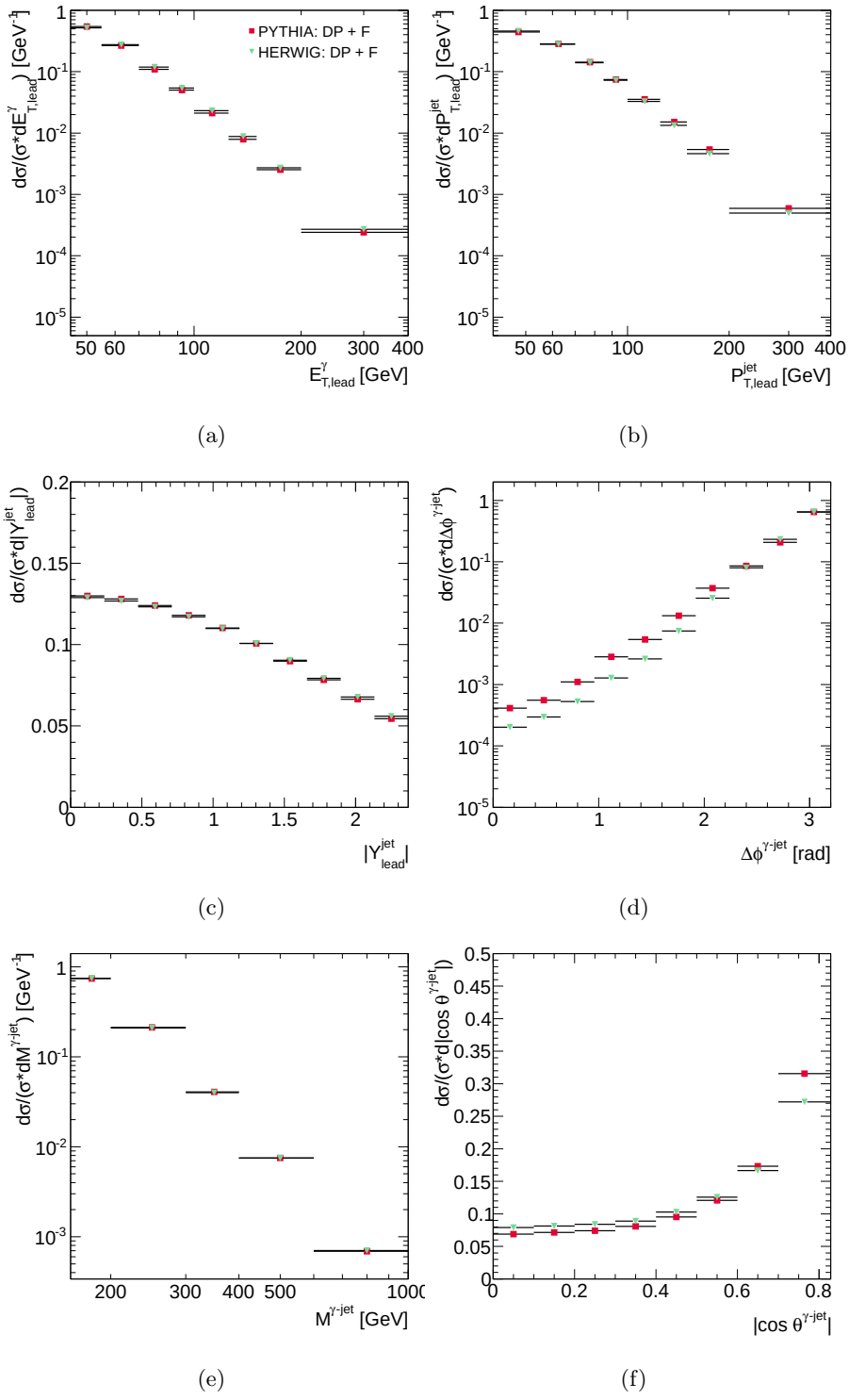

Figure 4.6: Parton-level predictions of the normalised differential cross section by PYTHIA (squares) and by HERWIG (triangles) for photon plus jet production through direct-photon and fragmentation processes as a function of (a) $E^{\gamma}_{T,\mathrm{lead,PL}}$, (b) $P^{\mathrm{jet}}_{T,\mathrm{lead,PL}}$, (c) $|Y^{\mathrm{jet}}_{\mathrm{lead,PL}}|$, (d) $\Delta\phi^{\gamma-\mathrm{jet}}_{PL}$, (e) $M^{\gamma-\mathrm{jet}}_{PL}$ and (f) $|\cos\,\theta^{\gamma-\mathrm{jet}}_{PL}|$.

4.5 Hadronisation and underlying-event corrections to the NLO QCD calculations

Since the measurements refer to jets of hadrons, whereas the NLO QCD calculations refer to jets of partons, the predictions were corrected to the hadron level using MC models. For this method to be valid, the partonic level of the MC simulations must describe reasonably well the shape of the NLO QCD predictions. The comparison of the MC simulations and the NLO QCD calculations is shown in Figs. 4.7 and 4.8. Both PYTHIA and HERWIG partonic levels give a good description of the calculations after adjusting the relative contribution of direct-photon and fragmentation processes. The results of the fit for α are shown in Table 4.3 and the χ^2 distributions are shown in Figs. 4.9 and 4.10.

The multiplicative correction factor, C_{had}, was defined as the ratio of the cross section for jets of hadrons over that for jets of partons and was estimated by using the MC programs described in Section 4.2. Figure 4.11 shows the values of C_{had} for each cross section from PYTHIA and HERWIG separately. The correction factors from PYTHIA and HERWIG are very similar and close to unity, except at high $P_{T,\mathrm{lead}}^{\mathrm{jet}}$.

The NLO QCD calculations were also corrected to include the underlying event effects (UE), so as to provide a fair comparison to the data. The multiplicative correction factor, C_{MI}, was defined as the ratio of the cross section for jets of partons with UE over that for jets of partons without such effect and was estimated by using the MC programs described in Section 4.2. Figure 4.12 shows the values of C_{MI} for each cross section from PYTHIA and HERWIG separately. The correction factors from PYTHIA and HERWIG are very similar and close to unity.

The total multiplicative correction factor,

$$C_{\mathrm{NLO}} = C_{\mathrm{had}} \cdot C_{\mathrm{MI}} \ , \tag{4.1}$$

as obtained with PYTHIA or HERWIG as well as the average is shown in Fig. 4.13.

4.6 Simulation of detector effects

A detector simulation consists of reconstructing the signal produced in the different parts of the detector by the final-state particles based on the energy, position and kind of particles.

	PYTHIA	HERWIG
	α	α
$E_{T,\mathrm{lead}}^{\gamma}$	0.35	0.23
$P_{T,\mathrm{lead}}^{\mathrm{jet}}$	0.33	0.24
$\Delta\phi^{\gamma-\mathrm{jet}}$	0.94	1.0
$M^{\gamma-\mathrm{jet}}$	0.70	1.0
$\lvert\cos\,\theta^{\gamma-\mathrm{jet}}\rvert$	0.57	0.33

Table 4.3: Values of the free parameter α in the admixture of the direct-photon and fragmentation components in PYTHIA and HERWIG resulting from the fit to the NLO calculations.

All the samples of generated events listed in Tables 4.1 and 4.2 were passed through the GEANT4-based[60] (see section 4.6.1) detector simulation. They were reconstructed and analysed by the same program chain as the data.

4.6.1 Geant4

The standard simulation strategy of ATLAS is based on the Geant4 (G4) particle simulation toolkit and uses a highly-detailed detector description. G4 provides detailed models for physics processes and the infrastructure for particle transportation through a geometry.

The detector geometry itself is constructed in the G4 format. Physics models, which include the interactions of particles with matter, are typically chosen as physics lists. The ATLAS simulation has provided a challenging test-bed for the G4 toolkit. G4 has been extensively evaluated and validated during large-scale simulation production.

4.6.2 Pile-up

In high-luminosity colliders, there is a non-negligible probability that one single bunch crossing produces several separate events, so-called pile-up events. To reproduce the pile-up effect, several events are generated and put one after the other in the event record.

To get a reliable simulation of the pile-up, knowledge of the luminosity per bunch-bunch crossing is needed. Multiplied by the cross section for pile-up processes studied, σ_{pile}, this gives the average number of collisions per beam crossing, $\bar{n}$. Pile-up events usually are taken to be of the minimum-bias type, with diffractive and elastic events included or not. If pile-up is taken to be of the minimum-bias type events only, the number of events in a crossing is distributed according to a Poisson with the average number $\bar{n}$. The mean number of pile-up events is then given by

$$< n >= \frac{\bar{n}}{(1 - \exp(-\bar{n}))} \ . \tag{4.2}$$

Pile-up effects at detector level

The large instantaneous luminosity at the LHC leads to additional proton-proton interactions occurring in the same and previous bunch crossings, which produce particles overlapping with those of the event of interest which has resulted in the acceptance by the trigger. They are referred to as in-time and out-of-time pile-up, respectively. The in-time pile-up results in additional primary vertices. Pile-up can influence the reconstruction of the physics objects (e.g. jets), isolation requirements, etc. In order to model pile-up effects properly, these additional proton-proton interactions must be accounted for at detector level. These additional interactions are treated separately at the event generation and simulation stages. However, in the digitization step, hits from the hard-scattering event are overlaid with those from the requested number of these additional interactions before the detector response is calculated. Because of long signal integration times, most subdetector responses are affected by interactions from neighboring bunch crossings as well. Therefore, additional interactions offset in time are overlaid as necessary.

For the studies presented here, the Monte Carlo samples of events were simulated including pile-up effects in the so-called bunch train pile-up-setup. Minimum-bias interactions simulated with PYTHIA are overlaid on top of the hard-scattering event with the following timing structure: (a) individual bunches are separated by 150 ns and contained in trains of eight bunches length; (b) a second bunch train follows with a time separation equal to 225 ns, (c) followed by a longer pause before the next bunch train. The average amount of simulated additional minimum-bias interactions per bunch crossing was chosen to be Poisson distributed with an expectation value equal to 2.2. Since this can be measured well using the primary-vertex multiplicity in 2010 data, possible differences between data and Monte Carlo simulations can be corrected for by reweighting the primary-vertex multiplicity distribution in the simulation so as to match the data.

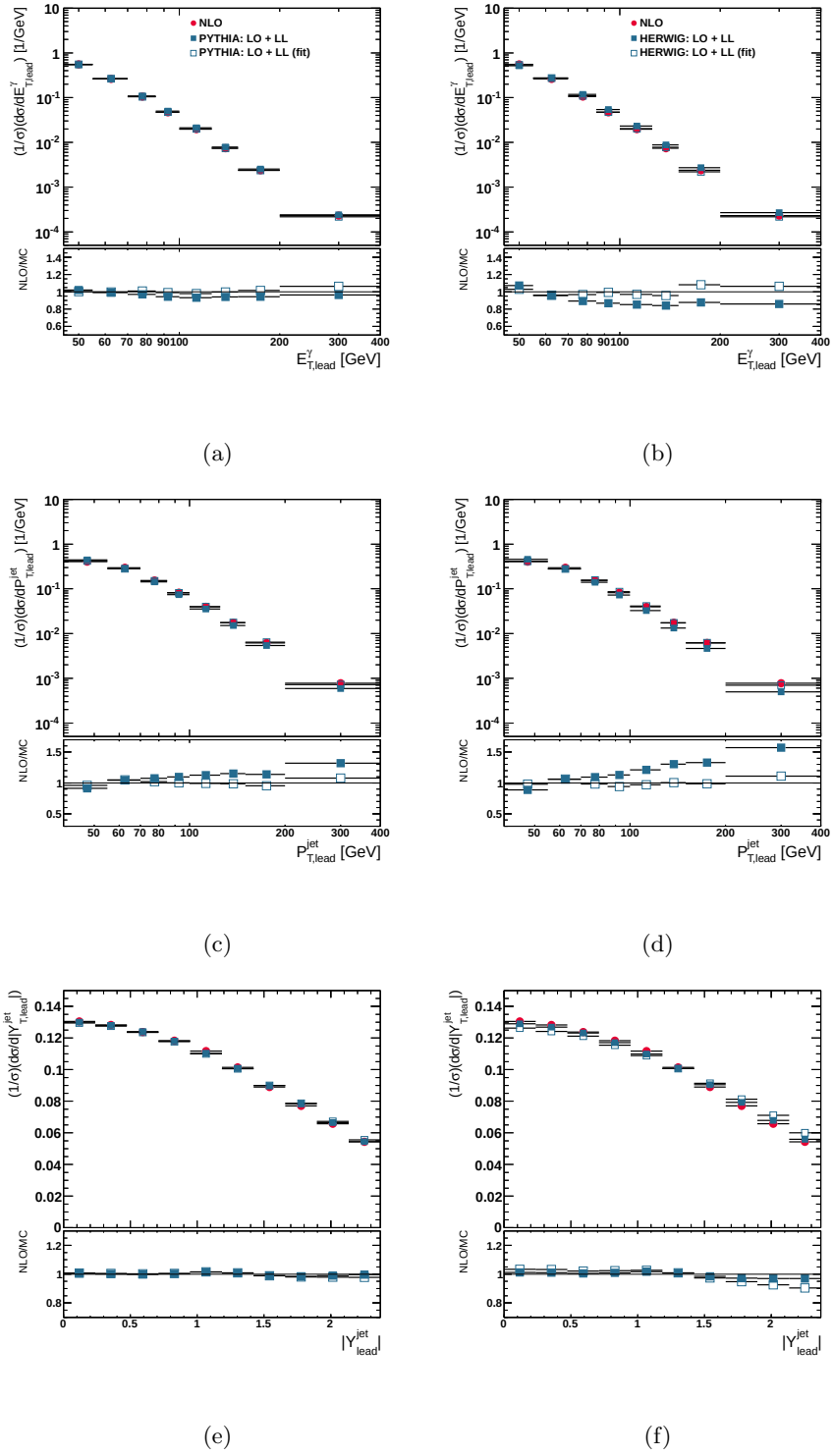

Figure 4.7: NLO QCD predicted differential cross sections as functions of (a,b) $E^{\gamma}_{T,\mathrm{lead}}$, (c,d) $P^{\mathrm{jet}}_{T,\mathrm{lead}}$ and (e,f) $|Y^{\mathrm{jet}}_{\mathrm{lead}}|$. The parton-level cross section from PYTHIA (left-hand side plots) and HERWIG (right-hand side plots) are also included with the default admixture (solid squares) and after the fit (open squares).

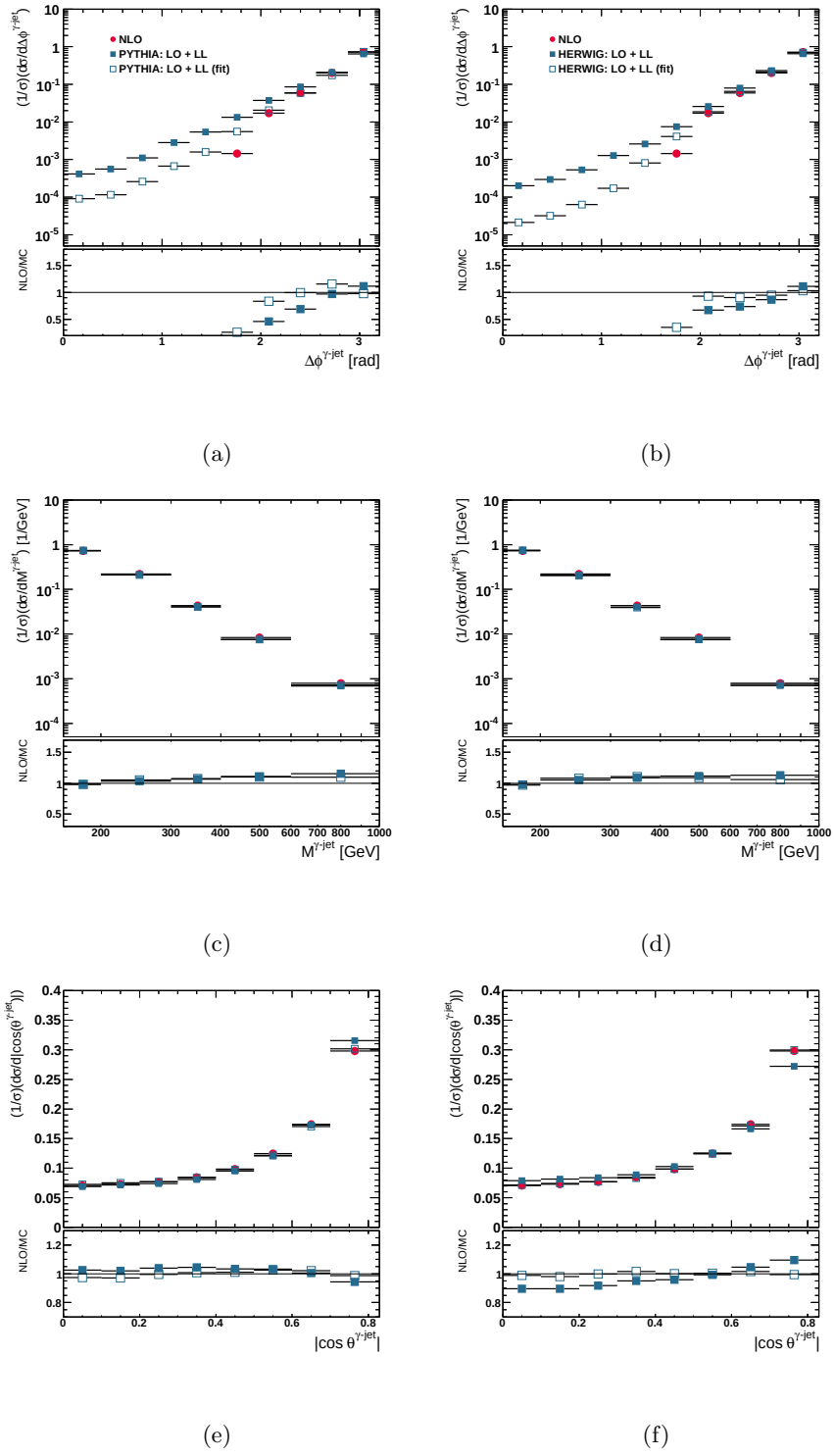

Figure 4.8: NLO QCD predicted differential cross sections as functions of (a,b) $\Delta\phi^{\gamma-\mathrm{jet}}$, (c,d) $M^{\gamma-\mathrm{jet}}$ and (e,f) $|\cos\,\theta^{\gamma-\mathrm{jet}}|$. The parton-level cross section from PYTHIA (left-hand side plots) and HERWIG (right-hand side plots) are also included with the default admixture (solid squares) and after the fit (open squares).

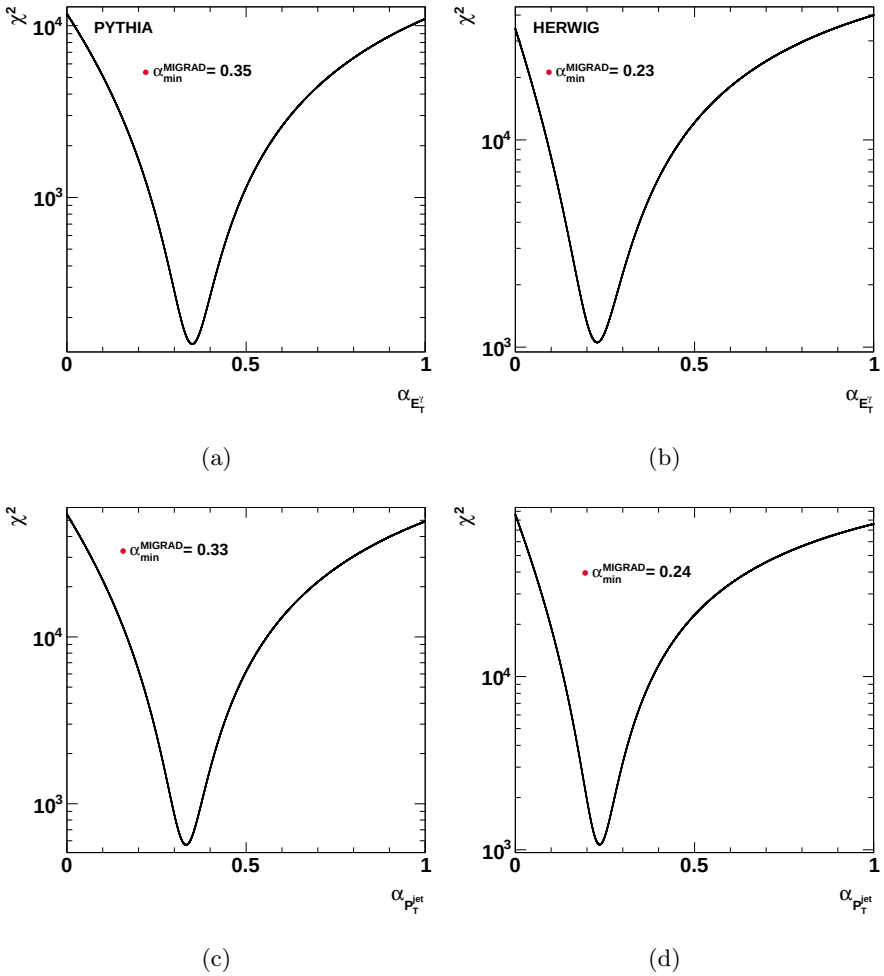

Figure 4.9: The χ^2 distribution resulting from the fit to the NLO calculations as functions of (a) $E_{T,\mathrm{lead}}^{\gamma}$ and (c) $P_{T,\mathrm{lead}}^{\mathrm{jet}}$ for the PYTHIA samples. The χ^2 distribution resulting from the fit to the NLO calculations as functions of (b) $E_{T,\mathrm{lead}}^{\gamma}$ and (d) $P_{T,\mathrm{lead}}^{\mathrm{jet}}$ for the HERWIG samples.

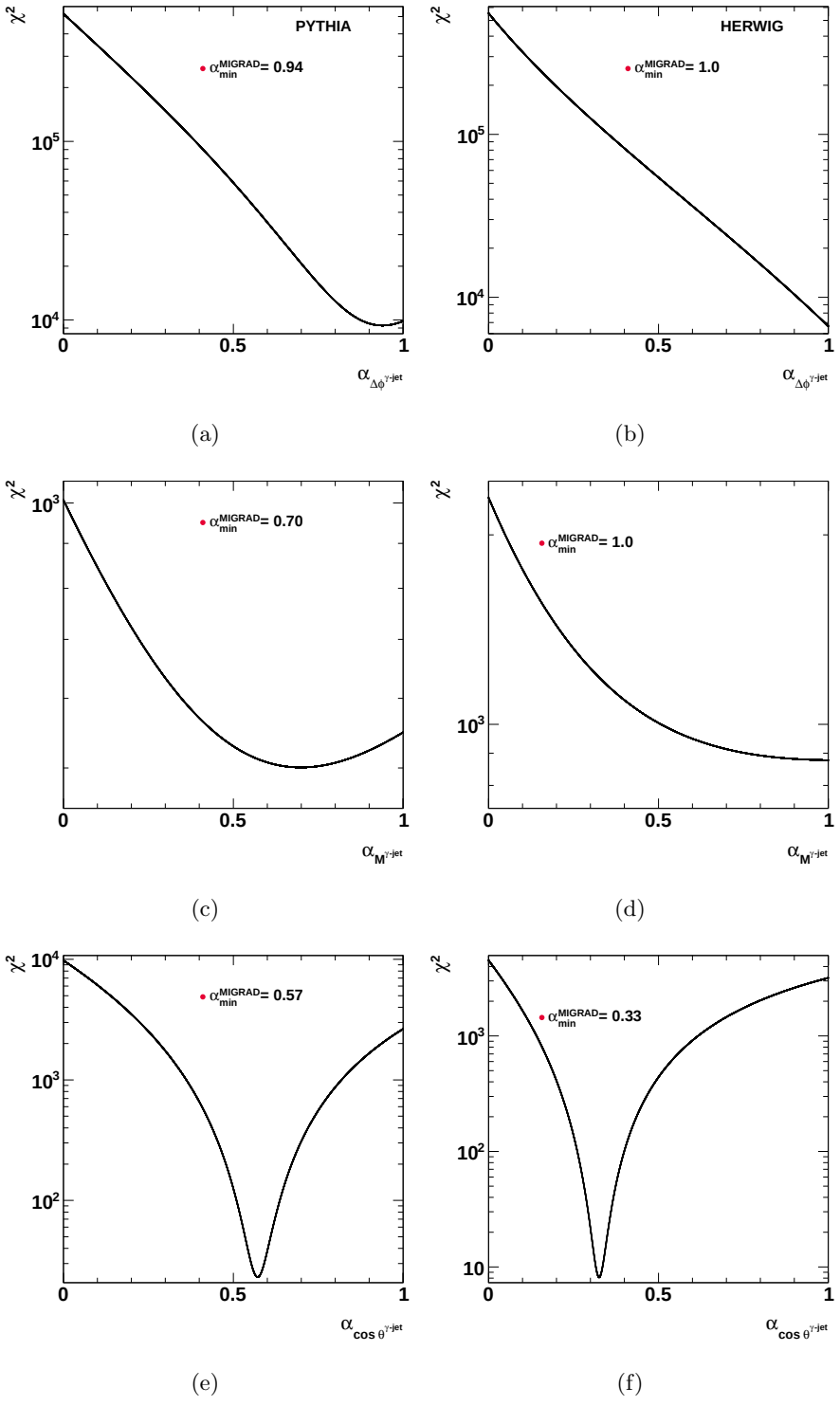

Figure 4.10: The χ^2 distribution resulting from the fit to the NLO calculations as functions of (a) $\Delta\phi^{\gamma-\text{jet}}$, (c) $M^{\gamma-\text{jet}}$ and (e) $|\cos\theta^{\gamma-\text{jet}}|$ for the PYTHIA samples. The χ^2 distribution resulting from the fit to the NLO calculations as functions of (b) $\Delta\phi^{\gamma-\text{jet}}$, (d) $M^{\gamma-\text{jet}}$ and (f) $|\cos\theta^{\gamma-\text{jet}}|$ for the HERWIG samples.

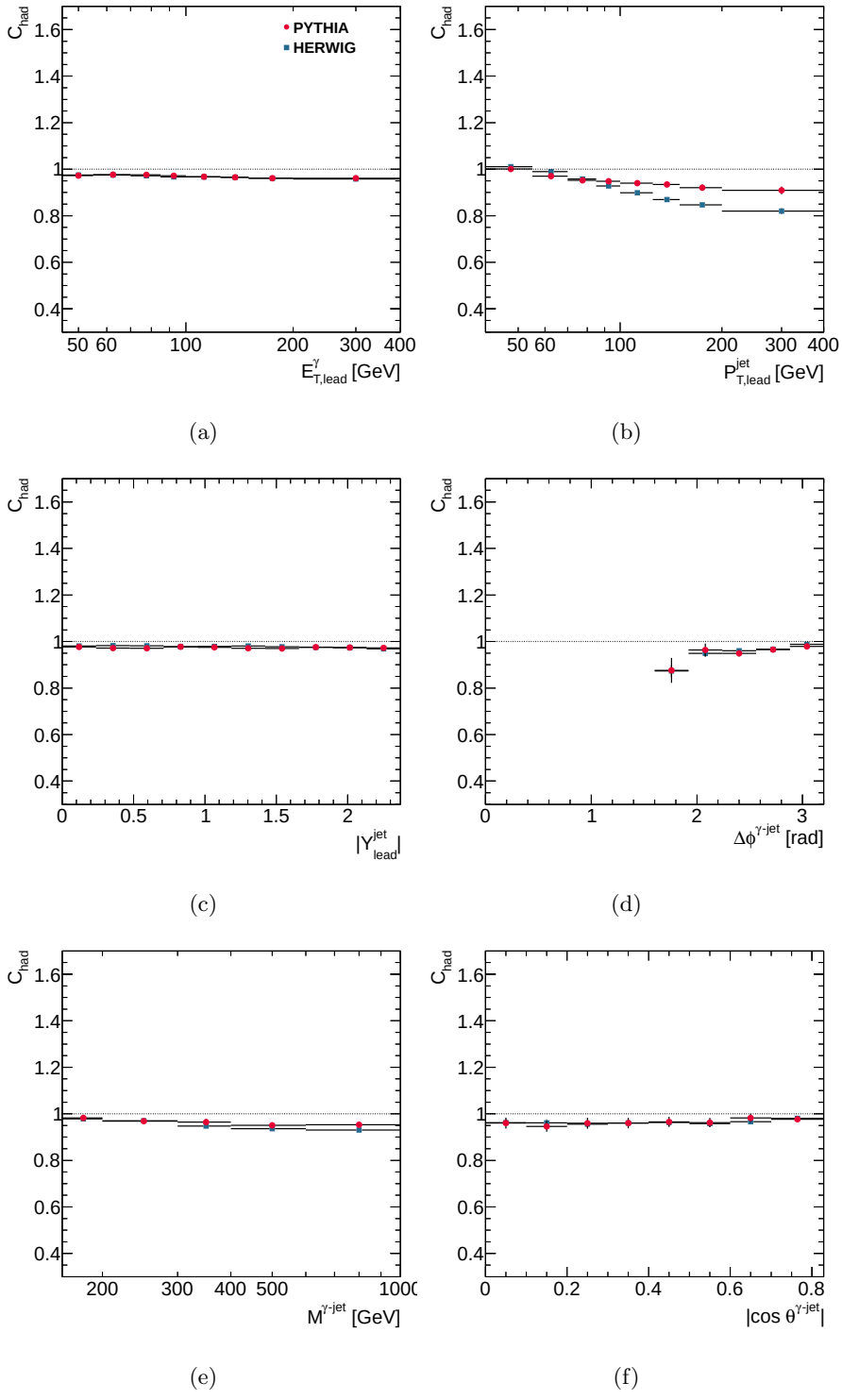

Figure 4.11: Hadronisation correction factors as functions of (a) $E^{\gamma}_{T,\mathrm{lead}}$, (b) $P^{\mathrm{jet}}_{T,\mathrm{lead}}$, (c) $|Y^{\mathrm{jet}}_{\mathrm{lead}}|$, (d) $\Delta\phi^{\gamma-\mathrm{jet}}$, (e) $M^{\gamma-\mathrm{jet}}$ and (f) $|\cos\,\theta^{\gamma-\mathrm{jet}}|$ from PYTHIA (dots) and HERWIG (squares).

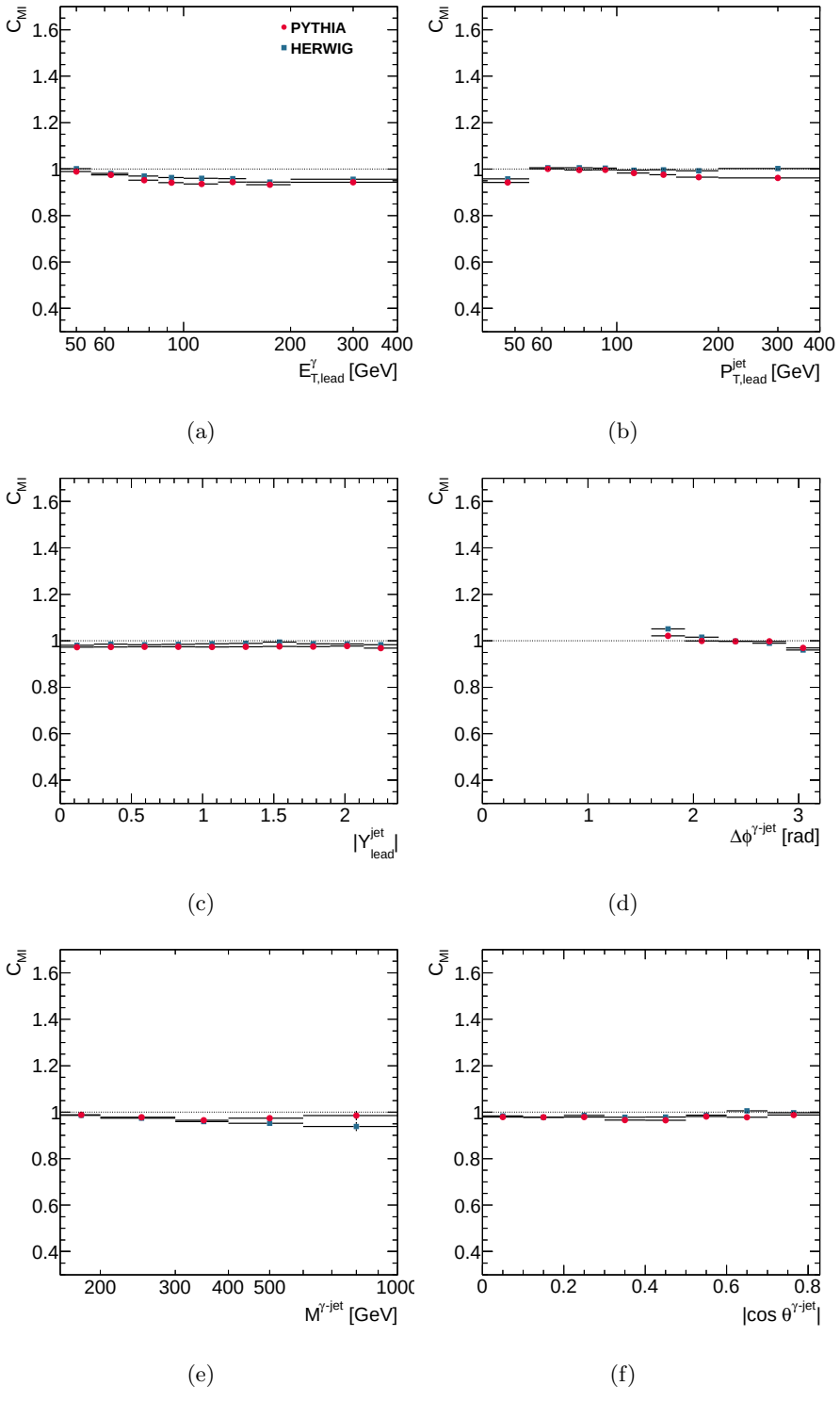

Figure 4.12: Correction factors for underlying-event effects as functions of (a) $E^{\gamma}_{T,\mathrm{lead}}$, (b) $P^{\mathrm{jet}}_{T,\mathrm{lead}}$, (c) $|Y^{\mathrm{jet}}_{\mathrm{lead}}|$, (d) $\Delta\phi^{\gamma-\mathrm{jet}}$, (e) $M^{\gamma-\mathrm{jet}}$ and (f) $|\cos\,\theta^{\gamma-\mathrm{jet}}|$ from PYTHIA (dots) and HERWIG (squares).

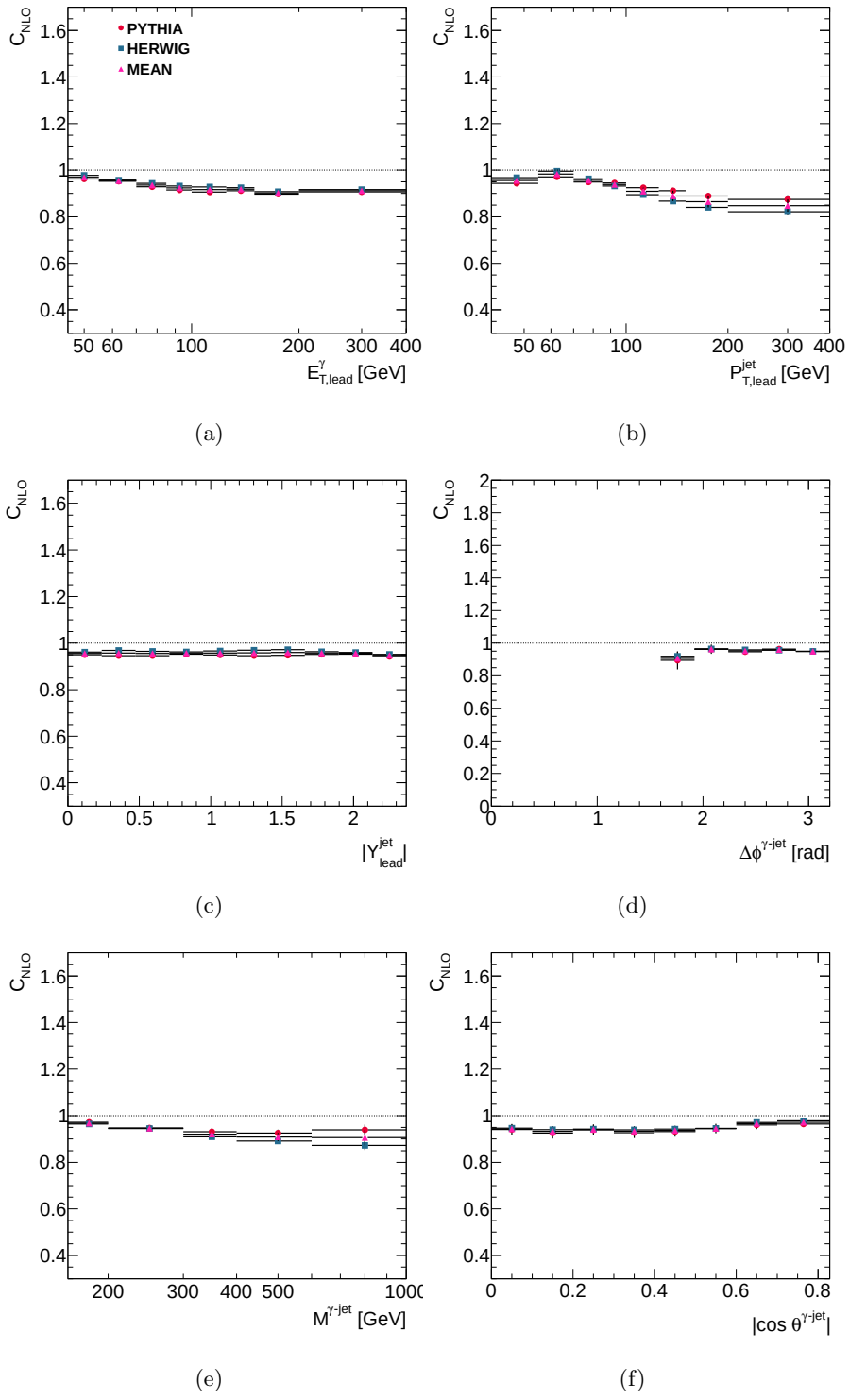

Figure 4.13: The C_{NLO} correction factors as functions of (a) $E^{\gamma}_{T,\mathrm{lead}}$, (b) $P^{\mathrm{jet}}_{T,\mathrm{lead}}$, (c) $|Y^{\mathrm{jet}}_{\mathrm{lead}}|$, (d) $\Delta\phi^{\gamma-\mathrm{jet}}$, (e) $M^{\gamma-\mathrm{jet}}$ and (f) $|\cos\theta^{\gamma-\mathrm{jet}}|$ from PYTHIA (dots) and HERWIG (squares). The mean value between the corrections from PYTHIA and HERWIG is shown as triangles.

Chapter 5

Photon and jet reconstruction and identification

This analysis refers to photons and jets and this chapter presents the main features of their reconstruction and identification.

This chapter is divided in two main parts. In the first part, the main aspects of photon recontruction, triggering, identification and calibration are explained. Finally, in the last part of the chapter the main aspects of jet reconstruction, calibration and quality are described.

5.1 Photon reconstruction and identification

Photons are identified by the ATLAS detector exploiting the characteristics of the EM calorimeter. Photons are reconstructed as EM clusters and since they are neutral, it is also required that they do not have tracks pointing to the cluster. Photons can convert into pairs of electrons and positrons due to the interaction with the detector material. In that case, not only a EM cluster is required but also a secondary reconstructed vertex with at least two tracks pointing to the cluster is required.

The photon identification and variable reconstruction algorithms [61, 64] used in the ATLAS experiment were designed to achieve both high and uniform efficiency over the full acceptance of the detector for transverse energies above 20 GeV and a large background rejection. At transverse energies above 20 GeV, neutral hadron decays, mainly from the decay $\pi^0 \to \gamma\gamma$, are responsible for the majority of background photons.

The LAr calorimeter has a fine segmentation in both the lateral and longitudinal directions of the electromagnetic showers, as explained in Chapter 2. At high energy, most of the EM-shower energy is collected in the second layer of the LAr calorimeter. The first layer consists of fine-grained strips in the η-direction which offer excellent γ/π^0 discrimination. The transition region between the barrel and end-cap EM calorimeters, $1.37< |\eta| <1.52$, is expected to have poor performance because of the large amount of material in front of the first active calorimeter layer. It is usually excluded from the fiducial regions.

The photon must pass through the ATLAS tracker before depositing their energy in the LAr. The interaction of the photons with the ID is completely dominated by e^+e^- pair production in the presence of material, known as photon conversions. The reconstruction of photon conversions is a particular challenge for the ID, since between 10% and 50% of photons convert into an e^+e^- pair. The pixel vertexing layer, located in the innermost part of the ID, provides precision vertexing and significant rejection of contributions from photon conversions.

5.1.1 Triggering photon candidates

As explained in Chapter 2, the ATLAS trigger system is divided into three levels. In this Section, a detailed explanation of the trigger chain used for selecting photon candidates is presented.

At L1, the selection of photon candidates is based on calorimeter information, using the so-called trigger towers to construct EM clusters. These clusters are retained if their transverse energies are above a certain threshold, specified in a trigger menu. If the event is accepted by L1, it passes to the next level, L2, which uses the EM-cluster position calculated by L1. Already at this level, full LAr information is available and the calorimeter reconstruction works very similarly to the offline algorithm (see Chapter 2). The main difference with the offline reconstruction is in the cluster seed finding step, which is done using the most energetic cell in the second EM layer at L2 and the "sliding window algorithm" in the offline reconstruction (see Section 5.1.2). Cluster building, calibration and cluster corrections are the same as in the offline reconstruction. The EF uses the offline reconstruction algorithms, but reconstruction of converted photons is not attempted.

Level-1 selection

At L1, information from the LAr and hadronic calorimeter system in the form of "trigger towers" is used. A trigger tower consists of towers with dimension $\Delta\eta \times \Delta\phi$ ~0.1×0.1. In this region, all the cells are summed over the full depth of either the electromagnetic or hadronic calorimeter. The L1 selection algorithm for electromagnetic clusters is based on a sliding 4×4 window of trigger towers which looks for local maxima. The triggered object is considered to contain a photon candidate if the following requirements are satisfied:

- the central 2×2 "core" cluster consisting of both EM and hadronic towers is a local E_T maximum. This requirement prevents double counting of clusters by overlapping windows;
- the most energetic of the four combinations of two neighboring EM towers passes the electromagnetic cluster threshold.

Figure 5.1 shows the L1 trigger-tower schema used to determine the L1 selection variables.

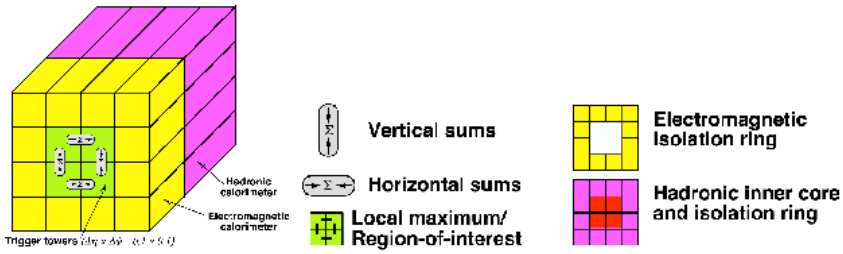

Figure 5.1: L1 calorimeter trigger schema, showing how trigger towers are used to determine the energy for the electromagnetic cluster as well as for the electromagnetic isolation, hadronic core and hadronic isolation.

At this level, isolation requirements can be imposed, if required, to control the rate:

- $E_{\text{isol}}^{\text{EM}}$: the total E_T in the 12 EM towers surrounding the 2×2 core cluster is less than the electromagnetic isolation threshold;
- $E_{\text{core}}^{\text{HAD}}$: the total E_T in the 4 towers of the hadronic calorimeter behind the 2×2 core cluster of the electromagnetic calorimeter is less than the hadronic core threshold;

- $E_{\text{isol}}^{\text{HAD}}$: the total E_T in the 12 towers surrounding the 2×2 core cluster in the hadronic calorimeter is less than the hadronic isolation threshold.

Level-2 selection

L2 calorimeter reconstruction uses the η and ϕ positions provided by L1. Calorimeter cells in a window of size $\Delta\eta\times\Delta\phi = 0.4\times0.4$ are retrieved. At L2, the cluster-building algorithm scans the cells in the second layer of the EM calorimeter and searches for the cell with highest E_T. Subsequently, a cluster of 0.075×0.175 in $\eta \times \phi$ is built around this seed cell. The larger cluster size in ϕ reduces the low-energy tails due to photon conversion and electron bremsstrahlung. Photons deposit nearly all of their energy in the EM calorimeter and typically less than 1% of their energy into the hadronic calorimeter. In addition, showers from photons are typically smaller in the plane transverse to its direction than showers from jets. These quantities are used to select a low-background sample of photons.

The L2-photon algorithm selects events based on the following quantities:

- transverse energy of the EM cluster (E_T^{EM}): due to the energy dependence of the jet cross section, a cut on E_T^{EM} provides the best rejection against jet background for a given high p_T signal process;

- transverse energy in the first layer of the hadronic calorimeter (E_T^{Had}): this is required to be below a given threshold. This cut is relaxed for high E_T triggers (90 GeV and above) as the leakage into the hadronic calorimeter increases with energy;

- shower shape in η direction in the second EM sampling: the ratio of the energy deposit in 3×7 cells (corresponding to 0.075×0.175 in $\Delta\eta \times \Delta\phi$) over that in 7×7 cells is calculated, $R_{\text{core}} = E_{3\times7}/E_{7\times7}$. Photons deposit most of their energy in 3×7 cells and thus the corresponding ratio is typically larger than 80%;

- search for a second maximum in the first EM sampling: after applying the cuts in the hadronic calorimeter and the second sampling of the EM calorimeter, only jets with very little hadronic activity and narrow showers in the calorimeter remain. The fine granularity in rapidity of the first sampling of the EM calorimeter allows checks to be made for substructures within a shower for further rejection of background, such as single or multiple π^0's and η's decaying to photons. The energy deposit in a window $\Delta\eta \times \Delta\phi = 0.125\times0.2$ is examined.

The shower is scanned for local maxima in the η-direction. The ratio of the difference between the energy deposited in the bin with highest energy, $E_{1\mathrm{st}}$, and the energy deposited in the bin with second highest energy, $E_{2\mathrm{nd}}$, divided by the sum of these two energies is calculated, $R_{\mathrm{strips}} = (E_{1\mathrm{st}} - E_{2\mathrm{nd}})/(E_{1\mathrm{st}} + E_{2\mathrm{nd}})$. This ratio tends to one for an isolated photon and to zero for photons coming from π^0 decay.

Figure 5.2 shows typical distributions for the shower-shape variables defined above for a signal Monte Carlo sample of Higgs decaying into $\gamma\gamma$ and for a dijet background Monte Carlo sample. The high granularity of the first EM sampling of the ATLAS detector permits efficient photon identification using only calorimeter information; tracking information is not used at all in the selection up to this point.

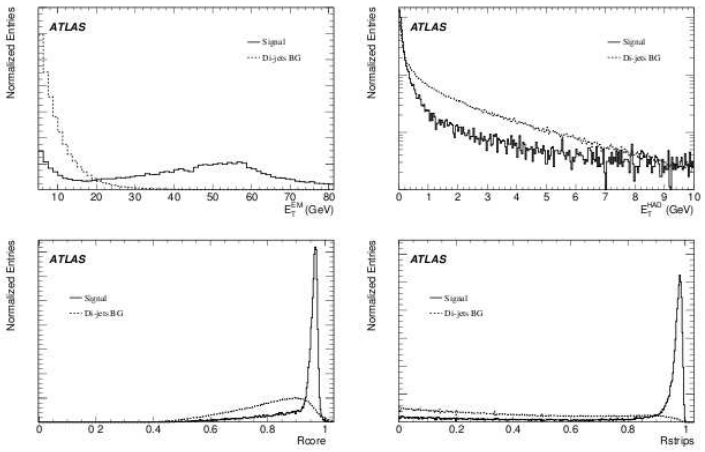

Figure 5.2: Selection variables for a L2 calorimeter energy cluster. The distributions are shown for signal Monte Carlo candidates $H \to \gamma\gamma$ sample (dashed line) and for the dijet background candidates that do not have a photon or electron matched within a ΔR of 0.1 and that have at least one jet with E_T >17 GeV (black solid line). Both distributions have been normalized to unity. The plots show the transverse energy of the EM cluster (top left), transverse energy deposited in the first layer of the hadronic calorimeter (top right), shower shape in the η direction in the second EM sampling (R_{core}) (bottom left), and the search for a second maximum in the first electromagnetic sampling (R_{strips}) (bottom right).

Event Filter selection

At the EF level, offline reconstruction algorithms and tools are used as much as possible.

Only calorimeter information is used and EM clusters are searched for and reconstructed in RoIs of size $\Delta\eta \times \Delta\phi = 0.4\times0.4$. Then, the algorithm searches for a local maximum within the trigger towers. For the photon reconstruction, only information from the EM calorimeter is used. The clusters should have an E_T above a given threshold. The default cluster size is 0.125×0.125 in $\eta \times \phi$. Once found by the clustering algorithm, the cluster parameters (position, energy, etc.) are computed and further refined by a set of cluster correction (position and energy calibration) tools.

Photon identification in the EF is very similar to the offline procedure (see Section 5.1.3). Calorimeter shower shapes, leakage into the hadronic calorimeter and the E_T of the EM cluster are used for the calorimeter-based selection for photons. Compared to L2, more shower-shape variables are used.

5.1.2 Photon reconstruction

The reconstruction of photons follows in its main aspect that of electrons [65]. Both objects are treated similarly within an overall reconstruction algorithm, though the reconstruction of photons is a bit more involved, due to the fact that photons can be classified into two main categories: converted and unconverted. Photons reconstructed as converted are characterised by the presence of at least one track matching an electromagnetic cluster originating from a vertex inside the tracker volume, whereas unconverted photons do not have such a matched track. There is an underlying similarity between electrons and converted photons due to the presence of tracks associated with both objects; this results in a certain amount of ambiguity between the two.

The electron and photon reconstruction algorithm in the central region of the calorimeter system ($|\eta|$ <2.47) starts by assembling the energy deposits in clusters. A sliding-window algorithm searches for a cluster of longitudinal towers with total transverse energy above 2.5 GeV. The window size is 3×5 in middle layer cell units ($\eta \times \phi = 0.025\times0.025$). Afterwards, the matching of a track with an EM cluster is made by extrapolating from the last measured point to the middle layer cluster of the EM calorimeter. The distance between the track and the cluster position has to be less than 0.05 along η and less than 0.1 along ϕ to take into account bremsstrahlung losses. In case of multiple tracks matching the same cluster, tracks with hits in the silicon detectors are preferred and the closest in $\Delta R = \sqrt{(}\Delta\eta^2 + \Delta\phi^2)$ is chosen.

Photons are identified as unconverted if the cluster does not match any track in the ID; electrons are selected when at least one track can be associated to the reconstructed cluster. To recover photons that have converted into an e^+e^- pair, the cluster is required to match pairs of tracks originating from a reconstructed conversion vertex. For unconverted photons, the cluster size in the barrel is $\Delta\eta \times \Delta\phi = 3\times5$ whereas it is 3×7 for converted photons. In the end-cap, a cluster size of 5×5 is used for all photon candidates.

The energy of photons is computed by a weighted sum of four different contributions in the EM calorimeter system [62, 63]: the energy deposit in the material in front of the EM calorimeter, the energy deposit in the cluster, the external energy deposit outside the cluster (lateral leakage) and the energy deposit beyond the EM calorimeter (longitudinal leakage). Then, a dedicated energy calibration is applied separately for converted-and unconverted-photon candidates to account for upstream energy losses and both lateral and longitudinal leakage due to the fixed size of photon clusters. The position of the photon in η and ϕ is computed as follows: first, it is calculated independently for each calorimeter layer as the energy-weighted barycenter of all cluster cells in the layer; second, the individual layer measurements are corrected for known systematic biases and finally, the position measurements from layer 1 and 2 are combined to produce the overall cluster position.

Converted photons

Photons may convert at any point within the ID in the presence of material, so the ability to reconstruct converted photons depends strongly on the type of tracking algorithm used [66]. Due to the structure of the ATLAS ID, photons which convert within 300 mm of the beam axis may be reconstructed with a high efficiency with standard (inside-out) silicon seeded tracking, while photons which convert further from the beam pipe may only be reconstructed using (outside-in) tracks, which begin with TRT seeds with or without associated silicon hits.

Photon conversion is dominated by e^+e^- pair production. All other interactions between the photons and the ID material, such as Compton or Rayleigh scattering, have smaller cross sections and can be safely ignored. The leading-order Feynman diagrams for photon conversions in the presence of material are shown in Fig. 5.3.

The cross section for the conversion of photons in the presence of material is both well understood theoretically and measured with high precision. For photon

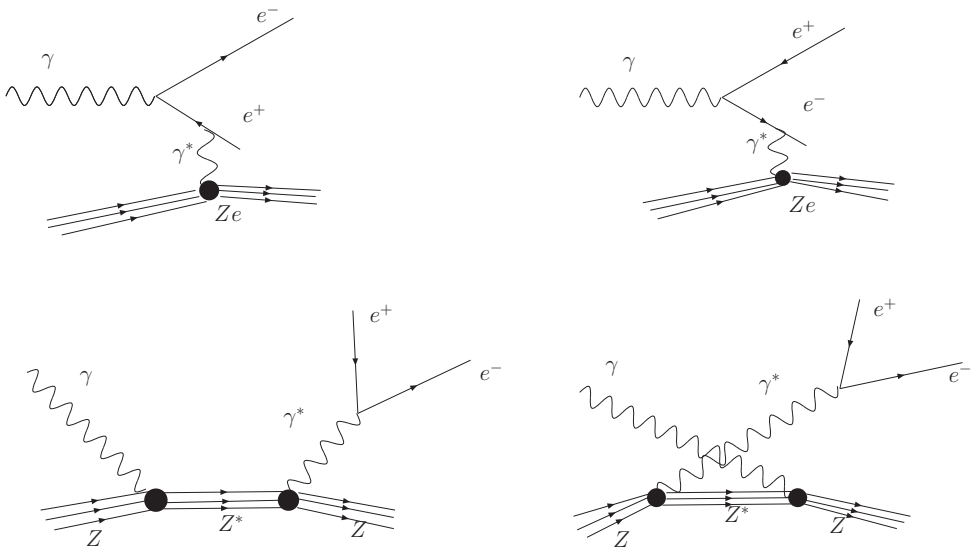

Figure 5.3: Leading-order Feynman diagrams for photon conversions.

conversions of energies of 1 GeV and above, the cross section is given by

$$\frac{d\sigma}{dx} = \frac{A}{X_0 N_A}(1 - \frac{4}{3}x(1-x)) \ , \tag{5.1}$$

where $x = E_e/E_\gamma$, X_0 is the radiation length defined as 7/9 of the mean free path for photon conversion, A is the atomic mass and N_A is Avogadro's number. This expression indicates that the momentum of the photon is not simply shared equally between the electron and the positron. In some fraction of the photon conversions, the electron or the positron may be produced with a very low energy. If this energy falls below the threshold required to produce a reconstructed track in the ID, then the converted photon will appear to have only one track.

The photon-conversion reconstruction algorithm starts by selecting single tracks with transverse momentum p_T >500 MeV and a significant fraction of high-thresholds hits in the TRT, as expected from transition radiation. Photon-conversion candidates are then reconstructed by pairing oppositely-charged tracks. Three possible combinations of track pairs are considered:

- two tracks with at least four silicon hits each (Silicon-Silicon track pairs);
- two stand-alone TRT tracks (TRT-TRT track pairs);
- pairs with one track with at least four silicon hits and one stand-alone TRT track (Silicon-TRT track pairs).

To reduce the combinatorial background, several selection criteria are applied taking advantage of the specific features expected for secondary vertices from photon conversions. Since the photon is massless, the emerging tracks are almost parallel at the vertex. The tracks are therefore required to be close in space and to have a small opening angle. An additional cut requires the sum of the radii of the helices of the electron and positron tracks, R_1 and R_2, to be comparable to the distance between the centers of the two helices, D. The selected track pairs are then fitted to a common vertex with the constraint that they be parallel at the vertex. The final set of photon conversion candidates is then selected based on the quality of the vertex fit.

In the case of conversions produced asymmetrically, as well as cases where the conversion happens so late that the two tracks are essentially merged, there is a significant number of conversions where only one of the two tracks from the photon conversion is reconstructed. Depending on the photon momentum scale, these "single-track" conversions saturate those that happen inside the TRT. Pair of tracks that result in a new photon-conversion vertex candidate are marked as "assigned" to a vertex. The remaining tracks are then examined once more on an individual basis in order to determine whether they can be considered as products of a photon conversion. For a track to be considered as such, it must have its first hit beyond the pixel vertexing layer. Furthermore, the track should be electron-like, where the probability reconstructed by using the ratio of the high-threshold TRT hits over the total number of TRT hits is used to select electron tracks. A conversion vertex candidate is then reconstructed at the position of the first track hit. A new vertex candidate is then stored, identical in structure to the one derived from a vertex fit, except that it has only one track assigned to it. The effect of including the single-track conversions into the overall reconstruction efficiency is significant, as shown in Fig. 5.4.

5.1.3 Photon identification

At the end of the reconstruction stage, not all reconstructed photon candidates are real photons. To separate real photons from fake photons resulting from jets, several discriminating variables are defined using the information both from the calorimeters and the inner tracking system. Cuts on these variables were developed to maintain high photon efficiency even in the presence of pile-up resulting from the overlapping minimum bias events due to the high instantaneous luminosity at the LHC. Two reference sets of cuts -loose and tight- were designed.

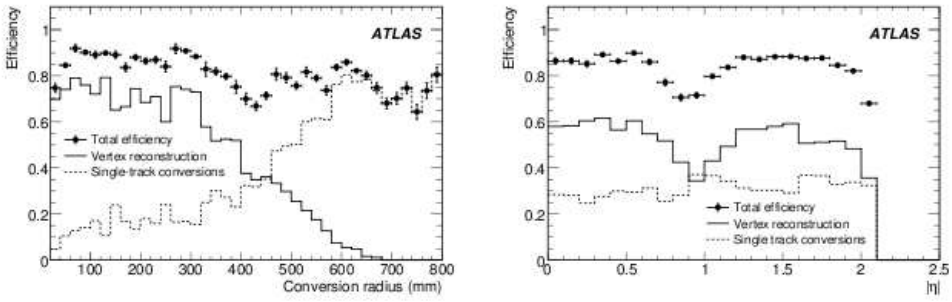

Figure 5.4: Reconstruction efficiency for conversions from 20 GeV-p_T photons as a function of conversion radius (left) and pseudorapidity (right). The dots with error bars show the total reconstruction efficiency, the solid histograms show the conversion vertex reconstruction efficiency, and the dashed histograms show the single-track conversion reconstruction efficiency.

Discriminating variables

In the electromagnetic calorimeter, photons are narrow and well contained objects, while fake photons induced from jets tend to have a broader profile and can deposit a substantial fraction of their energy in the hadronic calorimeter. Hence, longitudinal and transverse shower-shape variables can be used to reject fake photons [67]. They are

- **hadronic leakage**: the hadronic leakage (R_{had1}) is defined as the ratio of the transverse energy in the first layer of the hadronic calorimeter in a window $\Delta\eta \times \Delta\phi = 0.24{\times}0.24$ to the transverse energy of the cluster. In the region $0.8{<}\ |\eta^{\mathrm{cluster}}|\ {<}1.37$, R_{had} is used, which is defined as in the same way as R_{had1} but using the total transverse energy in the hadronic calorimeter instead. Fake photons induced from jets contain hadrons that would penetrate deeper into the calorimeter depositing sizeable energies beyond the electromagnetic calorimeter;

- **variables using the second compartment of the ECAL**: EM showers deposit most of their energy in the second layer of the electromagnetic calorimeter. For this reason several variables that measure the shape of the shower are available as follows:

  - Real photons deposit most of their energy in a $\Delta\eta \times \Delta\phi = 3{\times}7$ window. The lateral shower-shape variables, R_η and R_ϕ, are given by the ratio of the energy reconstructed in $3{\times}7$ middle cells to the energy in $7{\times}7$ cells

and the ratio of the energy reconstructed in 3×3 cells to the energy in 3×7 cells, respectively. Due to the effect of the magnetic field increasing the width of the converted-photon contributions in the ϕ direction, R_ϕ is less discriminating than R_η;

- the lateral width in η is calculated in a window of 3×5 cells using the energy weighted sum over all cells. The variable w_2 is defined as $w_2 = \sqrt{\frac{\Sigma E_c \times \eta_c^2}{\Sigma E_c} - [\frac{\Sigma(E_c \times \eta_c)}{\Sigma E_c}]^2}$, where E_c is the energy deposit in each cell, and η_c is the actual η position of the cell represented by the center of the cell in η direction. Therefore, w_2 is given in units of η;

- **variables using the first compartment of the ECAL:** cuts applied on the variables in the hadronic calorimeter and the second layer of the EM calorimeter reject jets which contain high-energy hadrons and result in broad showers. Jets containing single or multiple neutral hadrons such as π^0 and η, provide the main origin of fake photons. The information from the very-fine granularity first layer can be used to identify substructures in the showers and distinguish isolated photons from the hard scatter and photons from π^0 decays efficiently. The lateral shower shape in the strips is exploited for $|\eta| < 2.37$, where the strip granularity is sufficiently fine.

  - since the energy-deposit pattern from π^0s is often found to have two maxima due to $\pi^0 \to \gamma\gamma$ decay, showers are studied in a window $\Delta\eta \times \Delta\phi = 0.125\times0.2$ around the cell with the highest E_T to look for a second-highest maximum. If more than two maxima are found the second highest maximum is considered. The following two variables are constructed using the information from the identified second maximum:

    * $\Delta E_s = E_{\text{max2}} - E_{\text{min}}$, the difference between the energy associated with the second-highest maximum, E_{max2}, and the energy reconstructed in the strip with the minimum value, found in between the first and second maxima, E_{min}.
    * E_{ratio}, the difference between the largest maximum E_{max1} and the second largest maximum E_{max2} deposits over the sum of these energies $E_{\text{ratio}} = \frac{E_{\text{max1}} - E_{\text{max2}}}{E_{\text{max1}} + E_{\text{max2}}}$.

  – $F_{\text{side}} = [E(\pm3) - E(\pm1)]/E(\pm1)$, the fraction of the energy deposited outside the shower core of three central strips. The variable $E(\pm n)$ is the energy deposited in $\pm n$ strips around the strip with the highest energy.

  – $w_{s3} = \sqrt{\Sigma E_i \times (i - i_{\text{max}})^2 / \Sigma E_i}$, the shower width over the three strips around the one with the maximum energy deposit. The index i is the strip identification number, i_{max} the identification number of the most

energetic strip and E_i is the energy deposit in strip i; w_{s3} is expressed in units of strip cells and corrected for impact point dependence.

– w_{stot}, the shower width over the strips that cover 2.5 cells of the second layer (20 strips in the barrel for instance). It is expressed in units of strip cells.

To keep the photon selection as simple as possible, no E_T dependence of the cut thresholds is introduced at any selection level. The cut thresholds are optimised in $|\eta|$ bins. Figure 5.5 (5.6) shows an example of the normalised distributions of the calorimetric discriminating variables in the region $0 < |\eta| < 0.6$ for $E_T > 20$ GeV for real and fake unconverted (converted) photons before any selection. The distributions for real photons shown in Figs. 5.5 and 5.6 were obtained from photon candidates reconstructed in a sample of γ-jet events and matched to true prompt photons. The distributions for fake photons were obtained from photon candidates reconstructed in a sample of QCD dijets events that were not matched to true photons originating from parton bremsstrahlung.

The cut values were tuned separately in six pseudorapidity intervals in $|\eta| < 2.37$ to reflect the pseudorapidity dependence of these variables. The subdivision is motivated by the varying granularity and material in front of the EM calorimeter.

Loose selection

This basic selection includes shower-shape variables based on information from the EMC Middle layer (R_η, w_2), together with hadronic leakage, the fraction of the cluster energy deposited in the hadronic calorimeter layers beyond the EM calorimeter (R_{had} or R_{had1}) [65]. This subset of discriminating variables shows relatively small differences for unconverted and converted photons, so using only these variables in the loose selection keeps the efficiencies for the two types of photon very similar.

Tight selection

The tight photon requirements are also optimised to provide good rejection of the background [65]. They comprise tighter cuts on the variables (R_η, w_2, E_{had1}, R_{had} or R_{had1}), used for the loose selection, and additional cuts on one of the middle layer quantities (R_ϕ) and, especially, cuts on quantities computed from the energy deposited in the strip layer (w_{s3}, w_{stot}, F_{side}, ΔE_s, E_{ratio}). As a consequence, photon candidates are required to lie in the pseudorapidity region covered by the first layer of the electromagnetic calorimeter: photon candidates in the regions $1.37 < |\eta| < 1.52$

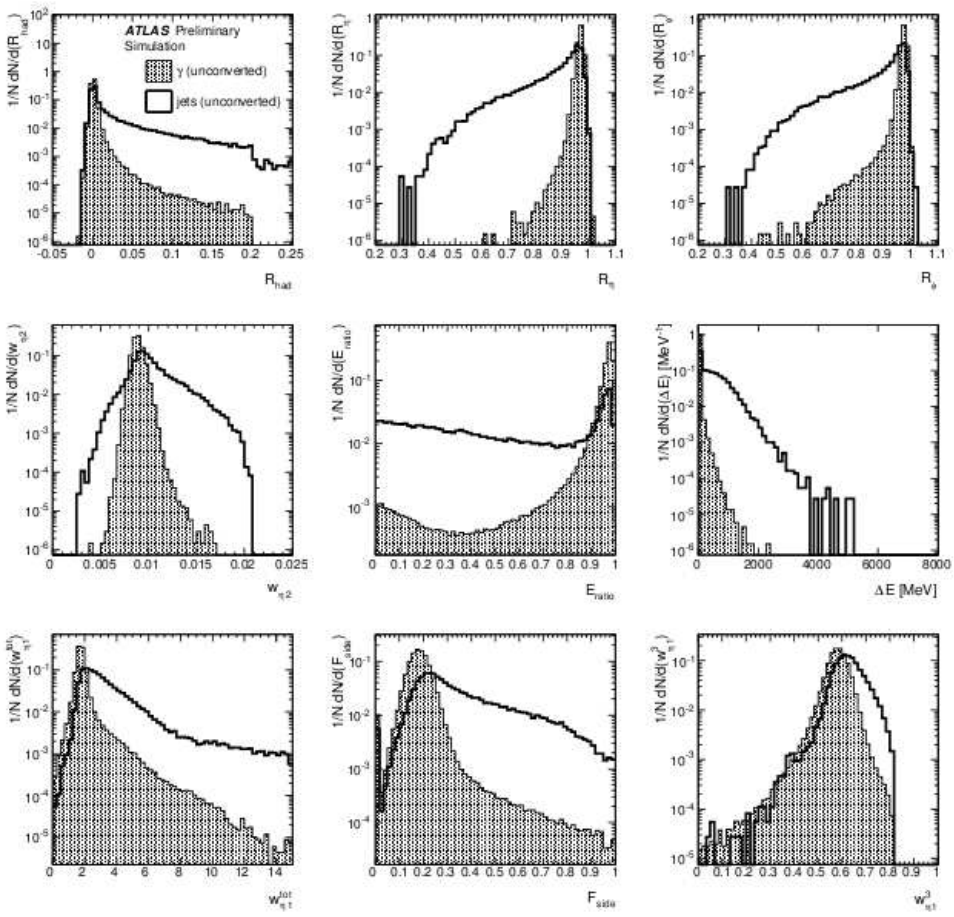

Figure 5.5: Normalised distributions of the calorimetric discriminating variables in the region $0< |\eta| <0.6$ for $E_T > 20$ GeV for real and fake photons reconstructed as unconverted before any selection.

and $|\eta| >2.37$ are thus rejected by the tight identification criteria.

The tight cuts are separately optimised for unconverted and converted photon candidates, to take into account the fact that the EM deposits are different in the two cases. The cut thresholds are chosen to provide an identification efficiency around 85% with respect to the initial collection of reconstructed candidates for both unconverted and converted photons with $E_T > 20$ GeV (see Table 5.1 and Fig. 5.7).

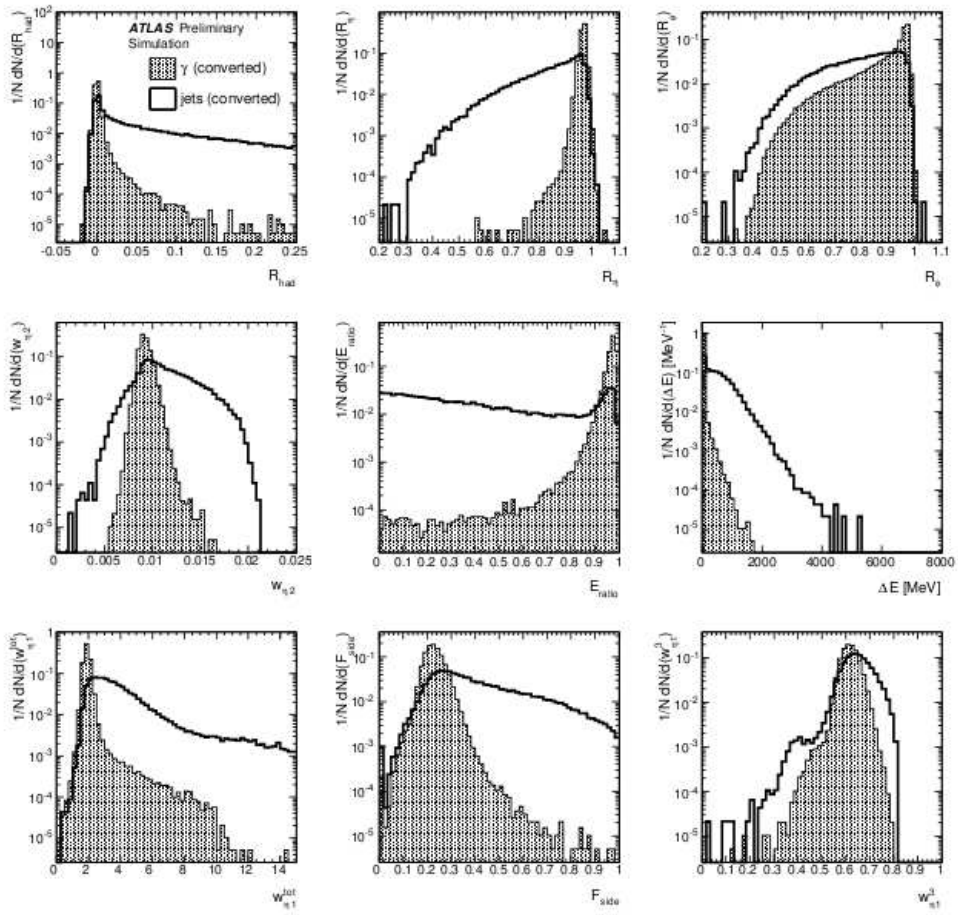

Figure 5.6: Normalised distributions of the calorimetric discriminating variables in the region $0< |\eta| <0.6$ for $E_T > 20$ GeV for real and fake photons reconstructed as converted before any selection.

5.1.4 Photon isolation

The photon identification procedure explained above does not include dedicated isolation cuts. An isolation requirement is essential to perform meaningful studies of prompt-photon production from both the experimental and theoretical points of view. Prompt photons are expected to be more isolated than the background from π^0's and η^0's arising from jet fragmentation. Furthermore, an isolation requirement suppresses the non-perturbative contribution from fragmentation-photon processes. Various analyses may require different isolation criteria of different tightness and, therefore, isolation cuts are applied on top of the photon identification criteria.

A calorimetric isolation discriminator, $E_T^{\rm iso}(R_0)$, was computed as the transverse

		Efficiency (%)	Jet rejection
Loose	All	95.45±0.01	908±4
	Unconverted	97.80±0.01	
	Converted	91.73±0.01	
Tight	All	82.88±0.02	4770±40
	Unconverted	85.04±0.03	
	Converted	79.44±0.04	

Table 5.1: Expected overall (reconstruction+identification) efficiencies and jet background rejections for the two sets of identification cuts and an E_T-threshold of 20 GeV.

energy flow calculated from the cell energies surrounding the photon candidate in a cone of size $\sqrt{((\eta^{\text{cell}} - \eta^{\gamma})^2 + (\phi^{\text{cell}} - \phi^{\gamma})^2)} < R_0$, where ($\eta^{\text{cell}}$,$\phi^{\text{cell}}$) are the cell coordinates. The core, containing the photon shower, was excluded. The small leakage from the photon outside this region, evaluated as a function of photon transverse energy on simulated samples of single photons, was subtracted from $E_T^{\text{iso}}(R_0)$. After this correction, the $E_T^{\text{iso}}(R_0)$ of simulated photons is independent of the photon transverse energy. Further corrections were then applied to $E_T^{\text{iso}}(R_0)$ to reduce the uncertainties from underlying-event modelling and pile-up effects. This correction comes from the so-called "jet-area" method [57]. In this method, low-energy jets were used to compute an event-by-event ambient energy density, which was then multiplied by the area of the isolation cone and subtracted from the isolation energy. For the analysis presented here R_0 was set to 0.4. For that choice, the ambient energy correction to the isolation energy in data is typically 900 MeV for the 2010 data-taking period (see Fig. 5.8).

5.2 Photon calibration

After identification and reconstruction of a photon candidate, a calibration procedure is applied. This prodecure corrects for energy losses of the photon due to the interaction with the material in front of the LAr. It is essential to know the electromagnetic energy scale and resolution of the LAr to improve the calibration of the photon energy. In the following subsections, the procedure for calibrating the photon energy is discussed in detail.

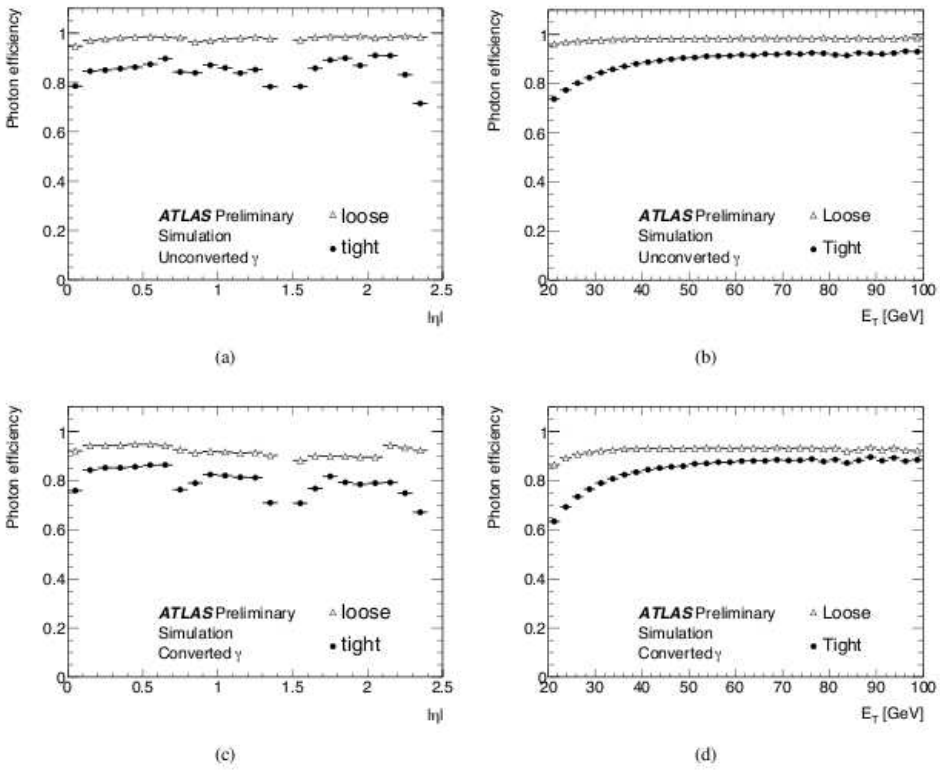

Figure 5.7: Expected photon efficiency vs $|\eta|$ (left) and E_T (right) for loose and tight selection criteria and for unconverted (top) and converted (bottom) photons.

5.2.1 Electromagnetic energy-scale calibration

Photons and electrons are reconstructed using the EM calorimeter. Therefore, the knowledge of the EM energy scale is crucial to calibrate the photon and electron energy. The EM calorimeter energy scale has been derived from test-beam measurements with an uncertainty of $\pm 3\%$ in the central region, covering $|\eta| < 2.47$, and $\pm 5\%$ in the forward region, covering $2.5 < |\eta| < 4.9$, with the dominant uncertainty given by the extrapolation of the test-beam results to the ATLAS environment.

The in-situ calibration of the EM calorimeter is performed using the precise knowledge of the Z mass and the decay channel $Z \to ee$. It is cross-checked in terms of linearity of response versus energy and of uniformity, with limited accuracy, using the $J/\psi \to ee$ and $W \to e\nu$ decays in the central region.

The EM calorimeter energy calibration is divided into three steps [61, 68]:

- the raw signal extracted from each cell in ADC counts is converted into a

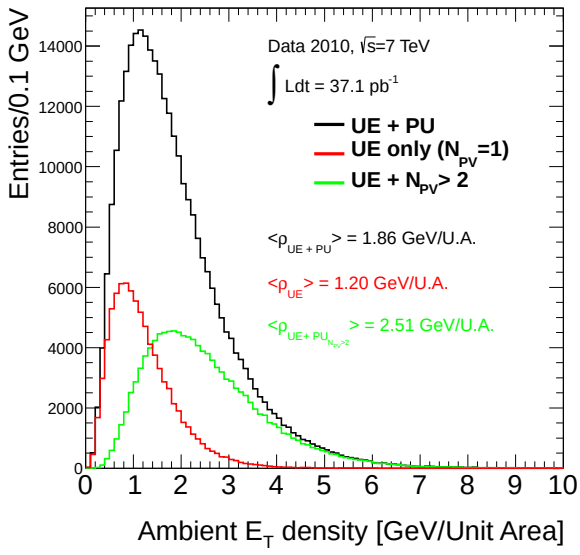

Figure 5.8: The distribution of the ambient transverse energy density per unit of area for all events ("UE+PU", black histogram), events with one primary vertex ("UE only, ($N_{PV} = 1$)", red histogram) and events with more than two primary vertices ("UE+$N_{PV} > 2$", green histogram).

deposit energy using the electronic calibration of the EM calorimeter [68–70];

- then, MC-based calibration [61] corrections are applied at the cluster level for energy loss due to absorption in the passive material and leakage outside the cluster. These corrections include four different contributions: the energy deposited in the material in front of the EM calorimeter, that deposited in the calorimeter inside the cluster, that deposited outside the cluster (lateral leakage) and that deposited beyond the EM calorimeter (longitudinal leakage). The calibration correction factors are different depending whether the object is an electron, a converted photon or an unconverted photon. This is due to the fact that the clustering size is different between them and that the energy lost by photons and electrons interacting with matter is different;

- the in-situ calibration using physics events recorded by the ATLAS detector determines the energy scale and intercalibrates the different regions of the calorimeter covering $|\eta| < 4.9$.

The in-situ electron calibration factors extracted from $Z \to ee$ events are extrapolated to photons using MC-based methods. For calibrated electrons with transverse energy larger than 20 GeV, the ratio between the reconstructed and true particle energy is expected to be within $\pm 1\%$ in almost all pseudorapidity regions. The energy

resolution is below $\pm 2\%$ for $E_T > 25$ GeV in the most central region, $|\eta| < 0.6$, and only exceeds $\pm 3\%$ close to the transition region of the barrel and end-cap calorimeters where the amount of passive material in front of the calorimeter is largest.

The well-known masses of the Z and J/ψ particles can be used to improve the electron energy-scale measurement and to study the linearity of the EM calorimeter.

Energy scale determination using dielectron decays of Z and J/ψ

The electron energy can be calibrated in situ using the precise knowledge of the Z mass [71, 72]. Any residual miscalibration for a given η region i is parametrised by:

$$E^{\text{meas}} = E^{\text{true}}(1 + \alpha_i) \tag{5.2}$$

where E^{true} is the true electron energy, E^{meas} is the energy measured by the calorimeter after MC-based energy scale corrections and α_i measures the residual miscalibration. The α energy-scale correction factors are determined using a fit which minimises the unbinned log-likelihood [61]:

$$-\ln L_{\text{tot}} = \sum_{k=1}^{N_{\text{events}}} -\ln L_{ij}\left(\frac{M_k}{1 + \frac{\alpha_i + \alpha_j}{2}}\right) \tag{5.3}$$

where the i, j indices denote the η regions considered for the calibration, N_{events} is the total number of selected events compatible with a $Z \to ee$ process, M_k is the measured dielectron mass in a given event and $L_{ij}(M)$ is the probability density function (pdf) quantifying the compatibility of an event with the Z lineshape. The pdf is obtained from the PYTHIA MC simulation and takes into account both theoretical and experimental effects on the Z lineshape. It is then smoothed to get a continuous distribution. The resulting α values are shown in Fig. 5.9(a).

The same procedure was applied using $J/\psi \to ee$ events to determine the electron energy scale. The resulting α values are in good agreement with the $Z \to ee$ measurement and the observed small differences were used to estimate the uncertainty specific to low E_T electrons (see Fig. 5.9(b)).

Systematic uncertainties of the energy-scale determination

Several sources of systematic uncertainty contribute to the in-situ calibration method:

- **additional material:** the imperfect knowledge of the amount of material in front of the EM calorimeter affects the electron energy measurement since

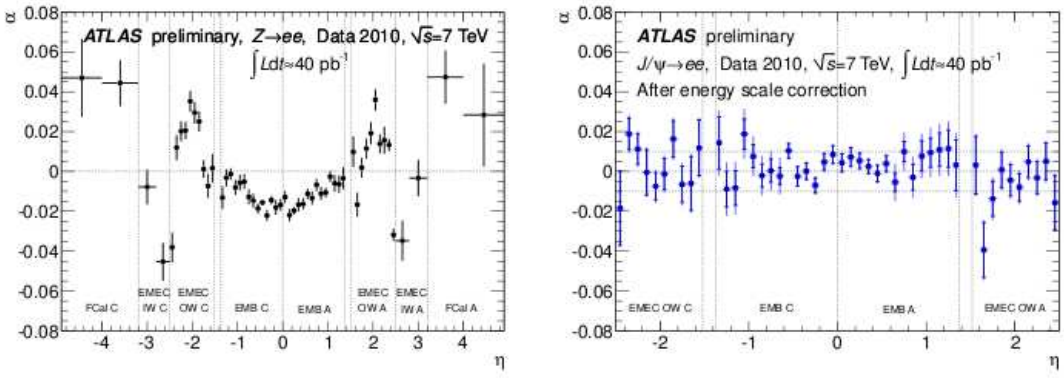

(a) (b)

Figure 5.9: The α energy-scale correction factors as a function of the pseudorapidity of the electron cluster derived from fits to (a) $Z \to ee$ data and (b) $J/\psi \to ee$ data. The uncertainties of the $Z \to ee$ measurement are statistical only. The $J/\psi \to ee$ measurement was done after the $Z \to ee$ calibration shown on the left has been applied. Its results are given with statistical (inner error bars) and total (outer error bars) uncertainties. The boundaries of the different detector parts are indicated by dotted lines.

the energy deposited in any additional material is neither measured nor accounted for in the MC-based calibration. Nonetheless, if additional material were present, the α values extracted from $Z \to ee$ events would restore the electron energy scale on average. Electrons from Z decays have an E_T spectrum with a mean value around 40 GeV. Away from this region, a residual uncertainty arises due to the extrapolation of the calibration to lower and higher E_T. This effect was estimated in two steps. First the calibration procedure was applied to a $Z \to ee$ MC sample produced using a dedicated detector geometry model with additional material in front of the calorimeters using the nominal MC sample to provide the reference Z lineshape. Then, the non-linearity (arising because passive material affects lower-energy electrons more severely) was measured using MC truth information by comparing the most probable value of the $E_{\text{reco}}/E_{\text{truth}}$ distributions between the nominal MC and the one with additional material in bins of electron E_T. The systematic uncertainty varies from -2% to +1.2%;

- **low-E_T electrons:** the energy-scale calibration using $J/\psi \to ee$ and $Z \to ee$ events are compared. As shown in Fig. 5.9, the α coefficients extracted using $J/\psi \to ee$ decays after applying the baseline calibration using $Z \to ee$ events are within $\pm 1\%$, despite the very different E_T regimes of the two processes (the mean electron E_T in the J/ψ selection is about 9 GeV). This shows the good

linearity of the EM calorimeter and also that the amount of material in front of the calorimeter is reasonably well modelled. Nonetheless, a +1% additional uncertainty must be added for electrons with $E_T = 10$ GeV, decreasing linearly to 0 at $E_T = 20$ GeV;

- **presampler energy scale:** since the in-situ calibration only fixes an overall scale, it cannot correct for a difference between the presampler and the EM calorimeter energy scale. By comparing the energy deposited in the presampler by electrons from $W \to e\nu$ events in data and in MC simulations, an upper limit on the presampler energy scale uncertainty can be extracted: it is $\sim \pm 5\%$ in the barrel and $\pm 10\%$ in the end-cap regions up to $|\eta| = 1.8$. The bias on the electron energy scale due to a shift of the presampler energy scale depends on η, due to the distribution of material in front of the calorimeter, and also depends on E_T, since the fraction of energy deposited in the presampler is larger for lower-energy electrons. The resulting uncertainty increases to $\pm 1.4\%$ at $E_T = 1$ TeV for $1.52 < |\eta| < 1.8$; the material budget and the uncertainty on the presampler energy scale are the largest contributions;

- **calorimeter electronic calibration and cross talk:** cells belonging to different longitudinal layers in the calorimeters can have a different energy scale due to cross talk and imperfect determination of the electronic calibration. The uncertainty on the energy scale relative to the middle layer for cells in the strip (back) layer of the calorimeter is estimated to be $\pm 1\%$ (2%) [73, 74]. The uncertainty on the back-layer energy scale is negligible, as the energy deposited there is small, while on the strip-layer energy scale is taken to be $\pm 0.1\%$ for all η and E_T;

- **readout electronic non-linearity:** the readout electronics are linear to typically 0.1% [75]. This number is taken as a systematic uncertainty on the extrapolation of the electron energy scale extracted from $Z \to ee$ events to higher energies;

- **object quality requirements:** to check the possible bias due to object quality requirement applied to the electrons in the event selection, the procedure was redone by applying a tighter veto on electrons falling close to dead regions and also by vetoing regions with non-nominal high voltage. No effect was observed for central electrons, while ± 0.6-0.8% differences are seen for forward electrons;

- **background:** the effect of the background, predominantly from jets, on the extracted α values was studied by changing the Z mass fit range from [80,100]

GeV to [75,105] GeV and [85,95] GeV and by tightening the electron selection, thereby decreasing the amount of background significantly. The resulting uncertainties from the fit range (tighter electron selection) are ±0.1% (0.1%) in the central barrel and grow to ±0.6% (1%) in the forward calorimeter;

- **pile-up:** the effect of pile-up was studied by determining the α coefficients varying the requirement on the number of reconstructed primary vertices from 1 to 4. The average value $< \alpha >$ increases with the number of primary vertices and a systematic uncertainty of ±0.1% was assigned;

- **possible bias of the method:** from a closure test of the fit procedure on MC events, a systematic uncertainty of ±0.1% (0.2%) was assigned in the central (forward) region. Moreover, the results of alternative fit methods were compared on data and agree within ±0.1-0.5% (0.8-1.0%), which is assigned as an additional uncertainty on the possible bias of the method;

- **theoretical inputs:** in the extraction of the α coefficients from the data, the MC simulation serves as a reference. Uncertainties related to the imperfect physics modelling of QED final-state radiation, the proton structure functions and the underlying event are found to be negligible.

The overall systematic uncertainty on the electron energy scale varies from ±0.3% to 1.6% for central electrons, $|\eta| < 2.47$. For forward electrons, $2.5 < |\eta| < 4.9$, the uncertainty is larger and of the order of ±2% to 3%.

Systematic uncertainties for photons

If the energy scale non-uniformities measured with electrons were only due to calorimeter inhomogeneities (e.g. LAr temperature), then the in-situ energy-scale correction determined for electrons can also be applied to photons. However, if the energy scale non-uniformities are due to different effects, such as wrong presampler energy scale or due to additional material, the energy-scale correction determined for electrons cannot be applied to photons since electrons and photons interact differently with matter and have different EM-shower profile.

The way to measure in-situ the photon energy scale would be via the $Z \to ee\gamma$ process. However, the cross section for this process is very small and the luminosity of the 2010 period was not large enough to obtain a significant sample of events. Therefore, the energy scale measured from electrons was used instead together with dedicated systematics estimated from Monte Carlo.

The main systematic uncertainties on the electron energy scale are the ones associated with the imperfect knowledge of the material in front of the calorimeter and of the presampler energy scale and they are expected to be different between electrons and photons. If additional material was present, applying the α correction extracted from $Z \to ee$ events would overcorrect the photon energy scale, since photons deposit less energy in dead material. By taking into account the difference in the energy scale between a nominal γ+jet Monte Carlo sample and a Monte Carlo sample with additional material, where the energy correction was determined from $Z \to ee$ events with the same additional material detector configuration, is possible to extract a systematic uncertainty on the photon energy scale (see Table 5.2).

The uncertainties on the presampler energy scale are different between electrons and photons since the energy fraction in the presampler is smaller for photons than for electrons for the same energy and η. The bias on the photon energy scale due to a $\pm 5\%$ (10%) shift of the barrel (end-cap) presampler energy scale is smaller than the bias on the electron energy scale. The energy-scale corrections extracted from $Z \to ee$ events ($f^{\eta_i}_{\mathrm{ps,ele}}(p_T = 40\ \mathrm{GeV})$) overcorrects the photon energy scale. The positive uncertainty due to presampler energy scale for a given η bin is estimated via

$$er^{\mathrm{up}}_{\mathrm{ps},\gamma} = |f^{\eta_i}_{\mathrm{ps},\gamma}(p_T) - f^{\eta_i}_{\mathrm{ps,ele}}(p_T = 40\ \mathrm{GeV})|\ , \tag{5.4}$$

where $f^{\eta_i}_{\mathrm{ps},\gamma}(p_T)$ are the parametrisations of the bias on the photon energy scale due to a $\pm 5\%$ (10%) shift of the barrel (end-cap) presampler energy scale in a γ+jets nominal Monte Carlo sample. The $f^{\eta_i}_{\mathrm{ps,ele}}(p_T = 40\mathrm{GeV})$ are extracted in the same way but for a $Z \to ee$ nominal Monte Carlo sample. The negative uncertainty is simply given by $er^{\mathrm{down}}_{\mathrm{ps},\gamma} = -er^{\mathrm{up}}_{\mathrm{ps},\gamma}$.

The overall systematic uncertainty on the photon energy scale is shown in Fig. 5.10.

	[0.0,0.6]	**[0.6,1.0]**	**[1.0,1.37]**	**[1.52,1.8]**	**[1.8,2.5]**
Uncertainty	+0.3	+0.5	+0.8	+1.0	+1.0

Table 5.2: Systematic uncertainties on the photon energy scale due to additional material in %.

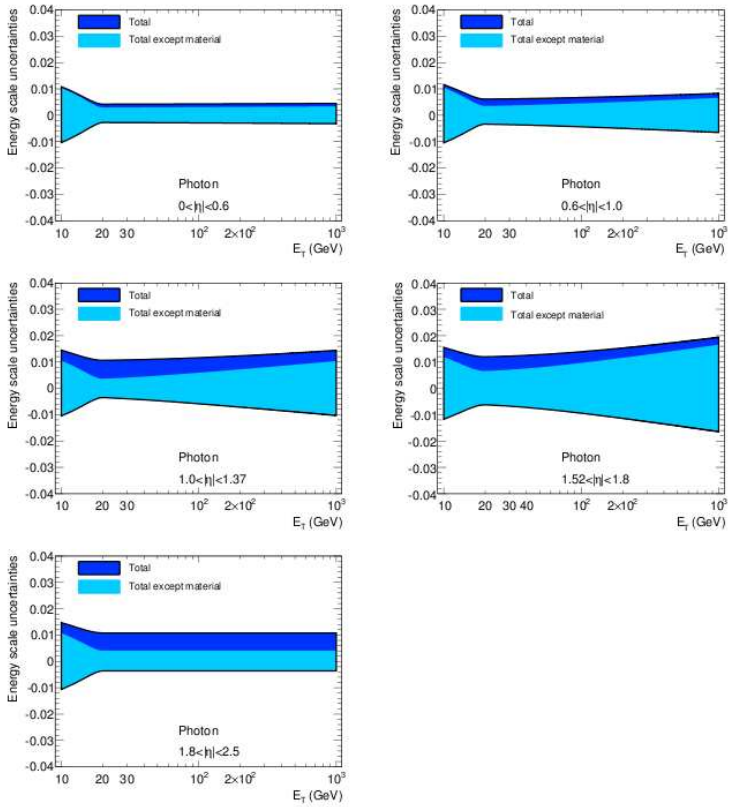

Figure 5.10: Uncertainty on the photon energy scale with (dark) and without (light) the uncertainty due to additional material.

5.2.2 Electromagnetic energy-resolution calibration

The relative energy resolution in the calorimeter is parametrised as

$$\frac{\sigma_E}{E} = \frac{a}{\sqrt{E}} \oplus \frac{b}{E} \oplus c, \tag{5.5}$$

where a is the sampling term, b is the noise term and c is the constant term.

Great care was taken during the construction of the calorimeter to limit all sources of energy response non-uniformity to the minimum achievable, as any non-uniformity has a direct impact on the constant term of the energy resolution. The construction tolerances and the electronic calibration system ensures that the calorimeter response is locally uniform, with a local constant term below $\pm 0.5\%$ [76] over regions of typical size $\Delta\eta \times \Delta\phi = 0.2 \times 0.4$.

To extract all terms from data, more statistics are needed than available in the

2010 data. Therefore, only the constant term was determined from a simultaneous analysis of the measured and predicted dielectron invariant mass resolution from $Z \to ee$ decays. The measured dielectron mass distribution of electrons coming from $J/\psi \to ee$ decays is in good agreement with the MC prediction, for both the mean and the width. As the electron energy resolution at low energies is dominated by the contribution from the sampling term, it is assumed to be well described by the MC: $a_{MC} = a_{\text{data}}$, within a $\pm 10\%$ uncertainty. The noise term has a significant contribution only at low energies and its effect on the measurement cancels out at first order as the noise description in the MC is derived from calibration data runs. These assumptions lead to the formula

$$c_{\text{data}} = \sqrt{2 \times \left(\left(\frac{\sigma_M}{M} \right)^2_{\text{data}} - \left(\frac{\sigma_M}{M} \right)^2_{MC} \right) + c^2_{MC}} \ , \tag{5.6}$$

where c_{MC} is the constant term of about 0.5% in the MC simulation. The parameter c_{data} is an effective constant term which includes both the calorimeter constant term and the effect of inhomogeneities due to possible additional material.

The resolutions are derived from fits to the invariant-mass distributions using a Breit-Wigner convoluted with a Crystal Ball function in the mass range 80-100 GeV for events where both electrons are central ($|\eta| < 2.47$) and in the mass range 75-105 GeV for events where one electron is central and the other one is foward ($|\eta| > 2.47$). The Breit-Wigner width is fixed to the measured Z width of 2.49 GeV [71] and the resolution comes from the Gaussian component of the Crystal Ball function.

The results on the effective constant term are shown in Table 5.3.

	Effective constant term, c_{data}
EMB	$1.2\% \pm 0.1\%(\text{stat})^{+0.5}_{-0.6}(\text{syst})$
EMEC-Inner wheel	$1.8\% \pm 0.4\%(\text{stat}) \pm 0.4(\text{syst})$
EMEC-Outer wheel	$3.3\% \pm 0.2\%(\text{stat}) \pm 1.1(\text{syst})$
FCal	$2.5\% \pm 0.4\%(\text{stat})^{+1.0}_{-1.5}(\text{syst})$

Table 5.3: Measured effective constant term c_{data} from the observed width of the $Z \to ee$ peak for different calorimeter regions.

Several sources of systematic uncertainties were investigated [72]. The dominant uncertainty is due to the uncertainty on the sampling term, as the constant term was extracted assuming that the sampling term is correctly reproduced by the simulation. To assign a systematic uncertainty due to this assumption, the simulation was modified by increasing the sampling term by 10%. The difference in the mea-

sured constant term is found to be about 0.4% for the EM calorimeter and 1% for the forward calorimeter. The uncertainty due to the fit procedure was estimated by varying the fit range. The uncertainty due to pile-up was investigated by comparing simulated MC samples with and without pile-up and was found to be negligible.

5.3 Jet reconstruction and calibration

The principal detector for jet reconstruction in ATLAS is the calorimeter system. It provides almost hermetic coverage in the range $|\eta|$ <4.9 [61].

The ATLAS software framework provides the implementation of many jet finding algorithms, such as cone and sequential recombination algorithms and an algorithm based on event-shape analysis. This approach is a response to the fact that there is no universal jet finder for the hadronic final state in all topologies of interest [77].

The common feature of all jet-algorithm implementations in ATLAS is full four-momentum recombination. In the ATLAS reconstruction software framework, the same jet-algorithm code can be run on objects like calorimeter signal towers, topological cell clusters in the calorimeter, reconstructed tracks and generated hadrons and partons.

There are experimental aspects of jet reconstruction in ATLAS which includes features reflected in the design of the detector. They can be divided into three classes:

- **detector technology independence:** the reconstructed jet and its kinematic variables should not depend on the signal source, i.e. all detector-specific signal characteristics and inefficiencies must be calibrated out or corrected for. The main effects are:
  - **detector resolution:** contributions from the finite spatial and energy resolution must be minimised;
  - **detector environment:** effects from the detector environment, such as electronics noise, signal losses in un-instrumented (inactive) materials and cracks between detectors must be minimised;
  - **stable signals:** the detector signal reconstruction and calibration must provide a stable input signal to the jet reconstruction;

- **environment independence:** the jet reconstruction is affected by additional activity present in the collision, such as multiple interactions and pile-up, the underlying event activity, and other features of *pp* collisions at LHC:
  - **stability:** a jet should be reconstructed even in the case of changing underlying-event activity and changing instantaneous luminosity;
  - **efficiency:** all physically interesting jets from energetic partons must be identified with high efficiency;
- **implementations:** the jet-algorithm implementation must be fully specified. The jet definition, which consists of the jet finder and its configuration together with the choice of kinematic recombination, must be complete. In addition, the implementation of the jet reconstruction must make efficient use of computing resources; it must be fast and avoid excessive memory consumption.

5.3.1 Calorimeter jet reconstruction

The ATLAS calorimeter system [78] has ≈200,000 individual cells of various sizes with different readout technologies and electrode geometries. For jet finding it is necessary to first combine these cell signals into larger signal objects with physically meaningful four-momenta. Two different signal objects are available for a such purpose: *signal towers* and *topological cell clusters*.

Calorimeter signal towers

To construct signal towers, calorimeter cells are projected into a fixed η-ϕ grid. The tower bin size is $\Delta\eta \times \Delta\phi = 0.1 \times 0.1$ in the whole acceptance region of the calorimeters. Projective calorimeter cells which completely fit inside a tower contribute their total signal, as reconstructed on a basic electromagnetic energy scale[1], to the tower signal. Non-projective and projective cells larger than the tower bin size contribute a fraction of their signal to several towers, depending on the overlap fraction of the cell area with the tower (see Fig. 5.11). The signal contribution is expressed as a geometrical weight and is calculated as the ratio of the tower bin area over the projective cell area in η and ϕ.

[1] This is the raw signal from the ATLAS calorimeters. The nomenclature indicates that this scale has been derived from electron signals, but it lacks all corrections applied in high-precision electron or photon reconstruction. It typically includes all electronic correction and the geometrically-motivated corrections for high-voltage problems, such as inactive electrode sub-gaps and similar effects.

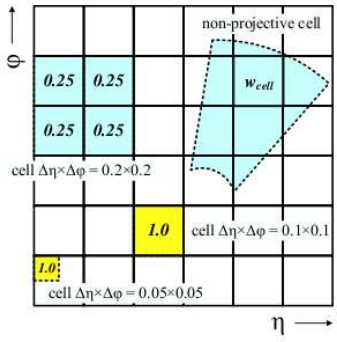

Figure 5.11: Calorimeter cell signal contributions to towers on a regular $\Delta\eta \times \Delta\phi = 0.1 \times 0.1$ grid, for projective and non-projective cells.

Thus, the tower signal is the nondiscriminatory sum of possibly weighted cell signals. As the cell signals are at the basic electromagnetic energy scale, the resulting tower signal is at the same scale. No further corrections or calibrations are applied at this stage.

Reconstruction sequence

Jet reconstruction from calorimeter towers starts with a re-summation step, which addresses a possible unphysical four-momentum due to a negative tower signal $E_{\text{tower}} < 0$. This can be generated by signal fluctuations from noise (electronics and physics from pile-up) in the cells entering into the corresponding towers. Combining negative tower signals with nearby positive signals such that the combined four-momentum is physical with $E_{\text{tower}} > 0$, leads to cancellation of some of the noise fluctuations and avoids signal biases. The negative tower signals without nearby positive signals are dropped. The resulting "protojets" have all physically valid four-momenta. They are the input to the jet-finding algorithm. The output of the jet finder is then jets with energies at the electromagnetic energy scale and their constituents are the original calorimeter towers.

Topological cell clusters

The alternative representation of the calorimeter signals for jet reconstruction is topological cell clusters. These clusters are basically an attempt to reconstruct three-dimensional "energy blobs" which represent the showers that a particle develops after entering the calorimeter. The clustering procedure uses seed cells with a signal-to-noise ratio, or signal significance $\Gamma = E_{\text{cell}}/\sigma_{\text{noise,cell}}$, above a certain

threshold ($|\Gamma| > S$=4). All neighbouring cells, in all three dimensions, are collected into the cluster. Next neighbours are included for those cells which have Γ above a certain secondary threshold N ($|\Gamma| > N$=2). Finally, a ring of "guard" cells with a signal significance above a basic threshold, $|\Gamma| > P$=0, is included in the cluster. After the initial clusters are formed, local signal maxima are searched for using a splitting algorithm; the clusters are split between those maxima. The final object, called topocluster, has an energy equal to the energy sum of all the cells included, zero mass and a reconstructed direction given by a unit vector originating from the center of the ATLAS coordinate system pointing to the energy-weighted topocluster barycenter.

As in the case of the tower signals, clusters are initially formed using the basic EM energy-scale cell signals. The topoclusters can already be used for jet reconstruction. In addition, clusters can be calibrated to a local hadronic energy scale. This calibration starts with a classification step characterising clusters as electromagnetic, hadronic or noise, based on their location and shape. After that, cell signals inside hadronic clusters are weighted with functions depending on cluster position, energy and the cell signal density. Then, a correction for energy losses in inactive material close to or inside the cluster is applied. Finally, a correction for signal losses due to the clustering itself (out-of-cluster correction) is applied. All calibrations and corrections for topological clusters are derived from single-particle Monte Carlo simulations.

Reconstruction sequence

The reconstruction flow is rather similar to the tower-signal jet reconstruction. The main difference is the treatment of the negative signals. Due to the symmetric noise cut applied in the cell selection in the clustering step, some clusters may have net negative signal as well. These can be ignored for jet reconstruction without significantly biasing the jet signal by positive noise contributions because the noise suppression applied by the cell clustering already severely reduces any noise contribution. The cluster jets are initially at the electromagnetic energy scale. After the jet reconstruction, they are calibrated to correct effects such as residual non-linearities in the jet response due to algorithm effects, missing energy from the jet or adding energy not belonging to the jet in the jet clustering procedure, suppression of signal contributions from the underlying event and/or pile-up, etc.

5.3.2 Calorimeter-jet calibration

As mentioned above, jets are reconstructed at the electromagnetic scale, which is the basic signal scale for the ATLAS calorimeters. This energy scale of the electromagnetic calorimeters has been corrected using the invariant mass of $Z \to ee$ events from collision events.

The goal of the jet energy-scale calibration is to correct the energy and momentum of the jets measured in the calorimeter to those of the Monte Carlo truth jets. Monte Carlo truth jets are reconstructed from the stable particles with a lifetime longer than 10 ps in the MC event record, as explained in Section 4. The hadronic jet energy scale is on average restored using data-derived corrections and calibration constants derived from the comparison of the reconstructed jet kinematics to the one of the corresponding truth-level jet in Monte Carlo studies.

The jet energy-scale calibration is then validated with in-situ techniques. The jet calibration corrects for detector effects that affect the jet energy measurement:

- partial measurement of the energy deposited by hadrons (calorimeter non-compensation);
- energy losses in inactive regions of the detector (dead material);
- energy deposits from particles not contained in the calorimeter (leakage);
- energy deposits of particles inside the truth jet that are not included in the reconstructed jet;
- signal losses in calorimeter clustering and jet reconstruction.

The ATLAS collaboration has developed several calibration schemes with different levels of complexity and different sensitivity to systematic effects, which are complementary in how they contribute to the understanding of the jet energy measurement [61, 79]. These schemes are:

- **simple p_T- and η-dependent calibration scheme (EM+JES calibration):** this calibration scheme corrects for the non-linear correlation between the energy reconstructed in the calorimeter and the energy of the particles forming jets. Jets are found from clusters or towers at the electromagnetic scale and the calibration constants are applied as functions of the uncalibrated jet p_T and η;

- **global sequential calibration scheme (GS calibration):** this calibration scheme uses longitudinal and transverse properties of the jet structure to reduce fluctuations in the jet energy measurement. In this scheme, the jet energy response is first calibrated with the EM+JES calibration. Then the different jet properties are used to improve the jet energy resolution without changing the mean value of the response;
- **global cell energy-density weighting calibration scheme (GCW calibration):** this calibration scheme attempts to compensate for the different calorimeter response to hadronic and electromagnetic energy depositions. The hadronic signal is characterised by low cell-energy densities and, thus, weighted up. The weights, which depend on the cell energy density and the calorimeter layer only, are determined by minimising the energy fluctuations between the reconstructed and particle jets in Monte Carlo simulation. The weights also compensate for energy losses in dead material. Jets are found from uncalibrated clusters or towers, then cells are weighted and a final p_T and η dependent correction is added to ensure that the jet energy is properly reconstructed;
- **local cluster weighting calibration scheme (LCW calibration):** this calibration scheme uses properties of clusters to calibrate them individually. These weights are determined from Monte Carlo simulations of charged and neutral pions. Jets are found from calibrated clusters and a final correction of the jet energy is applied to account for jet-level effects.

Jets calibrated with the EM+JES scheme were used in this analysis. Therefore, the EM+JES calibration scheme is explained in detail in the following section.

EM+JES calibration scheme

The EM+JES calibration scheme consists of three subsequent steps:

- the average additional energy due to pile-up is subtracted form the energy measured in the calorimeters using correction constants extracted from an in-situ measurement (pile-up correction);
- the position of the jet is corrected such that the jet direction points to the primary vertex of the interaction instead of the geometrical center of ATLAS detector (jet-origin correction);
- the jet energy and position as reconstructed in the calorimeters are corrected using constants derived from the comparison of the kinematics of reconstructed jets and corresponding truth jets in Monte Carlo (final jet-energy correction).

The calibration restores the jet energy scale within ±2% for the full kinematic range and a systematic uncertainty is assigned for the remaining non-closure.

Pile-up correction

The energy of jets can include contributions that do not come from the event of interest, but are produced instead by multiple proton-proton interactions within the same bunch crossing. A correction is derived from minimum bias data as a function of the number of reconstructed primary vertex, N_{PV}, and η^{jet} [80].

Jet-origin correction

Calorimeter jets are reconstructed using the geometrical center of the ATLAS detector as reference to calculate the direction of jets and their constituents. The direction of each topocluster is corrected to point back to the primary vertex with the highest associated sum of track transverse momenta squared ($\Sigma p^2_{T,\text{track}}$) in the event. The kinematics of each topocluster is recalculated using the vector from the primary vertex to the topocluster centroid as its direction. The raw jet four-momentum is thereafter redefined as the vector sum of the topoclusters four-momenta. The jet energy is unaffected.

Final jet-energy correction

The final step of the EM+JES jet calibration corrects the reconstructed jet energy to the energy of the Monte Carlo truth jet.

The calibration is derived using all isolated calorimeter jets that have a matching isolated truth jet within $\Delta R = 0.3$ ($\Delta R = \sqrt{\Delta\eta^2 + \Delta\phi^2}$). Here, an isolated calorimeter (truth) jet is defined as a jet that has no other calorimeter (truth) jet with EM-scale (truth) $p_T > 7$ GeV within ΔR=2.5R, where R is the distance parameter of the jet algorithm. The EM-scale energy response $R = E^{\text{EM}}_{\text{calo}}/E_{\text{truth}}$ for each calorimeter-truth jet pair is measured in bins of the truth jet energy E_{truth} and calorimeter jet detector pseudorapidity η_{det}, referring to the pseudorapidity of the original reconstructed jet before the origin correction. For each (E_{truth},η_{det})-bin, the measured EM-scale energy response ($< R >$) is defined as the peak position of a Gaussian fit to the $E^{\text{EM}}_{\text{calo}}/E_{\text{truth}}$ distribution and the average calorimeter jet energy $< E^{\text{EM}}_{\text{calo}} >$ is determined.

For a given $\eta_{\rm det}$-bin k, a function $F_{{\rm calib},k}(E^{EM}_{\rm calo})$ of the jet response is obtained using a fit of the $(< E^{EM}_{\rm calo} >_j, < R >_j)$ points for each $E_{\rm truth}$-bin j, where the fitting function is parametrised as:

$$F_{{\rm calib},k}(E^{\rm EM}_{\rm calo}) = \sum_{i=0}^{N_{\rm max}} a_i (\ln E^{\rm EM}_{\rm calo})^i \tag{5.7}$$

where a_i are free parameters and N_{max} is chosen between 1 and 6 depending on the goodness of the fit. The final jet energy correction that relates the measured calorimeter jet energy scale to the hadronic energy scale is then defined as $1/F_{{\rm calib},k}(E^{\rm EM}_{\rm calo})$ as follows:

$$E^{\rm EM+JES}_{\rm calo} = \frac{E^{\rm EM}_{\rm calo}}{F_{\rm calib}(E^{EM}_{\rm calo}|_{\eta_{\rm det}})} \tag{5.8}$$

where $F_{\rm calib}(E^{\rm EM}_{\rm calo}|_{\eta_{\rm det}})$ is $F_{{\rm calib},k}(E^{\rm EM}_{\rm calo})$ for the relevant $\eta_{\rm det}$-bin k. The average jet energy-scale correction $< 1/F_{{\rm calib},k}(E^{\rm EM}_{\rm calo}) >$ is shown as a function of calibrated jet transverse momentum $p_T^{\rm jet}$ for three jet η intervals in Fig. 5.12.

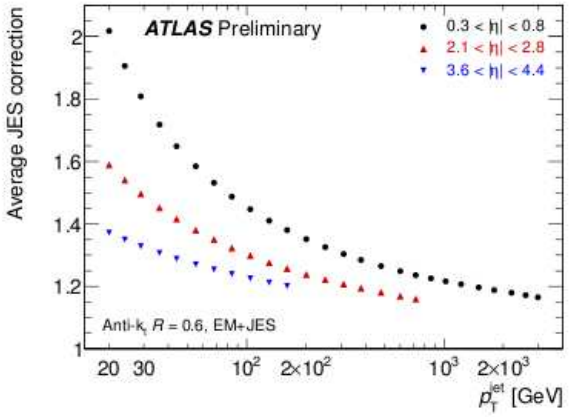

Figure 5.12: Average jet energy scale correction as a function of calibrated jet transverse momentum for three representative η-intervals.

5.3.3 Uncertainties in the EM+JES scheme calibration

The jet energy scale (JES) systematic uncertainty is derived combining information from in-situ and single pion test-beam measurements, uncertainties on the material budget of the ATLAS detector, the description of the electronic noise and the Monte Carlo modelling used in the event generation.

The JES systematic uncertainty for all jets with pseudorapidity $|\eta|$ >0.8 is determined using the JES uncertainty for the central barrel region (0.3< $|\eta|$ <0.8) as a baseline and adding a contribution from the relative calibration of the jets with respect to the central barrel region. This choice is motivated by the better knowledge of the detector geometry in the central region and by the use of test-beam measurements only extending up to the Tile calorimeter barrel for the estimate of the calorimeter response uncertainty.

The effects which contribute to EM-JES jet calibration scheme systematic uncertainty are the following:

- **uncertainty due to the JES calibration method:** after the jet is calibrated, the jet energy and p_T response still shows slight deviations from unity at low p_T (non-closure). This is mostly due to the following:

  - there is an underlying assumption that every constituent needs the same average compensation when deriving the calibration constants;
  - the same correction factor for energy and transverse momentum are used. In the case of a non-zero jet mass restoring only the jet energy and η will lead to a bias in the p_T calibration;

  The systematic uncertainty due to the non-closure of the nominal JES calibration is taken as the largest deviation of the response from unity between energy and p_T.

- **uncertainty due to the calorimeter response:** the uncertainty of the calorimeter response to jets can then be obtained from the response uncertainty of the individual particles making up the jet [81]. The following single-particle response measurements are used:

  - the single hadron energy measured in a cone around an isolated track with respect to the track momentum (E/p) in the momentum range from 0.5< p <20 GeV;
  - the pion response [82];

- **uncertainty due to the detector simulation:** this uncertainty takes into account the following effects:

  – discrepancies between the simulated and the real calorimeter cell noise thresholds [83];
  – uncertainty in the detector material simulation [84–86];

- **uncertainty due to the physics model and parameters employed in the Monte Carlo event generator:** the contribution to the JES uncertainty from the modelling of the fragmentation and underlying event and other parameter of the Monte Carlo event generator are obtained using the following Monte Carlo samples:

  - Alpgen+Herwig+Jimmy;
  - Perugia2010 Pythia tune [87];

  The uncertainty is estimated by comparing the Monte Carlo baseline with the previous ones;

- **uncertainty due to the relative calibration for jets with $|\eta|$ >0.8** [88];

- **uncertainty due to multiple interactions** [89].

There are two additional systematic sources that arise from the fact that the jet energy scale has been derived using a simulated sample of QCD jets with a particular mixture of quark- and gluon-initiated jets and with a particular selection of isolated jets. The differences in fragmentation between quark- and gluon-initiated jets and the effect of close-by jets give rise to a particular topology and flavor dependence of the energy scale. Since the event topology and flavour composition (quark and gluon fractions) may be different in final states other than the QCD jets considered, the dependence of the jet energy response on jet flavour and topology has to be taken into account in each physics analysis.

5.3.4 Jet quality criteria

Jet quality criteria are applied to data to reject jets reconstructed from calorimeter signals not originating from a proton-proton collision [90]. The main sources of fake jets in data were found to be:

- noise burst in the hadronic endcap calorimeter electronics;
- coherent noise from the electromagnetic calorimeters;
- cosmic rays;
- beam-related background (beam gas, beam-halo).

Jet quality selections were performed to reduce sporadic noise bursts from noisy calorimeter cells; cosmic rays or non-collision backgrounds can induce events where

	Loose	Medium
HEC spikes	($f_{\text{HEC}} > 0.5$ and $\lvert f_{\text{quality}}\rvert > 0.5$) or $\lvert E_{\text{neg}}\rvert > 60$ GeV	Loose or $f_{\text{HEC}} > 1 - \lvert f_{\text{quality}}\rvert$
Coherent EM noise	$f_{\text{EM}} > 0.95$ and $f_{\text{quality}} > 0.8$ and $\lvert\eta^{\text{jet}}\rvert < 2.8$	Loose or $f_{\text{EM}} > 0.9$ and $f_{\text{quality}} > 0.8$ and $\lvert\eta^{\text{jet}}\rvert < 2.8$
Non-collision background	$\lvert t_{\text{jet}}\rvert > 25$ ns or ($f_{\text{EM}} < 0.05$ and $f_{\text{ch}} < 0.05$ and $\lvert\eta^{\text{jet}}\rvert < 2$) or ($f_{\text{EM}} < 0.05$ and $\lvert\eta^{\text{jet}}\rvert \geq 2$) or ($f_{\text{max}} > 0.99$ and $\lvert\eta^{\text{jet}}\rvert < 2$)	Loose or $\lvert t_{\text{jet}}\rvert > 10$ ns or ($f_{\text{EM}} < 0.05$ and $f_{\text{ch}} < 0.1$ and $\lvert\eta^{\text{jet}}\rvert < 2$) or ($f_{\text{EM}} > 0.95$ and $f_{\text{ch}} < 0.05$ and $\lvert\eta^{\text{jet}}\rvert < 2$)

Table 5.4: Selection criteria used to reject fake jets and non-collision background.

the jet candidates are not in-time with the beam collision.

Two reference sets of cuts -loose and medium- were defined for the jet quality criteria (see Table 5.4).

Chapter 6

Event selection

The event selection requirements as well as the comparison between the data and the signal prediction by MC are described in this chapter.

6.1 Event selection

The data used in this analysis were collected with the ATLAS detector during the proton-proton collision running period 2010, which corresponds to a total integrated luminosity of 45 pb^{-1} (see Fig. 6.1), when the LHC operated at a centre-of-mass energy of $\sqrt{s}$= 7 TeV. This data set was chosen to study the dynamics of isolated-photon plus jet production at low E_T^γ starting[1] at E_T^γ = 45 GeV. The dynamics of isolated-photon plus jet production depend on E_T^γ, mainly due to the relative contributions of the different subprocesses (direct photon and fragmentation), which change with E_T^γ. Furthermore, in order to measure the differential cross section as a function of $|\cos\theta^{\gamma-\text{jet}}|$ in an unbiased way, a cut at $\sim$ 400 GeV in $M^{\gamma-\text{jet}}$ would have to be applied on 2011 data, which would leave out the interesting low $M^{\gamma-\text{jet}}$ region. Therefore, the study of photons with 45< E_T^γ <100 GeV can only be done with 2010 data. In addition, the pile-up conditions in 2011 data would make measurements of isolated-photon plus jet production with R=0.6, as it is done in this analysis, less precise.

The analysis was done using a restricted data set that corresponds to an integrated luminosity of 37.1$\pm$1.3 pb^{-1} [91]. This luminosity corresponds to the sample passing data quality requirements, where the calorimeter and the inner detector were operational and had good data quality, and collected with the "EF_g40_loose"

[1]The lowest unprescaled trigger in 2011 was "EF_g80_loose", which only allows the study of photons with $E_T^\gamma \geq$ 100 GeV.

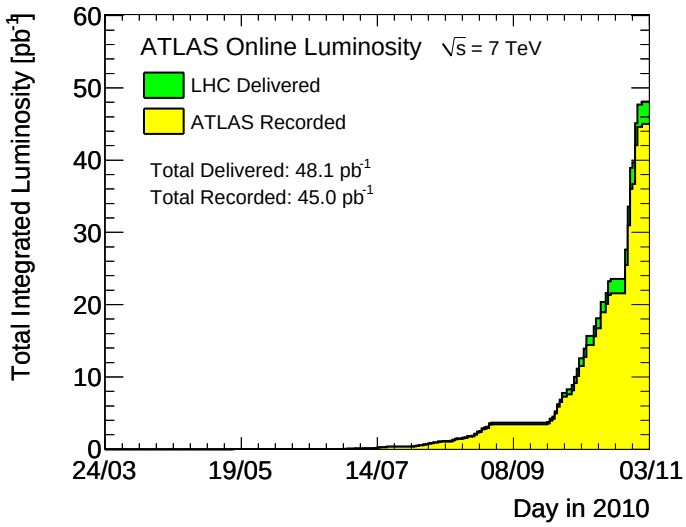

Figure 6.1: Cumulative luminosity versus day delivered to (green) and recorded by ATLAS (yellow) during stable beams and for pp collisions at 7 TeV centre-of-mass energy during the 2010 data taking period.

trigger (see below). A full list of the runs used in this analysis and their integrated luminosity was shown previously (See Table 1 in ref. [56]).

The data sample used consists of events triggered by a single-photon high-level trigger with a nominal transverse energy threshold of 40 GeV, seeded by a L1 trigger with nominal threshold equal to 14 GeV. The selection criteria applied by the trigger on shower-shape variables computed from the energy profiles of the showers in the calorimeters are looser than the photon identification criteria applied in the offline analysis and allow a plateau of constant efficiency close to 100% (see Fig. 6.2) for true prompt photons with $E_T^\gamma > 43$ GeV and pseudorapidity $|\eta^\gamma| < 2.37$. The "EF_g40_loose" trigger was the lowest-threshold unprescaled photon trigger during the 2010 data-taking period.

The efficiency of this trigger for $E_T^\gamma > 45$ GeV was measured to be $99.4^{+0.6}_{-0.2}\%$ for $|\eta^\gamma| < 2.37$ [92] (see Fig. 6.2).

The average number of interaction per bunch crossing is 2.1 for the data collected with the "EF_g40_loose" (see Fig. 6.3). The contamination from pile-up jets in the selected sample was estimated to be negligible, as expected from the low pile-up conditions.

The sample of isolated-photon plus jet events was selected offline by applying

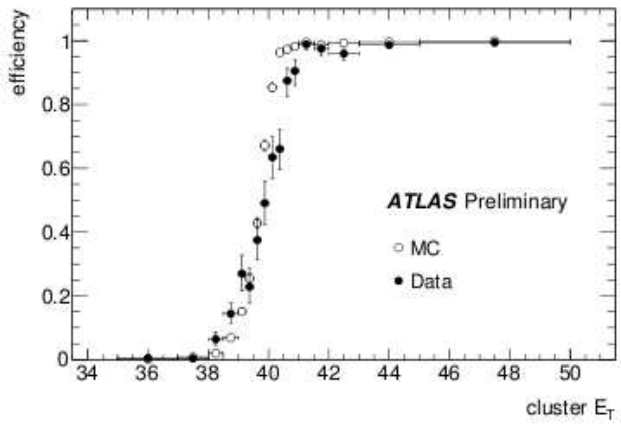

Figure 6.2: Photon-trigger efficiency with respect to the offline photon selection as measured in data (dots) and MC (open circles) for the "EF_g40_loose" trigger, computed for photon candidates passing the "tight" identification criteria and with isolation energy lower than 3 GeV.

the following selection criteria:

- events were required to have a reconstructed primary vertex, with at least five associated tracks, consistent with the average beam-spot position. This requirement reduced non-collision backgrounds. The effect of this requirement on the signal is expected to be negligible (see Chapter 9). The remaining amount of non-collision background was estimated by using control samples collected during normal data-taking conditions with dedicated low-thresholds triggers that were activated in events where either no proton bunch of only one of the two beams crossed the interaction region. The estimated contribution to the final sample is less than 0.1% [93, 94].

- the photon-candidate selection is based on the reconstruction of an isolated electromagnetic cluster. Background from non-prompt photons originating from decays of energetic π^0 and η mesons inside jets was suppressed by means of shower-shape and isolation variables (see Chapter 5). The photon-candidate selection criteria are:

  - photons were reconstructed from electromagnetic clusters and tracking information provided by the inner detector as described in Chapter 5. Both converted and unconverted candidates were kept. Photons reconstructed near regions of the calorimeter affected by read-out or high-voltage calorimeter failures were not considered. Energy calibration was

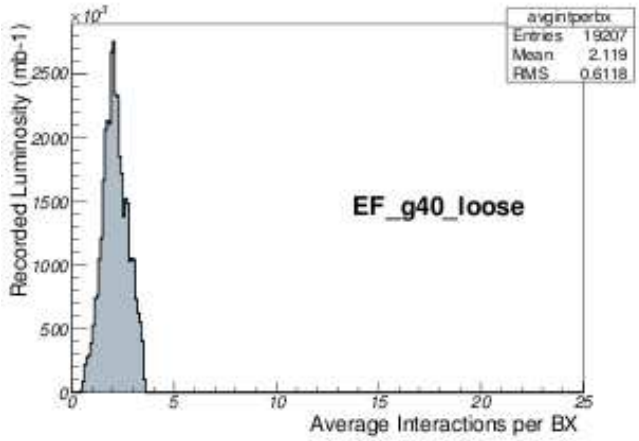

Figure 6.3: Luminosity-weighted average interactions per bunch crossing for data collected with the "EF_g40_loose" trigger.

then applied to account for energy loss and leakage (see Chapter 5);

- events with at least one photon candidate with $E_T^\gamma > 45$ GeV and $|\eta^\gamma| < 2.37$ were selected. The candidate was excluded if $1.37 < |\eta^\gamma| < 1.52$ (crack region);
- the candidates were required to pass "loose" identification criteria based on five discriminating variables[2] computed from the lateral and longitudinal profiles of the energy deposited in the calorimeter, namely $R_{\rm had}$, R_η, w_2, R_ϕ and $w_{\rm stot}$ (see Chapter 5). The average photon multiplicity after applying these requirements is 1.00088. In events with multiple candidates satisfying these requirements, the candidate with highest transverse energy (leading photon) was retained for further study;
- the leading photon was required to pass "tight" identification criteria based on nine discriminating variables computed from the lateral and longitudinal profiles of the energy deposited in the calorimeters (see Chapter 5). The sample of photon candidates that pass the "loose" selection criteria but fail the "tight" identification criteria are used in the determination of the background (see Chapter 7);
- the isolation transverse energy, $E_T^{\rm iso}(R_0 = 0.4)$ (see Chapter 5), of the leading photon was required to be lower than 3 GeV;

- jets were reconstructed from topoclusters at the EM scale, using the anti-k_T algorithm with radius $R = 0.6$. The jet four-momenta were computed from the sum of the jet-constituent four-momenta, treating each as a four-vector with

[2]This definition is known as " loose' " in the context of the ATLAS collaboration.

zero mass. The jet four-momenta were then recalibrated at the EM+JES jet energy scale as described in Chapter 5. The selection criteria applied to the jets were:

- jets with negative calibrated energy or not passing medium quality criteria were rejected;
- if the jet axis lay within a cone of radius $R = 0.3$ around an electron candidate passing "tight" identification criteria and having calorimeter isolation lower than 4 GeV, the jet was discarded. This requirement reduces the background form $Z \to e^+e-$ and $W \to e\nu_e$ and has an effect smaller than 0.05% on the signal;
- jets with $P_T^{\rm jet} > 40$ GeV were selected;
- jets were required to be separated from the leading-photon direction by a distance greater than one unit in the $\eta - \phi$ plane. This condition rejects the overlap between photons and jets and ensures that the leading-photon isolation energy is not contaminated by the jet activity;

– in events with multiple jets satisfying these requirements, the jet with highest transverse momentum (leading jet) was retained for further study;

– the leading-jet rapidity was required to be in the region $|Y_{\rm lead}^{\rm jet}| < 2.37$.

The number of data events selected by using the requirements listed above amounts to $\approx$ 124000. The average photon (jet) multiplicity in the data after the previous requirements is 1.00026 (1.19). The signal Monte Carlo prediction for the jet multiplicity is 1.21 (1.19) using PYTHIA (HERWIG); the measured jet-multiplicity distribution is shown in Fig. 6.4.

For the measurement of the $M^{\rm jet}$ and $|\cos\,\theta^{\gamma-{\rm jet}}|$ cross sections, additional cuts were imposed to remove the bias due to the rapidity and transverse-momentum cuts on the photon and the jet. To perform unbiased measurements of the differential cross sections as functions of $M^{\gamma-{\rm jet}}$ and $|\cos\,\theta^{\gamma-{\rm jet}}|$, the cuts $|\eta_{\rm lead}^{\gamma} + Y_{\rm lead}^{\rm jet}| <$2.37, $|\cos\,\theta^{\gamma-{\rm jet}}| < 0.83$ and $M^{\gamma-{\rm jet}} > 161$ GeV were imposed. The selected unbiased kinematic regions are shown as hatched areas in Fig. 6.5. The number of events selected in the data after these cuts is $\approx$ 26000.

6.2 Observable reconstruction

This analysis presents the measurements of the differential cross sections as functions of $E_{T,{\rm lead}}^{\gamma}$, $P_{T,{\rm lead}}^{\rm jet}$, $|Y_{\rm lead}^{\rm jet}|$, $\Delta\phi^{\gamma-{\rm jet}}$, $M^{\rm jet}$ and $|\cos\,\theta^{\gamma-{\rm jet}}|$. The $E_{T,{\rm lead}}^{\gamma}$ variable is defined

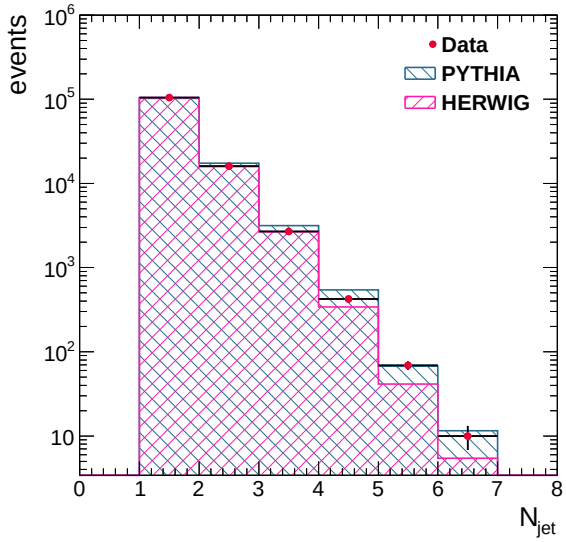

Figure 6.4: The measured jet-multiplicity distribution (dots). For comparison, the MC simulations of the signal from PYTHIA (right-hatched histogram) and HERWIG (left-hatched histogram) are also included. The MC distribution are normalised to the total number of data events.

as

$$E^{\gamma}_{T,\mathrm{lead}} = E^{\gamma}_{\mathrm{clus}} \sin\,\theta^{\gamma}_{\mathrm{clus}} \ , \tag{6.1}$$

where $E^{\gamma}_{\mathrm{clus}}$ is the energy of the EM photon cluster and $\theta^{\gamma}_{\mathrm{clus}}$ is the angle between the cluster and the collison axis with respect to the center of ATLAS reference system (interaction point). The $P^{\mathrm{jet}}_{T,\mathrm{lead}}$ is the jet tranverse momentum component, calculated using the E-scheme (see Chapter 3), as the sum of all topocluster four-momentum $P^{\mathrm{jet}} = \sum_i P^{\mathrm{topoclus}}_i$, where $P^{\mathrm{topoclus}}_i = (e^{\mathrm{topoclus}}_i, p^{\mathrm{topoclus}}_{x,i}, p^{\mathrm{topoclus}}_{y,i}, p^{\mathrm{topoclus}}_{z,i})$, inside the jet and then taking the transverse spatial component. The components of the topocluster four-momentum are defined as

$$p^{\mathrm{topoclus}}_x = e^{\mathrm{topoclus}} \sin\,\theta^{\mathrm{topoclus}} \cos\,\phi^{\mathrm{topoclus}} \ , \tag{6.2}$$

$$p^{\mathrm{topoclus}}_y = e^{\mathrm{topoclus}} \sin\,\theta^{\mathrm{topoclus}} \sin\,\phi^{\mathrm{topoclus}} \ , \tag{6.3}$$

$$p^{\mathrm{topoclus}}_z = e^{\mathrm{topoclus}} \cos\,\theta^{\mathrm{topoclus}} \ , \tag{6.4}$$

$$\tag{6.5}$$

where e^{topoclus} is the energy and $(\theta^{\mathrm{topoclus}}, \phi^{\mathrm{topoclus}})$ the position of the topocluster. The $Y^{\mathrm{jet}}_{\mathrm{lead}}$ observable represents the rapidity of the leading jet and is defined as

$$Y^{\mathrm{jet}} = \frac{1}{2} \ln \frac{E^{\mathrm{jet}} + p^{\mathrm{jet}}_z}{E^{\mathrm{jet}} - p^{\mathrm{jet}}_z} \ , \tag{6.6}$$

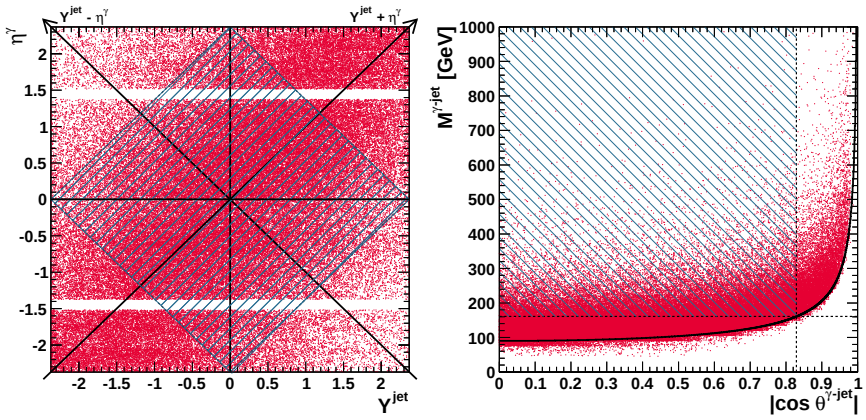

(a) (b)

Figure 6.5: (a) The η^{γ}-$Y^{\rm jet}$ plane. (b) The $M^{\gamma-{\rm jet}}$-$|\cos\,\theta^{\gamma-{\rm jet}}|$ plane. In both figures, the hatched area represents the selected unbiased kinematic region.

where $E^{\rm jet}$ and $p_z^{\rm jet}$ are the energy and longitudinal momentum component of the jet. The $\Delta\phi^{\gamma-{\rm jet}}$ is defined as the difference in azimuthal angle between the leading photon and the leading jet,

$$\Delta\phi^{\gamma-{\rm jet}} = \phi^{\gamma}_{\rm lead} - \phi^{\rm jet}_{\rm lead}\ . \tag{6.7}$$

The $M^{\gamma-{\rm jet}}$ represents the invariant mass of the γ-jet system and is defined as

$$(M^{\gamma-{\rm jet}})^2 = (m^{\rm jet})^2 + 2(E_T^{\gamma}E_T^{\rm jet}\cosh(\Delta Y^{\gamma-{\rm jet}}) - P_T^{\gamma}P_T^{\rm jet}\cos(\Delta\phi^{\gamma-{\rm jet}})) \tag{6.8}$$

where $\Delta Y^{\gamma-{\rm jet}} = Y^{\rm jet} - \eta^{\gamma}$ and $E_T^{\rm jet} = \sqrt{(P_T^{\rm jet})^2 + (m^{\rm jet})^2}$. The $\cos\,\theta^{\gamma-{\rm jet}}$ approximates the cosine of the polar angle between the photon and the z-axis in the centre-of-mass system ($\theta^{\gamma-{\rm jet}}_{\rm CM}$). It is defined as

$$\cos\,\theta^{\gamma-{\rm jet}} = \tanh\Big(\frac{\Delta Y^{\gamma-{\rm jet}}}{2}\Big)\ . \tag{6.9}$$

This observable, which makes use only of the rapidities, gives a better handle on $\theta^{\gamma-{\rm jet}}_{\rm CM}$ since it is not affected by the relatively large uncertainties associated to the measurement of the jet energy.

6.3 Comparison between data and Monte Carlo

Figure 6.6(a) shows the $E^{\gamma}_{T,{\rm lead}}$ data distribution for $45 < E^{\gamma}_{T,{\rm lead}} < 400$ GeV. The measured photon transverse-energy spectrum decreases as E_T^{γ} increases. For $E_T^{\gamma} >$

400 GeV, the data statistics are very poor to make a precise measurement. The MC simulation of the signal from PYTHIA and HERWIG, normalised to the total number of events in the data distribution, are also included. The simulation of the signal from PYTHIA and HERWIG give an adequate description of the data.

The data distribution as a function of $P^{\rm jet}_{T,\rm lead}$ is shown in Fig 6.6(b) for 40 $< P^{\rm jet}_{T,\rm lead} <$ 400 GeV. The measured jet transverse momentum spectrum decreases as $P^{\rm jet}_{T,\rm lead}$ increases. The simulations of the signal from PYTHIA and HERWIG give an adequate description of the data. At $P^{\rm jet}_{T,\rm lead} \sim$ 100 GeV, the simulation of PYTHIA (HERWIG) has a tendency to be somewhat above (below) the data. Figure 6.6(c) shows the $|Y^{\rm jet}_{\rm lead}|$ distribution. The data distribution presents a maximum at $|Y^{\rm jet}_{\rm lead}|$ = 0. Both the simulations of PYTHIA and HERWIG give a reasonable description of the data. Figure 6.6(d) shows the data distribution as a function of $\Delta\phi^{\gamma-\rm jet}$. The measured distribution increases as $\Delta\phi^{\gamma-\rm jet}$ increases. The simulation of PYTHIA provides an adequate description of the data, whereas HERWIG fails to describe the data in the range 0.5$< \Delta\phi^{\gamma-\rm jet} <$2. The data distribution as a function of $M^{\gamma-\rm jet}$ is shown in Fig 6.6(e) for 161 $< M^{\gamma-\rm jet} <$ 1000 GeV. The measured invariant mass distribution decreases as $M^{\gamma-\rm jet}$ increases. The simulations of PYTHIA and HERWIG provide an adequate description of the data. In Fig. 6.6(f), it is shown the data distribution as a function of $|\cos\,\theta^{\gamma-\rm jet}|$ for $|\cos\,\theta^{\gamma-\rm jet}| < 0.83$; it is observed that the measured distribution increases as $|\cos\,\theta^{\gamma-\rm jet}|$ increases. Neither PYTHIA nor HERWIG describe the data precisely.

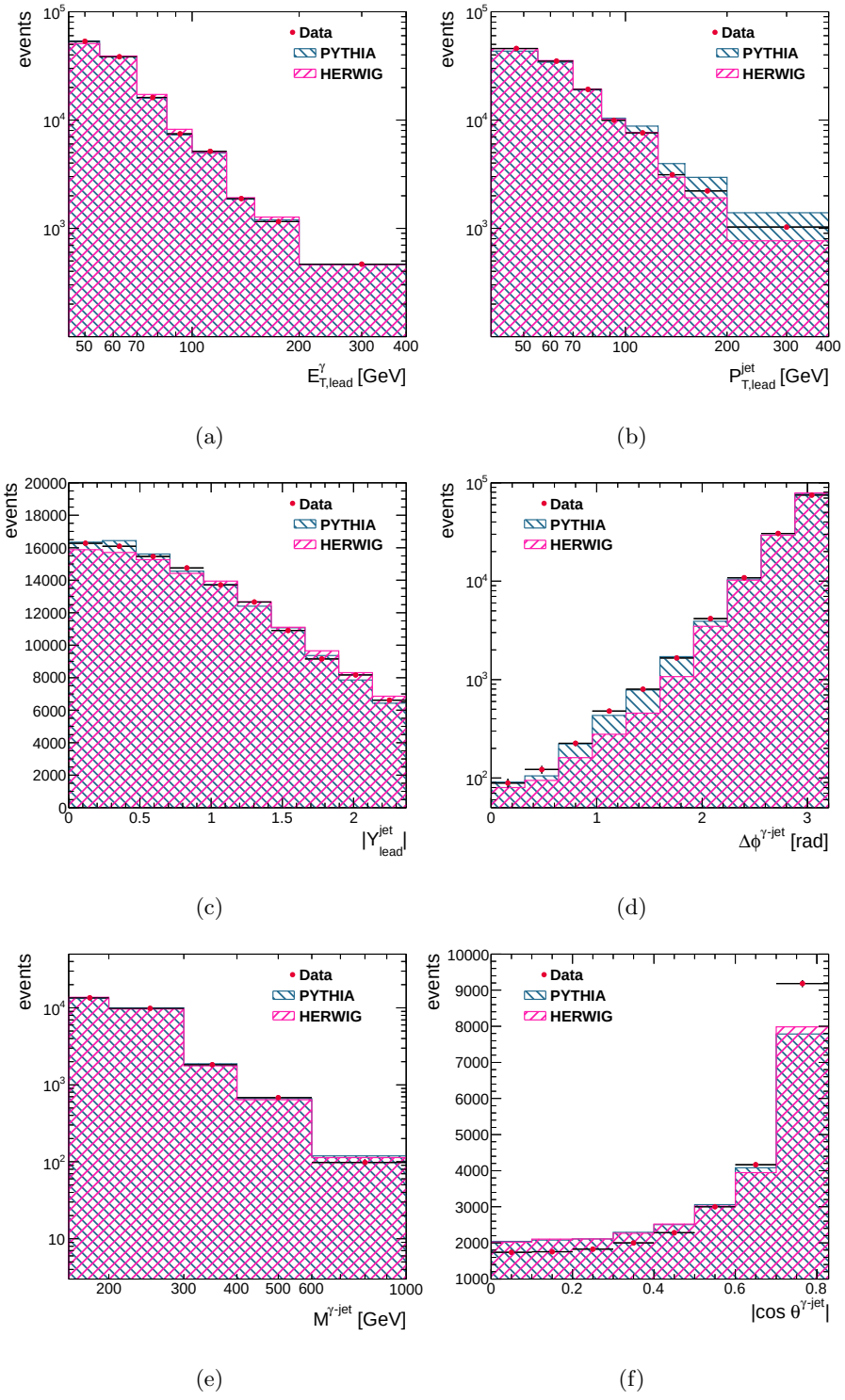

(a) (b)

(c) (d)

(e) (f)

Figure 6.6: The measured (a) $E^{\gamma}_{T,lead}$, (b) $P^{\rm jet}_{T,\rm lead}$, (c) $|Y^{\rm jet}_{\rm lead}|$, (d) $\Delta\phi^{\gamma-\rm jet}$, (e) $M^{\gamma-\rm jet}$ and (f) $|\cos\,\theta^{\gamma-\rm jet}|$ distributions (dots). For comparison, the MC simulations of the signal from PYTHIA (right-hatched histogram) and HERWIG (left-hatched histogram) are also included. The MC distributions are normalised to the total number of data events.

Chapter 7

Background subtraction and the MC optimisation method

After the data selection, there is still a significant amount of background in the selected events. To obtain the signal data, it is necessary to subtract the background. The technique to perform the background subtraction is discussed in detail in this chapter. The method to improve the data description by the Monte Carlo is also explained.

7.1 Background-subtraction technique

After applying the selection criteria explained in chapter 6, a non-negligible contribution of background still remains in the selected data sample, even after the application of the tight identification and isolation requirements. This background comes mainly from QCD multijet processes, in which a jet is misidentified as a photon. This jet contains usually a light neutral meson, predominantly a π^0 that decays into two collimated photons, which carries most of the energy of the jet.

As an illustration of the presence of background, Fig. 7.1(a) shows the measured E_T^{iso} distribution, before applying any requirement on this variable, for the events which satisfy the tight identification criteria and those which fail ("non-tight") photons candidates[1], separately. The non-tight events have the same shape than the background which passes tight identification criteria. Fig 7.1(b) shows the tight data distribution after performing a subtraction of the non-tight data distribution.

[1] "non-tight" photons candidates are defined as photons which pass the "loose" selection criteria but fail tight selection requirements.

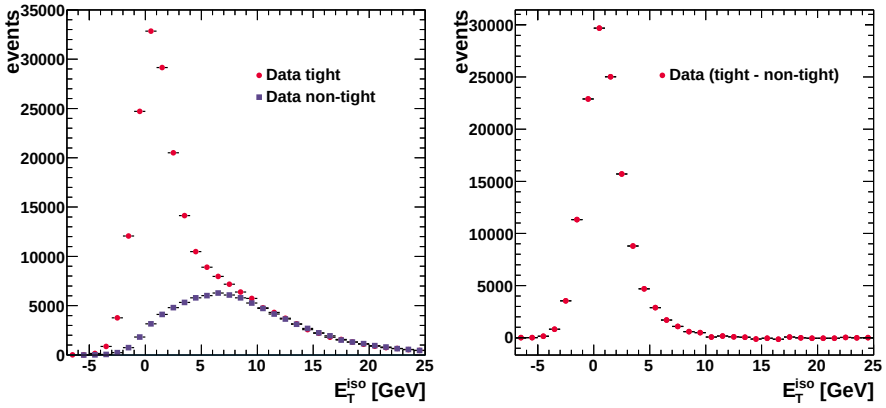

(a) (b)

Figure 7.1: (a) the measured $E_T^{\rm iso}$ distribution before the isolation requirements and after applying the tight identification criteria (dots) and for those events which fail the tight identification ("non-tight") (squares). The normalisation of the "non-tight" histogram is such that the integrals of the "tight" and "non-tight" distributions for $E_T^{\rm iso} > 10$ GeV coincide. (b) the measured $E_T^{\rm iso}$ distribution before the isolation requirement and after applying the tight identification criteria and after subtracting the contribution from non-tight events (dots).

The background contamination was subtracted from the selected photon signal sample using the so-called "two-dimensional sideband" (2D-sideband) method [56]. The main advantage of this method is that no precise knowledge of the signal is required and the background properties are deduced from data. It is based on the definition of a "tight-isolated" signal region and three background control regions that contain photons that fail either the "tight" identification or the isolation criteria or both, as shown in Fig. 7.2. The four regions are defined as

- **A** is the signal region, which contains tight and isolated photon candidates;
- **B** is the control region with non-isolated background, which contains tight and non-isolated photon candidates;
- **C** is the control region with non-identified background, which contains isolated and non-tight photon candidates;
- **D** is the background control region, which contains non-isolated and non-tight photon candidates.

The method assumes that background control regions have weak signal contam-

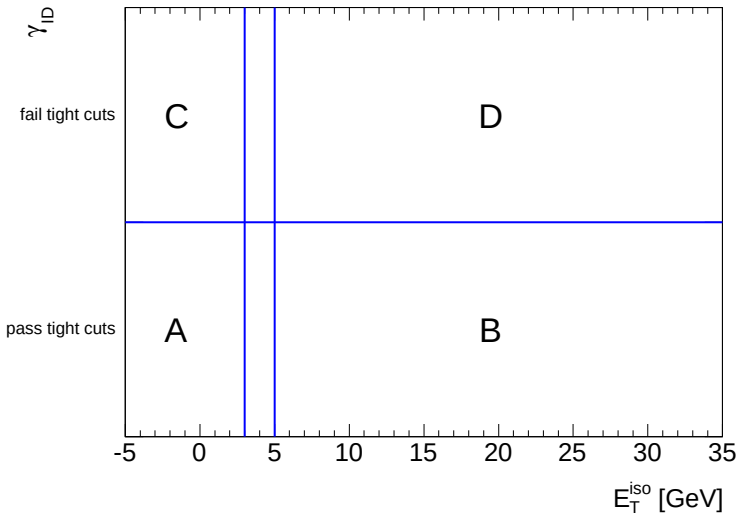

Figure 7.2: Illustration of the two-dimensional plane of the photon identification variable vs. the isolation transverse energy used to estimate the background yield in the signal region, A, from the observed yields in the three control regions B, C and D.

ination and that, in the same regions, the photon identification variables (γ_{ID}) are essentially uncorrelated to the isolation variable ($E_T^{\rm iso}$).

Therefore, the number of signal events in the signal region A is given by

$$N_A^{\rm sig} = N_A - R^{\rm bg} \cdot (N_B - \epsilon_B N_A^{\rm sig}) \cdot \frac{N_C - \epsilon_C N_A^{\rm sig}}{N_D - \epsilon_D N_A^{\rm sig}}, \tag{7.1}$$

where $N_A^{\rm sig}$ is the expected number of signal events, N_K with $K = A, B, C, D$ is the number of observed events in each region and

$$R^{\rm bg} = \frac{N_A^{\rm bg} \cdot N_D^{\rm bg}}{N_B^{\rm bg} \cdot N_C^{\rm bg}} \tag{7.2}$$

was taken as $R^{\rm bg} = 1$ (photon-identification and photon isolation variables assumed not to be correlated) for the nominal results; $N_K^{\rm bg}$ with $K = A, B, C, D$ is the number of background events in each region. Deviations with respect to unity for $R^{\rm bg}$ were taken as systematic uncertainties (see Chapter 9).

Equation (7.1) takes also into account the expected number of signal events in the three background control regions via the signal leakage fractions, $\epsilon_K = N_K^{\rm sig}/N_A^{\rm sig}$ with $K = B, C, D$. The signal leakage fractions were extracted from the MC simulations of the signal and are shown in Figs. 7.3 and 7.4.

The signal yield was determined from the observed yields in the data in the four regions of the $\gamma_{\rm ID}$ vs. $E_T^{\rm iso}$ plane and the signal leakage fractions from the simulated events using Eq. 7.1. The signal purity, computed as $P = N_A^{\rm sig}/N_A$, is shown in Fig 7.5. The purity is above ≈90% and very similar for the estimation using either PYTHIA or HERWIG to compute the signal leakage fractions.

The purity increases as $E_{T,\rm lead}^{\gamma}$, $P_{T,\rm lead}^{\rm jet}$, and $M^{\gamma-\rm jet}$ increase, is approximately constant as a function of $|Y_{\rm lead}^{\rm jet}|$ and $\Delta\phi^{\gamma-\rm jet}$, and decreases as $|\cos\theta^{\gamma-\rm jet}|$ increases.

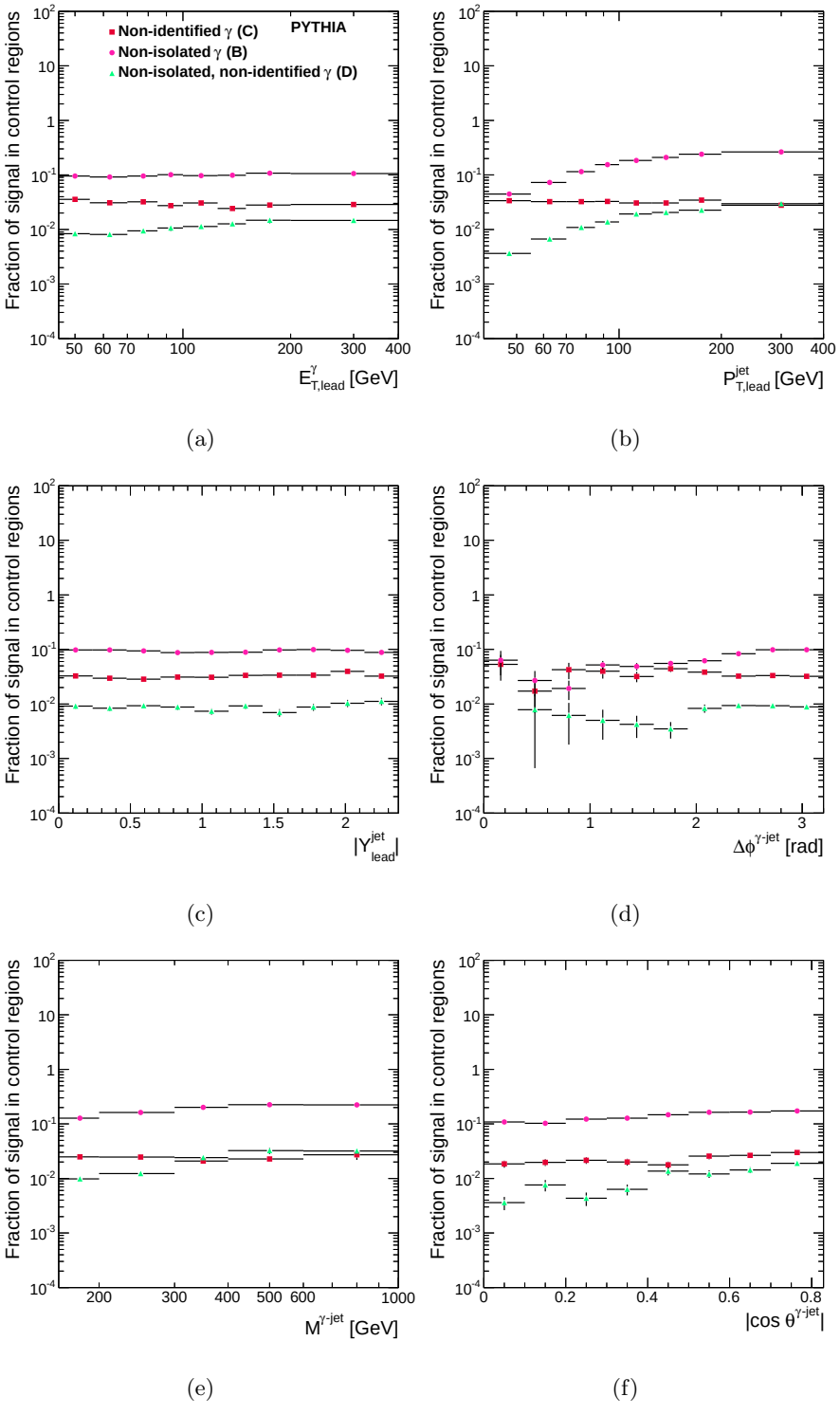

Figure 7.3: Signal leakage fractions from PYTHIA for the B (dots), C (squares) and D (triangles) control regions as functions of (a) $E^{\gamma}_{T,lead}$, (b) $P^{\rm jet}_{T,\rm lead}$, (c) $|Y^{\rm jet}_{\rm lead}|$, (d) $\Delta\phi^{\gamma-\rm jet}$, (e) $M^{\gamma-\rm jet}$ and (f) $|\cos\,\theta^{\gamma-\rm jet}|$.

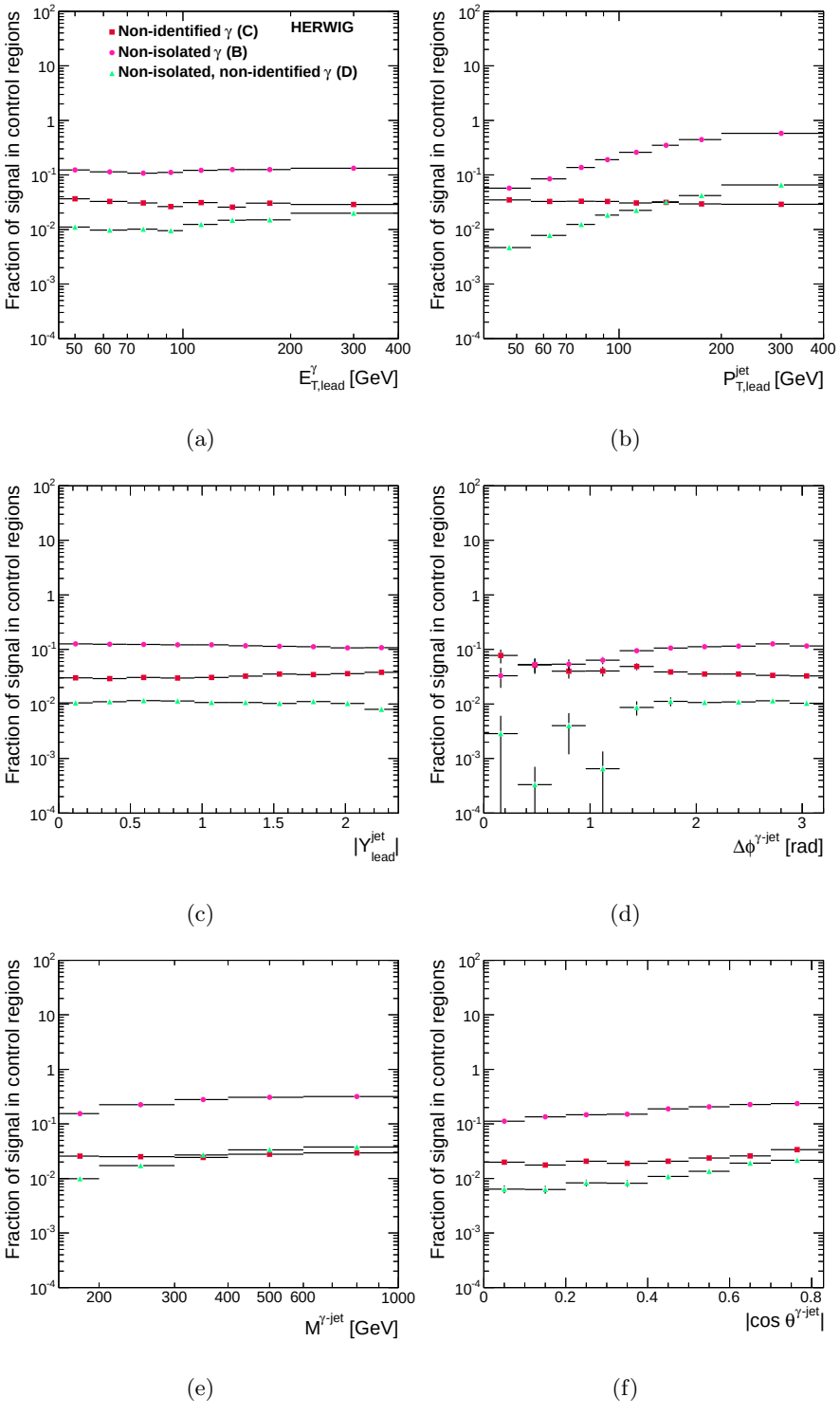

Figure 7.4: Signal leakage fractions from HERWIG for the B (dots), C (squares) and D (triangles) control regions as functions of (a) $E^{\gamma}_{T,\mathrm{lead}}$, (b) $P^{\mathrm{jet}}_{T,\mathrm{lead}}$, (c) $|Y^{\mathrm{jet}}_{\mathrm{lead}}|$, (d) $\Delta\phi^{\gamma-\mathrm{jet}}$, (e) $M^{\gamma-\mathrm{jet}}$ and (f) $|\cos\,\theta^{\gamma-\mathrm{jet}}|$.

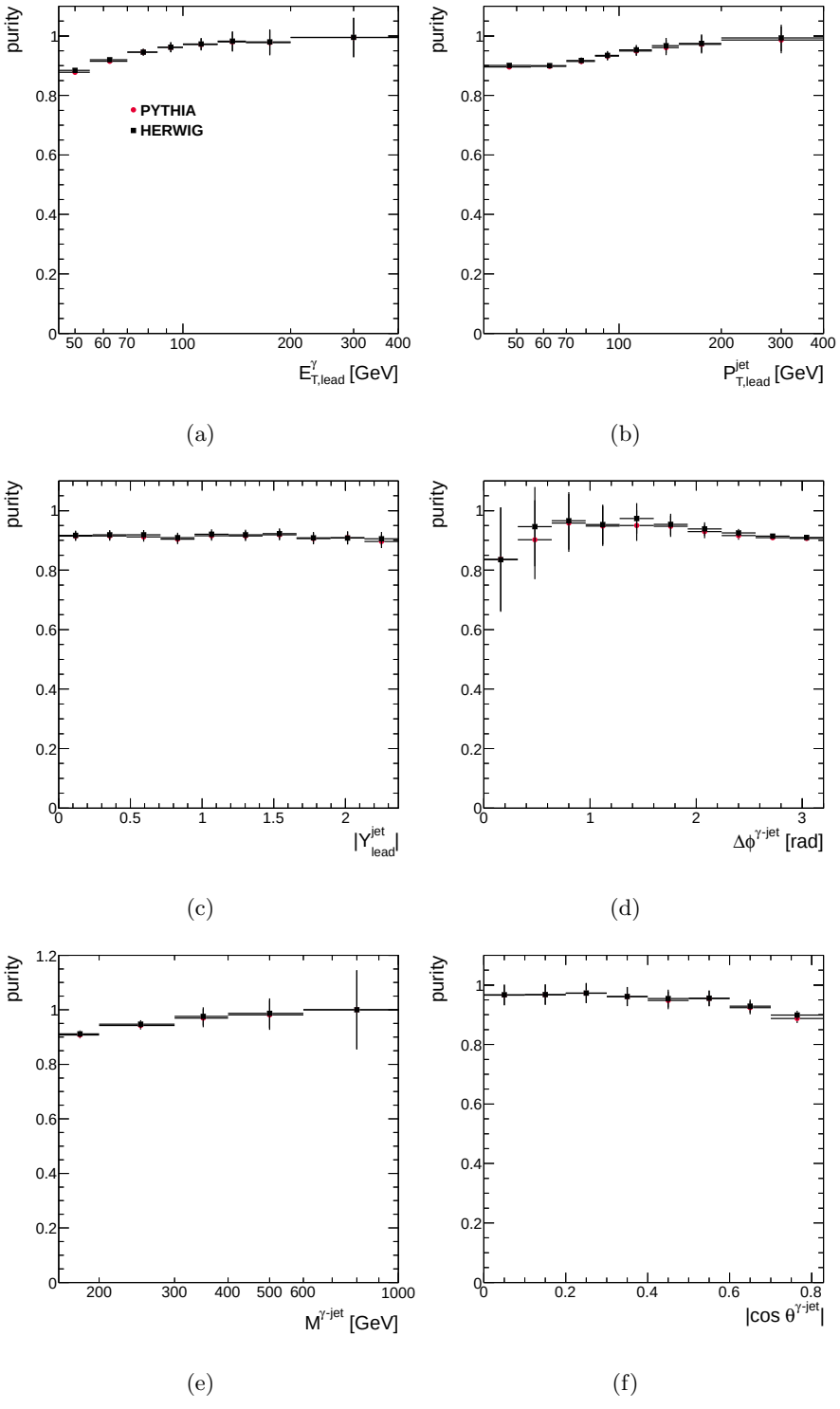

(a) (b) (c) (d) (e) (f)

Figure 7.5: Estimated signal purities in data using signal leakage fractions from PYTHIA (dots) and HERWIG (squares) as functions of (a) $E^{\gamma}_{T,\mathrm{lead}}$, (b) $P^{\mathrm{jet}}_{T,\mathrm{lead}}$, (c) $|Y^{\mathrm{jet}}_{\mathrm{lead}}|$, (d) $\Delta\phi^{\gamma-\mathrm{jet}}$, (e) $M^{\gamma-\mathrm{jet}}$ and (f) $|\cos\,\theta^{\gamma-\mathrm{jet}}|$. The error bars are statistical only.

7.1.1 Comparison between background-subtracted data and signal MC

The estimated signal yields using the signal leakage fractions from PYTHIA or HERWIG are shown in Figs. 7.6 and 7.7. After background subtraction, as shown in Fig. 7.6, the $E_{T,\mathrm{lead}}^{\gamma}$ data distribution is reasonably well described by PYTHIA and HERWIG signal Monte Carlo predictions. The $P_{T,\mathrm{lead}}^{\mathrm{jet}}$ distribution is well described by both Monte Carlo generators except in the tail, where HERWIG (PYTHIA) prediction are above (below) the measured distribution. In contrast, the $|Y_{\mathrm{lead}}^{\mathrm{jet}}|$ distribution is well described by PYTHIA and HERWIG. As shown in Fig. 7.7, the $\Delta\phi^{\gamma-\mathrm{jet}}$ background-subtracted data distribution is well described by PYTHIA but HERWIG fails in the region $0.5 < \Delta\phi^{\gamma-\mathrm{jet}} < 2.0$. The distribution of $M^{\gamma-\mathrm{jet}}$ is reasonably well described by both Monte Carlos generators whereas that of $|\cos\theta^{\gamma-\mathrm{jet}}|$ is not described precisely by either of them.

7.2 Monte Carlo optimisation method

To study in more detail the success or failure of the MC simulations to describe the data distributions, Figs. 7.8 and 7.9 show the same distributions as in Figs. 7.6 and 7.7 together with the individual MC components, namely the direct-photon and fragmentation contributions. It is observed that for most of the distributions studied, the shape of these two components is different. Therefore, the shape of the MC distributions depends on the relative fraction of the two prompt-photon contributions. An improvement of the description of the data by the MC was achieved by performing a χ^2 fit to each data distribution with the relative fraction of the direct-photon (α) and the fragmentation (1-α) contributions as the free parameter. The χ^2 function used is

$$\chi^2(\alpha) = \sum_i \left(\frac{N_A^{\mathrm{sig}}(i) - N_A^{MC}(i,\alpha)}{\Delta N_A^{\mathrm{sig}}(i)}\right)^2, \tag{7.3}$$

where

$$N_A^{\mathrm{MC}}(i,\alpha) = \frac{N_A^{\mathrm{sig,TOT}}}{\alpha N_A^{\mathrm{MC,DP,TOT}} + (1-\alpha) N_A^{\mathrm{MC,F,TOT}}} \left(\alpha N_A^{\mathrm{MC,DP}}(i) + (1-\alpha) N_A^{\mathrm{MC,F}}(i)\right) \tag{7.4}$$

and α is the free parameter in the fit. To be consistent, the optimisation of the admixture of the two components should be done simultaneously with the background subtraction since the signal leakage fractions ϵ_K also depend on the admixture.

However, such a procedure would result in an estimated signal yield which would depend on the fitted variable. To obtain a signal yield independent of the observable, except for statistical fluctuations, the background subtraction was performed using the default admixture of the two components and a systematic uncertainty on the background subtraction due to this admixture was included (see Chapter 9).

The χ^2 distributions for each observable are shown in Figs. 7.10 and 7.11. As can be seen in Fig. 7.8(e) and 7.8(f), the shape of the $|Y^{\rm jet}_{\rm lead}|$ distributions is approximately constant and provides little sensitivity to the two prompt-photon components. Therefore, no fit was attempted for this observable and the α value obtained from the $P^{\rm jet}_{T,{\rm lead}}$ data distribution was used instead.

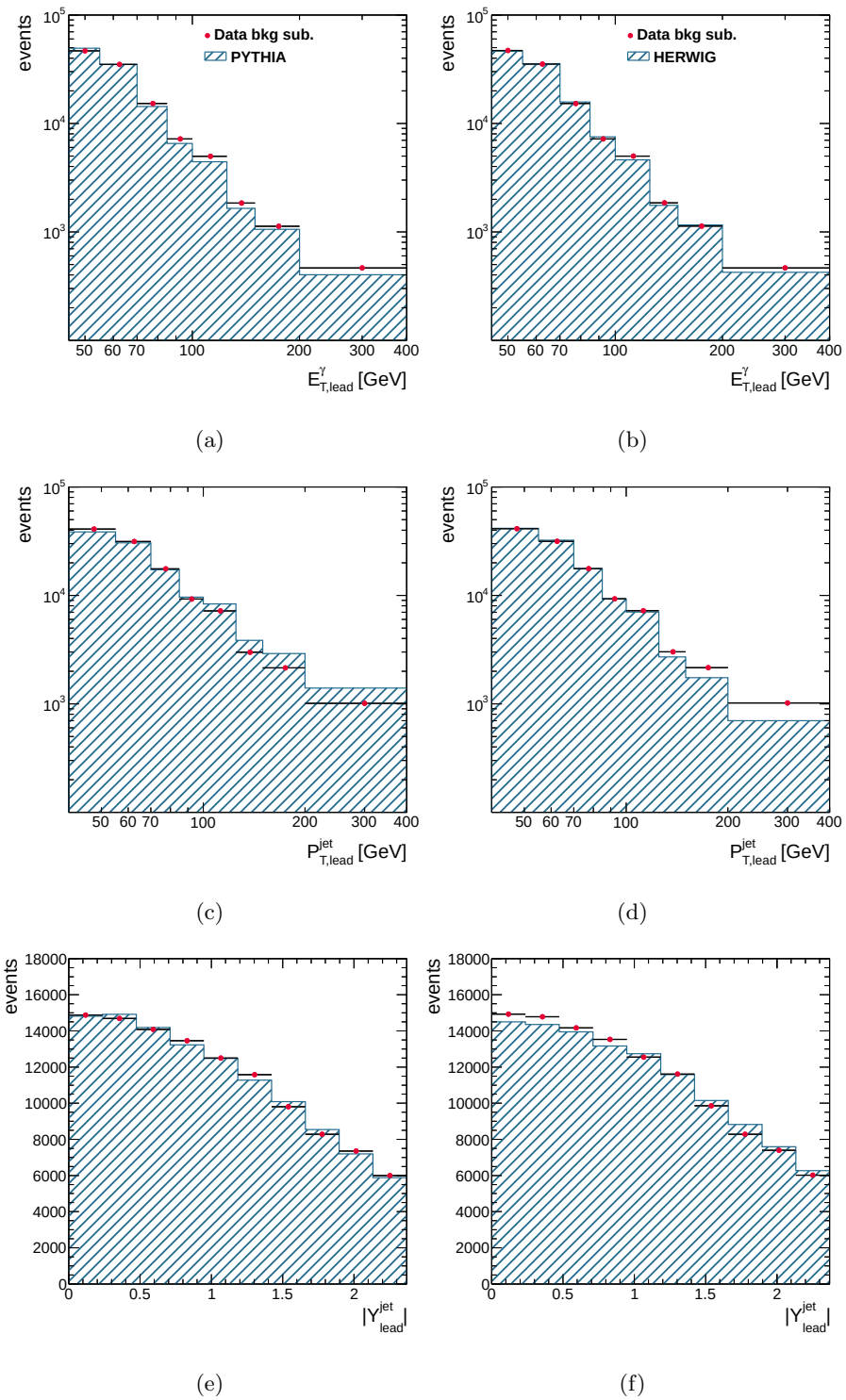

Figure 7.6: The estimated signal yield in data (dots) using signal leakage fractions from PYTHIA (a,c,e) or HERWIG (b,d,f) as functions of (a,b) $E^{\gamma}_{T,\mathrm{lead}}$, (c,d) $P^{\mathrm{jet}}_{T,\mathrm{lead}}$ and (e,f) $|Y^{\mathrm{jet}}_{\mathrm{lead}}|$. For comparison, the MC simulations of the signal from PYTHIA (hatched histogram (a,c,e)) and HERWIG (hatched histograms in (b,d,f)) are also included. The MC distributions are normalised to the total number of data events.

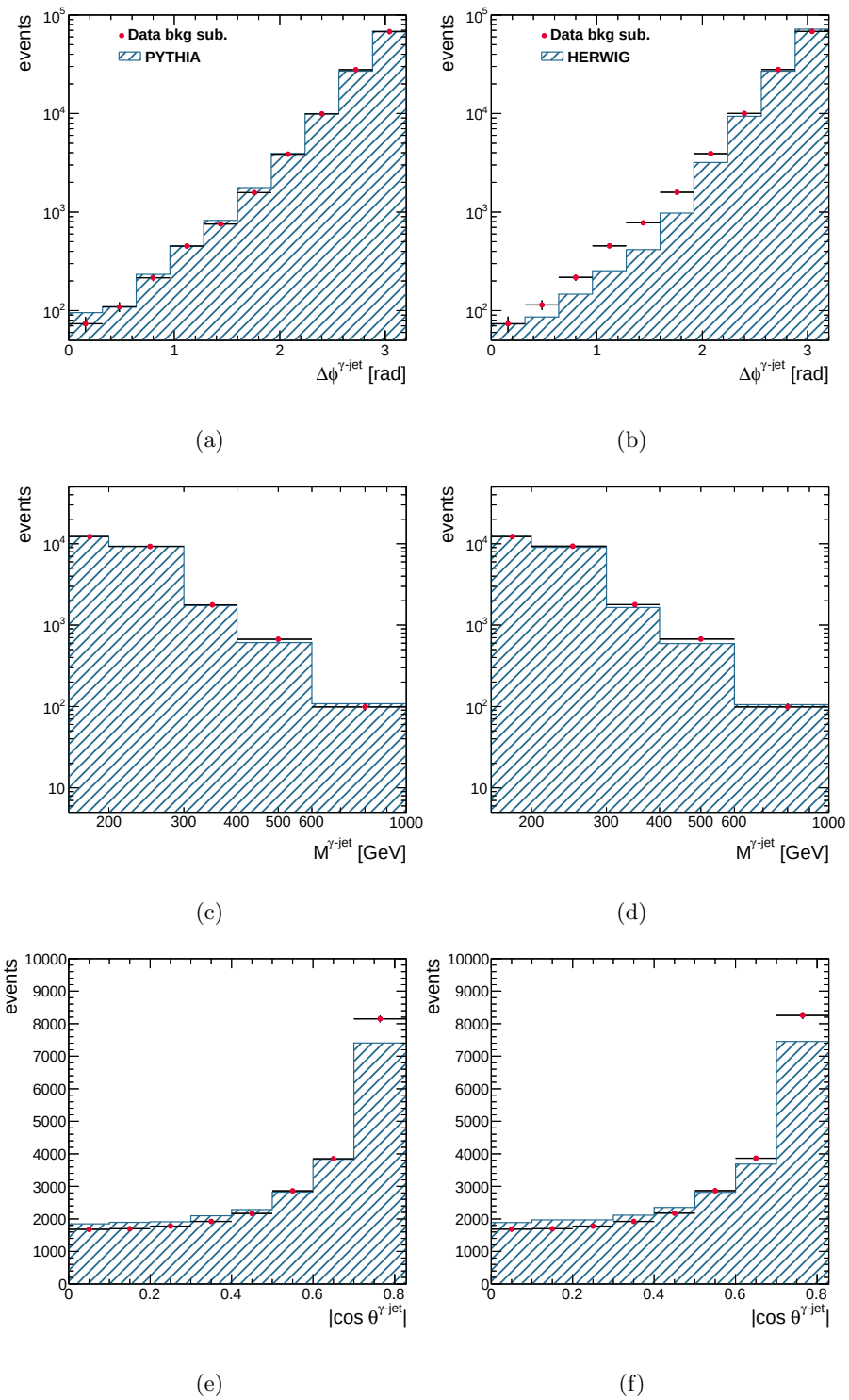

Figure 7.7: The estimated signal yield in data (dots) using signal leakage fractions from PYTHIA (a,c,e) or HERWIG (b,d,f) as functions of (a,b) $\Delta\phi^{\gamma-\text{jet}}$, (c,d) $M^{\gamma-\text{jet}}$ and (e,f) $|\cos\,\theta^{\gamma-\text{jet}}|$. For comparison, the MC simulations of the signal from PYTHIA (hatched histogram (a,c,e)) and HERWIG (hatched histograms in (b,d,f)) are also included. The MC distributions are normalised to the total number of data events.

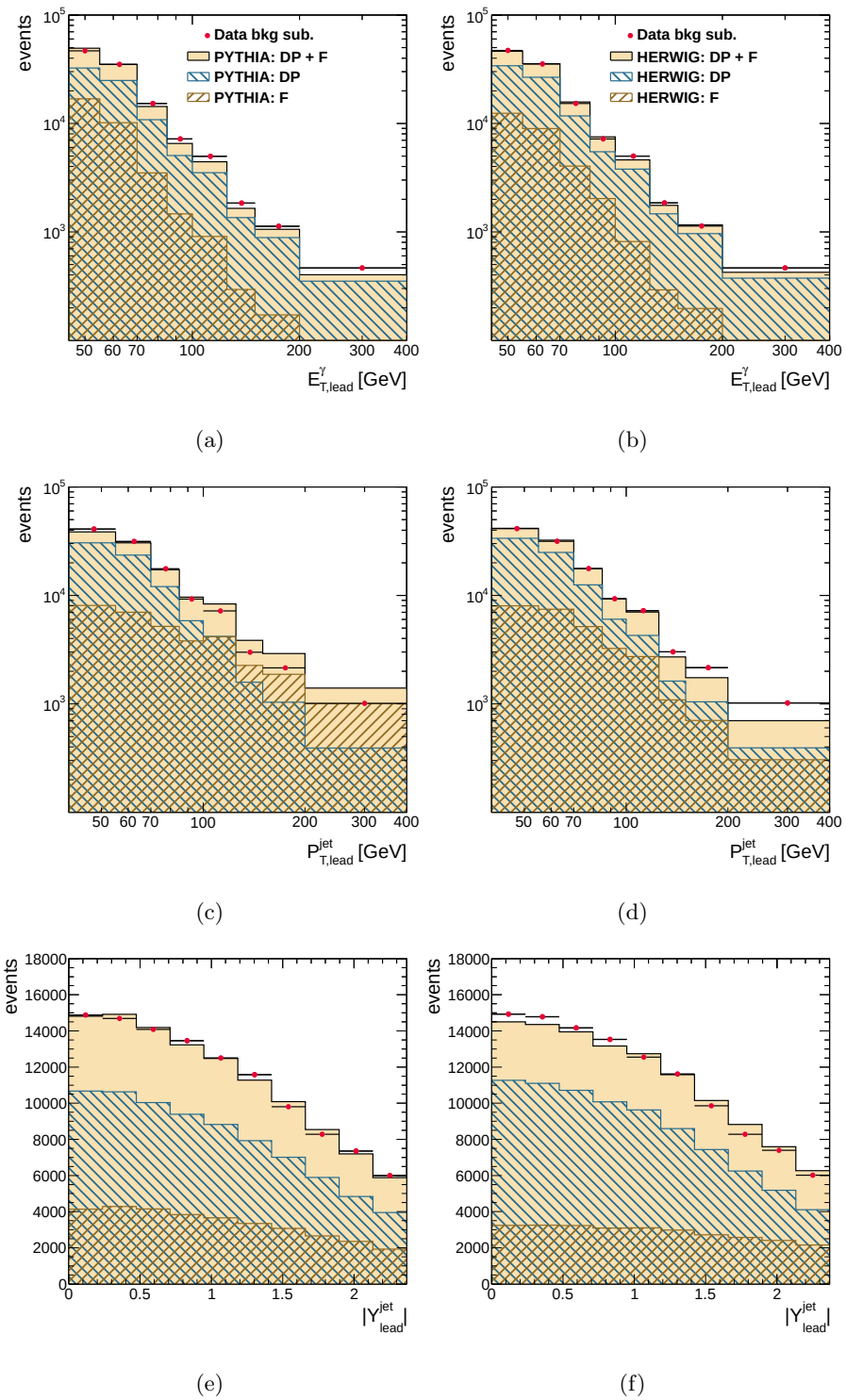

Figure 7.8: The estimated signal yield in data (dots) using signal leakage fractions from PYTHIA (a,c,e) or HERWIG (b,d,f) as functions of (a,b) $E^{\gamma}_{T,\mathrm{lead}}$, (c,d) $P^{\mathrm{jet}}_{T,\mathrm{lead}}$ and (e,f) $|Y^{\mathrm{jet}}_{\mathrm{lead}}|$. For comparison, the MC simulations of the signal from PYTHIA (dashed histograms in (a,c,e)) and HERWIG (dashed histograms in (b,d,f)) are also included. The MC distributions are normalised to the total number of data events. The direct-photon (right-hatched histograms) and fragmentation (left-hatched histograms) components of the MC simulations are also shown.

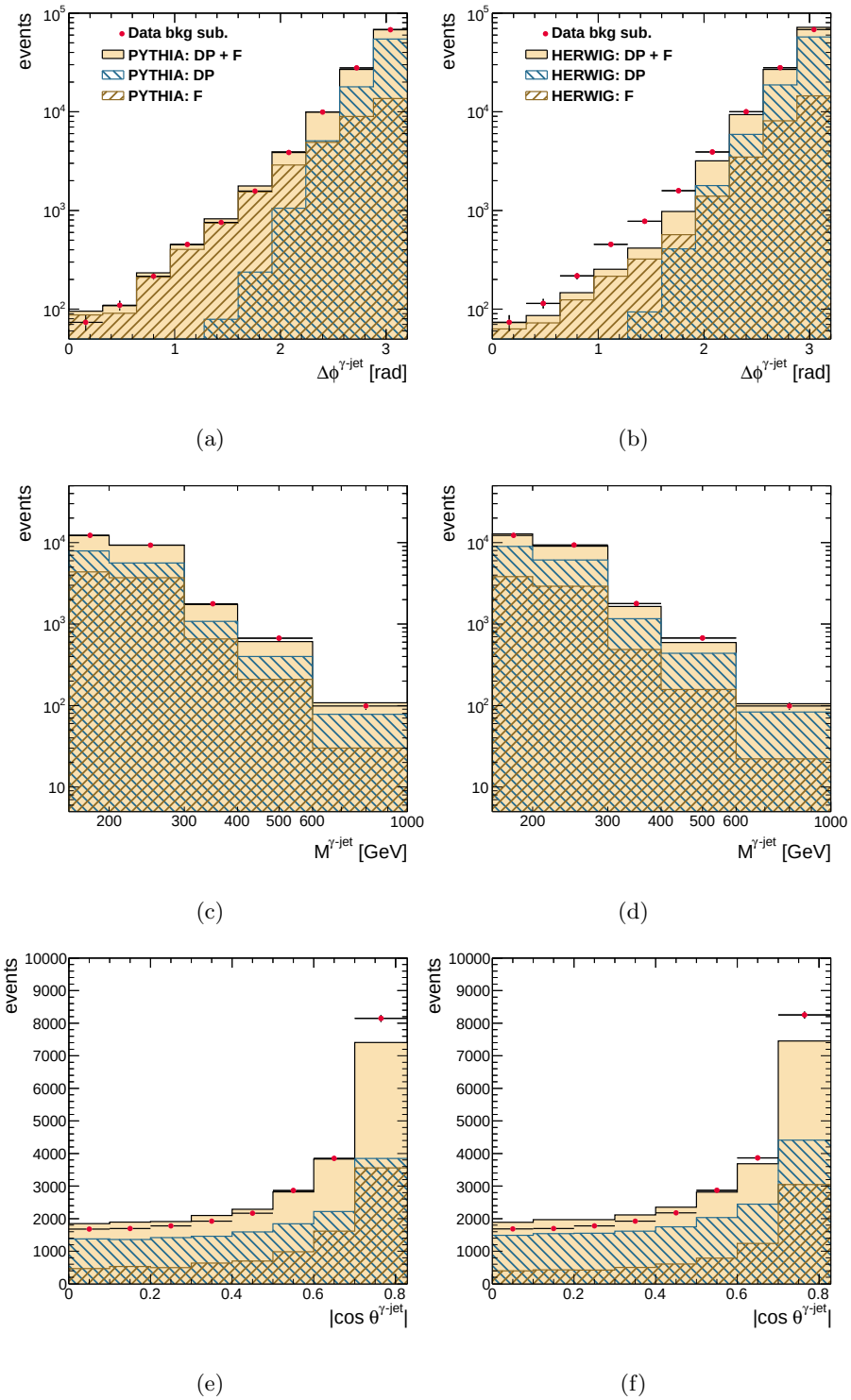

Figure 7.9: The estimated signal yield in data (dots) using signal leakage fractions from PYTHIA (a,c,e) or HERWIG (b,d,f) as functions of (a,b) $\Delta\phi^{\gamma-\mathrm{jet}}$, (c,d) $M^{\gamma-\mathrm{jet}}$ and (e,f) $|\cos\,\theta^{\gamma-\mathrm{jet}}|$. For comparison, the MC simulations of the signal from PYTHIA (dashed histograms in (a,c,e)) and HERWIG (dashed histograms in (b,d,f)) are also included. The MC distributions are normalised to the total number of data events. The direct-photon (right-hatched histograms) and fragmentation (left-hatched histograms) components of the MC simulations are also shown.

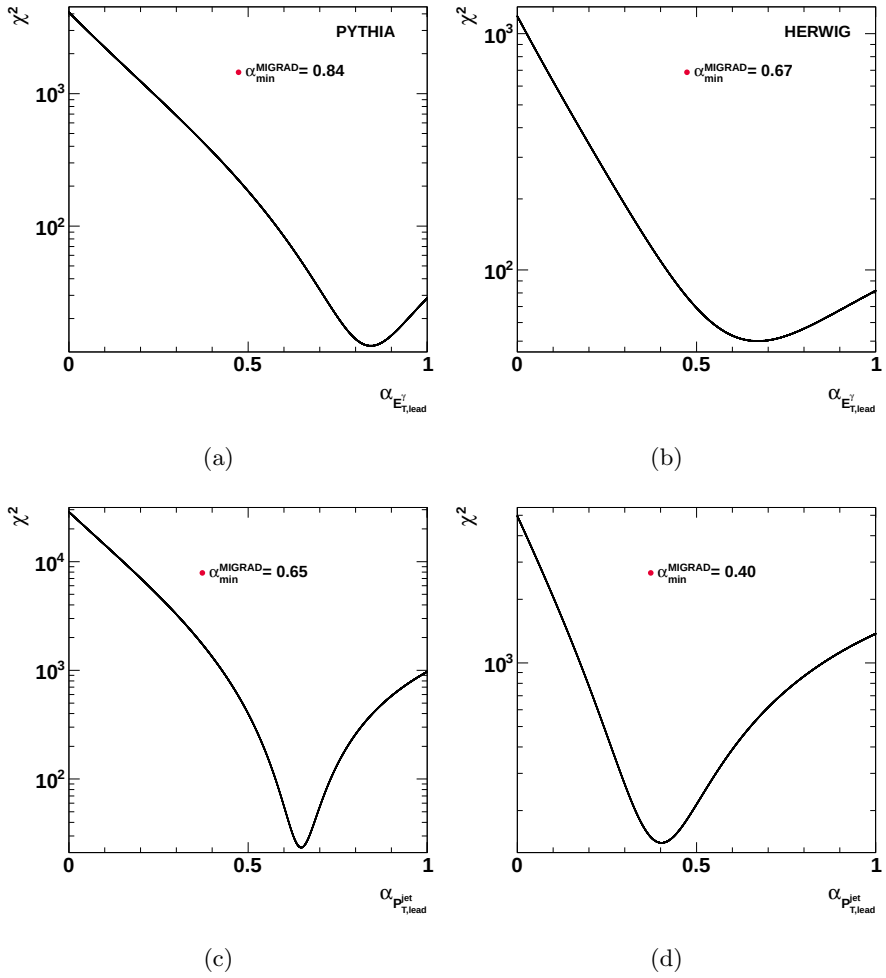

Figure 7.10: The χ^2 distributions from the fit to the data distributions as functions of (a) $E_{T,\mathrm{lead}}^{\gamma}$ and (c) $P_{T,\mathrm{lead}}^{\mathrm{jet}}$ for the PYTHIA samples. The χ^2 distributions resulting from the fit to the data distributions as functions of (b) $E_{T,\mathrm{lead}}^{\gamma}$ and (d) $P_{T,\mathrm{lead}}^{\mathrm{jet}}$ for the HERWIG samples.

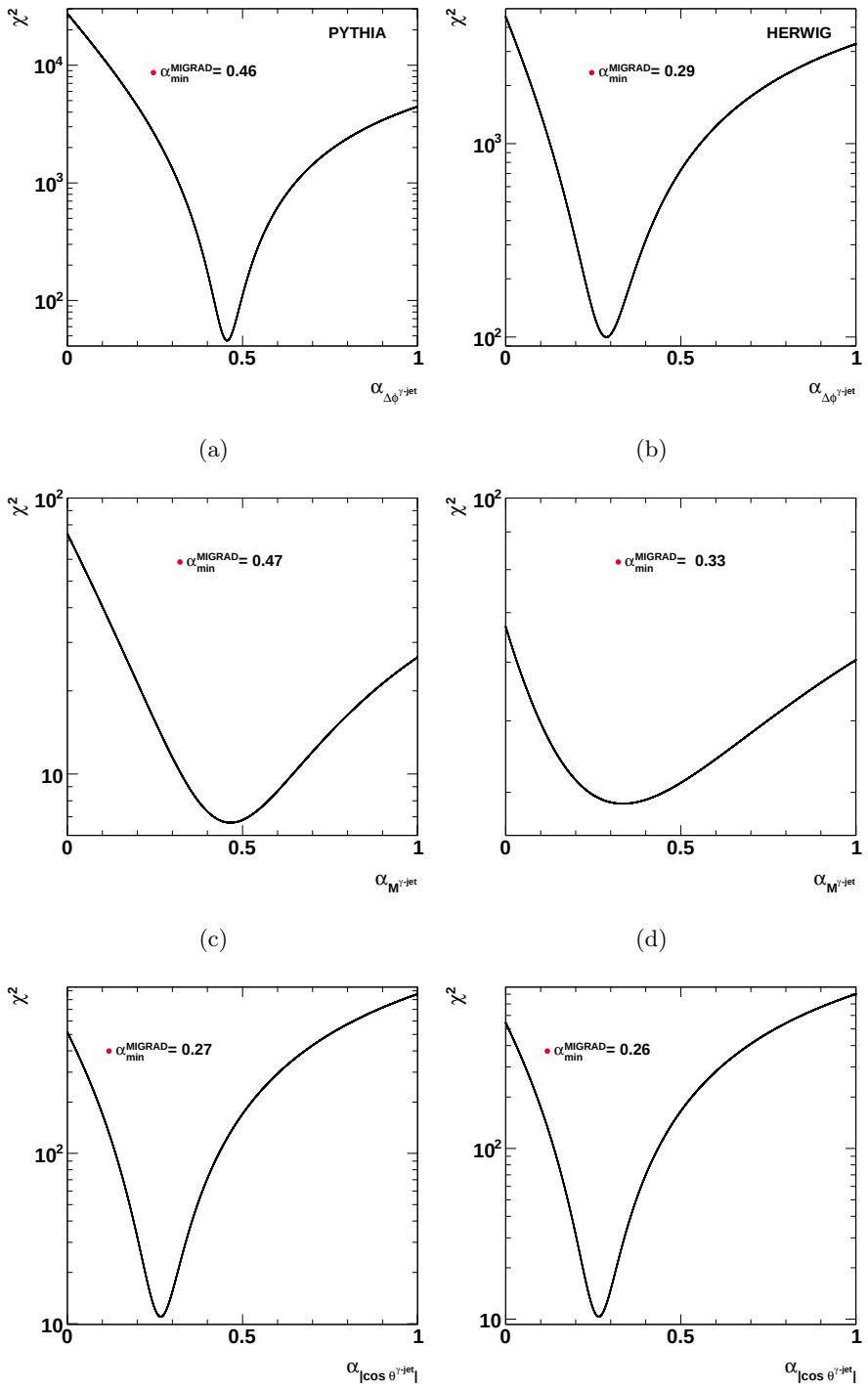

Figure 7.11: The χ^2 distributions from the fit to the data distributions as functions of (a) $\Delta\phi^{\gamma-\text{jet}}$, (c) $M^{\gamma-\text{jet}}$ and (e) $|\cos\,\theta^{\gamma-\text{jet}}|$ for the PYTHIA samples. The χ^2 distributions resulting from the fit to the data distributions as functions of (b) $\Delta\phi^{\gamma-\text{jet}}$, (d) $M^{\gamma-\text{jet}}$ and (f) $|\cos\,\theta^{\gamma-\text{jet}}|$ for the HERWIG samples.

7.2.1 Comparison between background-subtracted data and optimised MC

Figures 7.12 and 7.13 show the data distributions for the six observables studied after background subtraction (using the default admixture of the components in the MC) compared to the MC simulations of PYTHIA and HERWIG, after optimising the admixture of the two prompt-photon components. A good description of the data is obtained by both PYTHIA and HERWIG MC simulations for all signal observables.

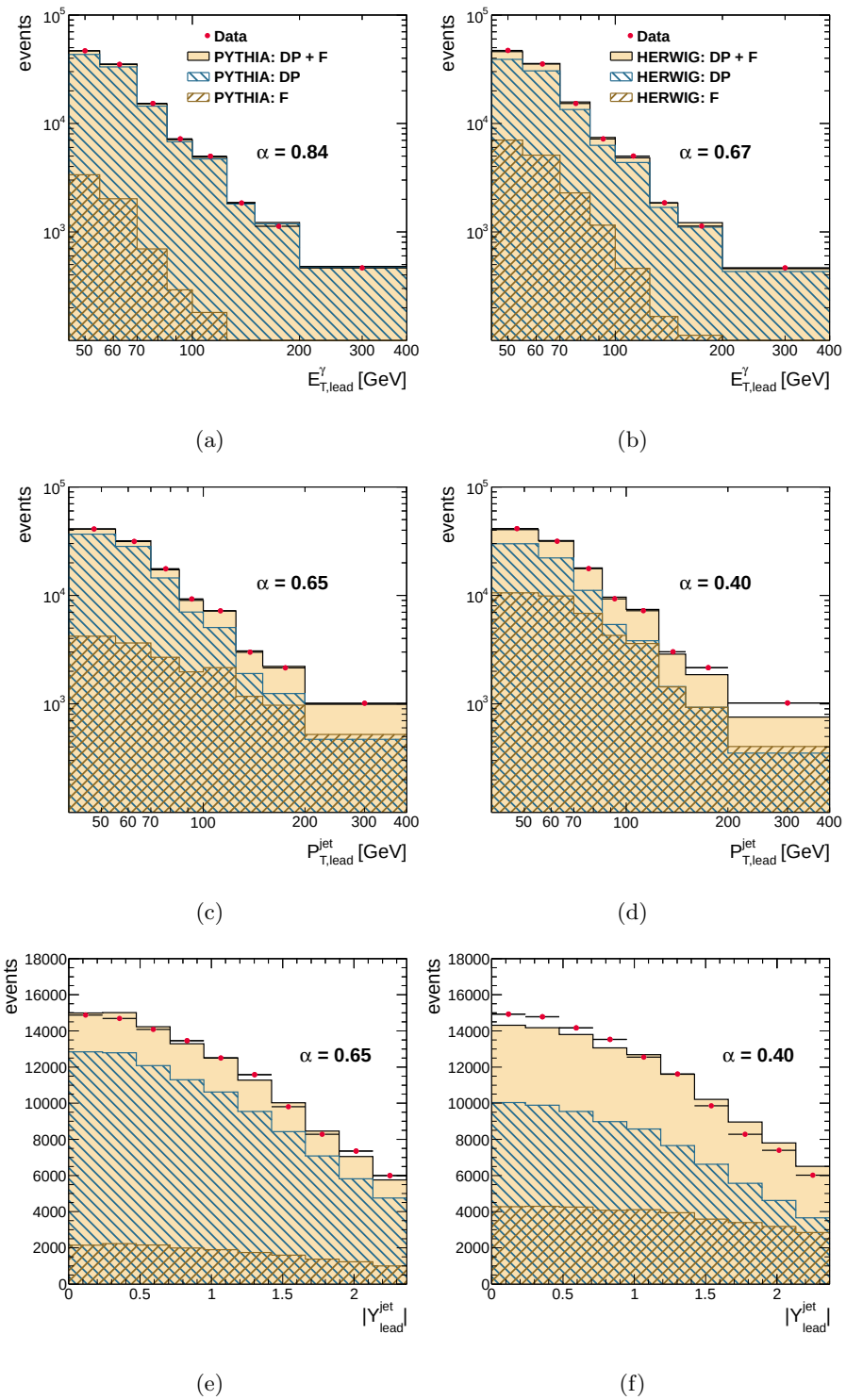

Figure 7.12: The estimated signal yield in data (dots) using signal leakage fractions from PYTHIA (a,c,e) or HERWIG (b,d,f) as functions of (a,b) $E^{\gamma}_{T,\mathrm{lead}}$, (c,d) $P^{\mathrm{jet}}_{T,\mathrm{lead}}$ and (e,f) $|Y^{\mathrm{jet}}_{\mathrm{lead}}|$. For comparison, the MC simulations of the signal from PYTHIA (dashed histograms in (a,c,e)) and HERWIG (dashed histograms in (b,d,f)) using the corresponding optimal admixture of direct-photon and fragmentation components are also included. The MC distributions are normalised to the total number of data events. The direct-photon (right-hatched histograms) and fragmentation (left-hatched histograms) components of the MC simulations are also shown.

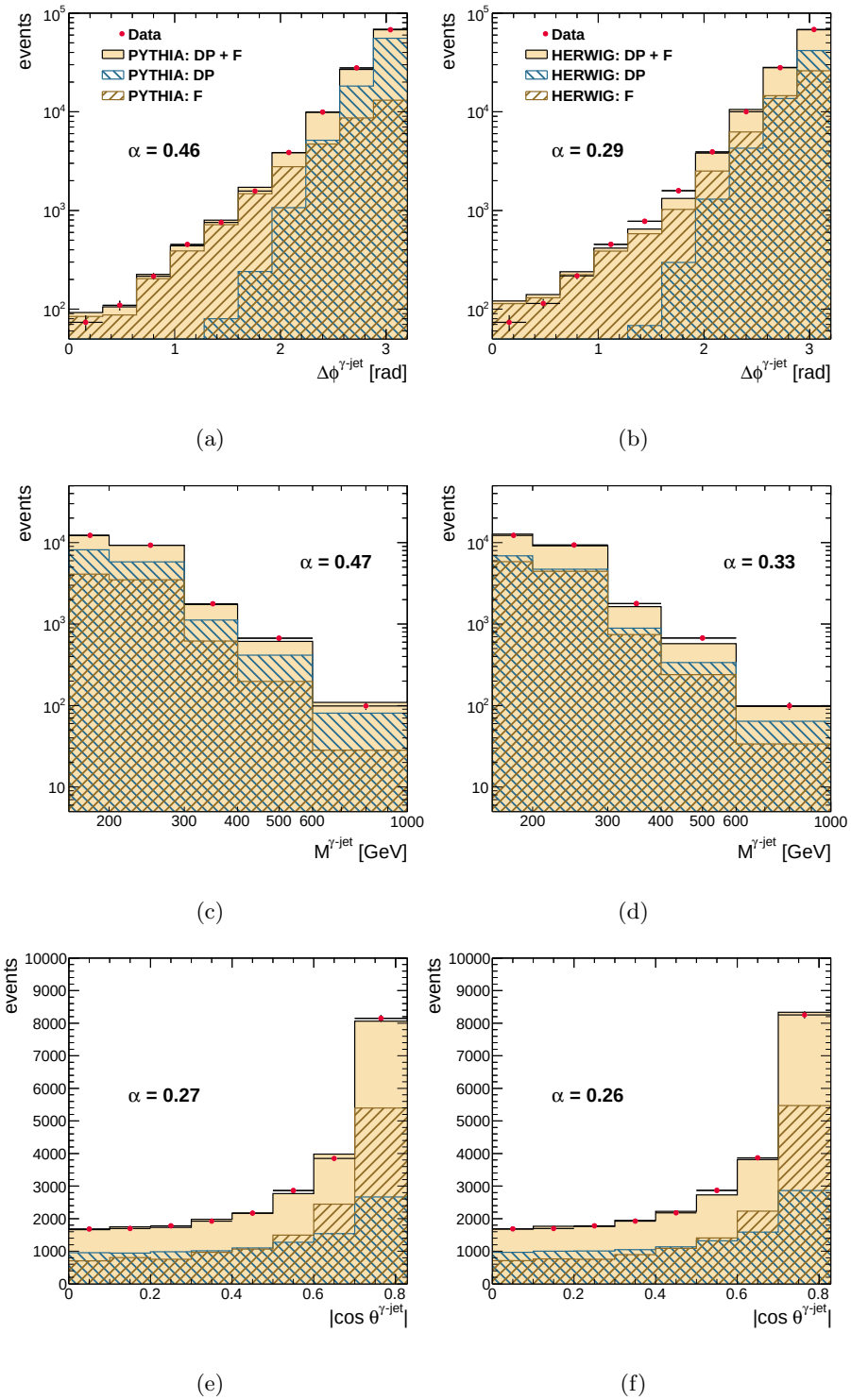

Figure 7.13: The estimated signal yield in data (dots) using signal leakage fractions from PYTHIA (a,c,e) or HERWIG (b,d,f) as functions of (a,b) $\Delta\phi^{\gamma-\mathrm{jet}}$, (c,d) $M^{\gamma-\mathrm{jet}}$ and (e,f) $|\cos\,\theta^{\gamma-\mathrm{jet}}|$. For comparison, the MC simulations of the signal from PYTHIA (dashed histograms in (a,c,e)) and HERWIG (dashed histograms in (b,d,f)) using the corresponding optimal admixture of direct-photon and fragmentation components are also included. The MC distributions are normalised to the number of data events.The direct-photon (right-hatched histograms) and fragmentation (left-hatched histograms) components of the MC simulations are also shown.

Chapter 8

Efficiencies and acceptance corrections

The efficiency of the selection criteria used to extract the signal is discussed in this chapter. It is focused in three main aspects

- trigger efficiency;
- selection efficiency;
- jet-quality cut efficiency.

To calculate the cross section at hadronic level, the data must be corrected with a factor to compensate for detector effects. This is done via the acceptance correction factors which are defined in the last part of the chapter.

8.1 Signal efficiency

The photon trigger and selection efficiencies were determined from the Monte Carlo simulated signal samples. Whenever possible, efficiencies were estimated using data-driven methods. The following efficiencies in this analysis were evaluated:

- the photon trigger efficiency;
- the selection efficiency;
- the jet-quality cut efficiency.

8.1.1 Trigger efficiency

The efficiency of the calorimeter trigger relative to the photon reconstruction and offline selection is defined as the probability of a true prompt photon to pass the

"g40_loose" trigger selection, where the true prompt photon is reconstructed with isolation transverse energy lower than 3 GeV and satisfies the tight photon identification criteria.

The efficiency of the trigger selection for photons fulfilling the requirements was evaluated using data in two steps: (a) the efficiency of the high-level trigger "EF_g40_loose" was measured with respect to that of the level 1 trigger "L1_EM14" using events collected with the HLT set in passthrough mode; (b) the efficiency of the "L1_EM14" trigger was measured with respect to that of the lower threshold "L1_EM5" trigger using events collected with "L1_EM5" where the HLT chains are in passthrough mode for both L1 EM triggers. Using events collected with minimum bias triggers it was checked that the efficiency of the "L1_EM5" trigger was 100% for photons with transverse energies above 10 GeV. The product of the two efficiencies mentioned above represents the overall trigger efficiency for those photons fulfilling the offline selection criteria and is found to be consistent with 100% for photons with transverse energies above 43 GeV. In particular, the efficiency of "EF_g40_loose" relative to "L1_EM14" for photons with transverse energies above 45 GeV is $99.87 \pm 0.01 \pm 0.10\%$. The combined (L1+EF) efficiency is measured to be $99.6 \pm 0.08 \pm 0.25\%$ (see Fig. 6.2).

8.1.2 Selection efficiency

The quality of the reconstruction of the signal was evaluated using the MC samples. To asses the quality of the reconstruction of the variables studied, the reconstructed and true observables were compared in an event-by-event basis.

A MC generated event was required to fulfill both the requirements at the reconstruction and true levels. The true- and detector-level leading jets were required to be matched ($\Delta R \leq 0.6$).

Figures 8.1 to 8.12 show the correlation between the detector- and true-level values for the six observables using the samples of PYTHIA and HERWIG, separately for the direct-photon and fragmentation components. A very good reconstruction quality is obtained for all variables. However, the reconstruction of the leading-jet transverse momentum seems to overestimate that of the true level; it should be noted that the standard jet calibration refers to particle jets with muons and neutrinos being excluded and to the specific admixture of quarks- and gluon-initiated jets in QCD dijet processes. These differences in the particle jet definition are accounted for through the acceptance corrections. The increase in the first bin of the profiles

in Figs. 8.9(e,f) and 8.10(e,f) is an artifact of the jet selection at detector level.

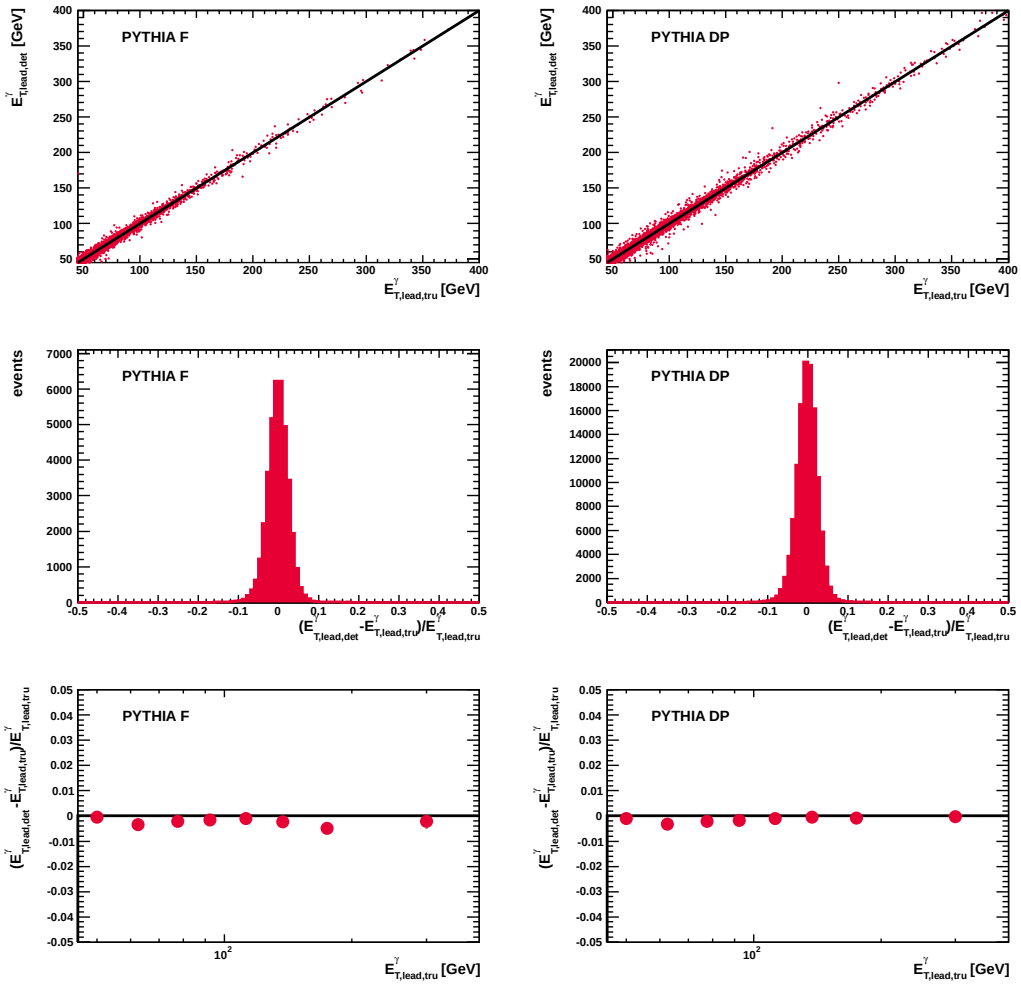

Figure 8.1: (a,b) $(E^{\gamma}_{T,\mathrm{lead}})_{\mathrm{rec}}$ vs. $(E^{\gamma}_{T,\mathrm{lead}})_{\mathrm{truth}}$ correlation; (c,d) $[(E^{\gamma}_{T,\mathrm{lead}})_{\mathrm{rec}}$-$(E^{\gamma}_{T,\mathrm{lead}})_{\mathrm{truth}}]/(E^{\gamma}_{T,\mathrm{lead}})_{\mathrm{truth}}$ distribution; and (e,f) average of $[(E^{\gamma}_{T,\mathrm{lead}})_{\mathrm{rec}}$-$(E^{\gamma}_{T,\mathrm{lead}})_{\mathrm{truth}}]/(E^{\gamma}_{T,\mathrm{lead}})_{\mathrm{truth}}$ as a function of $(E^{\gamma}_{T,lead})_{\mathrm{truth}}$. The results are shown for PYTHIA MC fragmentation (left) and direct-photon (right) events.

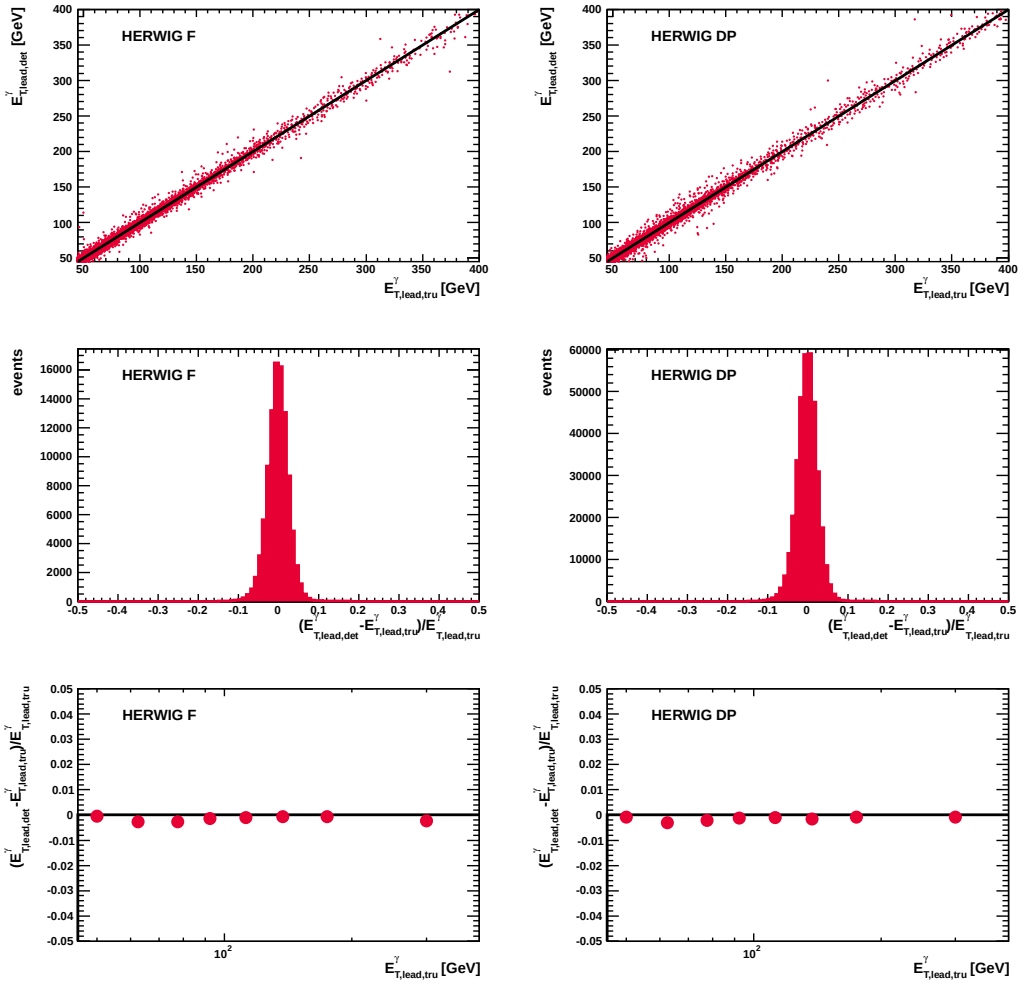

Figure 8.2: (a,b) $(E^{\gamma}_{T,\mathrm{lead}})_{\mathrm{rec}}$ vs. $(E^{\gamma}_{T,\mathrm{lead}})_{\mathrm{truth}}$ correlation; (c,d) $[(E^{\gamma}_{T,\mathrm{lead}})_{\mathrm{rec}}$-$(E^{\gamma}_{T,\mathrm{lead}})_{\mathrm{truth}}]/(E^{\gamma}_{T,\mathrm{lead}})_{\mathrm{truth}}$ distribution; and (e,f) average of $[(E^{\gamma}_{T,\mathrm{lead}})_{\mathrm{rec}}$-$(E^{\gamma}_{T,\mathrm{lead}})_{\mathrm{truth}}]/(E^{\gamma}_{T,\mathrm{lead}})_{\mathrm{truth}}$ as a function of $(E^{\gamma}_{T,\mathrm{lead}})_{\mathrm{truth}}$. The results are shown for HERWIG MC fragmentation (left) and direct-photon (right) events.

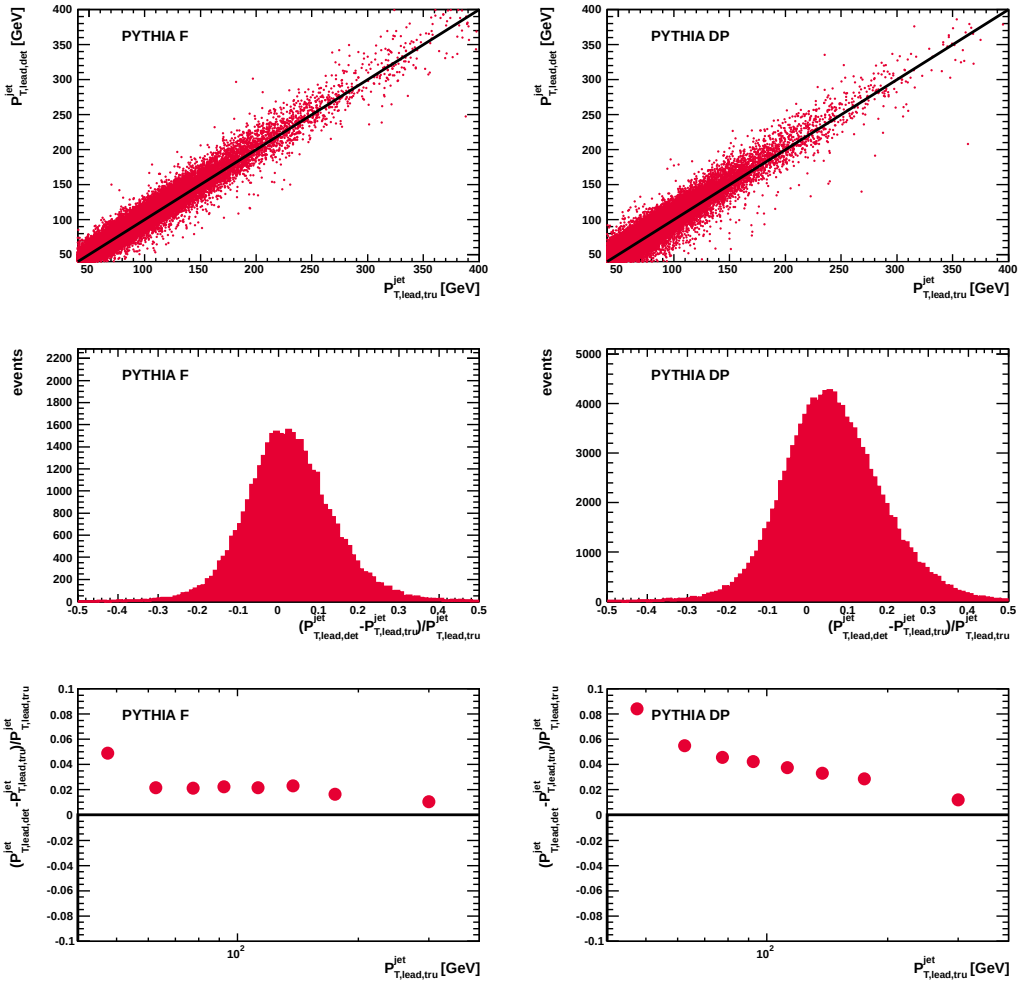

Figure 8.3: (a,b) $(P^{\rm jet}_{T,\rm lead})_{\rm rec}$ vs. $(P^{\rm jet}_{T,\rm lead})_{\rm truth}$ correlation; (c,d) $[(P^{\rm jet}_{T,\rm lead})_{\rm rec}$-$(P^{\rm jet}_{T,\rm lead})_{\rm truth}]/(P^{\rm jet}_{T,\rm lead})_{\rm truth}$ distribution; and (e,f) average of $[(P^{\rm jet}_{T,\rm lead})_{\rm rec}$-$(P^{\rm jet}_{T,\rm lead})_{\rm truth}]/(P^{\rm jet}_{T,\rm lead})_{\rm truth}$ as a function of $(P^{\rm jet}_{T,\rm lead})_{\rm truth}$. The results are shown for PYTHIA MC fragmentation (left) and direct-photon (right) events.

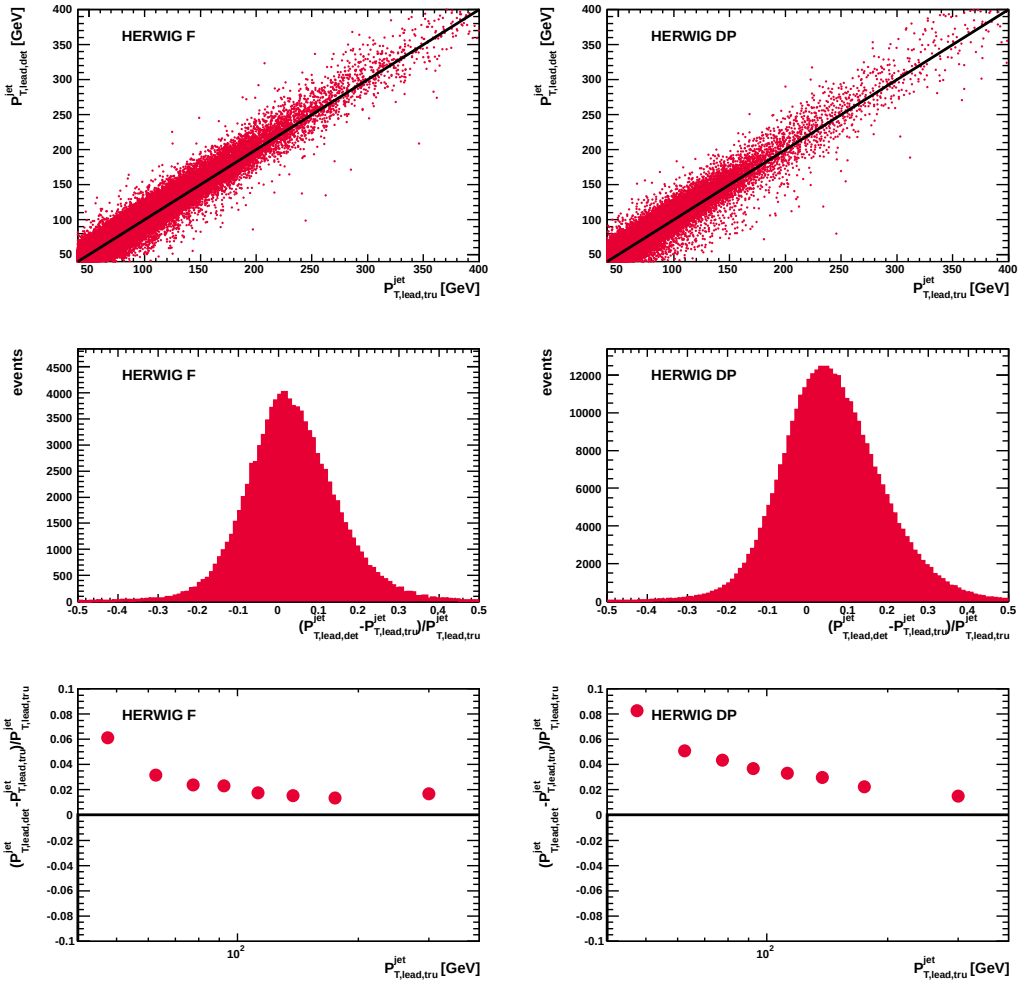

Figure 8.4: (a,b) $(P^{\rm jet}_{T,\rm lead})_{\rm rec}$ vs. $(P^{\rm jet}_{T,\rm lead})_{\rm truth}$ correlation; (c,d) $[(P^{\rm jet}_{T,\rm lead})_{\rm rec}$-$(P^{\rm jet}_{T,\rm lead})_{\rm truth}]/(P^{\rm jet}_{T,\rm lead})_{\rm truth}$ distribution; and (e,f) average of $[(P^{\rm jet}_{T,\rm lead})_{\rm rec}$-$(P^{\rm jet}_{T,\rm lead})_{\rm truth}]/(P^{\rm jet}_{T,\rm lead})_{\rm truth}$ as a function of $(P^{\rm jet}_{T,\rm lead})_{\rm truth}$. The results are shown for HERWIG MC fragmentation (left) and direct-photon (right) events.

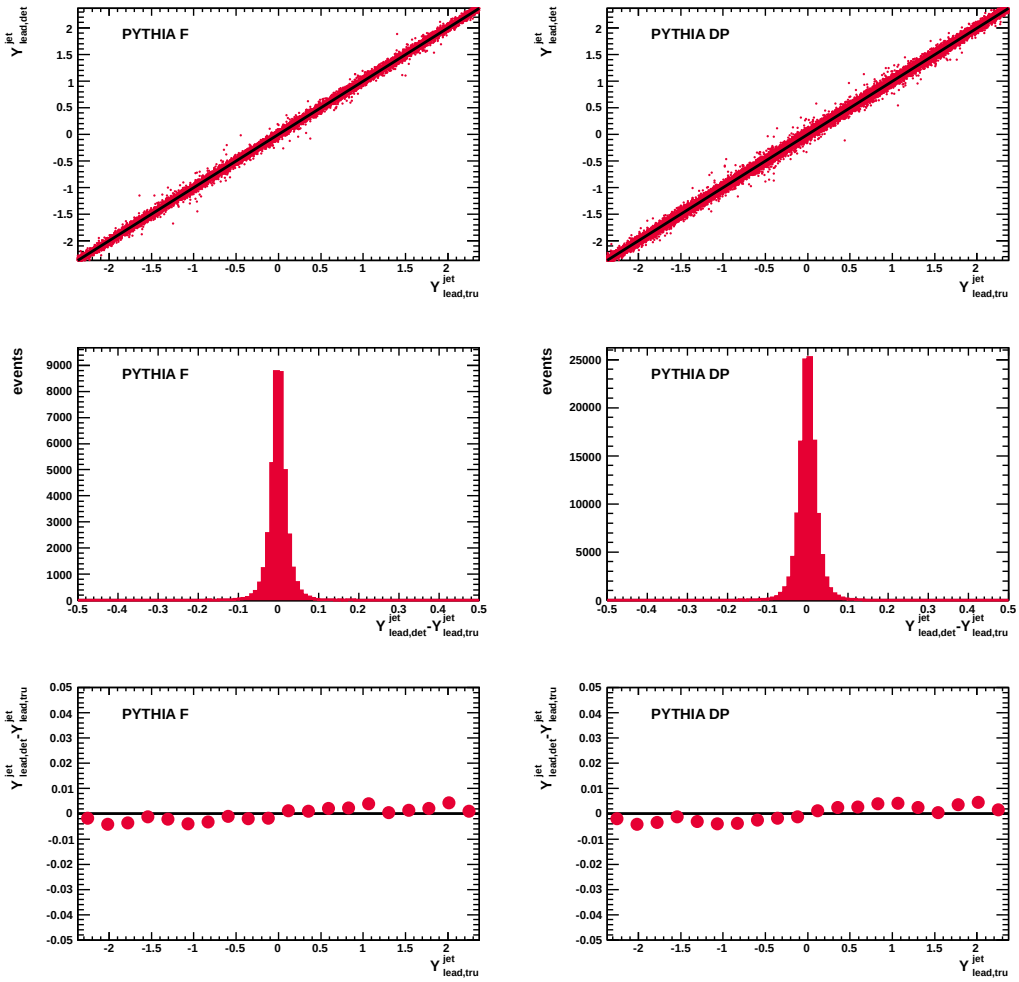

Figure 8.5: (a,b) $(Y^{\rm jet}_{\rm lead})_{\rm rec}$ vs. $(Y^{\rm jet}_{\rm lead})_{\rm truth}$ correlation; (c,d) $(Y^{\rm jet}_{\rm lead})_{\rm rec}$-$(Y^{\rm jet}_{\rm lead})_{\rm truth}$ distribution; and (e,f) average of $(Y^{\rm jet}_{\rm lead})_{\rm rec}$-$(Y^{\rm jet}_{\rm lead})_{\rm truth}$ as a function of $(Y^{\rm jet}_{\rm lead})_{\rm truth}$. The results are shown for PYTHIA MC fragmentation (left) and direct-photon (right) events.

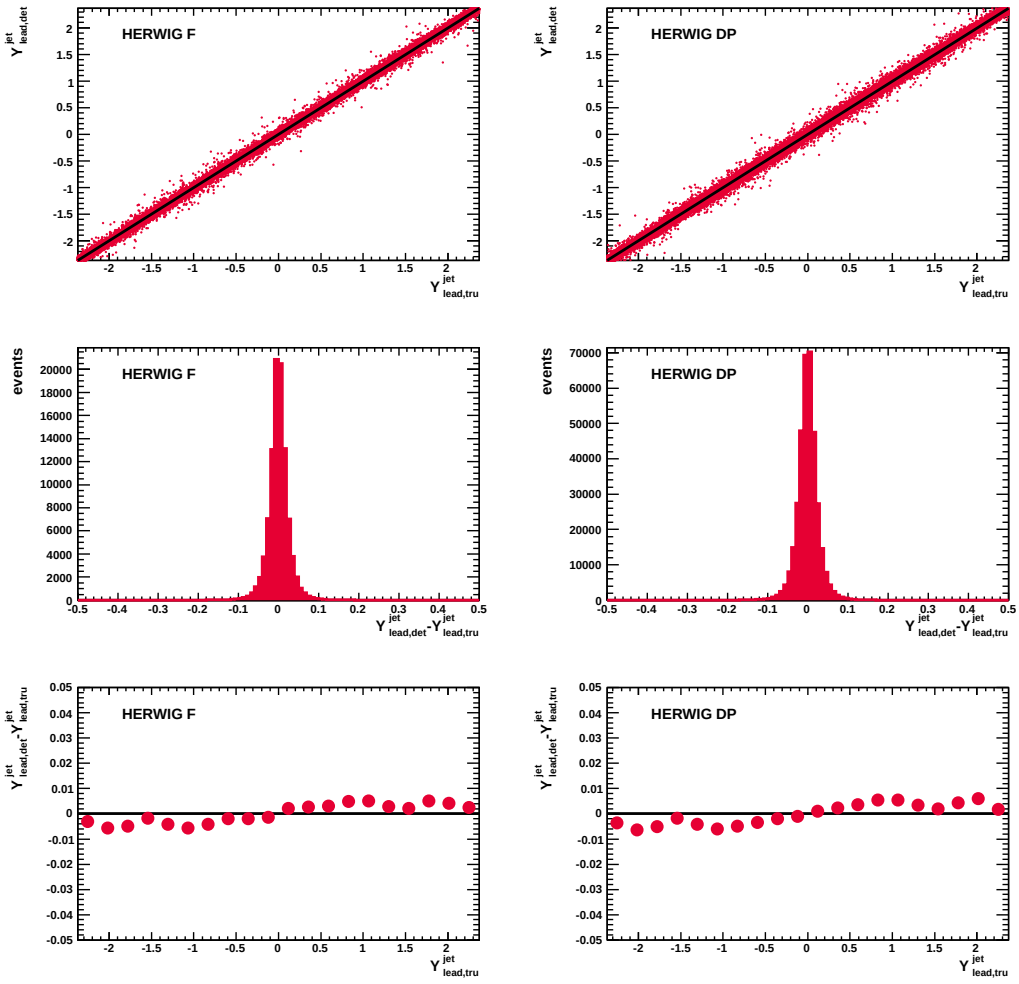

Figure 8.6: (a,b) $(Y^{\mathrm{jet}}_{\mathrm{lead}})_{\mathrm{rec}}$ vs. $(Y^{\mathrm{jet}}_{\mathrm{lead}})_{\mathrm{truth}}$ correlation; (c,d) $(Y^{\mathrm{jet}}_{\mathrm{lead}})_{\mathrm{rec}}$-$(Y^{\mathrm{jet}}_{\mathrm{lead}})_{\mathrm{truth}}$ distribution; and (e,f) average of $(Y^{\mathrm{jet}}_{\mathrm{lead}})_{\mathrm{rec}}$-$(Y^{\mathrm{jet}}_{\mathrm{lead}})_{\mathrm{truth}}$ as a function of $(Y^{\mathrm{jet}}_{\mathrm{lead}})_{\mathrm{truth}}$. The results are shown for HERWIG MC fragmentation (left) and direct-photon (right) events.

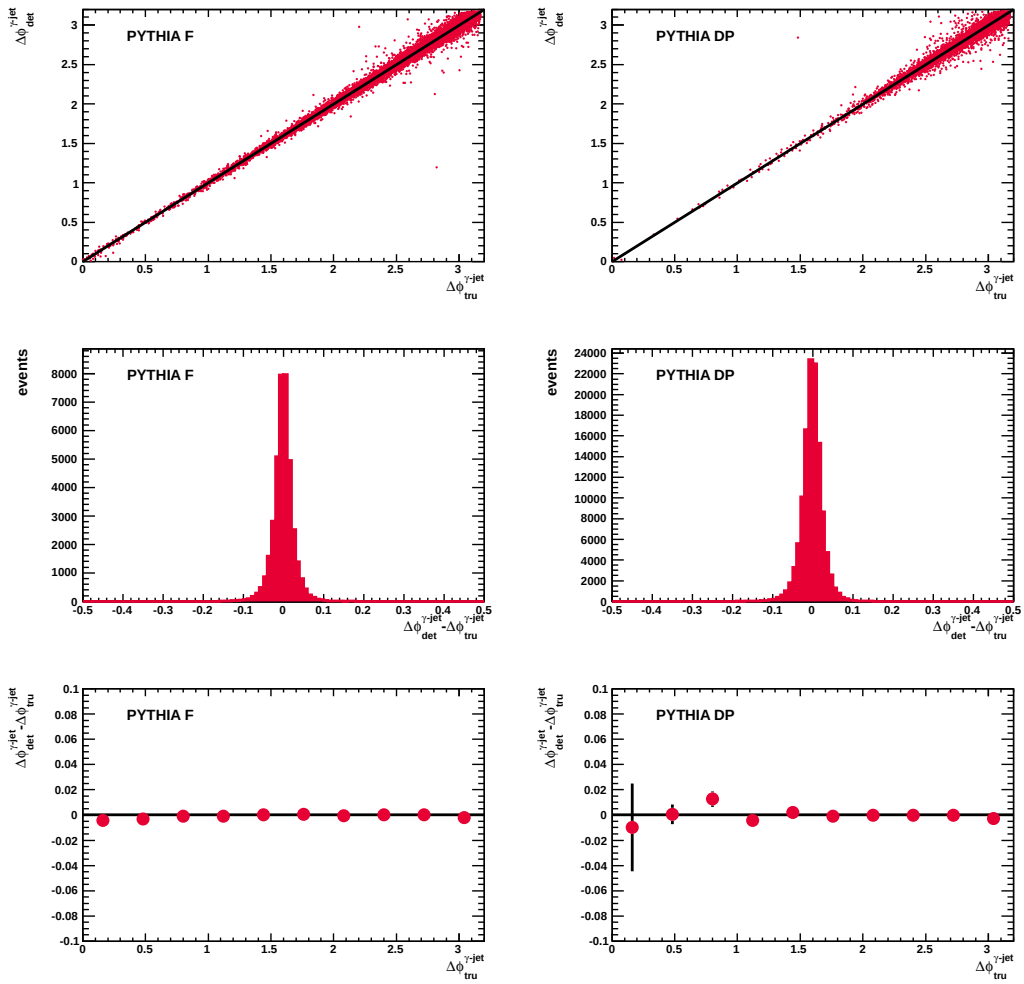

Figure 8.7: (a,b) $(\Delta\phi^{\gamma-\mathrm{jet}})_{\mathrm{rec}}$ vs. $(\Delta\phi^{\gamma-\mathrm{jet}})_{\mathrm{truth}}$ correlation; (c,d) $(\Delta\phi^{\gamma-\mathrm{jet}})_{\mathrm{rec}}$-$(\Delta\phi^{\gamma-\mathrm{jet}})_{\mathrm{truth}}$ distribution; and (e,f) average of $(\Delta\phi^{\gamma-\mathrm{jet}})_{\mathrm{rec}}$-$(\Delta\phi^{\gamma-\mathrm{jet}})_{\mathrm{truth}}$ as a function of $(\Delta\phi^{\gamma-\mathrm{jet}})_{\mathrm{truth}}$. The results are shown for PYTHIA MC fragmentation (left) and direct-photon (right) events.

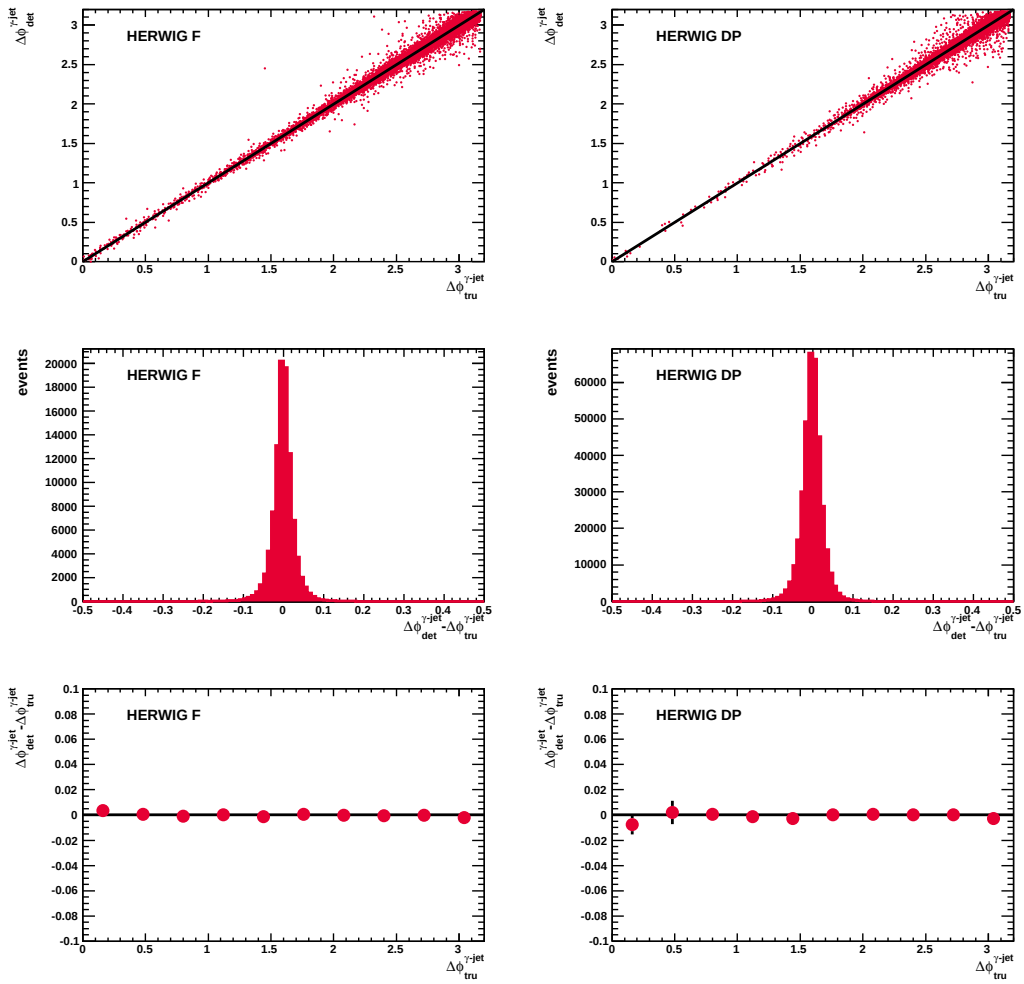

Figure 8.8: (a,b) $(\Delta\phi^{\gamma-\mathrm{jet}})_{\mathrm{rec}}$ vs. $(\Delta\phi^{\gamma-\mathrm{jet}})_{\mathrm{truth}}$ correlation; (c,d) $(\Delta\phi^{\gamma-\mathrm{jet}})_{\mathrm{rec}}$-$(\Delta\phi^{\gamma-\mathrm{jet}})_{\mathrm{truth}}$ distribution; and (e,f) average of $(\Delta\phi^{\gamma-\mathrm{jet}})_{\mathrm{rec}}$-$(\Delta\phi^{\gamma-\mathrm{jet}})_{\mathrm{truth}}$ as a function of $(\Delta\phi^{\gamma-\mathrm{jet}})_{\mathrm{truth}}$. The results are shown for HERWIG MC fragmentation (left) and direct-photon (right) events.

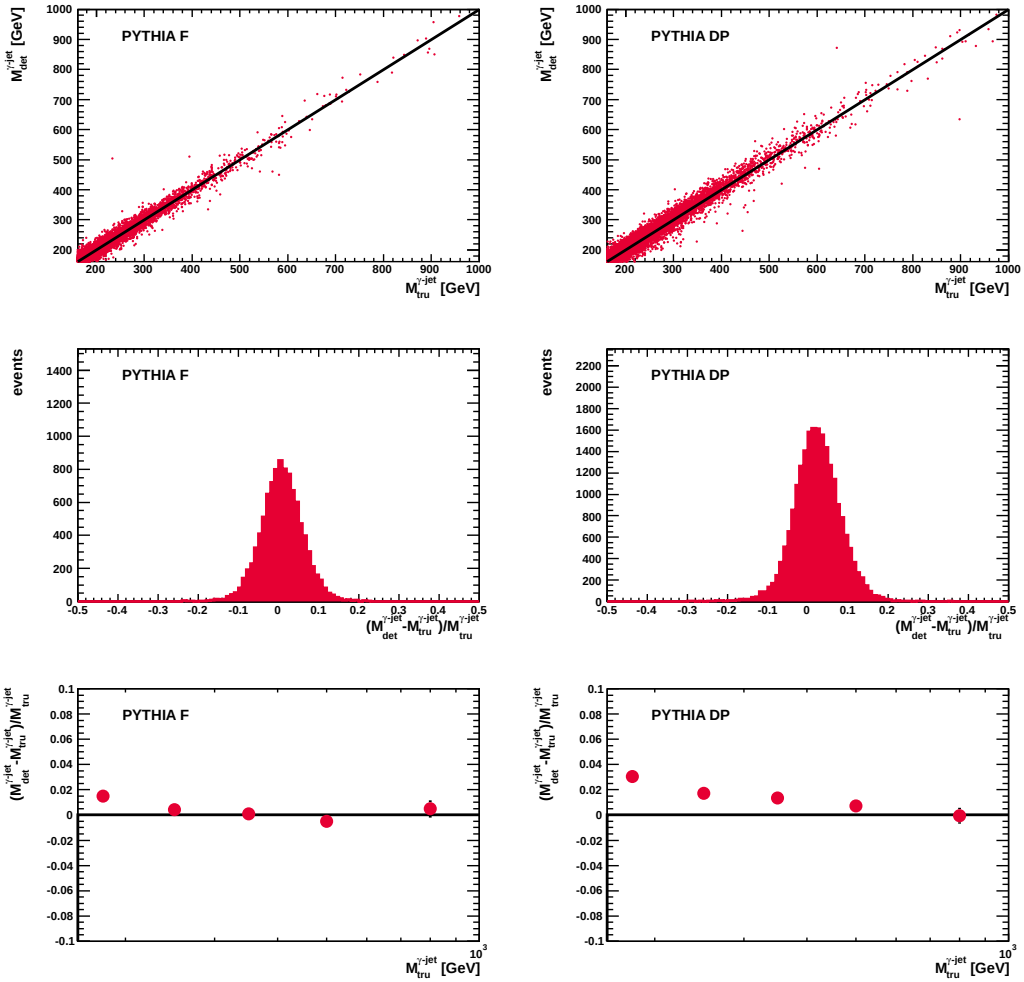

Figure 8.9: (a,b) $(M^{\gamma-\mathrm{jet}})_{\mathrm{rec}}$ vs. $(M^{\gamma-\mathrm{jet}})_{\mathrm{truth}}$ correlation; (c,d) $[(M^{\gamma-\mathrm{jet}})_{\mathrm{rec}}$-$(M^{\gamma-\mathrm{jet}})_{\mathrm{truth}}]/(M^{\gamma-\mathrm{jet}})_{\mathrm{truth}}$ distribution; and (e,f) average of $[(M^{\gamma-\mathrm{jet}})_{\mathrm{rec}}$-$(M^{\gamma-\mathrm{jet}})_{\mathrm{truth}}]/(M^{\gamma-\mathrm{jet}})_{\mathrm{truth}}$ as a function of $(M^{\gamma-\mathrm{jet}})_{\mathrm{truth}}$. The results are shown for PYTHIA MC fragmentation (left) and direct-photon (right) events.

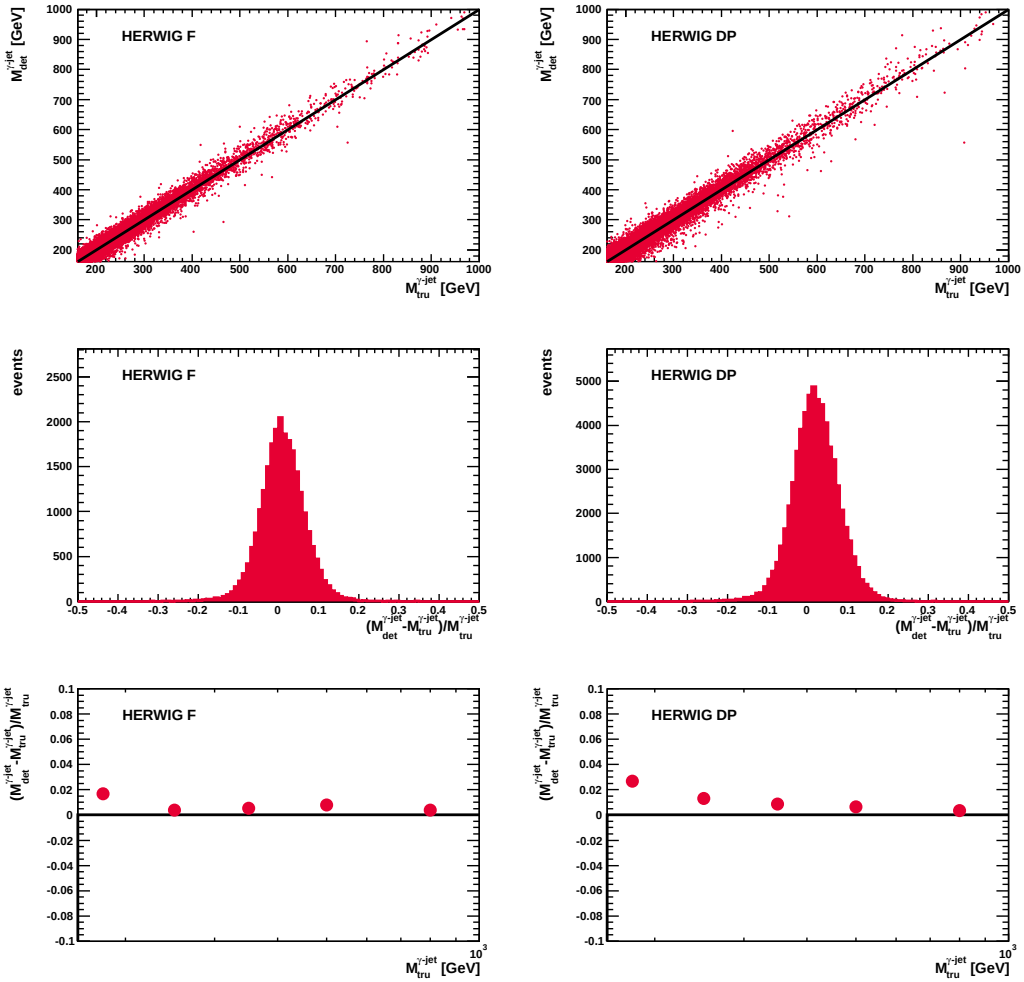

Figure 8.10: (a,b) $(M^{\gamma-\mathrm{jet}})_{\mathrm{rec}}$ vs. $(M^{\gamma-\mathrm{jet}})_{\mathrm{truth}}$ correlation; (c,d) $[(M^{\gamma-\mathrm{jet}})_{\mathrm{rec}}$-$(M^{\gamma-\mathrm{jet}})_{\mathrm{truth}}]/(M^{\gamma-\mathrm{jet}})_{\mathrm{truth}}$ distribution; and (e,f) average of $[(M^{\gamma-\mathrm{jet}})_{\mathrm{rec}}$-$(M^{\gamma-\mathrm{jet}})_{\mathrm{truth}}]/(M^{\gamma-\mathrm{jet}})_{\mathrm{truth}}$ as a function of $(M^{\gamma-\mathrm{jet}})_{\mathrm{truth}}$. The results are shown for HERWIG MC fragmentation (left) and direct-photon (right) events.

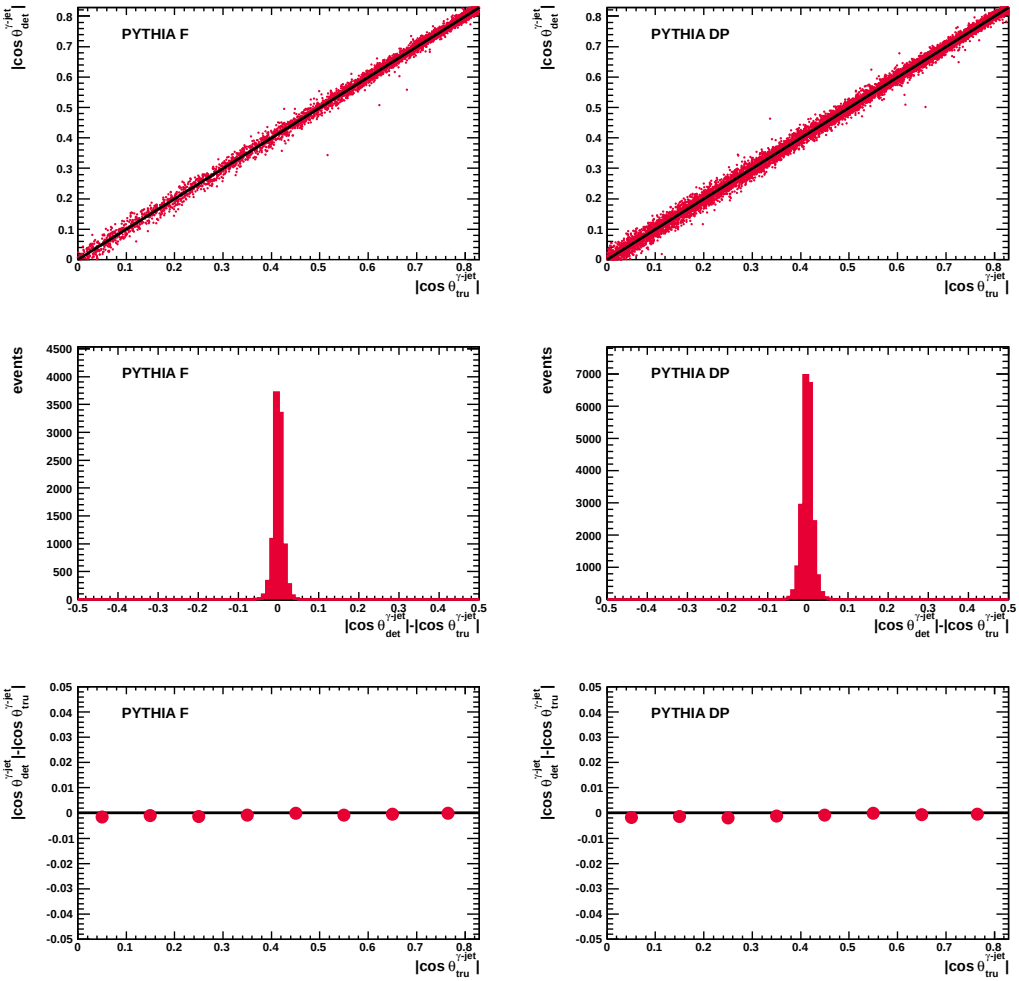

Figure 8.11: (a,b) $(|\cos\,\theta^{\gamma-\mathrm{jet}}|)_{\mathrm{rec}}$ vs. $(|\cos\,\theta^{\gamma-\mathrm{jet}}|)_{\mathrm{truth}}$ correlation; (c,d) $(|\cos\,\theta^{\gamma-\mathrm{jet}}|)_{\mathrm{rec}}$-$(|\cos\,\theta^{\gamma-\mathrm{jet}}|)_{\mathrm{truth}}$ distribution; and (e,f) average of $(|\cos\,\theta^{\gamma-\mathrm{jet}}|)_{\mathrm{rec}}$-$(|\cos\,\theta^{\gamma-\mathrm{jet}}|)_{\mathrm{truth}}$ as a function of $(|\cos\,\theta^{\gamma-\mathrm{jet}}|)_{\mathrm{truth}}$. The results are shown for PYTHIA MC fragmentation (left) and direct-photon (right) events.

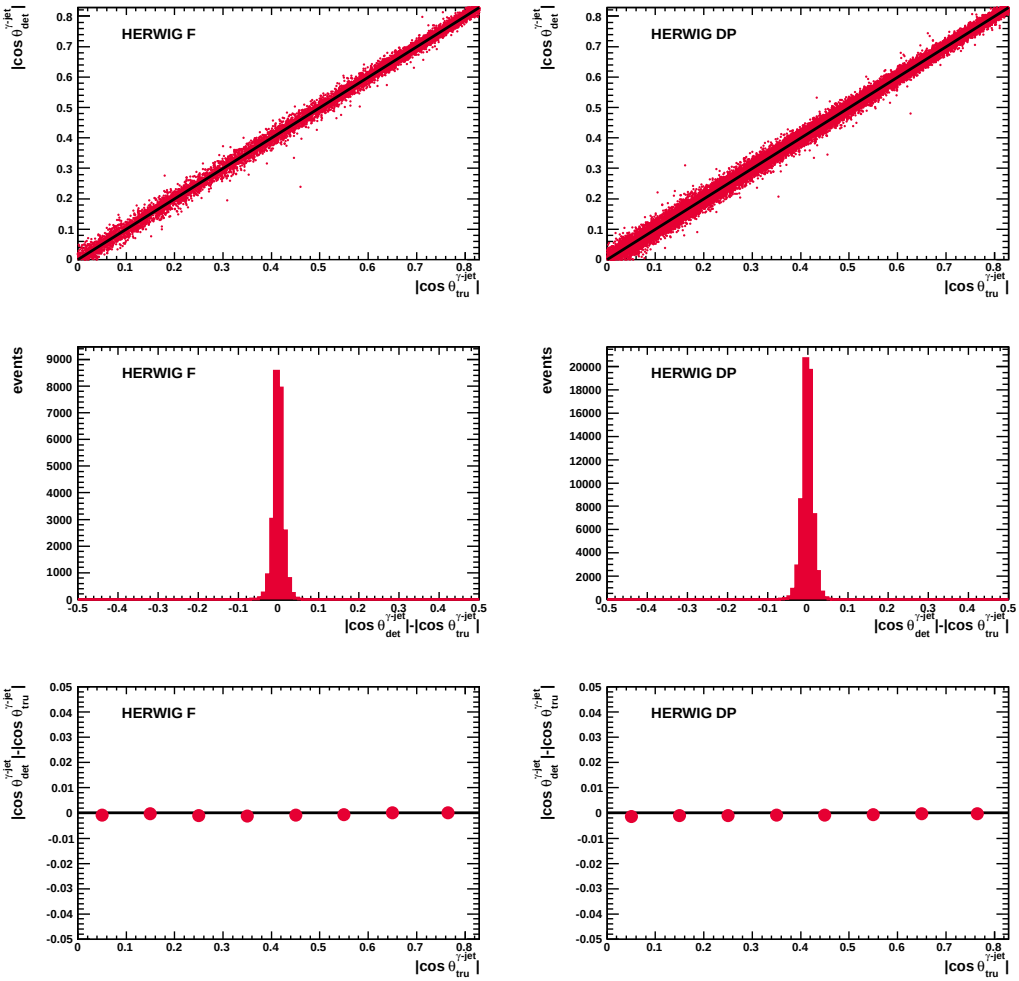

Figure 8.12: (a,b) $(|\cos\,\theta^{\gamma-\mathrm{jet}}|)_{\mathrm{rec}}$ vs. $(|\cos\,\theta^{\gamma-\mathrm{jet}}|)_{\mathrm{truth}}$ correlation; (c,d) $(|\cos\,\theta^{\gamma-\mathrm{jet}}|)_{\mathrm{rec}}$-$(|\cos\,\theta^{\gamma-\mathrm{jet}}|)_{\mathrm{truth}}$ distribution; and (e,f) average of $(|\cos\,\theta^{\gamma-\mathrm{jet}}|)_{\mathrm{rec}}$-$(|\cos\,\theta^{\gamma-\mathrm{jet}}|)_{\mathrm{truth}}$ as a function of $(|\cos\,\theta^{\gamma-\mathrm{jet}}|)_{\mathrm{truth}}$. The results are shown for HERWIG MC fragmentation (left) and direct-photon (right) events.

The overall signal-selection efficiency was evaluated using the MC samples. The integrated efficiency was computed as

$$\epsilon = \frac{N^{\mathrm{rec,tru}}}{N^{\mathrm{tru}}} \ , \tag{8.1}$$

where $N^{\mathrm{rec,tru}}$ is the number of MC events that pass all the selection requirements both at the detector and true levels and N^{tru} is the number of MC events that pass the selection requirements at the true level. The integrated efficiency was found to be 68.5% (67.9%) using the PYTHIA (HERWIG) samples.

The bin-to-bin efficiency was computed as

$$\epsilon = \frac{N_i^{\mathrm{rec,tru}}}{N_i^{\mathrm{tru}}} \ , \tag{8.2}$$

where $N_i^{\mathrm{rec,tru}}$ is the number of MC events that pass all the selection requirements both at the detector and true levels and are generated and reconstructed in bin i of a given observable and N^{tru} is the number of MC events that pass the selection requirements at the true level and are located in bin i. Figure 8.13 shows the bin-to-bin efficiencies as functions of the six observables as evaluated using either PYTHIA and HERWIG. The bin-to-bin efficiency is above 60% except at low $P_{T,\mathrm{lead}}^{\mathrm{jet}}$. The efficiency is very similar for PYTHIA and HERWIG.

8.1.3 Jet-quality cut efficiency

The efficiency of the jet-quality criteria applied to the data was estimated using a tag-and-probe method. The leading photon in each event was considered as the "tag" to probe the leading jet. Additional selection criteria, such as $\Delta\phi^{\gamma-\mathrm{jet}} > 2.6$ (probe and tag required to be back-to-back) and $|P_{T,\mathrm{lead}}^{\mathrm{jet}} - E_{T,\mathrm{lead}}^{\gamma}|/P_T^{\mathrm{avg}} < 0.4$, where $P_T^{\mathrm{avg}} = \frac{P_{T,\mathrm{lead}}^{\mathrm{jet}} + E_{T,\mathrm{lead}}^{\gamma}}{2}$ (to have well-balanced probe and tag), were applied.

The jet-quality criteria were then applied to the leading jet and the fraction of jets accepted was measured as a function of $P_{T,\mathrm{lead}}^{\mathrm{jet}}$ and $|Y_{\mathrm{lead}}^{\mathrm{jet}}|$. The efficiency to select a jet is shown in Fig. 8.14. The jet-quality selection efficiency is $\sim 99\%$. No correction for this efficiency was applied, but an uncertainty related to this effect was included in the measurements (see Chapter 9).

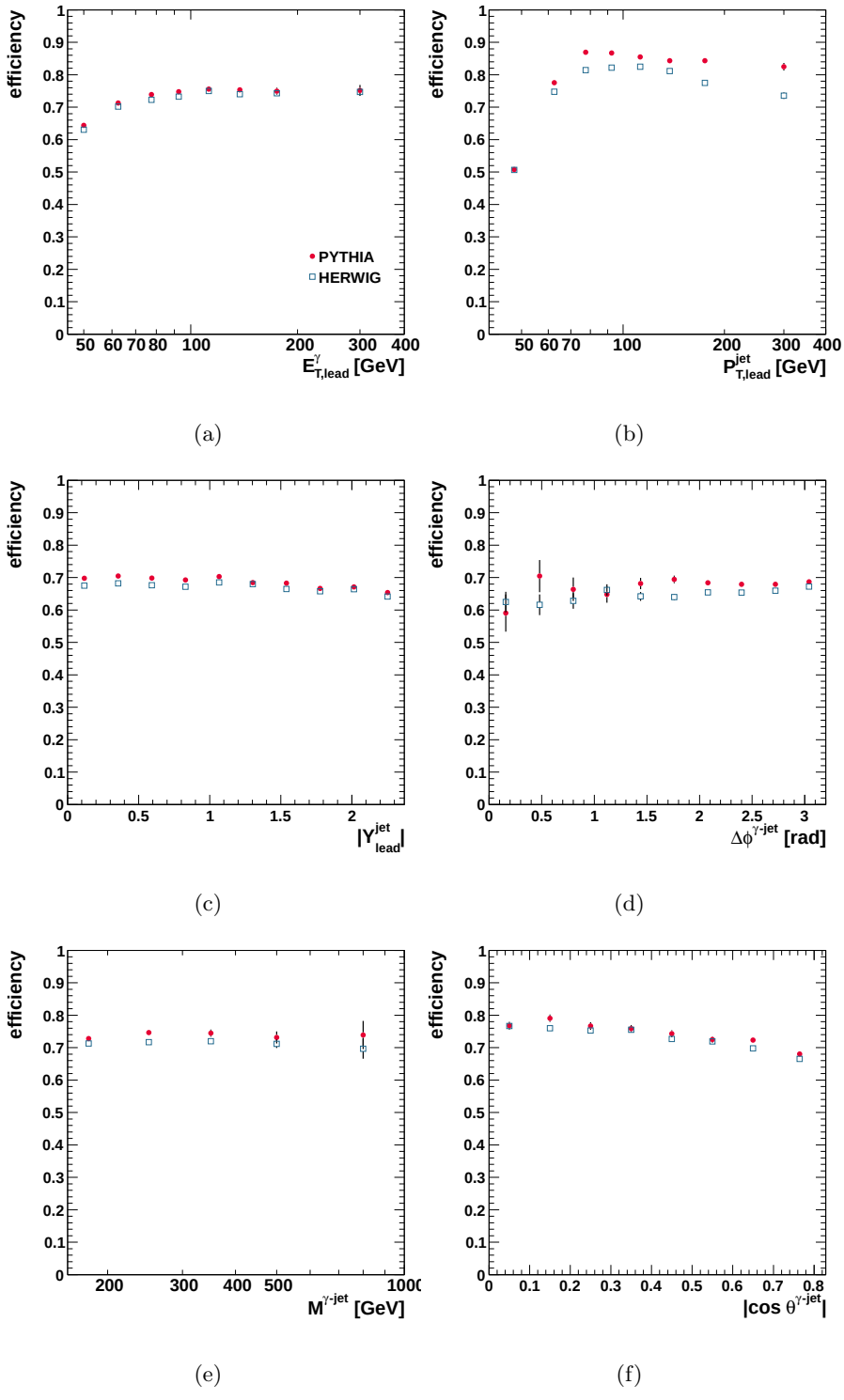

(a) (b) (c) (d) (e) (f)

Figure 8.13: Signal efficiency from PYTHIA (dots) and HERWIG (squares) as functions of (a) $E^{\gamma}_{T,\mathrm{lead}}$, (b) $P^{\mathrm{jet}}_{T,\mathrm{lead}}$, (c) $|Y^{\mathrm{jet}}_{\mathrm{lead}}|$, (d) $\Delta\phi^{\gamma-\mathrm{jet}}$, (e) $M^{\gamma-\mathrm{jet}}$ and (f) $|\cos\theta^{\gamma-\mathrm{jet}}|$. The error bars are statistical only.

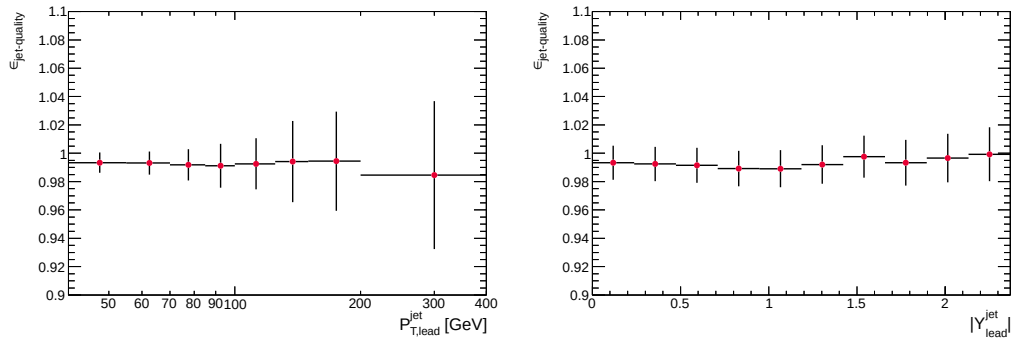

(a) (b)

Figure 8.14: Signal efficiency due to the jet-quality criteria (dots) as functions of (a) $P^{\text{jet}}_{T,\text{lead}}$ and (b) $|Y^{\text{jet}}_{\text{lead}}|$. The error bars are statistical only.

8.2 Acceptance corrections

The data distributions, after background subtraction, were corrected to the true level using bin-by-bin acceptance correction factors determined using the MC samples. These correction factors take into account the efficiency of the selection criteria, the purity and efficiency of the jet reconstruction and the efficiency of the photon reconstruction.

For this approach to be valid, the uncorrected distributions of the data must be adequately described by the MC simulations at the detector level. This condition was satisfied by both the PYTHIA and HERWIG MC samples after adjusting the relative fractions of the direct-photon and fragmentation components of MC to background subtracted data, as shown in Figs. 7.12 and 7.13.

The data distributions were corrected to the true level via the formula

$$\frac{d\sigma}{dA}(i) = \frac{N_A^{\text{sig}}(i) C^{\text{MC}}(i)}{\mathcal{L}\Delta A(i)}, \tag{8.3}$$

where $(d\sigma/dA)(i)$ is the differential cross section in bin i as a function of observable $A = E^{\gamma}_{T,\text{lead}}$, $P^{\text{jet}}_{T,\text{lead}}$, $|Y^{\text{jet}}_{\text{lead}}|$, $\Delta\phi^{\gamma-\text{jet}}$, $M^{\gamma-\text{jet}}$ or $|\cos\theta^{\gamma-\text{jet}}|$, $N_A^{\text{sig}}(i)$ is the number of background-subtracted data events in bin i, $C^{\text{MC}}(i)$ is the correction factor in bin i, $\mathcal{L}$ is the integrated luminosity and $\Delta A(i)$ is the width of bin i.

The acceptance correction factors were computed as

$$C^{\mathrm{MC}}(i) = \frac{\alpha N_{\mathrm{tru}}^{\mathrm{MC,DP}}(i) + (1-\alpha) N_{\mathrm{tru}}^{\mathrm{MC,F}}(i)}{\alpha N_{\mathrm{det}}^{\mathrm{MC,DP}}(i) + (1-\alpha) N_{\mathrm{det}}^{\mathrm{MC,F}}(i)}. \tag{8.4}$$

The acceptance correction factors are shown in Fig. 8.15. The corrections factors differ from unity by typically 20%. The correction factors are very similar for PYTHIA and HERWIG. The deviations in the differential cross section obtained by using either PYTHIA or HERWIG to correct the data from their average were taken to represent systematic uncertainties of the effect of the QCD-cascade and hadronisation models in the corrections (see chapter 10).

A more sophisticated unfolding method [95], based on an iterative application of Bayes' theorem [96, 97], was investigated to cross-check and validate the results obtained using the bin-by-bin method explained above. The Bayesian unfolding method takes properly into account the migrations between bins and the purity and efficiency of the selection criteria when the MC description of the data is not adequate.

The main requirement of this method is to have sufficiently large MC samples to construct the reference matrices, since otherwise the results are less reliable than those obtained from the bin-by-bin method because they are more affected by such lack of statistics. Another problem which affects the unfolding based on the Bayes' theorem is the abnormal blow up of the statistical uncertainty of the resulting cross sections which appears when a large number of iterations after convergence are used. To make a trustworthy comparison between the Bayes and the bin-by-bin methods, these issues were investigated before attempting the cross-check.

Figure 8.16 shows the relative difference between the results obtained based on N iterations with respect to those using $N+1$ iterations as a function of the number of iterations for the six observables studied; the comparison was done using the sum of the absolute values of the relative differences for each bin of each cross section.

The relative difference between iterations 1 and 2 is quite large; around iteration 4, the differences start to be small for all observables. Therefore, the nominal Bayes' unfolding was performed using 4 iterations. Figure 8.17 shows the relative difference between the results obtained using N iterations with respect to those obtained using 4 iterations for the six observables studied. As can be observed, the oscillations on the results for $N < 4$ are quite large; these oscillations disappear for $N > 4$. The correlation matrices used in the Bayes unfolding are shown in Figs. 8.18 and 8.19

for PYTHIA and HERWIG, respectively.

The comparison between the cross sections unfolded via the bin-by-bin and the Bayes' (using $N = 4$ iterations) methods for all six observables is shown in Fig. 8.20. As can be observed, the differences between the cross sections obtained via the two methods are smaller than the statistical uncertainty. They are typically smaller than 1%, except in the regions of phase space where the data statistics is poor. For comparison, the systematic uncertainty due to the fit (see Chapter 9) is also included in Fig. 8.20 and shows that the size of this uncertainty is typically of the same size or bigger than the difference between the two methods. These results validate the use of the bin-by-bin unfolding method with the optimised admixture of the MC components as the nominal method to measure the cross sections.

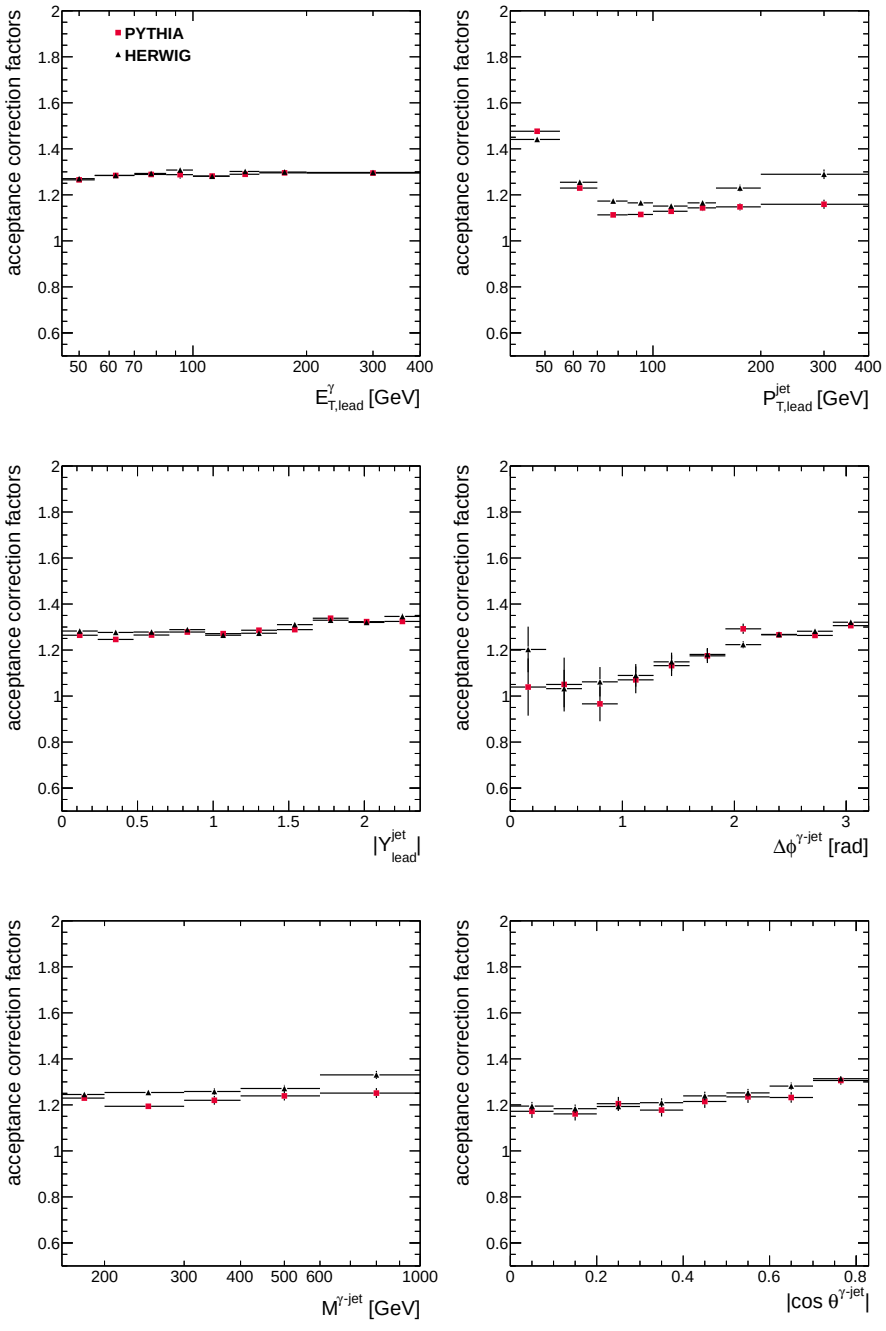

(e) (f)

Figure 8.15: Acceptance correction factors from PYTHIA (squares) and HERWIG (triangles) as functions of (a) $E^{\gamma}_{T,\mathrm{lead}}$, (b) $P^{\mathrm{jet}}_{T,\mathrm{lead}}$, (c) $|Y^{\mathrm{jet}}_{\mathrm{lead}}|$, (d) $\Delta\phi^{\gamma-\mathrm{jet}}$, (e) $M^{\gamma-\mathrm{jet}}$ and (f) $|\cos\,\theta^{\gamma-\mathrm{jet}}|$. The error bars are statistical only.

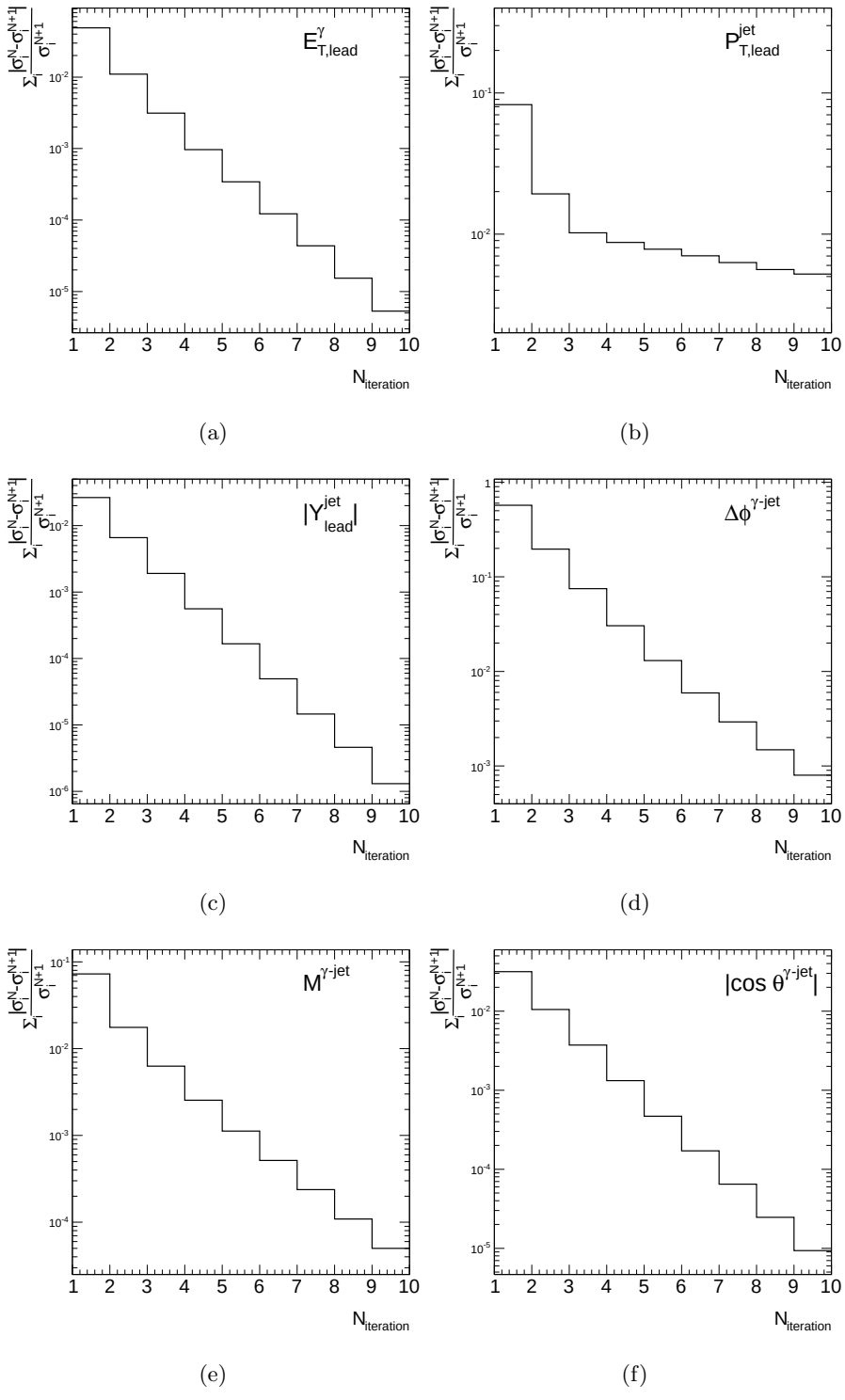

Figure 8.16: Relative differences between the cross sections unfolded using iterations N and $N+1$ as functions of the number of iterations for (a) $E^{\gamma}_{T,\mathrm{lead}}$, (b) $P^{\mathrm{jet}}_{T,\mathrm{lead}}$, (c) $|Y^{\mathrm{jet}}_{\mathrm{lead}}|$, (d) $\Delta\phi^{\gamma-\mathrm{jet}}$, (e) $M^{\gamma-\mathrm{jet}}$ and (f) $|\cos\,\theta^{\gamma-\mathrm{jet}}|$.

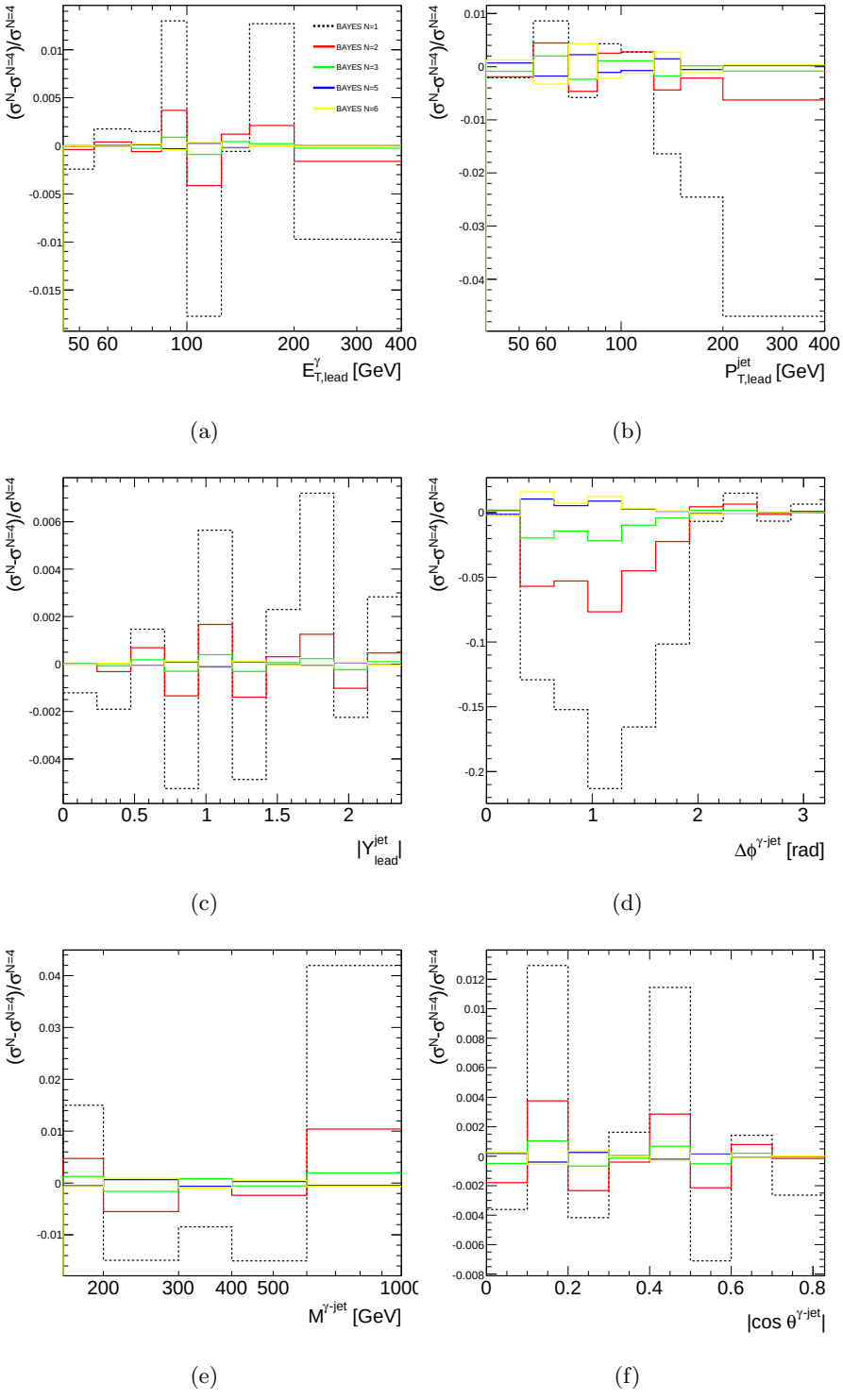

(a) (b) (c) (d) (e) (f)

Figure 8.17: Relative differences between the cross sections unfolded using N iterations with respect to the results unfolded using $N = 4$ iterations as functions of (a) $E^{\gamma}_{T,\mathrm{lead}}$, (b) $P^{\mathrm{jet}}_{T,\mathrm{lead}}$, (c) $|Y^{\mathrm{jet}}_{\mathrm{lead}}|$, (d) $\Delta\phi^{\gamma-\mathrm{jet}}$, (e) $M^{\gamma-\mathrm{jet}}$ and (f) $|\cos\,\theta^{\gamma-\mathrm{jet}}|$.

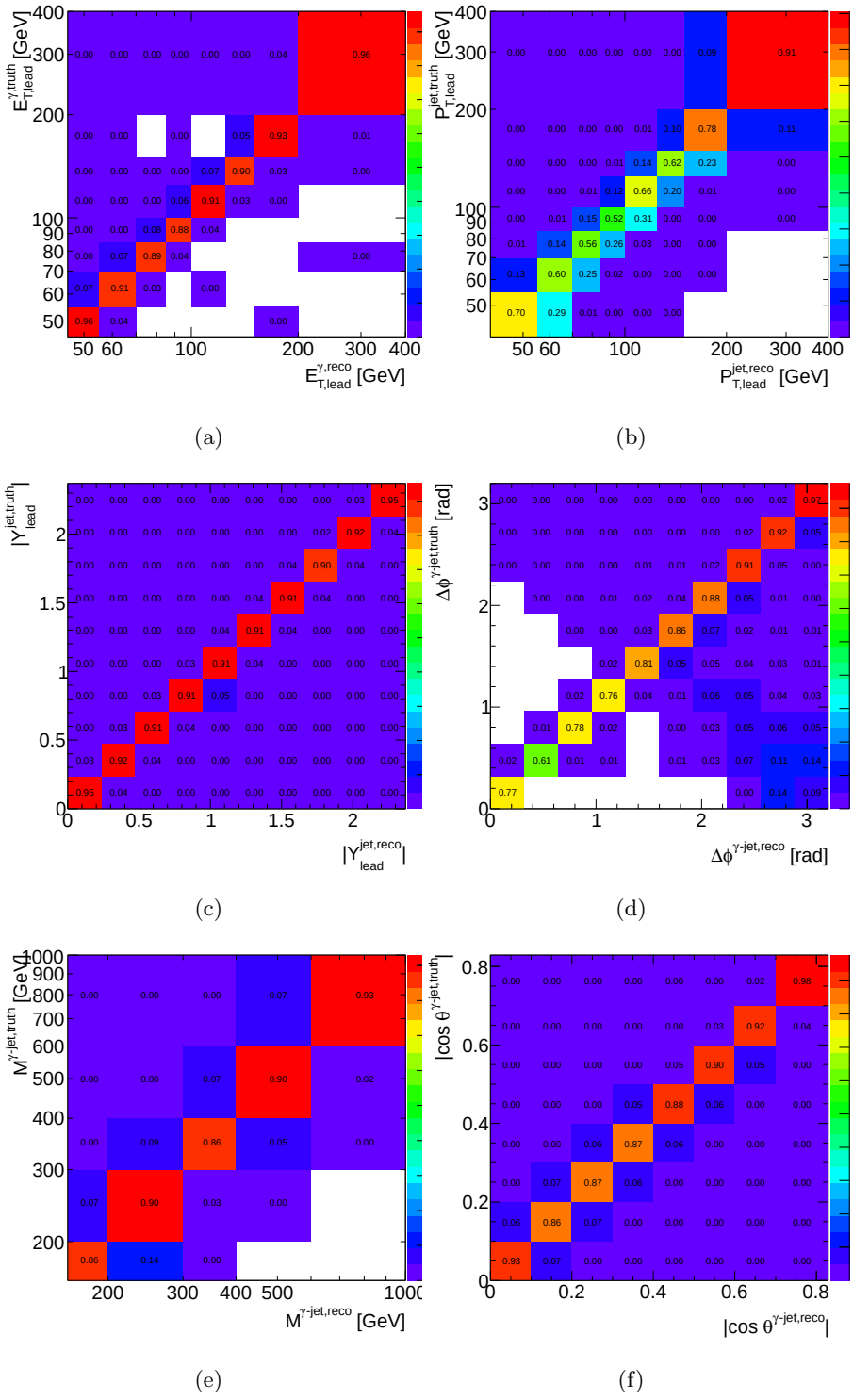

Figure 8.18: Correlation matrices as functions of (a) $E^{\gamma}_{T,\mathrm{lead}}$, (b) $P^{\mathrm{jet}}_{T,\mathrm{lead}}$, (c) $|Y^{\mathrm{jet}}_{\mathrm{lead}}|$, (d) $\Delta\phi^{\gamma-\mathrm{jet}}$, (e) $M^{\gamma-\mathrm{jet}}$ and (f) $|\cos\,\theta^{\gamma-\mathrm{jet}}|$ using the PYTHIA MC samples.

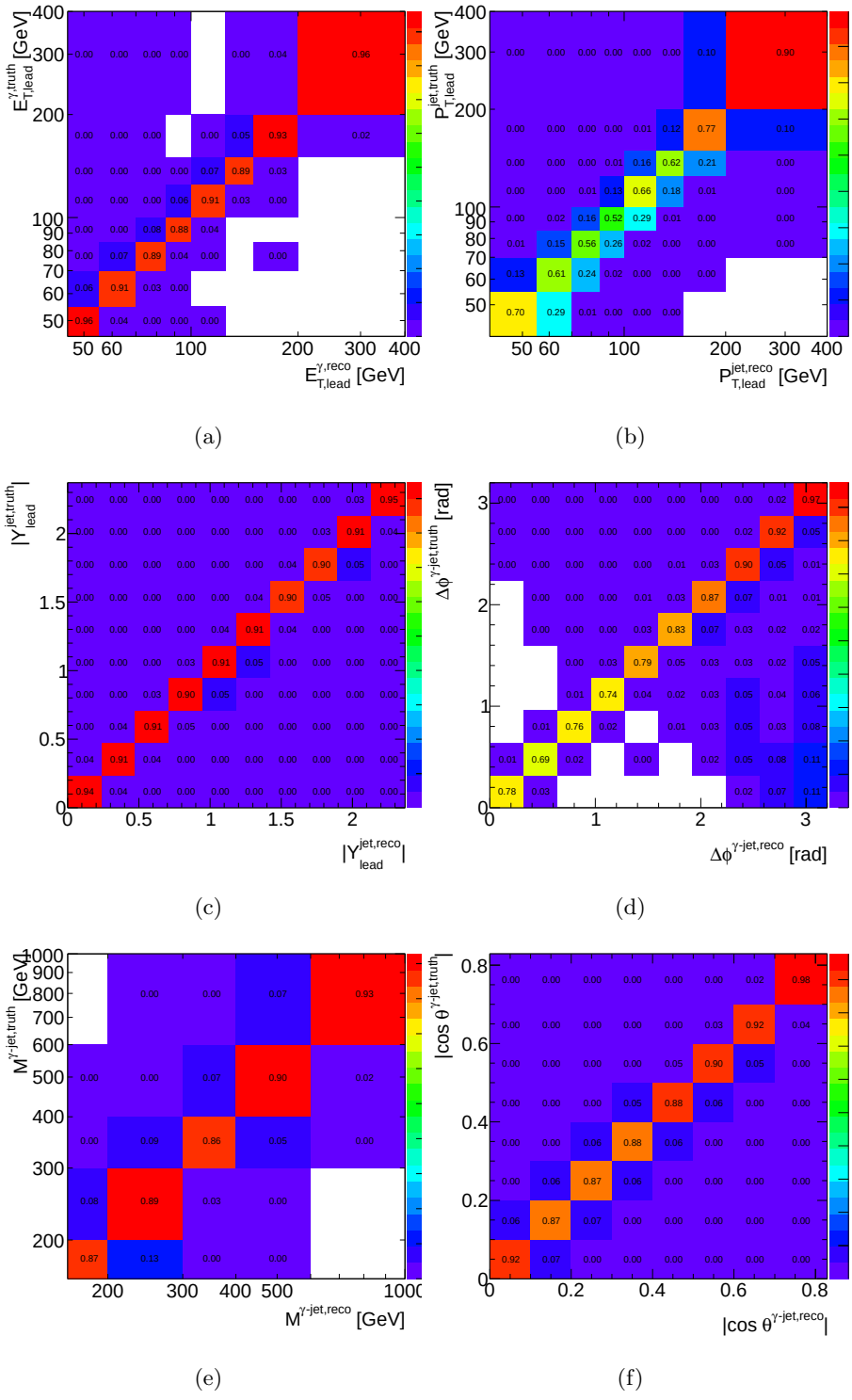

Figure 8.19: Correlation matrices as functions of (a) $E^{\gamma}_{T,\mathrm{lead}}$, (b) $P^{\mathrm{jet}}_{T,\mathrm{lead}}$, (c) $|Y^{\mathrm{jet}}_{\mathrm{lead}}|$, (d) $\Delta\phi^{\gamma-\mathrm{jet}}$, (e) $M^{\gamma-\mathrm{jet}}$ and (f) $|\cos\,\theta^{\gamma-\mathrm{jet}}|$ using the HERWIG MC samples.

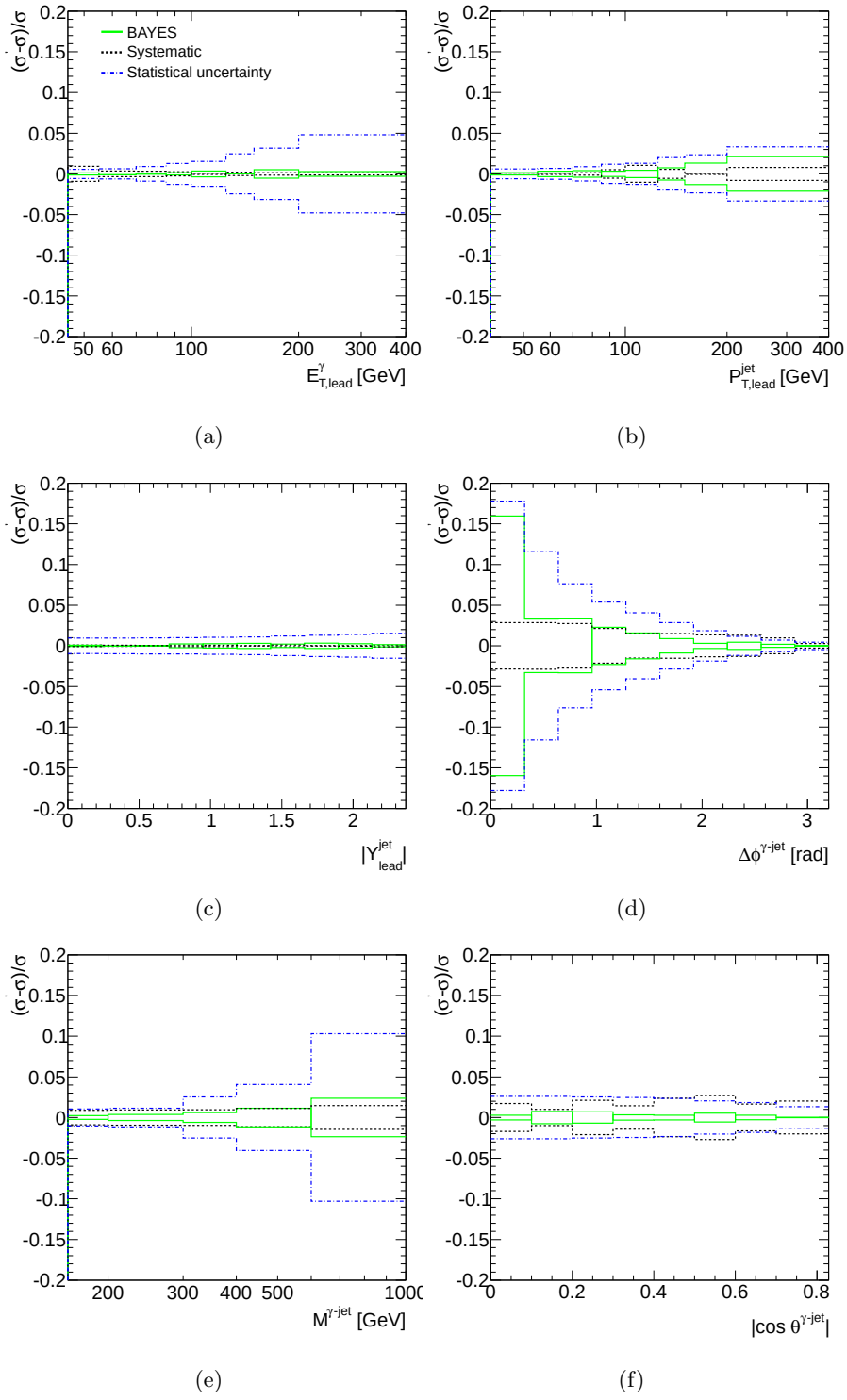

Figure 8.20: Relative differences between the cross sections unfolded using the Bayesian method and the nominal cross sections (solid green lines) as functions of (a) $E^{\gamma}_{T,\mathrm{lead}}$, (b) $P^{\mathrm{jet}}_{T,\mathrm{lead}}$, (c) $|Y^{\mathrm{jet}}_{\mathrm{lead}}|$, (d) $\Delta\phi^{\gamma-\mathrm{jet}}$, (e) $M^{\gamma-\mathrm{jet}}$ and (f) $|\cos\,\theta^{\gamma-\mathrm{jet}}|$. For comparison, the systematic uncertainty due to the fit (dashed black lines) (see Chapter 9) and the relative statistical error (dot-dashed blue lines) are also shown.

Chapter 9

Systematic uncertainties and cross checks

Several sources of systematic uncertainties that affect the measurements were investigated, such as the energy scale, the energy resolution, the model dependence, the fit dependence, the background subtraction, the detector simulation, etc. Each source is discussed in detail below. Other checks, namely the primary-vertex reweighting and pile-up effects, were also performed and are also discussed in this chapter.

9.1 Systematic uncertainties

As discussed previously, the cross-section measurements depend on a few quantities that are obtained from simulated signal samples: correction factors (see Chapter 8) and the signal leakage fractions (see Chapter 7) used to correct the data-driven purity estimation. This dependence introduces a systematic uncertainty in the measurements due to the imperfect knowledge and simulation of the detector response (the amount of material in front of the electromagnetic calorimeter, the photon and jet energy scales and resolutions) and to the uncertainties on the generated spectra. The main issue for the generated spectra is the amount of direct photons with respect to fragmentation photons: direct photons tend to be more isolated and usually yield narrower energy distributions in the electromagnetic calorimeter. In addition, systematic uncertainties arise from the choice of the background control regions and from the limited precision of the trigger efficiency and luminosity measurements.

9.1.1 Detector material in the simulation

In the study of photons in the final state, a good detector-material simulation by the Monte Carlo is essential. Differences in the amount of detector material between the ATLAS detector and the MC detector simulation give rise to several effects, in particular, to differences in the photon-conversion rate and the development of the electromagnetic showers.

To estimate, in a conservative way, the effect in the cross-section measurements due to an insufficient knowledge of the detector material in the simulation, a systematic uncertainty was evaluated by repeating the full analysis using a different detector simulation with a pessimistic estimation of the amount of dead material in front of the calorimeter.

In this configuration the whole non-sensitive material in the inner detector was increased by 5% while the material in the pixel and SCT services was increased by 20%. Additional material was placed just in front of the calorimeter (0.1 X0 in the barrel calorimeter cryostat and 0.05 X0 between barrel presampler and the strips), at the end of the 467 SCT/TRT end-caps (15% X0) and at the inner detector end-plate (15% X0).

Figure 9.1 shows the resulting relative uncertainties in the differential cross sections as functions of the six observables. For $\Delta\phi^{\gamma-\mathrm{jet}}$, the average of the relative systematic uncertainty in the last three bins has been used for the remaining bins.

9.1.2 Model and fit dependence

The MC simulation of the signal was used (i) to estimate the signal leakage fractions and (ii) to compute the acceptance correction factors.

For step (i), both the PYTHIA and HERWIG simulations were used with the admixture of the direct-photon and fragmentation components as given by each MC to yield two sets of background-subtracted data distributions.

The signal leakage fractions depend on the relative fraction of the two components. Figures 7.3 and 7.4 show the signal leakage fractions for the default admixture and Figs. 9.2 to 9.5 show the fractions for the direct-photon and fragmentation components separately. Therefore, the uncertainty related to the simulation of the

prompt-photon components in the signal leakage fractions was estimated (conservatively) by performing the background subtraction with only the direct-photon or with only the fragmentation component. Figure 9.6 shows the resulting relative uncertainties as functions of the six observables.

For step (ii), first the direct-photon and fragmentation relative fractions in PYTHIA and HERWIG were fitted to the background-subtracted data distributions and a set of correction factors was computed from each MC sample; two sets of measured cross sections were computed using these corrections factors. The nominal cross section was taken as the average of these two sets. The effect of the QCD-cascade and hadronisation models in the acceptance correction factors was estimated as deviations from the nominal cross sections by using either only PYTHIA or only HERWIG to correct the data. Figure 9.7 shows the resulting relative uncertainties as functions of the six observables.

The acceptance correction factors also depend on the relative fractions of direct-photon and fragmentation components; the nominal Monte-Carlo admixture was taken from the fit to the background-subtracted data distribution. A systematic uncertainty due to the fit of the two components to data was estimated (conservatively) by using the default Monte Carlo admixture of the two components. Figure 9.8 shows the resulting relative uncertainties in the differential cross sections as functions of the six observables.

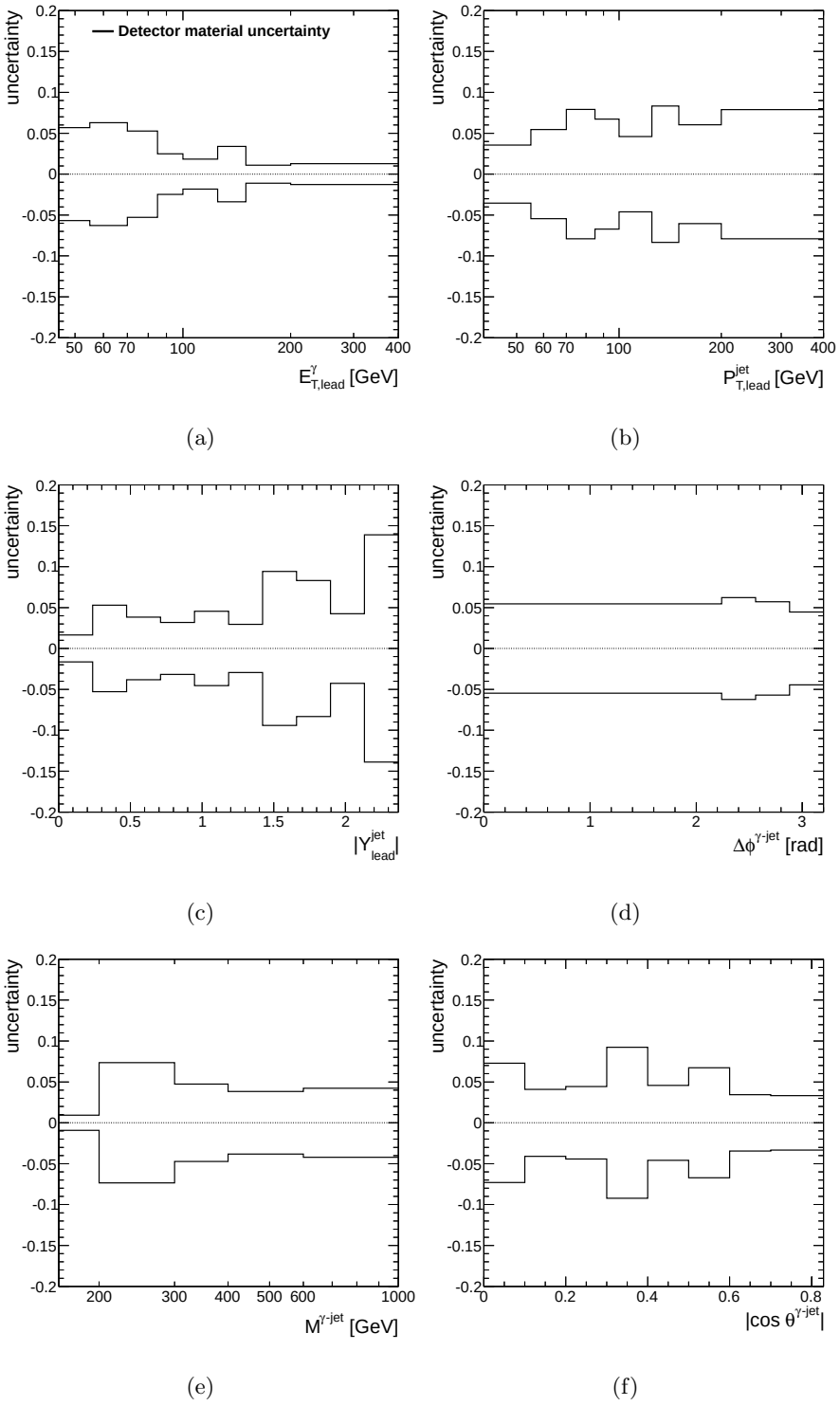

Figure 9.1: Relative systematic uncertainties due to the detector material in the simulation for the differential cross sections as functions of (a) $E^{\gamma}_{T,\mathrm{lead}}$, (b) $P^{\mathrm{jet}}_{T,\mathrm{lead}}$, (c) $|Y^{\mathrm{jet}}_{\mathrm{lead}}|$, (d) $\Delta\phi^{\gamma-\mathrm{jet}}$, (e) $M^{\gamma-\mathrm{jet}}$ and (f) $|\cos\,\theta^{\gamma-\mathrm{jet}}|$.

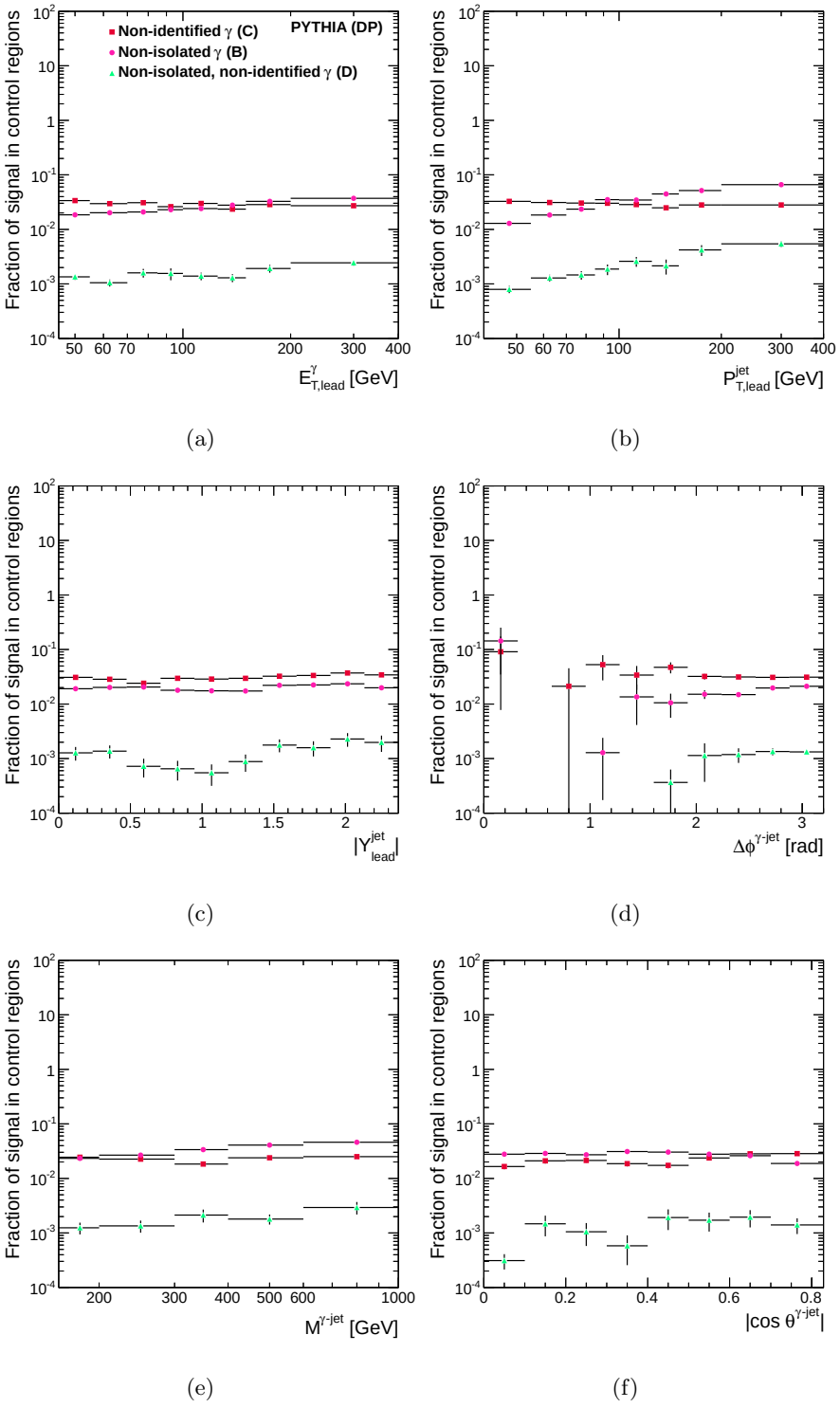

Figure 9.2: Signal leakage fractions from PYTHIA MC direct-photon events for the B (dots), C (squares) and D (triangles) control regions as functions of (a) $E^{\gamma}_{T,\mathrm{lead}}$, (b) $P^{\mathrm{jet}}_{T,\mathrm{lead}}$, (c) $|Y^{\mathrm{jet}}_{\mathrm{lead}}|$, (d) $\Delta\phi^{\gamma-\mathrm{jet}}$, (e) $M^{\gamma-\mathrm{jet}}$ and (f) $|\cos\,\theta^{\gamma-\mathrm{jet}}|$.

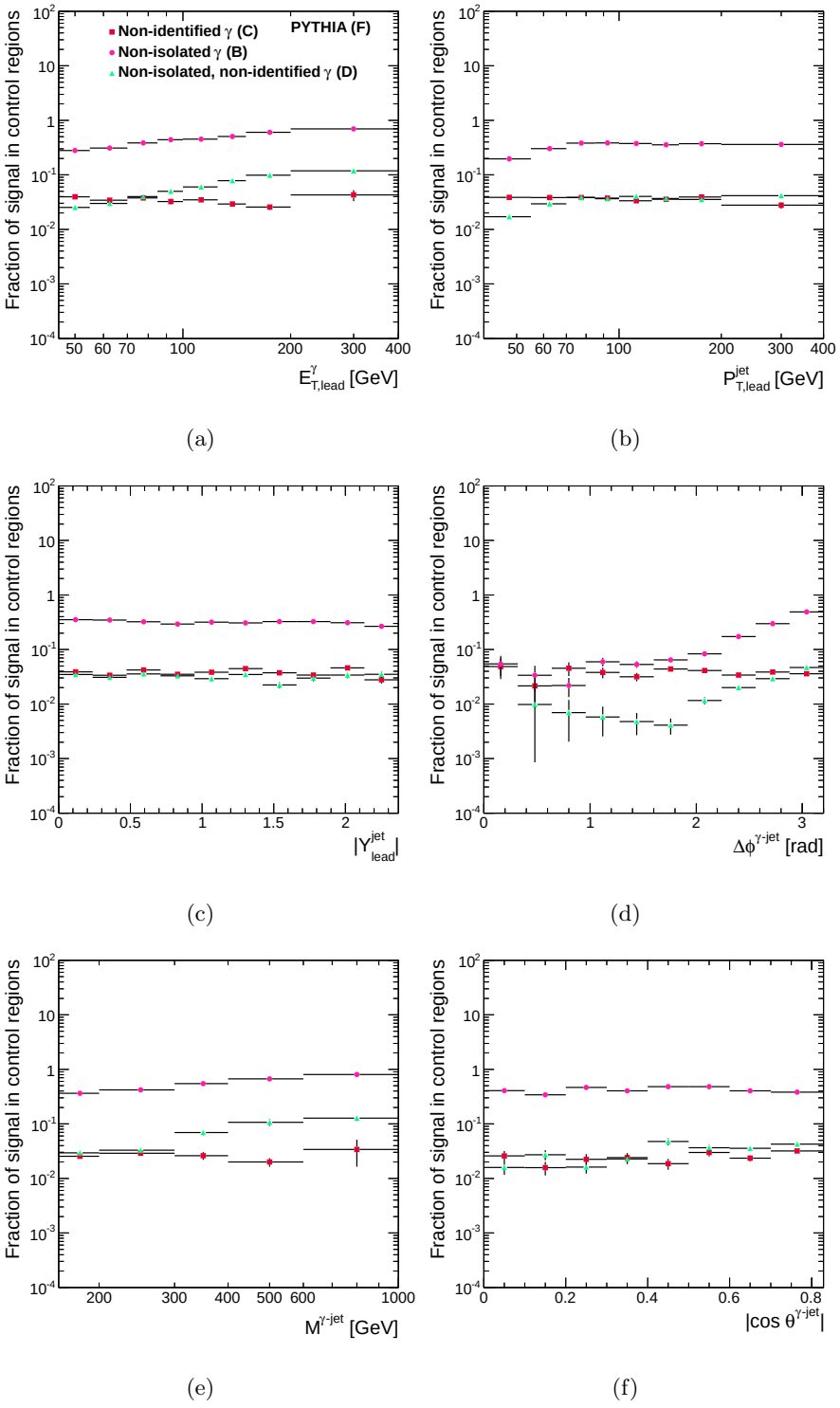

Figure 9.3: Signal leakage fractions from PYTHIA MC fragmentation events for the B (dots), C (squares) and D (triangles) control regions as functions of (a) $E^{\gamma}_{T,\mathrm{lead}}$, (b) $P^{\mathrm{jet}}_{T,\mathrm{lead}}$, (c) $|Y^{\mathrm{jet}}_{\mathrm{lead}}|$, (d) $\Delta\phi^{\gamma-\mathrm{jet}}$, (e) $M^{\gamma-\mathrm{jet}}$ and (f) $|\cos\,\theta^{\gamma-\mathrm{jet}}|$.

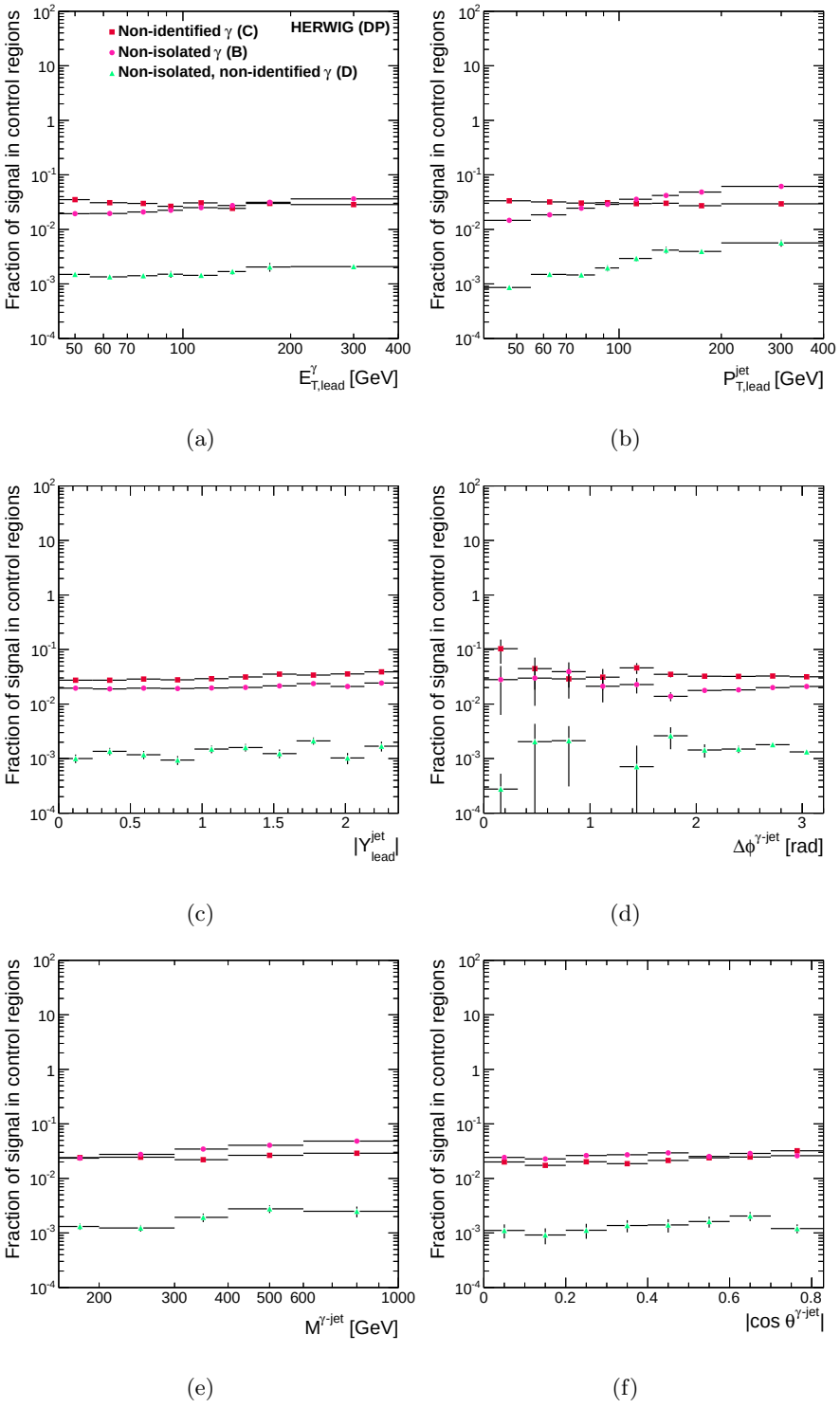

Figure 9.4: Signal leakage fractions from HERWIG MC direct-photon events for the B (dots), C (squares) and D (triangles) control regions as functions of (a) $E^{\gamma}_{T,\mathrm{lead}}$, (b) $P^{\mathrm{jet}}_{T,\mathrm{lead}}$, (c) $|Y^{\mathrm{jet}}_{\mathrm{lead}}|$, (d) $\Delta\phi^{\gamma-\mathrm{jet}}$, (e) $M^{\gamma-\mathrm{jet}}$ and (f) $|\cos\,\theta^{\gamma-\mathrm{jet}}|$.

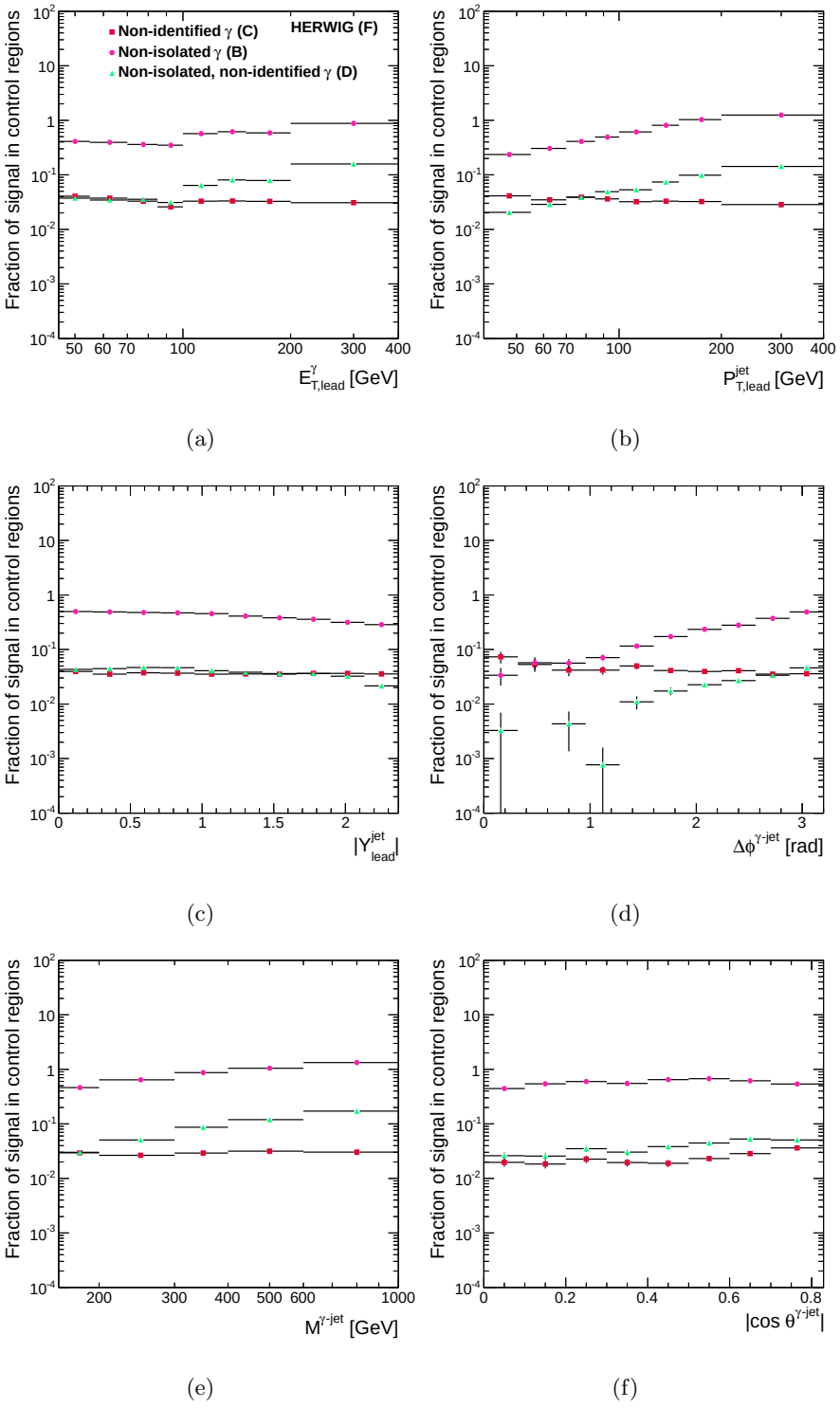

Figure 9.5: Signal leakage fractions from HERWIG MC fragmentation events for the B (dots), C (squares) and D (triangles) control regions as functions of (a) $E^{\gamma}_{T,\mathrm{lead}}$, (b) $P^{\mathrm{jet}}_{T,\mathrm{lead}}$, (c) $|Y^{\mathrm{jet}}_{\mathrm{lead}}|$, (d) $\Delta\phi^{\gamma-\mathrm{jet}}$, (e) $M^{\gamma-\mathrm{jet}}$ and (f) $|\cos\,\theta^{\gamma-\mathrm{jet}}|$.

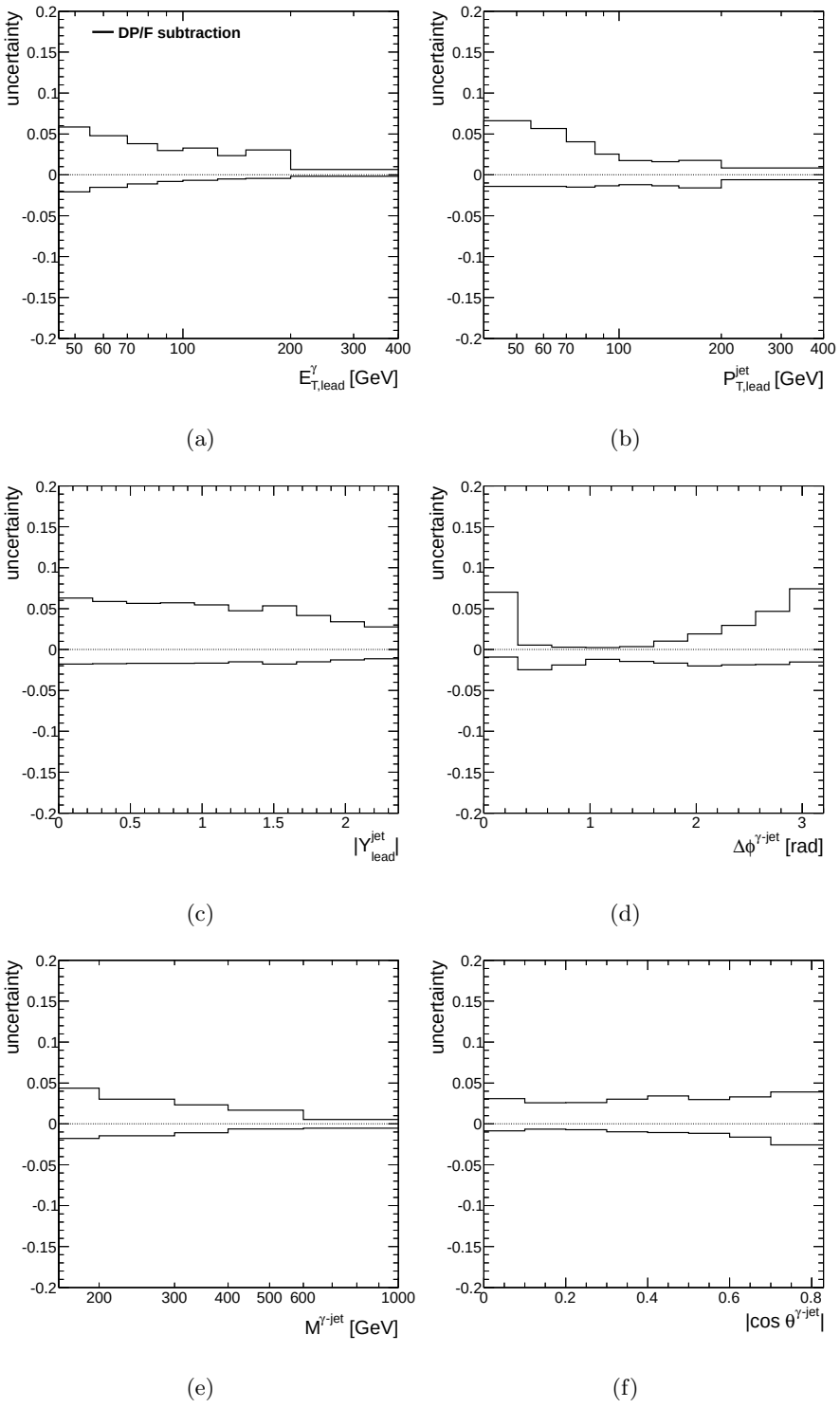

Figure 9.6: Relative systematic uncertainties due to the model dependence in the signal leakage fractions for the differential cross sections as functions of (a) $E^{\gamma}_{T,\mathrm{lead}}$, (b) $P^{\mathrm{jet}}_{T,\mathrm{lead}}$, (c) $|Y^{\mathrm{jet}}_{\mathrm{lead}}|$, (d) $\Delta\phi^{\gamma-\mathrm{jet}}$, (e) $M^{\gamma-\mathrm{jet}}$ and (f) $|\cos\,\theta^{\gamma-\mathrm{jet}}|$.

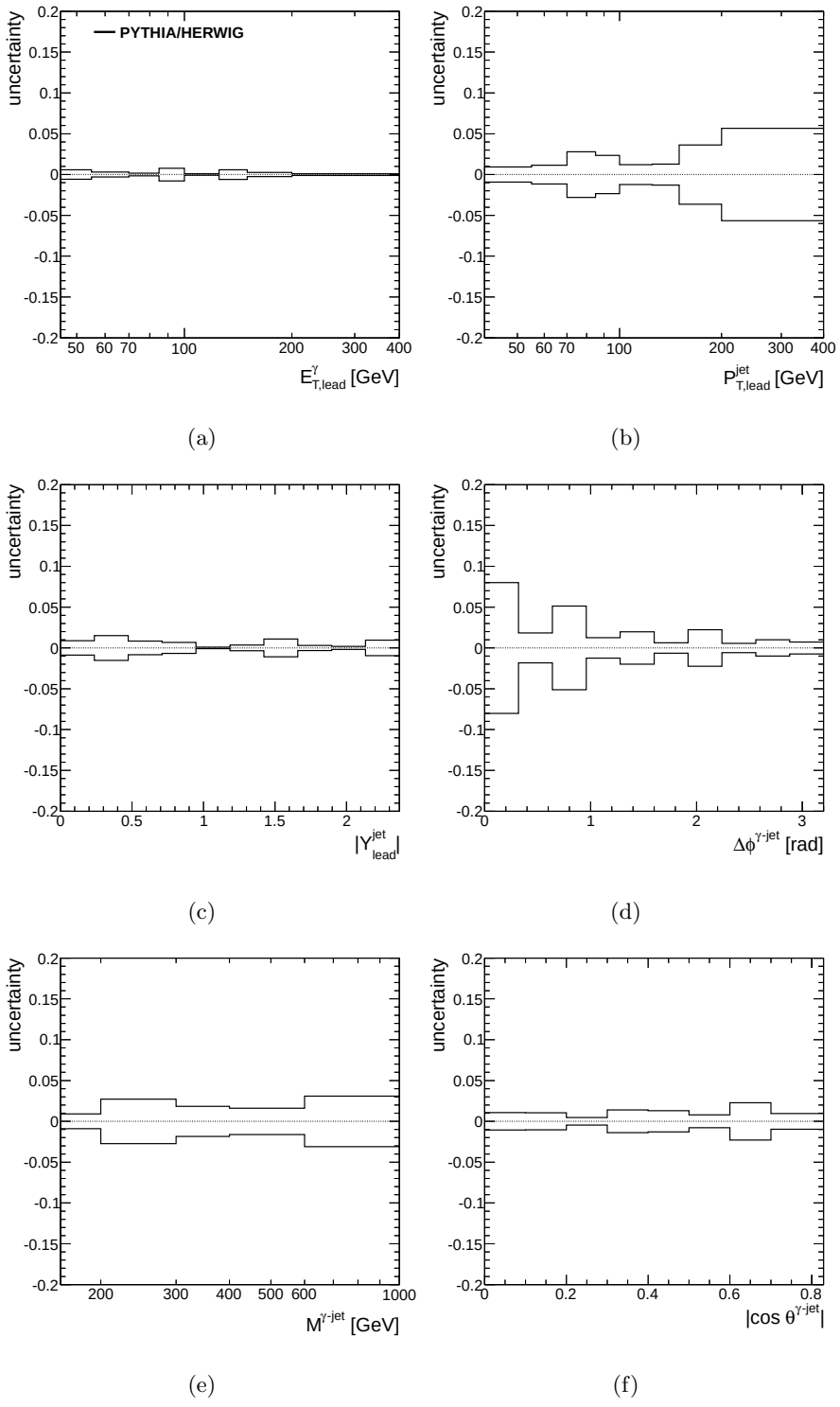

Figure 9.7: Relative systematic uncertainties due to the model dependence in the acceptance correction factors for the differential cross sections as functions of (a) $E^{\gamma}_{T,\mathrm{lead}}$, (b) $P^{\mathrm{jet}}_{T,\mathrm{lead}}$, (c) $|Y^{\mathrm{jet}}_{\mathrm{lead}}|$, (d) $\Delta\phi^{\gamma-\mathrm{jet}}$, (e) $M^{\gamma-\mathrm{jet}}$ and (f) $|\cos\,\theta^{\gamma-\mathrm{jet}}|$.

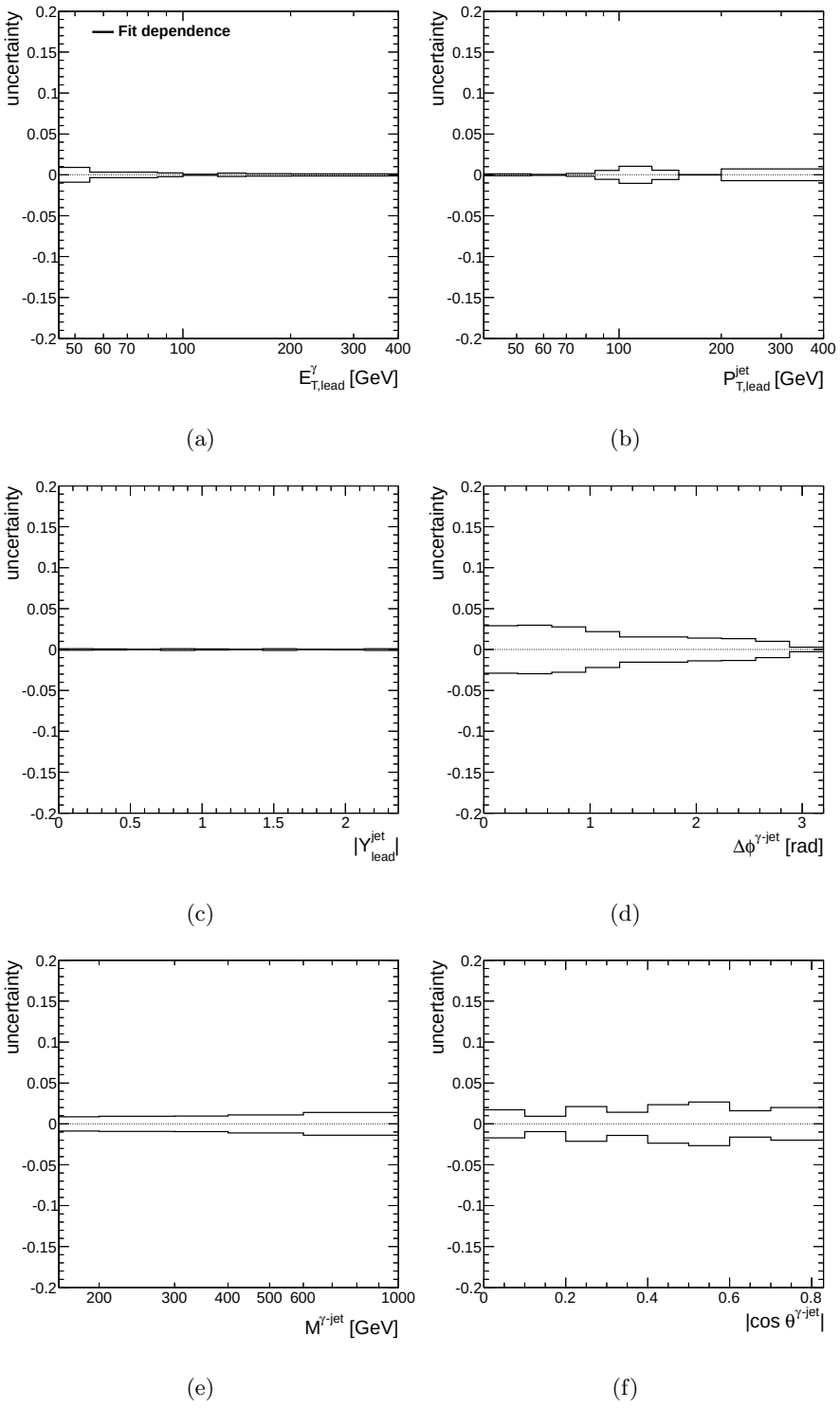

Figure 9.8: Relative systematic uncertainties due to the fit dependence in the acceptance correction factors for the differential cross sections as functions of (a) $E^{\gamma}_{T,\mathrm{lead}}$, (b) $P^{\mathrm{jet}}_{T,\mathrm{lead}}$, (c) $|Y^{\mathrm{jet}}_{\mathrm{lead}}|$, (d) $\Delta\phi^{\gamma-\mathrm{jet}}$, (e) $M^{\gamma-\mathrm{jet}}$ and (f) $|\cos\,\theta^{\gamma-\mathrm{jet}}|$.

9.1.3 Energy scale and resolution uncertainties

Differences between the simulation and the data in the electromagnetic (photon) or jet energy scale and/or resolution can lead to systematic uncertainties in the measurement of the cross sections. In the following, photon and jet energy scale and resolution uncertainties are discussed.

Photon energy scale and resolution uncertainties

The photon energy scale in data is corrected to compensate for the effect of the detector in the reconstruction of the photon energy. The uncertainty in the photon energy-scale correction factor is estimated taking into account all the different uncertainties explained in Chapter 5. The relative photon energy-scale uncertainty ($F^{\gamma}_{\pm,\text{uncert}}$) is shown in Figs. 9.9(a) and 9.9(b) as a function of E^{γ}_{T} for unconverted and converted photons, respectively. $F^{\gamma}_{\pm,\text{uncert}}$ as functions of η^{γ} for unconverted and converted photons are shown in Figs 9.9(c) and 9.9(d), respectively.

As seen in Fig. 9.9, the energy-scale uncertainty is slighly bigger for converted than for unconverted photons and has a strong dependence on η^{γ}. The uncertainty due to the photon energy scale in the cross sections was estimated by repeating the analysis after varying the energy scale of all reconstructed photon candidates with $E_T > 45$ GeV and $|\eta^{\gamma}| < 2.37$ by a factor $1 \pm F^{\gamma}_{\pm,\text{uncert}}$ in the data sample. The uncertainty in the cross section was estimated as the relative difference between the modified cross section and the nominal value.

The energy of the reconstructed photon candidates in the Monte Carlo samples was smeared to take into account the differences between the resolution of the EM-energy in data and Monte Carlo. This smearing factor has an uncertainty (see Chapter 5). To take into account this uncertainty, the analysis was repeated varying the smearing factor in the Monte Carlo samples. The uncertainty was estimated as the relative difference between the modified cross section due to the variation of the smearing factor and the nominal value.

Figure 9.10 shows the relative systematic uncertainties in the differential cross sections due to that on the photon energy scale and resolution.

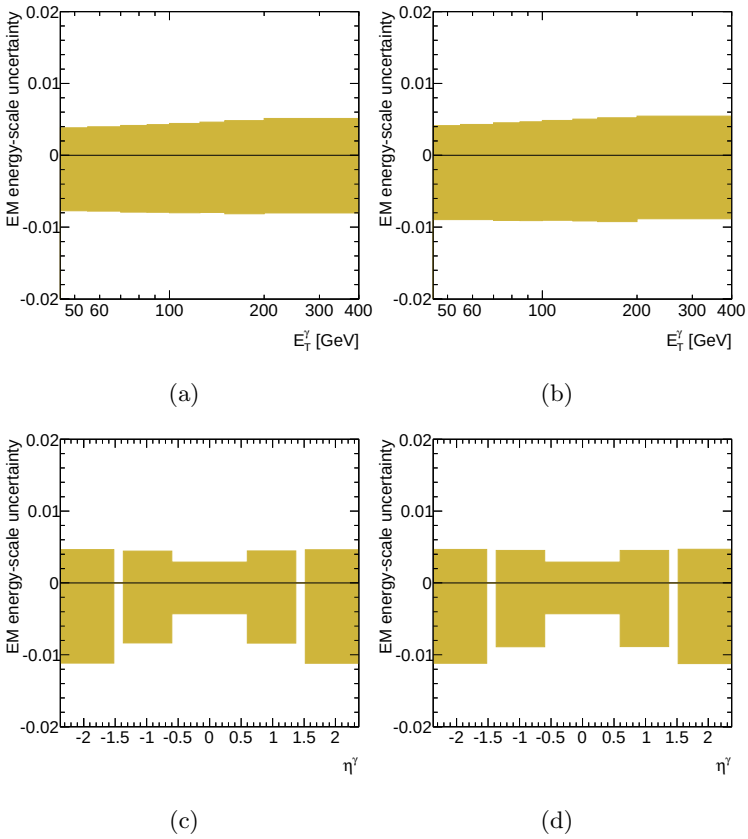

Figure 9.9: Relative photon energy-scale uncertainty as a function of E_T^γ and η^γ for (a,c) unconverted photons and (b,d) converted photons.

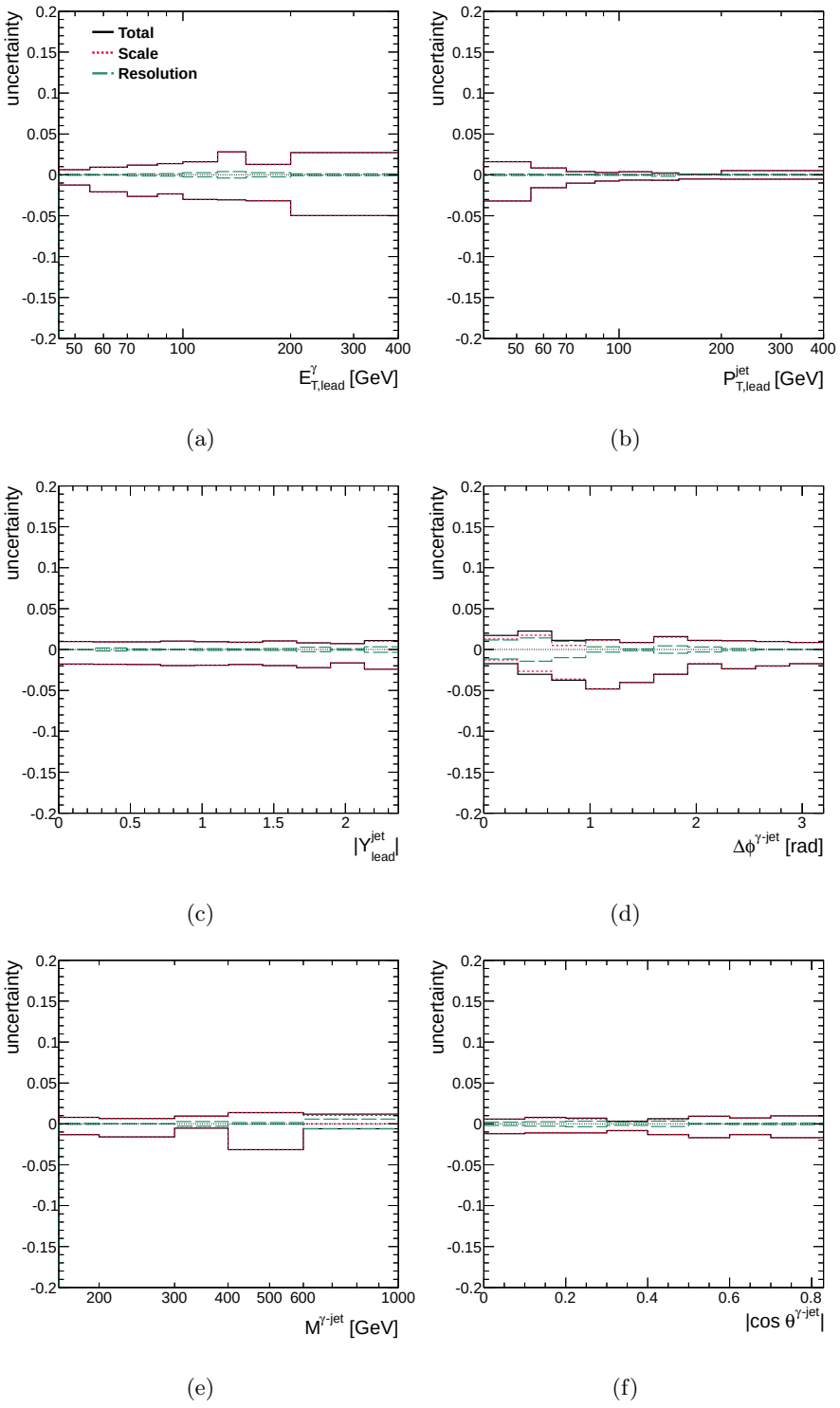

Figure 9.10: Relative systematic uncertainties due to the uncertainty in the photon energy scale and resolution for the differential cross sections as functions of (a) $E^{\gamma}_{T,\mathrm{lead}}$, (b) $P^{\mathrm{jet}}_{T,\mathrm{lead}}$, (c) $|Y^{\mathrm{jet}}_{\mathrm{lead}}|$, (d) $\Delta\phi^{\gamma-\mathrm{jet}}$, (e) $M^{\gamma-\mathrm{jet}}$ and (f) $|\cos\,\theta^{\gamma-\mathrm{jet}}|$.

Jet energy scale and resolution uncertainties

The relative uncertainty in the jet energy scale was estimated taking into account all the different uncertainties described in Chapter 5. The relative jet energy scale uncertainty ($F^{\mathrm{EM+JES}}_{\pm,\mathrm{uncert}}$) is shown in Figs. 9.11(a) and 9.11(b) as a function of $P^{\mathrm{jet}}_{T,\mathrm{lead}}$ and $Y^{\mathrm{jet}}_{\mathrm{lead}}$, respectively.

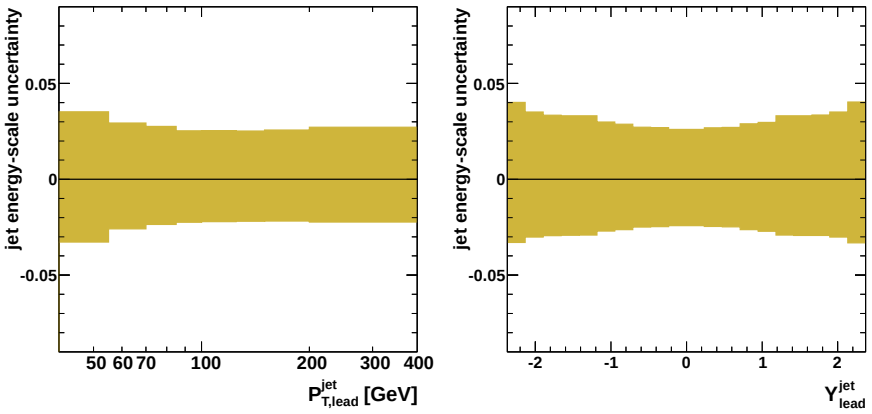

(a) (b)

Figure 9.11: Relative jet energy-scale uncertainty as a function of (a) $P^{\mathrm{jet}}_{T,\mathrm{lead}}$ and (b) $Y^{\mathrm{jet}}_{\mathrm{lead}}$.

As seen in Fig 9.11(a) and 9.11(b), the relative jet energy-scale uncertainty depends on both P^{jet}_T and Y^{jet}. The uncertainty in the cross section due to that on the jet energy scale was estimated by repeating the analysis after varying the P^{jet}_T and E^{jet} of all reconstructed jets with $P_T > 15$ GeV and $|Y^{\mathrm{jet}}| < 4.5$ in the simulated signal samples as follows:

$$\bar{E}^{\mathrm{jet}}_{\pm} = (1 \pm F^{\mathrm{EM+JES}}_{\pm,\mathrm{uncert}})E^{\mathrm{jet}} \tag{9.1}$$

$$\bar{P}^{\mathrm{jet}}_{\pm,T} = (1 \pm F^{\mathrm{EM+JES}}_{\pm,\mathrm{uncert}})P^{\mathrm{jet}}_T \ . \tag{9.2}$$

The uncertainty in the cross section was estimated as the relative difference between the modified cross section and the nominal value.

To evaluate the uncertainty related to the jet resolution, the cross sections were recomputed after including, in the simulated signal samples, an additional smearing to the P^{jet}_T and E^{jet} for each jet reconstructed in an event. In this case, for each jet candidate, an random quantity was applied multiplicatively to P^{jet}_T and E^{jet}. This random number was generated from a Gaussian distribution centered on unity with width equal to the data relative jet energy resolution ($\sigma^{\mathrm{jet}}_{\mathrm{data}}$) (see Figure 9.12).

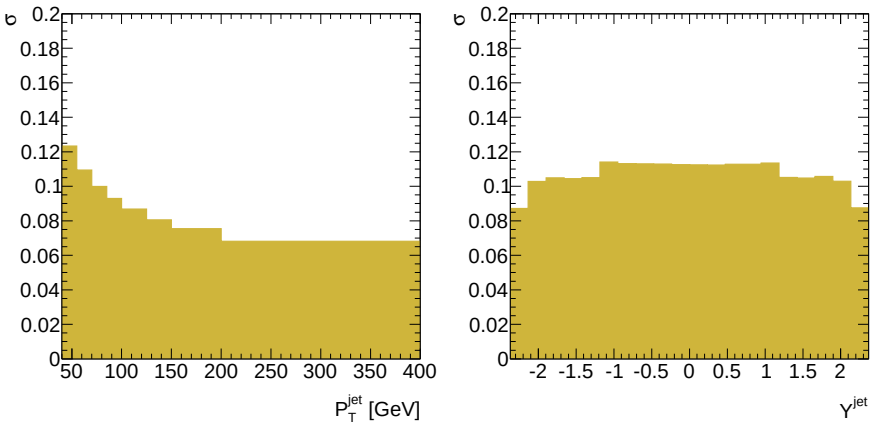

(a) (b)

Figure 9.12: Relative jet energy resolution as a function of (a) $P_{T,\mathrm{lead}}^{\mathrm{jet}}$ and (b) $Y_{\mathrm{lead}}^{\mathrm{jet}}$.

The relative systematic uncertainties in the differential cross sections due to the effects mentioned above are shown in Fig 9.13 as functions of the six observables.

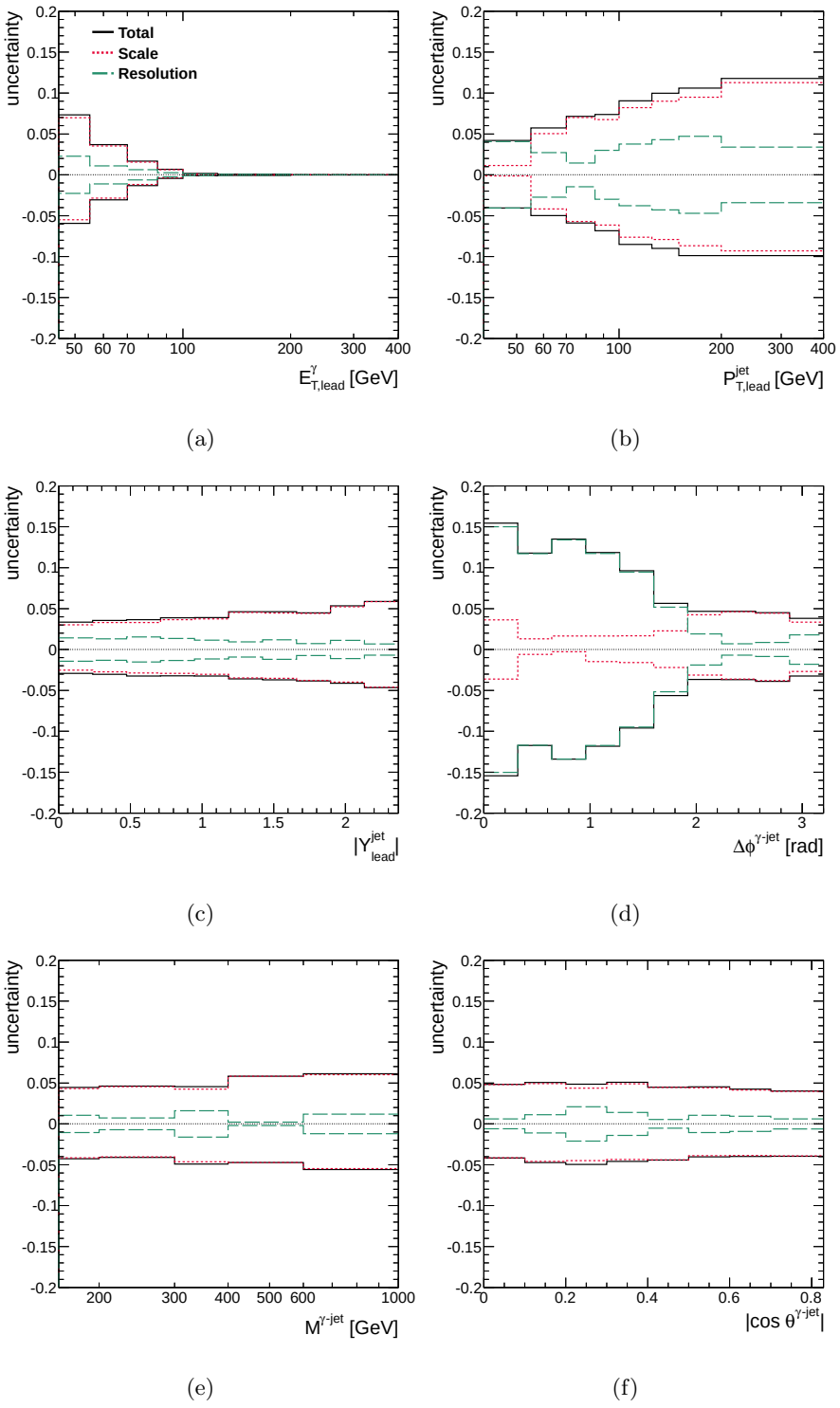

Figure 9.13: Relative systematic uncertainties due to the uncertainty in the jet energy scale and resolution for the differential cross sections as functions of (a) $E^{\gamma}_{T,\mathrm{lead}}$, (b) $P^{\mathrm{jet}}_{T,\mathrm{lead}}$, (c) $|Y^{\mathrm{jet}}_{\mathrm{lead}}|$, (d) $\Delta\phi^{\gamma-\mathrm{jet}}$, (e) $M^{\gamma-\mathrm{jet}}$ and (f) $|\cos\,\theta^{\gamma-\mathrm{jet}}|$.

9.1.4 Identification and isolation correlation in the background

The isolation and identification photon variables used to define the 2D plane to subtract the background contamination (see Chapter 7) were assumed to be uncorrelated for background events ($R^{\text{bg}} = 1$). Any correlation between these variables would affect the estimation of the purity of the signal and would lead to systematic uncertainties in the background-subtraction procedure.

The pseudo-correlation coefficient R^{bg} was estimated using a Monte Carlo background sample. As an example, Fig. 9.14(a) shows R^{bg} as a function of $E^{\gamma}_{T,\text{lead}}$. A straight-line fit to the distribution yields 1.012 ± 0.187.

A data-driven test of the no-correlation hypothesis was also performed. For this purpose, the 2D plane formed by the isolation and identification variables used for the background estimation was considered in which the E_T^{iso} isolation variable cut was varied from 3-5 GeV (the nominal values for the signal identification) up to 15-17 GeV in steps of 1 GeV. Figure 9.14(b) shows the mean value of R^{bg} as a function of the lower-boundary cut in E_T^{iso} for data. It is observed that in the region of the signal ($E_T^{\text{iso}} < 5$ GeV), the mean value of R^{bg} is small and increases as the cut in E_T^{iso} increases, reaching a plateau at ≈ 1 in the region $E_T^{\text{iso}} \approx 11$ GeV. Figure 7.1 shows that for $E_T^{\text{iso}} > 11$ GeV the data sample consists mainly of background; for this value of E_T^{iso}, the mean value of R^{bg} is 0.971 ± 0.014.

These estimations are consistent with those presented previously [56]. Therefore, the same upper limit on $|1 - R|$ of 0.1 was taken, conservatively, as the uncertainty related to the identification and isolation correlation in the background. Figure 9.15 shows the resulting relative uncertainties in differential cross sections as functions of the six observables.

9.1.5 Choice of background control region

The estimation of the purity of the signal is affected by the choice of the background control regions. The uncertainty due to this choice was estimated by repeating the analysis with identification criteria based on cuts in seven shower shapes variables (R_{had}, R_η, w_2, R_ϕ, w_{stot}, ΔE and E_{ratio}, see Chapter 5) or on cuts in four shower shapes variables (R_{had}, R_η, w_2, R_ϕ) instead of the nominal five variables and by changing the isolation boundary from the nominal of 5 GeV to 4 or 6 GeV. Figure 9.16 shows the resulting relative uncertainties in the differential cross sections

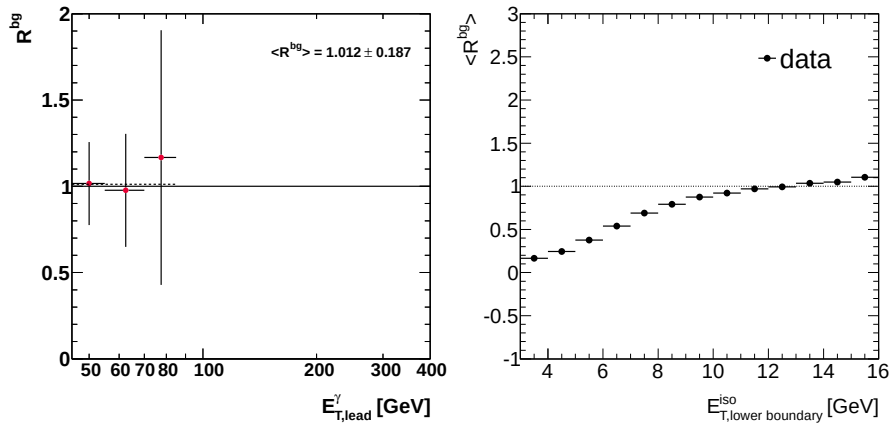

(a) (b)

Figure 9.14: (a) Background pseudo-correlation factor R^{bg} between the photon isolation and identification variables as a function of $E^{\gamma}_{T,\mathrm{lead}}$ for a PYTHIA MC background sample (dots). (b) Average background pseudocorrelation factor $< R^{\mathrm{bg}} >$ between the photon isolation and identification variables as a function of the E_T^{iso} cuts as extracted from data (dots).

as functions of the six observables.

9.1.6 Photon shower-shape correction

The shower-shape variables of the simulated photons were adjusted according to the observed differences between simulation and data (for photons passing the "tight" criteria). A factor was applied to each MC shower-shape variable which depends on E_T^{γ} and η^{γ} in order to match the mean values of each shower-shape variable between data and Monte Carlo [98].

Several sources of systematic uncertainty affect the precision of this method:

- intrinsic precision of the correction method for the shower-shape variables: depending on the η region, this uncertainty ranges between $\pm 1\%$ and $\pm 3\%$;
- choice of photon-candidate sample to estimate the correction factors: the photon identification efficiencies evaluated for different sample selections (e.g. using different photon shower-shape variables) agree within $\pm 0.5\%$;
- knowledge of the material in front of the calorimeter: this uncertainty is estimated to be $< 1\%$ in the barrel regions and $< 2\%$ in the end-cap regions;

- direct-photon/fragmentation-processes relative composition: varying the sample composition of the two types of photons by as much as 100% affects the global identification efficiencies by $< 1\%$. An additional 1% is assigned when a different MC generator is used;

- classification between converted and unconverted photon candidates: the impact of the classification between converted- and unconverted-photon candidates was studied by varying the efficiency of correctly classifying converted-photon candidates in the simulation. A loss of less than 1% on the overall efficiency is found for a -10% change in the efficiency to classify correctly converted photons;

Table 9.1 shows the total uncertainty due to the previously listed effects on the photon-identification efficiency. To estimate the photon shower-shape correction uncertainty the factors listed in Table 9.1 were used.

Figure 9.17 shows the resulting relative uncertainties in the differential cross sections as functions of the six observables.

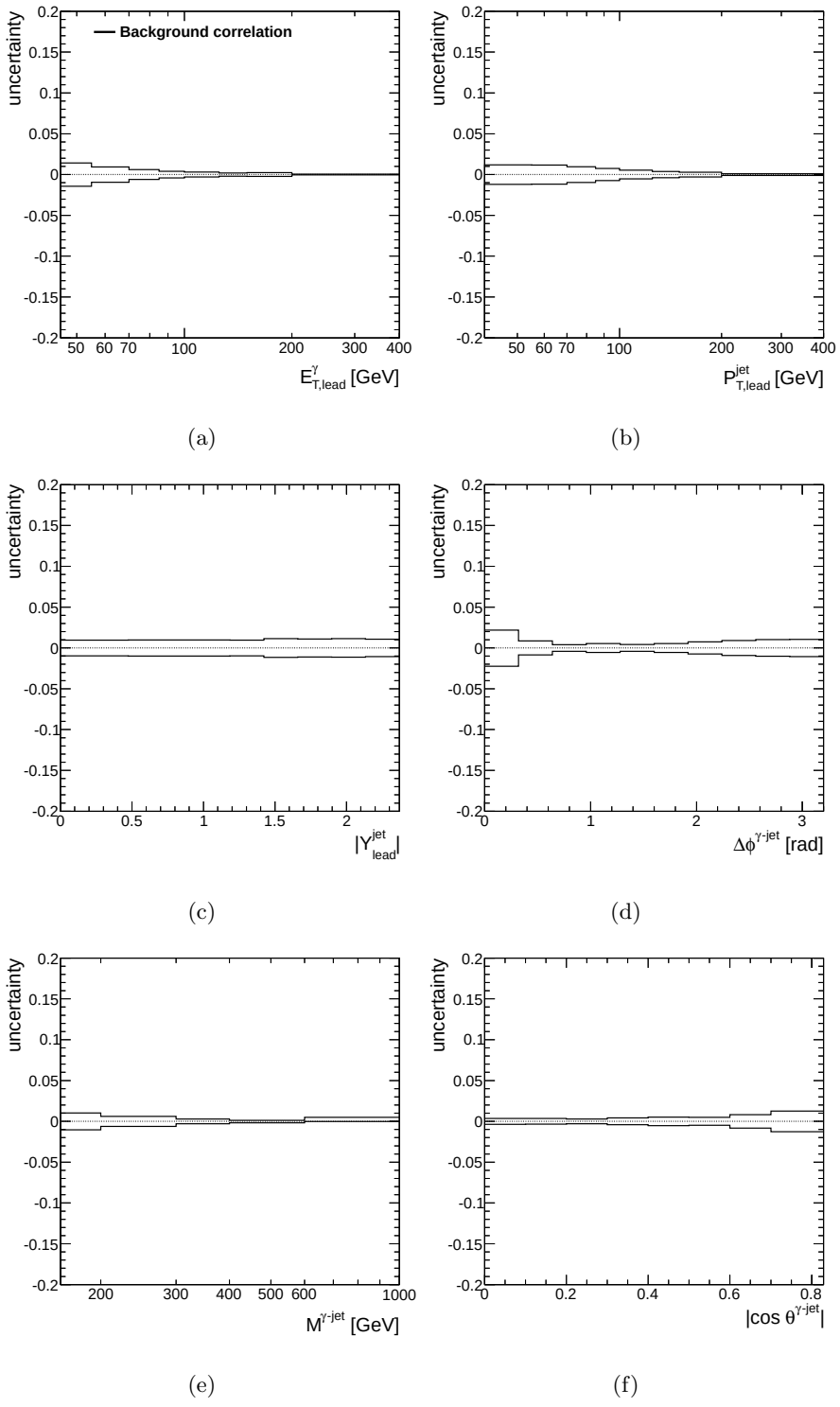

Figure 9.15: Relative systematic uncertainties due to the identification and isolation correlation in the background for the differential cross sections as functions of (a) $E^{\gamma}_{T,\mathrm{lead}}$, (b) $P^{\mathrm{jet}}_{T,\mathrm{lead}}$, (c) $|Y^{\mathrm{jet}}_{\mathrm{lead}}|$, (d) $\Delta\phi^{\gamma-\mathrm{jet}}$, (e) $M^{\gamma-\mathrm{jet}}$ and (f) $|\cos\,\theta^{\gamma-\mathrm{jet}}|$.

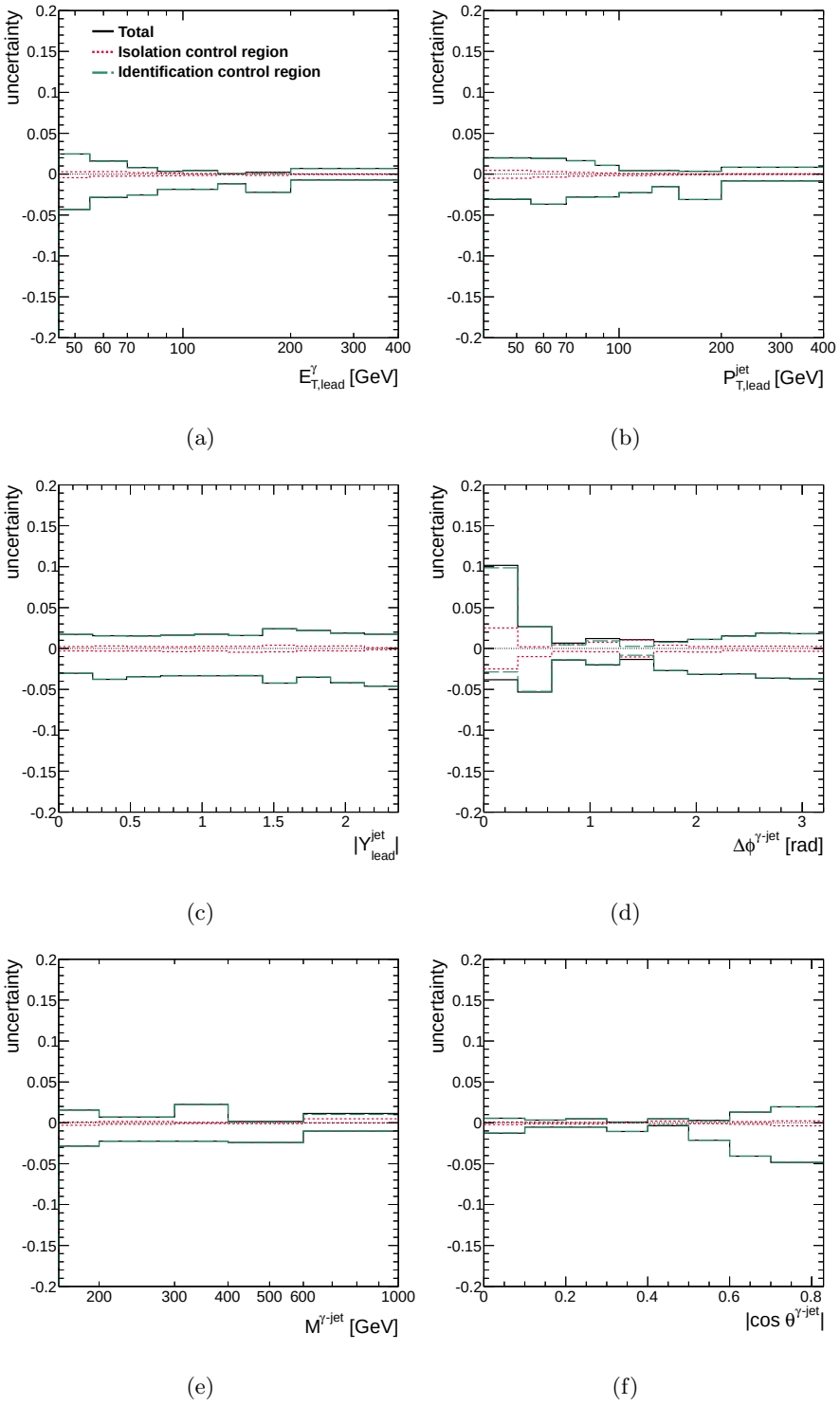

Figure 9.16: Relative systematic uncertainties due to the choice of the background control regions for the differential cross sections as functions of (a) $E^{\gamma}_{T,\mathrm{lead}}$, (b) $P^{\mathrm{jet}}_{T,\mathrm{lead}}$, (c) $|Y^{\mathrm{jet}}_{\mathrm{lead}}|$, (d) $\Delta\phi^{\gamma-\mathrm{jet}}$, (e) $M^{\gamma-\mathrm{jet}}$ and (f) $|\cos\,\theta^{\gamma-\mathrm{jet}}|$.

9.1.7 Jet-reconstruction efficiency

The uncertainty in the jet-reconstruction efficiency used in this analysis is based on the estimation of previous ATLAS jet cross-section measurements using the 2010 *pp* data [99].

The uncertainty on the jet-reconstruction efficiency was evaluated using jets reconstructed from tracks (track jets), which are used as a proxy for truth jets. The efficiency to reconstruct a calorimeter jet given a track jet nearby was studied in both data and Monte Carlo. The data vs. MC comparison of this efficiency was used to infer the degree up to which the calorimeter jet-reconstruction efficiency may be mis-modelled in the Monte Carlo. The disagreement had been found to be ±2% for $p_T^{\text{jet}} = 20$ GeV and less than ±1% for $p_T^{\text{jet}} > 30$ GeV. Therefore, a ±1% uncertainty was assigned to the jet-reconstruction efficiency.

Figure 9.18 shows the resulting relative uncertainties in the differential cross sections as functions of the six observables.

9.1.8 Jet-quality selection efficiency

The efficiency of the jet-quality criteria was determined to be 99% (see Chapter 5). Since no correction was applied due to these criteria, an uncertainty of +1% was included. Figure 9.19 shows the resulting relative uncertainties in the differential cross sections as functions of the six observables.

9.1.9 Trigger efficiency

The efficiency of the calorimeter trigger ϵ^{trig}, relative to the photon reconstruction and offline selection, is defined as the probability of a prompt photon to pass the EF_g40_loose trigger selection, where the prompt photon is reconstructed with experimental isolation lower than 3 GeV and passes the tight photon identification criteria. This was estimated in data using a bootstrap method, where the efficiency was measured for a sample of events passing the L1_EM14 trigger.

This trigger requires at least one electromagnetic cluster with $E_T > 14$ GeV and is fully efficient for photon clusters with $E_T > 20$ GeV.

The estimation of the EF_g40_loose efficiency in data was found to be $(99.4^{+0.6}_{-0.2})\%$ for $E_T^{\gamma} > 45$ GeV and all η bins, with a negligible η and E_T dependence. The un-

E_T^γ bin (GeV)	uncertainty (±%)
$\lvert\eta^\gamma\rvert < 0.6$	
$45 - 55$	2.3
$55 - 70$	2.0
$70 - 85$	2.0
$85 - 100$	1.8
$100 - 125$	1.8
$125 - 150$	1.8
$150 - 200$	1.8
$200 - 400$	1.8
$0.6 < \lvert\eta^\gamma\rvert < 1.37$	
$45 - 55$	2.0
$55 - 70$	2.0
$70 - 85$	1.8
$85 - 100$	1.8
$100 - 125$	1.7
$125 - 150$	1.7
$150 - 200$	1.7
$200 - 400$	1.7
$1.52 < \lvert\eta^\gamma\rvert < 1.81$	
$45 - 55$	2.2
$55 - 70$	2.0
$70 - 85$	1.8
$85 - 100$	1.8
$100 - 125$	1.7
$125 - 150$	1.8
$150 - 200$	1.8
$200 - 400$	1.7
$1.81 < \lvert\eta^\gamma\rvert < 2.37$	
$45 - 55$	3.5
$55 - 70$	3.0
$70 - 85$	3.1
$85 - 100$	3.5
$100 - 125$	3.2
$125 - 150$	3.0
$150 - 200$	3.1
$200 - 400$	2.9

Table 9.1: Uncertainty on the photon-identification efficiency due to the shower-shape corrections.

certainty on this value is taken from the statistical uncertainty of the efficiency measurement plus an upper error band to cover for systematic uncertainties related to residual background contamination.

The EF_g40_loose trigger efficiency in MC is 100%. Since no correction was applied due to these criteria, an uncertainty of +0.6% was included.

Figure 9.20 shows the resulting relative uncertainties in the differential cross sections as functions of the six observables.

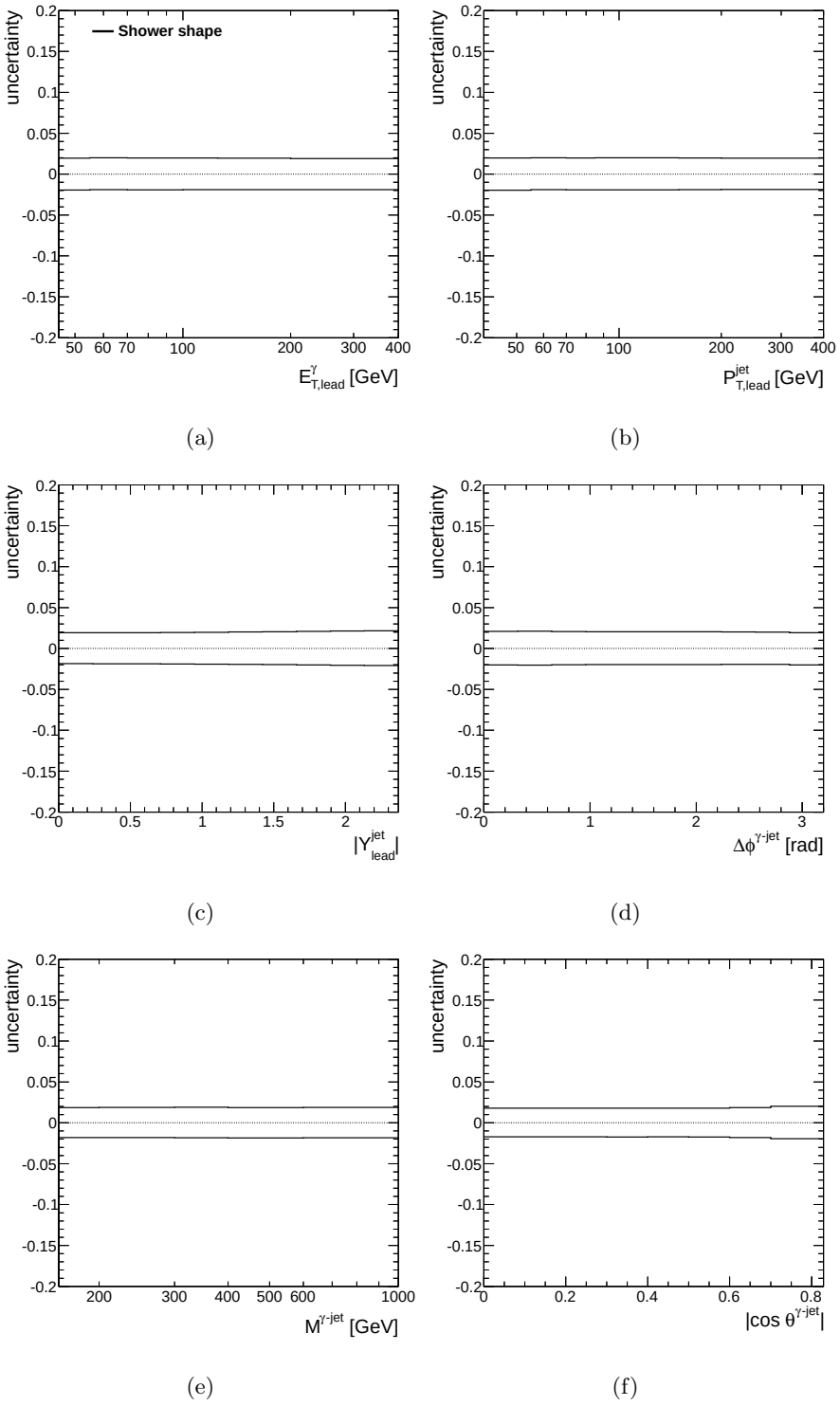

Figure 9.17: Relative systematic uncertainties due to the shower-shape corrections for the differential cross sections as functions of (a) $E^{\gamma}_{T,\mathrm{lead}}$, (b) $P^{\mathrm{jet}}_{T,\mathrm{lead}}$, (c) $|Y^{\mathrm{jet}}_{\mathrm{lead}}|$, (d) $\Delta\phi^{\gamma-\mathrm{jet}}$, (e) $M^{\gamma-\mathrm{jet}}$ and (f) $|\cos\,\theta^{\gamma-\mathrm{jet}}|$.

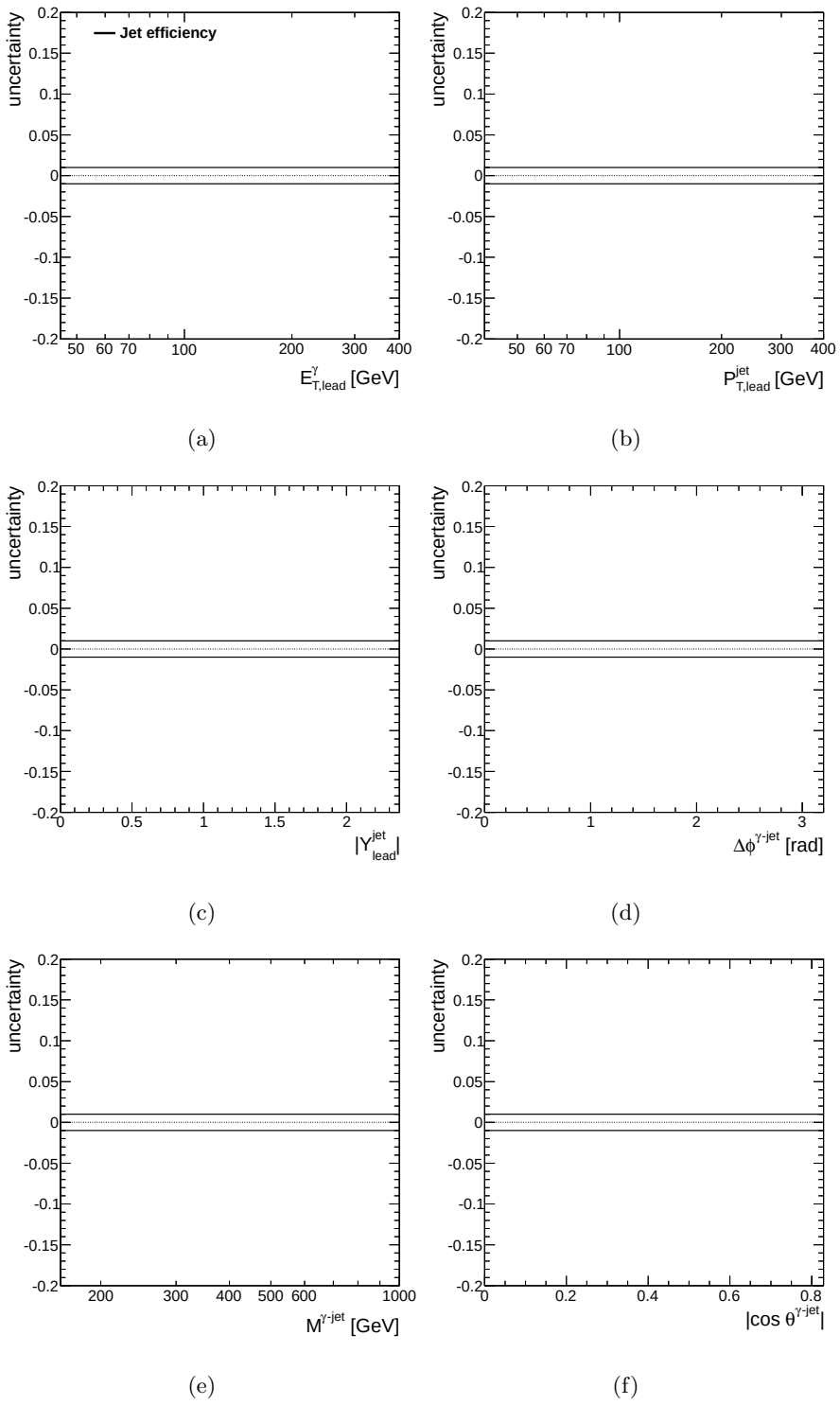

Figure 9.18: Relative systematic uncertainties due to the jet reconstruction efficiency for the differential cross sections as functions of a) $E^{\gamma}_{T,\mathrm{lead}}$, (b) $P^{\mathrm{jet}}_{T,\mathrm{lead}}$, (c) $|Y^{\mathrm{jet}}_{\mathrm{lead}}|$, (d) $\Delta\phi^{\gamma-\mathrm{jet}}$, (e) $M^{\gamma-\mathrm{jet}}$ and (f) $|\cos\,\theta^{\gamma-\mathrm{jet}}|$.

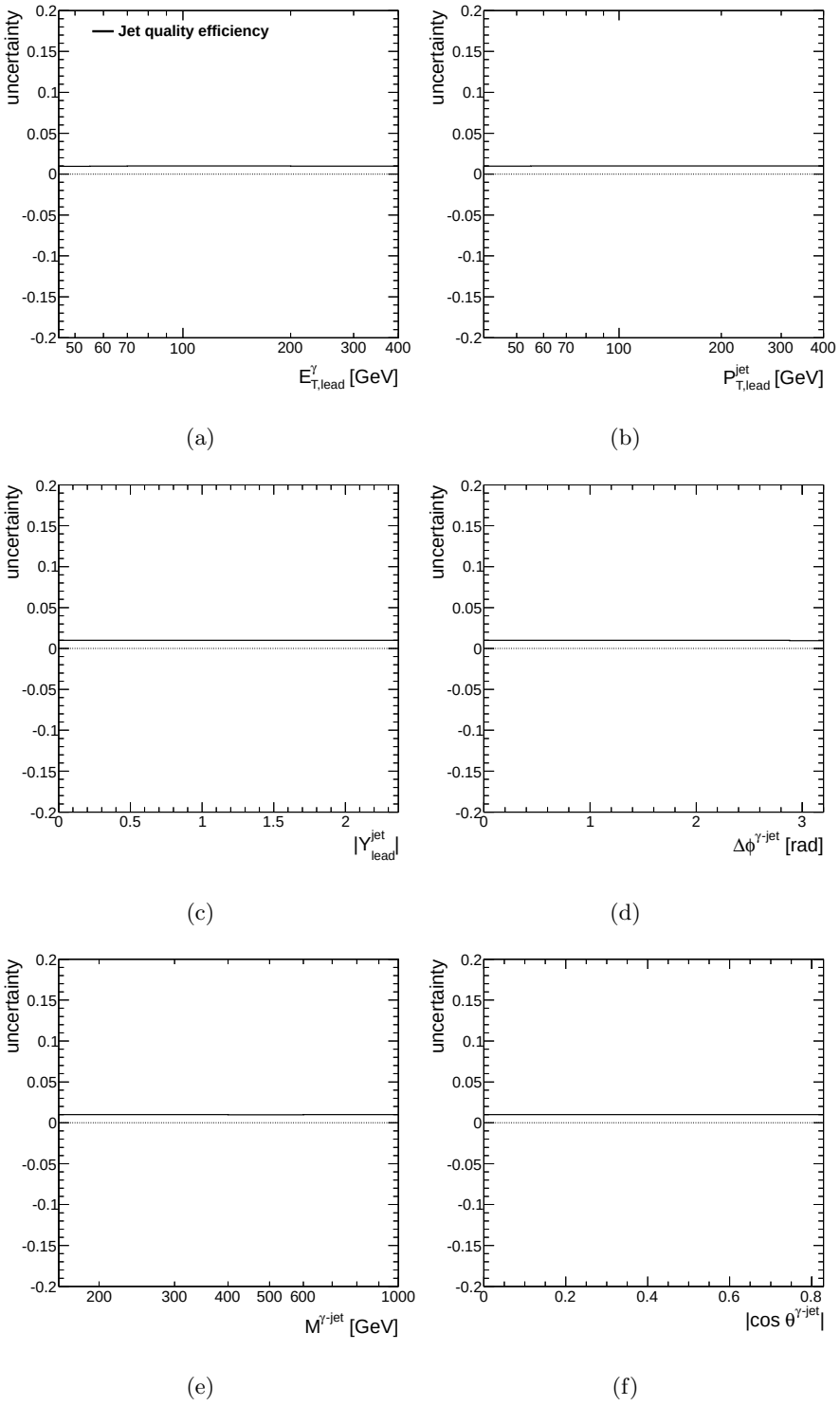

Figure 9.19: Relative systematic uncertainties due to the jet quality efficiency for the differential cross sections as functions of a) $E^{\gamma}_{T,\mathrm{lead}}$, (b) $P^{\mathrm{jet}}_{T,\mathrm{lead}}$, (c) $|Y^{\mathrm{jet}}_{\mathrm{lead}}|$, (d) $\Delta\phi^{\gamma-\mathrm{jet}}$, (e) $M^{\gamma-\mathrm{jet}}$ and (f) $|\cos\,\theta^{\gamma-\mathrm{jet}}|$.

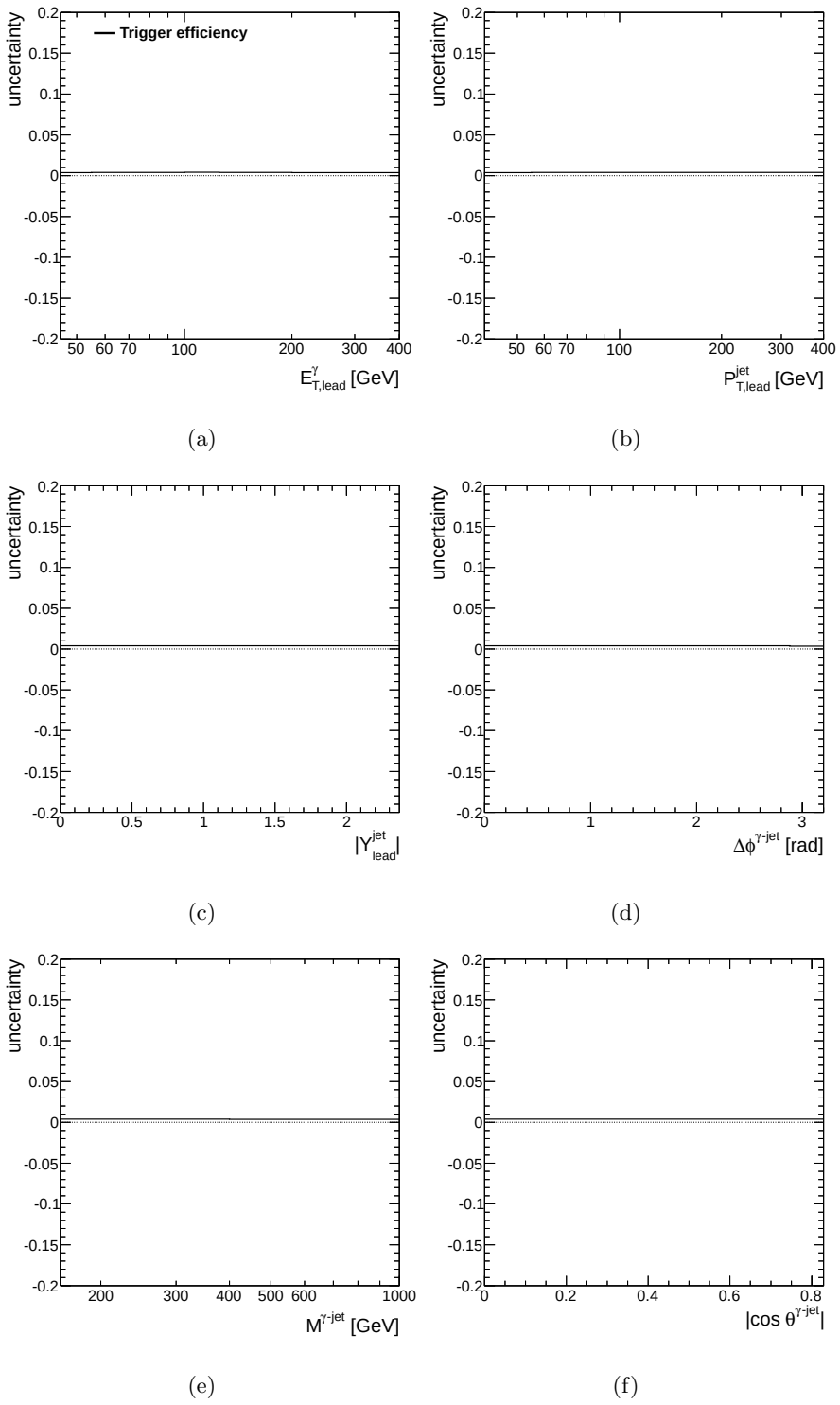

Figure 9.20: Relative systematic uncertainties due to the trigger efficiency for the differential cross sections as functions of a) $E^{\gamma}_{T,\mathrm{lead}}$, (b) $P^{\mathrm{jet}}_{T,\mathrm{lead}}$, (c) $|Y^{\mathrm{jet}}_{\mathrm{lead}}|$, (d) $\Delta\phi^{\gamma-\mathrm{jet}}$, (e) $M^{\gamma-\mathrm{jet}}$ and (f) $|\cos\,\theta^{\gamma-\mathrm{jet}}|$.

9.1.10 Luminosity-measurement uncertainty

The luminosity in ATLAS is estimated by measuring the interaction rate in the very forward direction, using detectors at small angles to the beam direction. An absolute calibration is obtained from van der Meer scans [100], where the beams are swept through each other.

Several sources of uncertainty affect the measurement of the luminosity. Table 9.2 summarizes the systematic sources considered to estimate the luminosity uncertainty. The estimated total uncertainty for the 2010 data-taking period is ±3.4% [91].

Uncertainty Source	δ**L/L**
Statistical	<0.1%
Bunch charge product	3.1%
Beam centering	0.1%
Emittance growth and other non-reproducibility	0.4%
Beam position jitter	0.2%
Length scale calibration	0.3%
Absolute ID length scale	0.3%
Fit model	0.2%
Transverse correlations	0.9%
μ dependence	0.6%
Long-term consistency	0.5%
Total	3.4%

Table 9.2: Relative uncertainty contributions to the luminosity measurement.

Figure 9.21 shows the resulting relative uncertainty in the differential cross sections as functions of the six observables.

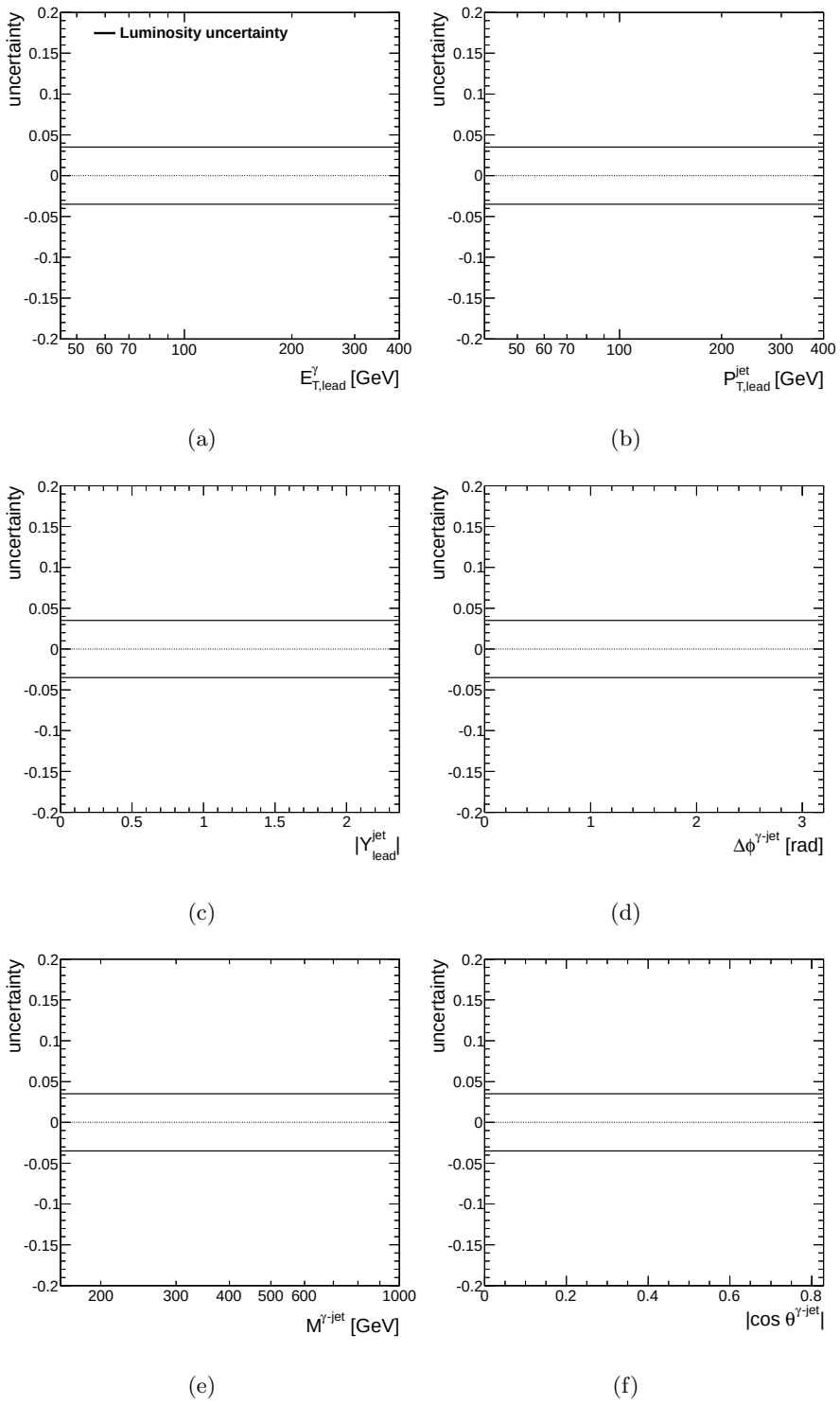

Figure 9.21: Relative systematic uncertainties due to the luminosity uncertainty for the differential cross sections as functions of a) $E^{\gamma}_{T,\mathrm{lead}}$, (b) $P^{\mathrm{jet}}_{T,\mathrm{lead}}$, (c) $|Y^{\mathrm{jet}}_{\mathrm{lead}}|$, (d) $\Delta\phi^{\gamma-\mathrm{jet}}$, (e) $M^{\gamma-\mathrm{jet}}$ and (f) $|\cos\,\theta^{\gamma-\mathrm{jet}}|$.

9.1.11 Total systematic uncertainty

Tables 9.3 to 9.8 show the individual relative systematic uncertainties listed above for each bin of each cross section measured. For comparison, the statistical uncertainty is also included.

For $E_{T.\mathrm{lead}}^{\gamma}$, the dominant uncertainties arise from the detector material in the simulation, the model dependence in the signal leakage fractions and the photon energy scale, though in some bins the uncertainty from the luminosity measurement provides the largest contribution. For $P_{T,\mathrm{lead}}^{\mathrm{jet}}$, the dominant uncertainty in the first bins is due to the model dependence in the signal leakage fractions; in the tail of the distribution, the jet energy-scale uncertainty is the most important uncertainty. For $|Y_{\mathrm{lead}}^{\mathrm{jet}}|$, the dominant uncertainties arise from the detector material in the simulation, the model dependence in the signal leakage fractions and the jet energy scale. The dominant uncertainty in the region of low $\Delta\phi^{\gamma-\mathrm{jet}}$ values is due to the jet-resolution uncertainty. However, this is not very meaningful, because the dominance of the jet-resolution uncertainty is probably due to the low statistics in the low $\Delta\phi^{\gamma-\mathrm{jet}}$ region. For values of $\Delta\phi^{\gamma-\mathrm{jet}}$ close to π, the dominant uncertainties are due to that on the detector material simulation and the model dependence in the signal leakage fractions. For $M^{\gamma-\mathrm{jet}}$, the statistical uncertainty is dominant in the last bin of the distribution, whereas the systematic uncertainty introduced by the jet energy scale dominates the rest of the distribution. For $|\cos\,\theta^{\gamma-\mathrm{jet}}|$, the dominant uncertainty comes from the uncertainty due to the detector material in the simulation.

All these systematic uncertainties were added in quadrature together with the statistical uncertainty and are shown as error bars in the figures of the differential cross sections. Figure 9.22 shows the total systematic uncertainties in the differential cross sections as functions of the six observables. The photon and the jet energy-scale uncertainties and, for comparison, the quadrature of the remaining uncertainties are also shown separately in the figure.

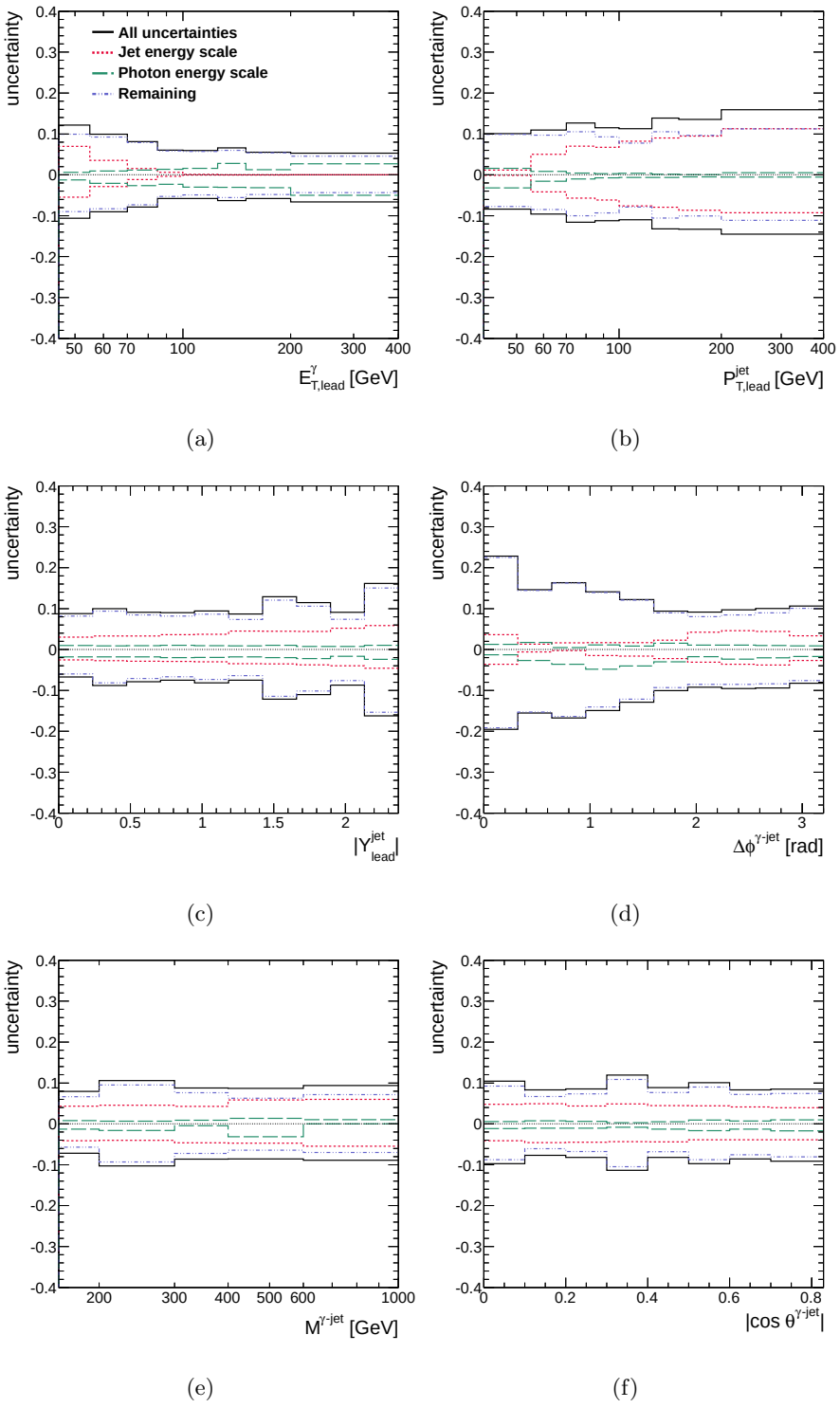

Figure 9.22: Relative total systematic, photon energy scale, jet energy scale and remaining uncertainties for the differential cross sections as functions of a) $E^{\gamma}_{T,\mathrm{lead}}$, (b) $P^{\mathrm{jet}}_{T,\mathrm{lead}}$, (c) $|Y^{\mathrm{jet}}_{\mathrm{lead}}|$, (d) $\Delta\phi^{\gamma-\mathrm{jet}}$, (e) $M^{\gamma-\mathrm{jet}}$ and (f) $|\cos\,\theta^{\gamma-\mathrm{jet}}|$.

$E^{\gamma}_{T,\mathrm{lead}}$ bin (GeV)	δ_{I}	δ_{II}	δ_{III}	δ_{IV}	δ_{V}	δ_{VI}	δ_{VII}	δ_{VIII}	δ_{IX} (%)	δ_{X}	δ_{XI}	δ_{XII}	δ_{XIII}	δ_{XIV}	δ_{XV}	δ_{XVI}	δ_{stat}
$45-55$	±5.7	$^{+5.8}_{-2.1}$	$^{+0.58}_{-0.58}$	±0.91	$^{+0.62}_{-1.3}$	$^{+7.0}_{-5.5}$	$^{+0.077}_{-0.077}$	$^{+2.3}_{-2.3}$	$^{+1.4}_{-1.4}$	$^{+0.27}_{-0.44}$	$^{+2.5}_{-4.3}$	$^{+1.9}_{-2.0}$	±1.0	$+0.4$	$+1.0$	±3.4	±0.56
$55-70$	±6.3	$^{+4.8}_{-1.5}$	$^{+0.30}_{-0.30}$	±0.34	$^{+0.94}_{-2.1}$	$^{+3.5}_{-2.9}$	$^{+0.041}_{-0.039}$	$^{+1.1}_{-1.1}$	$^{+0.94}_{-0.95}$	$^{+0.31}_{-0.26}$	$^{+1.6}_{-2.8}$	$^{+2.0}_{-1.9}$	±1.0	$+0.4$	$+1.0$	±3.4	±0.62
$70-85$	±5.3	$^{+3.8}_{-1.1}$	$^{+0.16}_{-0.16}$	±0.34	$^{+1.2}_{-2.6}$	$^{+1.5}_{-1.2}$	$^{+0.13}_{-0.13}$	$^{+0.63}_{-0.63}$	$^{+0.60}_{-0.61}$	$^{+0.19}_{-0.24}$	$^{+0.79}_{-2.5}$	$^{+2.0}_{-1.9}$	±1.0	$+0.4$	$+1.0$	±3.4	±0.91
$85-100$	±2.5	$^{+3.0}_{-0.82}$	$^{+0.78}_{-0.78}$	±0.23	$^{+1.4}_{-2.3}$	$^{+0.63}_{-0.36}$	$^{+0.15}_{-0.15}$	$^{+0.25}_{-0.25}$	$^{+0.41}_{-0.41}$	$^{+0.14}_{-0.20}$	$^{+0.33}_{-1.8}$	$^{+2.0}_{-1.9}$	±1.0	$+0.4$	$+1.0$	±3.4	±1.3
$100-125$	±1.8	$^{+3.3}_{-0.66}$	$^{+0.091}_{-0.091}$	±0.075	$^{+1.6}_{-3.0}$	$^{+0.11}_{-0.025}$	$^{+0.26}_{-0.26}$	$^{+0.12}_{-0.12}$	$^{+0.30}_{-0.30}$	$^{+0.074}_{-0.16}$	$^{+0.43}_{-1.9}$	$^{+2.0}_{-1.9}$	±1.0	$+0.4$	$+1.0$	±3.4	±1.5
$125-150$	±3.4	$^{+2.4}_{-0.51}$	$^{+0.59}_{-0.59}$	±0.21	$^{+2.8}_{-3.0}$	$^{+0.020}_{-0.020}$	$^{+0.40}_{-0.40}$	$^{+0.063}_{-0.063}$	$^{+0.19}_{-0.20}$	$^{+0.047}_{-0.067}$	$^{+0.026}_{-1.2}$	$^{+2.0}_{-1.9}$	±1.0	$+0.4$	$+1.0$	±3.4	±2.4
$150-200$	±1.1	$^{+3.0}_{-0.45}$	$^{+0.25}_{-0.25}$	±0.15	$^{+1.3}_{-3.2}$	$^{+0.016}_{-0.035}$	$^{+0.26}_{-0.26}$	$^{+0.064}_{-0.064}$	$^{+0.23}_{-0.23}$	$^{+0.21}_{-0.17}$	$^{+0.10}_{-2.2}$	$^{+2.0}_{-1.9}$	±1.0	$+0.4$	$+1.0$	±3.4	±3.1
$200-400$	±1.3	$^{+0.65}_{-0.19}$	$^{+0.11}_{-0.11}$	±0.13	$^{+2.7}_{-5.0}$	$^{+0.0059}_{-0.0065}$	$^{+0.11}_{-0.11}$	$^{+0.0039}_{-0.0039}$	$^{+0.053}_{-0.053}$	$^{+0.016}_{-0.034}$	$^{+0.71}_{-0.71}$	$^{+1.9}_{-1.9}$	±1.0	$+0.4$	$+1.0$	±3.4	±4.8

Table 9.3: Relative systematic uncertainties introduced by the detector material in the simulation (δ_{I}), the model dependence in the signal leakage fractions (δ_{II}), the model dependence in the acceptance correction factors (δ_{III}), the fit dependence (δ_{IV}), the photon energy scale (δ_{V}), the jet energy scale (δ_{VI}), the photon resolution scale (δ_{VII}), the jet resolution scale (δ_{VIII}), the identification and isolation correlation in background (δ_{IX}), the choice of background control regions (δ_{X} and δ_{XI}), the shower-shape corrections (δ_{XII}), the jet-reconstruction efficiency (δ_{XIII}), the trigger efficiency (δ_{XIV}), the jet-quality efficiency (δ_{XV}) and the luminosity-measurement uncertainty (δ_{XVI}) for the $d\sigma/dE^{\gamma}_{T,\mathrm{lead}}$ cross section. For comparison, the last column shows the statistical uncertainty.

$P_{T,\mathrm{lead}}^{\mathrm{jet}}$ bin (GeV)	δ_{I}	δ_{II}	δ_{III}	δ_{IV}	δ_{V}	δ_{VI}	δ_{VII}	δ_{VIII}	δ_{IX}	δ_{X}	δ_{XI}	δ_{XII}	δ_{XIII}	δ_{XIV}	δ_{XV}	δ_{XVI}	δ_{stat}
									(%)								
$40-55$	±3.5	$^{+6.6}_{-1.4}$	$^{+0.93}_{-0.93}$	±0.11	$^{+1.6}_{-3.2}$	$^{+1.1}_{-0.12}$	$^{+0.097}_{-0.097}$	$^{+4.1}_{-4.1}$	$^{+1.2}_{-1.2}$	$^{+0.46}_{-0.50}$	$^{+2.0}_{-3.0}$	$^{+2.0}_{-2.0}$	±1.0	$+0.4$	$+1.0$	±3.4	±0.60
$55-70$	±5.4	$^{+5.7}_{-1.4}$	$^{+1.2}_{-1.2}$	±0.058	$^{+0.83}_{-1.6}$	$^{+5.0}_{-4.2}$	$^{+0.065}_{-0.065}$	$^{+2.7}_{-2.7}$	$^{+1.2}_{-1.2}$	$^{+0.29}_{-0.37}$	$^{+1.9}_{-3.7}$	$^{+2.0}_{-1.9}$	±1.0	$+0.4$	$+1.0$	±3.4	±0.67
$70-85$	±7.9	$^{+4.0}_{-1.5}$	$^{+2.8}_{-2.8}$	±0.17	$^{+0.41}_{-1.0}$	$^{+7.0}_{-5.7}$	$^{+0.052}_{-0.018}$	$^{+1.5}_{-1.5}$	$^{+0.95}_{-0.96}$	$^{+0.21}_{-0.24}$	$^{+1.6}_{-2.8}$	$^{+2.0}_{-1.9}$	±1.0	$+0.4$	$+1.0$	±3.4	±0.85
$85-100$	±6.7	$^{+2.5}_{-1.3}$	$^{+2.3}_{-2.3}$	±0.54	$^{+0.28}_{-0.75}$	$^{+6.7}_{-6.1}$	$^{+0.066}_{-0.066}$	$^{+3.0}_{-3.0}$	$^{+0.74}_{-0.75}$	$^{+0.15}_{-0.17}$	$^{+1.1}_{-2.8}$	$^{+2.0}_{-1.9}$	±1.0	$+0.4$	$+1.0$	±3.4	±1.1
$100-125$	±4.6	$^{+1.7}_{-1.2}$	$^{+1.2}_{-1.2}$	±1.0	$^{+0.38}_{-0.63}$	$^{+8.2}_{-7.6}$	$^{+0.057}_{-0.057}$	$^{+3.8}_{-3.8}$	$^{+0.53}_{-0.54}$	$^{+0.078}_{-0.18}$	$^{+0.41}_{-2.3}$	$^{+2.0}_{-1.9}$	±1.0	$+0.4$	$+1.0$	±3.4	±1.3
$125-150$	±8.3	$^{+1.6}_{-1.3}$	$^{+1.3}_{-1.3}$	±0.57	$^{+0.16}_{-0.64}$	$^{+9.0}_{-7.9}$	$^{+0.17}_{-0.17}$	$^{+4.3}_{-4.3}$	$^{+0.38}_{-0.39}$	$^{+0.094}_{-0.11}$	$^{+0.44}_{-1.5}$	$^{+2.0}_{-1.9}$	±1.0	$+0.4$	$+1.0$	±3.4	±2.0
$150-200$	±6.0	$^{+1.8}_{-1.6}$	$^{+3.6}_{-3.6}$	±0.027	$^{+0.070}_{-0.50}$	$^{+9.4}_{-8.7}$	$^{+0.029}_{-0.028}$	$^{+4.7}_{-4.7}$	$^{+0.28}_{-0.29}$	$^{+0.030}_{-0.092}$	$^{+0.35}_{-3.1}$	$^{+2.0}_{-1.9}$	±1.0	$+0.4$	$+1.0$	±3.4	±2.3
$200-400$	±7.9	$^{+0.83}_{-0.60}$	$^{+5.7}_{-5.7}$	±0.72	$^{+0.51}_{-0.53}$	$^{+11.3}_{-9.3}$	$^{+0.068}_{-0.045}$	$^{+3.4}_{-3.4}$	$^{+0.10}_{-0.10}$	$^{+0.051}_{-0.050}$	$^{+0.84}_{-0.84}$	$^{+2.0}_{-1.9}$	±1.0	$+0.4$	$+1.0$	±3.4	±3.1

Table 9.4: Relative systematic uncertainties introduced by the detector material in the simulation (δ_{I}), the model dependence in the signal leakage fractions (δ_{II}), the model dependence in the acceptance correction factors (δ_{III}), the fit dependence (δ_{IV}), the photon energy scale (δ_{V}), the jet energy scale (δ_{VI}), the photon resolution scale (δ_{VII}), the jet resolution scale (δ_{VIII}), the identification and isolation correlation in background (δ_{IX}), the choice of background control regions (δ_{X} and δ_{XI}), the shower-shape corrections (δ_{XII}), the jet-reconstruction efficiency (δ_{XIII}), the trigger efficiency (δ_{XIV}), the jet-quality efficiency (δ_{XV}) and the luminosity-measurement uncertainty (δ_{XVI}) for the $d\sigma/dP_{T,\mathrm{lead}}^{\mathrm{jet}}$ cross section. For comparison, the last column shows the statistical uncertainty.

$\lvert Y^{\text{jet}}_{\text{lead}}\rvert$ bin	δ_{I}	δ_{II}	δ_{III}	δ_{IV}	δ_{V}	δ_{VI}	δ_{VII}	δ_{VIII}	δ_{IX} (%)	δ_{X}	δ_{XI}	δ_{XII}	δ_{XIII}	δ_{XIV}	δ_{XV}	δ_{XVI}	δ_{stat}
$0.000 - 0.237$	±1.7	$^{+6.3}_{-1.8}$	$^{+0.88}_{-0.88}$	±0.096	$^{+0.99}_{-1.8}$	$^{+3.0}_{-2.5}$	$^{+0.014}_{-0.044}$	$^{+1.4}_{-1.4}$	$^{+0.96}_{-0.97}$	$^{+0.23}_{-0.29}$	$^{+1.7}_{-3.0}$	$^{+1.9}_{-1.9}$	±1.0	$+0.4$	$+1.0$	±3.4	±0.95
$0.237 - 0.474$	±5.3	$^{+5.9}_{-1.7}$	$^{+1.5}_{-1.5}$	±0.072	$^{+0.91}_{-1.8}$	$^{+3.3}_{-2.7}$	$^{+0.18}_{-0.18}$	$^{+1.3}_{-1.3}$	$^{+0.95}_{-0.96}$	$^{+0.31}_{-0.33}$	$^{+1.5}_{-3.8}$	$^{+1.9}_{-1.9}$	±1.0	$+0.4$	$+1.0$	±3.4	±0.94
$0.474 - 0.711$	±3.8	$^{+5.6}_{-1.7}$	$^{+0.83}_{-0.83}$	±0.018	$^{+0.93}_{-1.8}$	$^{+3.3}_{-2.9}$	$^{+0.084}_{-0.084}$	$^{+1.5}_{-1.5}$	$^{+0.99}_{-1.0}$	$^{+0.24}_{-0.30}$	$^{+1.5}_{-3.4}$	$^{+1.9}_{-1.9}$	±1.0	$+0.4$	$+1.0$	±3.4	±0.98
$0.711 - 0.948$	±3.2	$^{+5.7}_{-1.7}$	$^{+0.67}_{-0.67}$	±0.10	$^{+1.0}_{-2.0}$	$^{+3.6}_{-2.9}$	$^{+0.022}_{-0.038}$	$^{+1.3}_{-1.3}$	$^{+0.98}_{-0.98}$	$^{+0.21}_{-0.40}$	$^{+1.6}_{-3.3}$	$^{+2.0}_{-1.9}$	±1.0	$+0.4$	$+1.0$	±3.4	±1.0
$0.948 - 1.185$	±4.5	$^{+5.5}_{-1.7}$	$^{+0.088}_{-0.088}$	±0.077	$^{+0.95}_{-1.9}$	$^{+3.7}_{-3.0}$	$^{+0.11}_{-0.11}$	$^{+1.1}_{-1.1}$	$^{+1.0}_{-1.0}$	$^{+0.27}_{-0.30}$	$^{+1.7}_{-3.3}$	$^{+2.0}_{-1.9}$	±1.0	$+0.4$	$+1.0$	±3.4	±1.0
$1.185 - 1.422$	±2.9	$^{+4.7}_{-1.5}$	$^{+0.35}_{-0.35}$	±0.017	$^{+0.88}_{-1.8}$	$^{+4.5}_{-3.5}$	$^{+0.081}_{-0.081}$	$^{+0.93}_{-0.93}$	$^{+0.96}_{-0.97}$	$^{+0.26}_{-0.45}$	$^{+1.6}_{-3.3}$	$^{+2.0}_{-1.9}$	±1.0	$+0.4$	$+1.0$	±3.4	±1.1
$1.422 - 1.659$	±9.4	$^{+5.3}_{-1.8}$	$^{+1.1}_{-1.1}$	±0.10	$^{+1.0}_{-2.0}$	$^{+4.5}_{-3.5}$	$^{+0.11}_{-0.11}$	$^{+1.2}_{-1.2}$	$^{+1.1}_{-1.2}$	$^{+0.40}_{-0.42}$	$^{+2.4}_{-4.2}$	$^{+2.1}_{-2.0}$	±1.0	$+0.4$	$+1.0$	±3.4	±1.2
$1.659 - 1.896$	±8.3	$^{+4.1}_{-1.5}$	$^{+0.31}_{-0.31}$	±0.022	$^{+0.77}_{-2.2}$	$^{+4.4}_{-3.8}$	$^{+0.27}_{-0.27}$	$^{+0.73}_{-0.73}$	$^{+1.2}_{-1.1}$	$^{+0.27}_{-0.26}$	$^{+2.2}_{-3.5}$	$^{+2.1}_{-2.0}$	±1.0	$+0.4$	$+1.0$	±3.4	±1.3
$1.896 - 2.133$	±4.3	$^{+3.4}_{-1.3}$	$^{+0.19}_{-0.19}$	±0.036	$^{+0.73}_{-1.7}$	$^{+5.2}_{-4.0}$	$^{+0.091}_{-0.091}$	$^{+1.1}_{-1.1}$	$^{+1.1}_{-1.1}$	$^{+0.30}_{-0.30}$	$^{+1.8}_{-4.2}$	$^{+2.1}_{-2.1}$	±1.0	$+0.4$	$+1.0$	±3.4	±1.4
$2.133 - 2.370$	±13.9	$^{+2.8}_{-1.1}$	$^{+0.95}_{-0.95}$	±0.10	$^{+1.0}_{-2.4}$	$^{+5.8}_{-4.6}$	$^{+0.34}_{-0.34}$	$^{+0.68}_{-0.68}$	$^{+1.1}_{-1.1}$	$^{+0.088}_{-0.16}$	$^{+1.8}_{-4.6}$	$^{+2.2}_{-2.1}$	±1.0	$+0.4$	$+1.0$	±3.4	±1.5

Table 9.5: Relative systematic uncertainties introduced by the detector material in the simulation (δ_{I}), the model dependence in the signal leakage fractions (δ_{II}), the model dependence in the acceptance correction factors (δ_{III}), the fit dependence (δ_{IV}), the photon energy scale (δ_{V}), the jet energy scale (δ_{VI}), the photon resolution scale (δ_{VII}), the jet resolution scale (δ_{VIII}), the identification and isolation correlation in background (δ_{IX}), the choice of background control regions (δ_{X} and δ_{XI}), the shower-shape corrections (δ_{XII}), the jet-reconstruction efficiency (δ_{XIII}), the trigger efficiency (δ_{XIV}), the jet-quality efficiency (δ_{XV}) and the luminosity-measurement uncertainty (δ_{XVI}) for the $d\sigma/d|Y^{\text{jet}}_{\text{lead}}|$ cross section. For comparison, the last column shows the statistical uncertainty.

$\Delta\phi^{\gamma-\text{jet}}$ bin (rad)	δ_{I}	δ_{II}	δ_{III}	δ_{IV}	δ_{V}	δ_{VI}	δ_{VII}	δ_{VIII}	δ_{IX}	δ_{X}	δ_{XI}	δ_{XII}	δ_{XIII}	δ_{XIV}	δ_{XV}	δ_{XVI}	δ_{stat}
									(%)								
$0.00-0.32$	±5.5	$^{+7.0}_{-0.93}$	$^{+8.0}_{-8.0}$	±2.9	$^{+1.3}_{-1.3}$	$^{+3.6}_{-3.6}$	$^{+1.2}_{-1.2}$	$^{+15.0}_{-15.0}$	$^{+2.2}_{-2.2}$	$^{+2.5}_{-2.5}$	$^{+9.8}_{-2.9}$	$^{+2.1}_{-2.0}$	±1.0	$+0.4$	$+1.0$	±3.4	±16.4
$0.32-0.64$	±5.5	$^{+0.54}_{-2.5}$	$^{+1.8}_{-1.8}$	±3.0	$^{+1.7}_{-2.7}$	$^{+1.3}_{-0.61}$	$^{+1.4}_{-1.4}$	$^{+11.7}_{-11.7}$	$^{+0.85}_{-0.86}$	$^{+0.20}_{-0.99}$	$^{+2.7}_{-5.2}$	$^{+2.1}_{-2.0}$	±1.0	$+0.4$	$+1.0$	±3.4	±11.4
$0.64-0.96$	±5.5	$^{+0.27}_{-1.9}$	$^{+5.1}_{-5.1}$	±2.8	$^{+0.48}_{-3.6}$	$^{+1.7}_{-0.29}$	$^{+1.0}_{-1.0}$	$^{+13.4}_{-13.4}$	$^{+0.41}_{-0.41}$	$^{+0.47}_{-0.38}$	$^{+0.44}_{-1.4}$	$^{+2.1}_{-2.0}$	±1.0	$+0.4$	$+1.0$	±3.4	±7.2
$0.96-1.28$	±5.5	$^{+0.23}_{-1.2}$	$^{+1.3}_{-1.3}$	±2.2	$^{+1.1}_{-4.8}$	$^{+1.7}_{-1.5}$	$^{+0.32}_{-0.32}$	$^{+11.7}_{-11.7}$	$^{+0.54}_{-0.55}$	$^{+0.77}_{-0.42}$	$^{+0.93}_{-2.0}$	$^{+2.0}_{-2.0}$	±1.0	$+0.4$	$+1.0$	±3.4	±5.3
$1.28-1.60$	±5.5	$^{+0.35}_{-1.5}$	$^{+2.0}_{-2.0}$	±1.5	$^{+0.85}_{-4.0}$	$^{+1.7}_{-1.6}$	$^{+0.065}_{-0.15}$	$^{+9.5}_{-9.5}$	$^{+0.41}_{-0.42}$	$^{+1.0}_{-1.0}$	$^{+0.25}_{-0.83}$	$^{+2.1}_{-2.0}$	±1.0	$+0.4$	$+1.0$	±3.4	±4.0
$1.60-1.92$	±5.5	$^{+1.0}_{-1.7}$	$^{+0.64}_{-0.64}$	±1.5	$^{+1.5}_{-3.0}$	$^{+2.3}_{-2.2}$	$^{+0.45}_{-0.45}$	$^{+5.2}_{-5.2}$	$^{+0.54}_{-0.55}$	$^{+0.39}_{-0.39}$	$^{+0.75}_{-2.7}$	$^{+2.0}_{-2.0}$	±1.0	$+0.4$	$+1.0$	±3.4	±2.8
$1.92-2.24$	±5.5	$^{+1.9}_{-2.0}$	$^{+2.2}_{-2.2}$	±1.4	$^{+1.1}_{-1.7}$	$^{+4.2}_{-3.1}$	$^{+0.30}_{-0.30}$	$^{+1.9}_{-1.9}$	$^{+0.74}_{-0.75}$	$^{+0.24}_{-0.45}$	$^{+1.1}_{-3.1}$	$^{+2.0}_{-2.0}$	±1.0	$+0.4$	$+1.0$	±3.4	±1.9
$2.24-2.56$	±6.2	$^{+2.9}_{-1.9}$	$^{+0.57}_{-0.57}$	±1.3	$^{+1.1}_{-2.3}$	$^{+4.6}_{-3.6}$	$^{+0.12}_{-0.12}$	$^{+0.69}_{-0.69}$	$^{+0.90}_{-0.91}$	$^{+0.29}_{-0.25}$	$^{+1.5}_{-3.1}$	$^{+2.0}_{-2.0}$	±1.0	$+0.4$	$+1.0$	±3.4	±1.2
$2.56-2.88$	±5.7	$^{+4.7}_{-1.8}$	$^{+0.99}_{-0.99}$	±1.0	$^{+0.99}_{-2.0}$	$^{+4.4}_{-3.8}$	$^{+0.017}_{-0.017}$	$^{+0.86}_{-0.86}$	$^{+1.0}_{-1.0}$	$^{+0.27}_{-0.31}$	$^{+1.9}_{-3.6}$	$^{+2.0}_{-1.9}$	±1.0	$+0.4$	$+1.0$	±3.4	±0.70
$2.88-3.14$	±4.4	$^{+7.4}_{-1.5}$	$^{+0.73}_{-0.73}$	±0.28	$^{+0.87}_{-1.7}$	$^{+3.4}_{-2.7}$	$^{+0.030}_{-0.030}$	$^{+1.8}_{-1.8}$	$^{+1.1}_{-1.1}$	$^{+0.26}_{-0.34}$	$^{+1.8}_{-3.7}$	$^{+1.9}_{-2.0}$	±1.0	$+0.4$	$+1.0$	±3.4	±0.45

Table 9.6: Relative systematic uncertainties introduced by the detector material in the simulation (δ_{I}), the model dependence in the signal leakage fractions (δ_{II}), the model dependence in the acceptance correction factors (δ_{III}), the fit dependence (δ_{IV}), the photon energy scale (δ_{V}), the jet energy scale (δ_{VI}), the photon resolution scale (δ_{VII}), the jet resolution scale (δ_{VIII}), the identification and isolation correlation in background (δ_{IX}), the choice of background control regions (δ_{X} and δ_{XI}), the shower-shape corrections (δ_{XII}), the jet-reconstruction efficiency (δ_{XIII}), the trigger efficiency (δ_{XIV}), the jet-quality efficiency (δ_{XV}) and the luminosity-measurement uncertainty (δ_{XVI}) for the $d\sigma/d\Delta\phi^{\gamma-\text{jet}}$ cross section. For comparison, the last column shows the statistical uncertainty.

$M^{\gamma-\text{jet}}$ bin (GeV)	δ_{I}	δ_{II}	δ_{III}	δ_{IV}	δ_{V}	δ_{VI}	δ_{VII}	δ_{VIII}	δ_{IX} (%)	δ_{X}	δ_{XI}	δ_{XII}	δ_{XIII}	δ_{XIV}	δ_{XV}	δ_{XVI}	δ_{stat}
$161-200$	±0.92	$^{+4.4}_{-1.8}$	$^{+0.91}_{-0.91}$	±0.87	$^{+0.78}_{-1.3}$	$^{+4.3}_{-4.1}$	$^{+0.072}_{-0.072}$	$^{+1.1}_{-1.1}$	$^{+1.0}_{-1.0}$	$^{+0.086}_{-0.29}$	$^{+1.6}_{-2.8}$	$^{+1.8}_{-1.8}$	±1.0	$+0.4$	$+1.0$	±3.4	±1.0
$200-300$	±7.4	$^{+3.0}_{-1.5}$	$^{+2.7}_{-2.7}$	±0.93	$^{+0.66}_{-1.6}$	$^{+4.6}_{-4.0}$	$^{+0.0060}_{-0.0060}$	$^{+0.73}_{-0.73}$	$^{+0.61}_{-0.61}$	$^{+0.16}_{-0.18}$	$^{+0.67}_{-2.2}$	$^{+1.9}_{-1.8}$	±1.0	$+0.4$	$+1.0$	±3.4	±1.1
$300-400$	±4.7	$^{+2.3}_{-1.1}$	$^{+1.8}_{-1.8}$	±0.95	$^{+0.90}_{-0.46}$	$^{+4.3}_{-4.6}$	$^{+0.27}_{-0.27}$	$^{+1.6}_{-1.6}$	$^{+0.28}_{-0.31}$	$^{+0.059}_{-0.082}$	$^{+2.2}_{-2.2}$	$^{+1.9}_{-1.8}$	±1.0	$+0.4$	$+1.0$	±3.4	±2.5
$400-600$	±3.8	$^{+1.7}_{-0.63}$	$^{+1.6}_{-1.6}$	±1.1	$^{+1.4}_{-3.2}$	$^{+5.8}_{-4.7}$	$^{+0.15}_{-0.042}$	$^{+0.20}_{-0.20}$	$^{+0.11}_{-0.18}$	$^{+0.11}_{-0.11}$	$^{+0.11}_{-2.4}$	$^{+1.9}_{-1.9}$	±1.0	$+0.4$	$+1.0$	±3.4	±4.0
$600-1000$	±4.2	$^{+0.54}_{-0.54}$	$^{+3.1}_{-3.1}$	±1.4	$^{+1.0}_{-0.0023}$	$^{+6.0}_{-5.5}$	$^{+0.59}_{-0.59}$	$^{+1.2}_{-1.2}$	$^{+0.48}_{-0.012}$	$^{+0.48}_{-0.012}$	$^{+1.0}_{-1.0}$	$^{+1.9}_{-1.8}$	±1.0	$+0.4$	$+1.0$	±3.4	±10.0

Table 9.7: Relative systematic uncertainties introduced by the detector material in the simulation (δ_{I}), the model dependence in the signal leakage fractions (δ_{II}), the model dependence in the acceptance correction factors (δ_{III}), the fit dependence (δ_{IV}), the photon energy scale (δ_{V}), the jet energy scale (δ_{VI}), the photon resolution scale (δ_{VII}), the jet resolution scale (δ_{VIII}), the identification and isolation correlation in background (δ_{IX}), the choice of background control regions (δ_{X} and δ_{XI}), the shower-shape corrections (δ_{XII}), the jet-reconstruction efficiency (δ_{XIII}), the trigger efficiency (δ_{XIV}), the jet-quality efficiency (δ_{XV}) and the luminosity-measurement uncertainty (δ_{XVI}) for the $d\sigma/dM^{\gamma-\text{jet}}$ cross section. For comparison, the last column shows the statistical uncertainty.

$\lvert\cos\theta^{\gamma-\text{jet}}\rvert$ bin	δ_{I}	δ_{II}	δ_{III}	δ_{IV}	δ_{V}	δ_{VI}	δ_{VII}	δ_{VIII}	δ_{IX} (%)	δ_{X}	δ_{XI}	δ_{XII}	δ_{XIII}	δ_{XIV}	δ_{XV}	δ_{XVI}	δ_{stat}
$0.00-0.10$	±7.3	$^{+3.1}_{-0.85}$	$^{+1.1}_{-1.1}$	±1.7	$^{+0.55}_{-1.2}$	$^{+4.8}_{-4.1}$	$^{+0.20}_{-0.20}$	$^{+0.60}_{-0.60}$	$^{+0.35}_{-0.36}$	$^{+0.090}_{-0.23}$	$^{+0.55}_{-1.24}$	$^{+1.8}_{-1.7}$	±1.0	$+0.4$	$+1.0$	±3.4	±2.6
$0.10-0.20$	±4.1	$^{+2.6}_{-0.66}$	$^{+1.0}_{-1.0}$	±0.94	$^{+0.74}_{-1.1}$	$^{+4.9}_{-4.6}$	$^{+0.27}_{-0.27}$	$^{+1.1}_{-1.1}$	$^{+0.34}_{-0.35}$	$^{+0.067}_{-0.14}$	$^{+0.33}_{-0.51}$	$^{+1.8}_{-1.7}$	±1.0	$+0.4$	$+1.0$	±3.4	±2.6
$0.20-0.30$	±4.4	$^{+2.6}_{-0.71}$	$^{+0.46}_{-0.46}$	±2.1	$^{+0.62}_{-1.1}$	$^{+4.4}_{-4.5}$	$^{+0.34}_{-0.34}$	$^{+2.1}_{-2.1}$	$^{+0.29}_{-0.29}$	$^{+0.052}_{-0.15}$	$^{+0.50}_{-0.50}$	$^{+1.8}_{-1.7}$	±1.0	$+0.4$	$+1.0$	±3.4	±2.5
$0.30-0.40$	±9.2	$^{+3.0}_{-0.97}$	$^{+1.4}_{-1.4}$	±1.4	$^{+0.27}_{-0.82}$	$^{+4.9}_{-4.4}$	$^{+0.18}_{-0.18}$	$^{+1.4}_{-1.4}$	$^{+0.41}_{-0.42}$	$^{+0.082}_{-0.020}$	$^{+0.051}_{-1.1}$	$^{+1.8}_{-1.7}$	±1.0	$+0.4$	$+1.0$	±3.4	±2.4
$0.40-0.50$	±4.6	$^{+3.4}_{-1.1}$	$^{+1.3}_{-1.3}$	±2.4	$^{+0.54}_{-1.3}$	$^{+4.5}_{-4.4}$	$^{+0.32}_{-0.32}$	$^{+0.54}_{-0.54}$	$^{+0.52}_{-0.53}$	$^{+0.21}_{-0.21}$	$^{+0.43}_{-0.29}$	$^{+1.8}_{-1.7}$	±1.0	$+0.4$	$+1.0$	±3.4	±2.3
$0.50-0.60$	±6.7	$^{+3.0}_{-1.1}$	$^{+0.78}_{-0.78}$	±2.7	$^{+0.93}_{-1.7}$	$^{+4.4}_{-3.9}$	$^{+0.040}_{-0.040}$	$^{+1.1}_{-1.1}$	$^{+0.49}_{-0.49}$	$^{+0.16}_{-0.12}$	$^{+0.26}_{-2.1}$	$^{+1.8}_{-1.7}$	±1.0	$+0.4$	$+1.0$	±3.4	±2.0
$0.60-0.70$	±3.4	$^{+3.3}_{-1.6}$	$^{+2.3}_{-2.3}$	±1.6	$^{+0.71}_{-1.3}$	$^{+4.1}_{-3.9}$	$^{+0.081}_{-0.081}$	$^{+0.93}_{-0.93}$	$^{+0.82}_{-0.83}$	$^{+0.14}_{-0.19}$	$^{+1.3}_{-4.1}$	$^{+1.9}_{-1.8}$	±1.0	$+0.4$	$+1.0$	±3.4	±1.8
$0.70-0.83$	±3.3	$^{+3.9}_{-2.6}$	$^{+0.96}_{-0.96}$	±2.0	$^{+0.97}_{-1.7}$	$^{+4.0}_{-3.9}$	$^{+0.11}_{-0.11}$	$^{+0.62}_{-0.62}$	$^{+1.3}_{-1.3}$	$^{+0.23}_{-0.37}$	$^{+1.9}_{-4.8}$	$^{+2.0}_{-1.9}$	±1.0	$+0.4$	$+1.0$	±3.4	±1.3

Table 9.8: Relative systematic uncertainties introduced by the detector material in the simulation (δ_{I}), the model dependence in the signal leakage fractions (δ_{II}), the model dependence in the acceptance correction factors (δ_{III}), the fit dependence (δ_{IV}), the photon energy scale (δ_{V}), the jet energy scale (δ_{VI}), the photon resolution scale (δ_{VII}), the jet resolution scale (δ_{VIII}), the identification and isolation correlation in background (δ_{IX}), the choice of background control regions (δ_{X} and δ_{XI}), the shower-shape corrections (δ_{XII}), the jet-reconstruction efficiency (δ_{XIII}), the trigger efficiency (δ_{XIV}), the jet-quality efficiency (δ_{XV}) and the luminosity-measurement uncertainty (δ_{XVI}) for the $d\sigma/d\lvert\cos\theta^{\gamma-\text{jet}}\rvert$ cross section. For comparison, the last column shows the statistical uncertainty.

9.2 Cross checks

Additional cross checks were performed on data and Monte Carlo, such as the description of the measured primary vertex by the MC and pile-up effects. The effects of the primary vertex and track requirements were also studied. They are described below.
Even though an average effect of the pile-up contribution was subtracted to minimise the effect both for the photon isolation and the jet reconstruction, some differences between data and MC might remain. Such effects were investigated by studying the primary vertex and the jet vertex fraction (JVF) distributions in data and MC.

9.2.1 Primary-vertex distribution

A primary-vertex is defined as a vertex which has been assigned more than four tracks with $p_T^{\text{track}} > 150$ MeV and is compatible with the beam spot position and bunch crossing. Due to the pile-up, it is possible that more than one collision takes place in the same bunch crossing. Therefore, the reconstruction by the inner detector of more than one primary vertex is expected. Figure 9.23(a) shows the distribution of the number of primary vertices (N_{PV}) together with the simulations of PYTHIA and HERWIG. The MC has a different shape than the data. Such an effect is mainly due to the simulation of pile-up by MC generators being not exactly equal to the pile-up observed in the data. To evaluate the effects of such a discrepancy, the MC distributions were reweighted to the data, as shown in Fig. 9.23(b). The cross-section nominal results, shown in Chapter 11, are based on the reweighted MC samples.

The effect of such a reweighting on the measured differential cross sections is shown in Fig. 9.24; it amounts to typically $\lesssim 1\%$, except in the tail of the $\Delta\phi^{\gamma-\text{jet}}$ distribution due to statistical fluctuations. The differences in the measured cross sections between the region of low pile-up conditions (N_{PV} =1) and regions of high pile-up conditions ($N_{\text{PV}} \geq 2$) were also investigated. Such differences show the possible dependence on pile-up in the cross-section measurements. Therefore, another cross-check was made by repeating separately the whole analysis selecting events with only one, two or $\geq$ three primary vertices in data and MC. Figures 9.25 to 9.27 show the effect with respect to the nominal analysis as a function of the six observables. Although in some cases fluctuations are observed due to limited statistics, the overall effect is small.

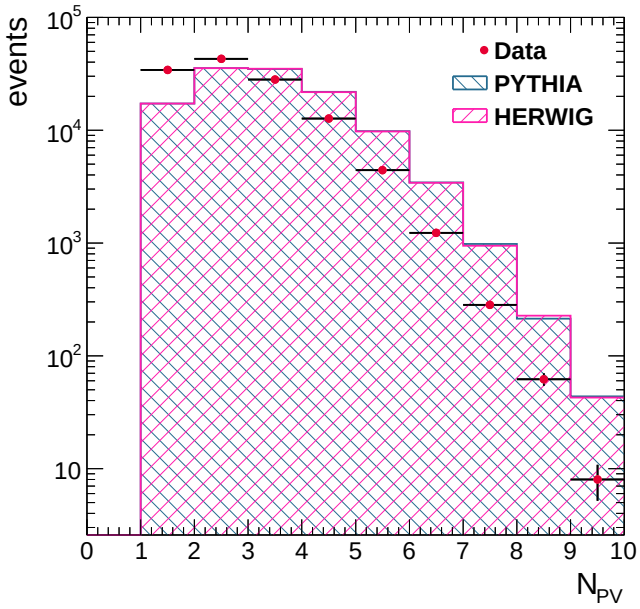

(a)

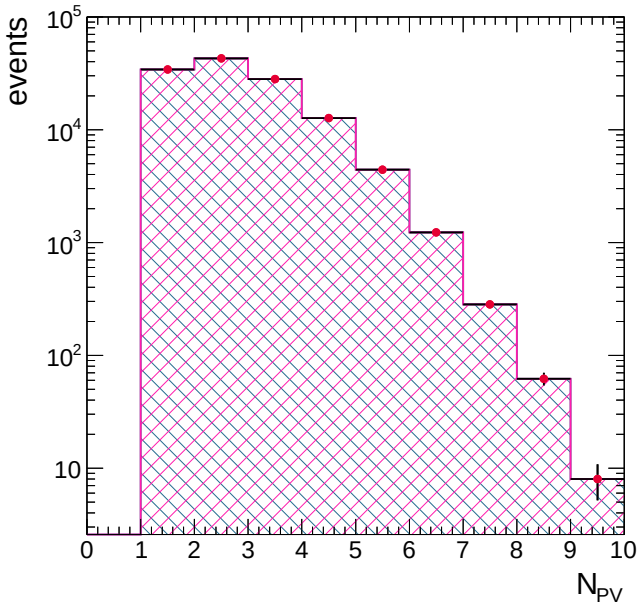

(b)

Figure 9.23: The measured distribution of the number of primary vertexes (dots). For comparison, the MC simulations of the signal from PYTHIA (right-hatched histograms) and HERWIG (left-hatched histograms) are also included in (a). In (b) the simulated distributions were reweighted to the data. In both cases, the MC distributions are normalised to the total number of data events.

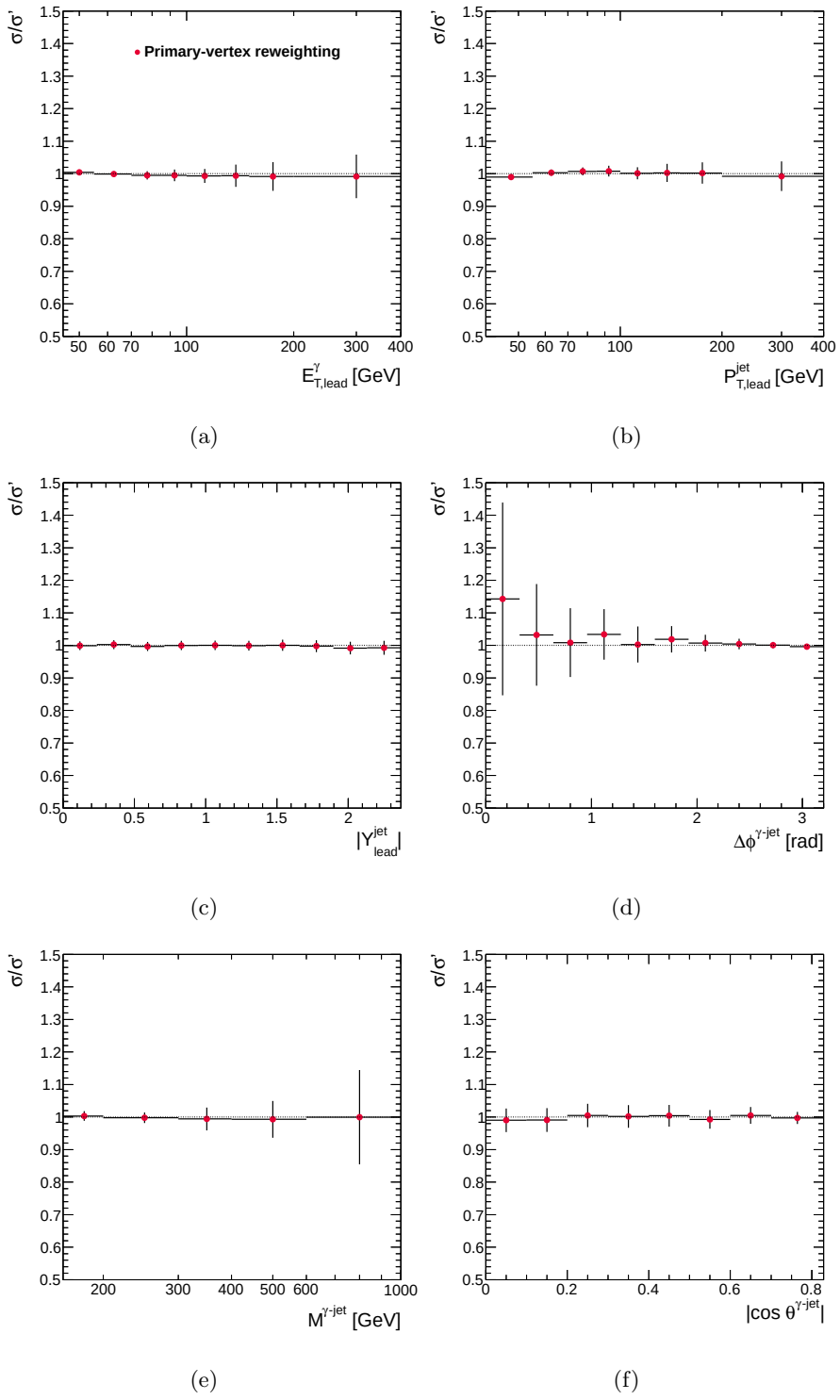

(a) (b) (c) (d) (e) (f)

Figure 9.24: Effect of primary-vertex reweighting in the differential cross sections as functions of (a) $E^{\gamma}_{T,\mathrm{lead}}$, (b) $P^{\mathrm{jet}}_{T,\mathrm{lead}}$, (c) $|Y^{\mathrm{jet}}_{\mathrm{lead}}|$, (d) $\Delta\phi^{\gamma-\mathrm{jet}}$, (e) $M^{\gamma-\mathrm{jet}}$ and (f) $|\cos\,\theta^{\gamma-\mathrm{jet}}|$.

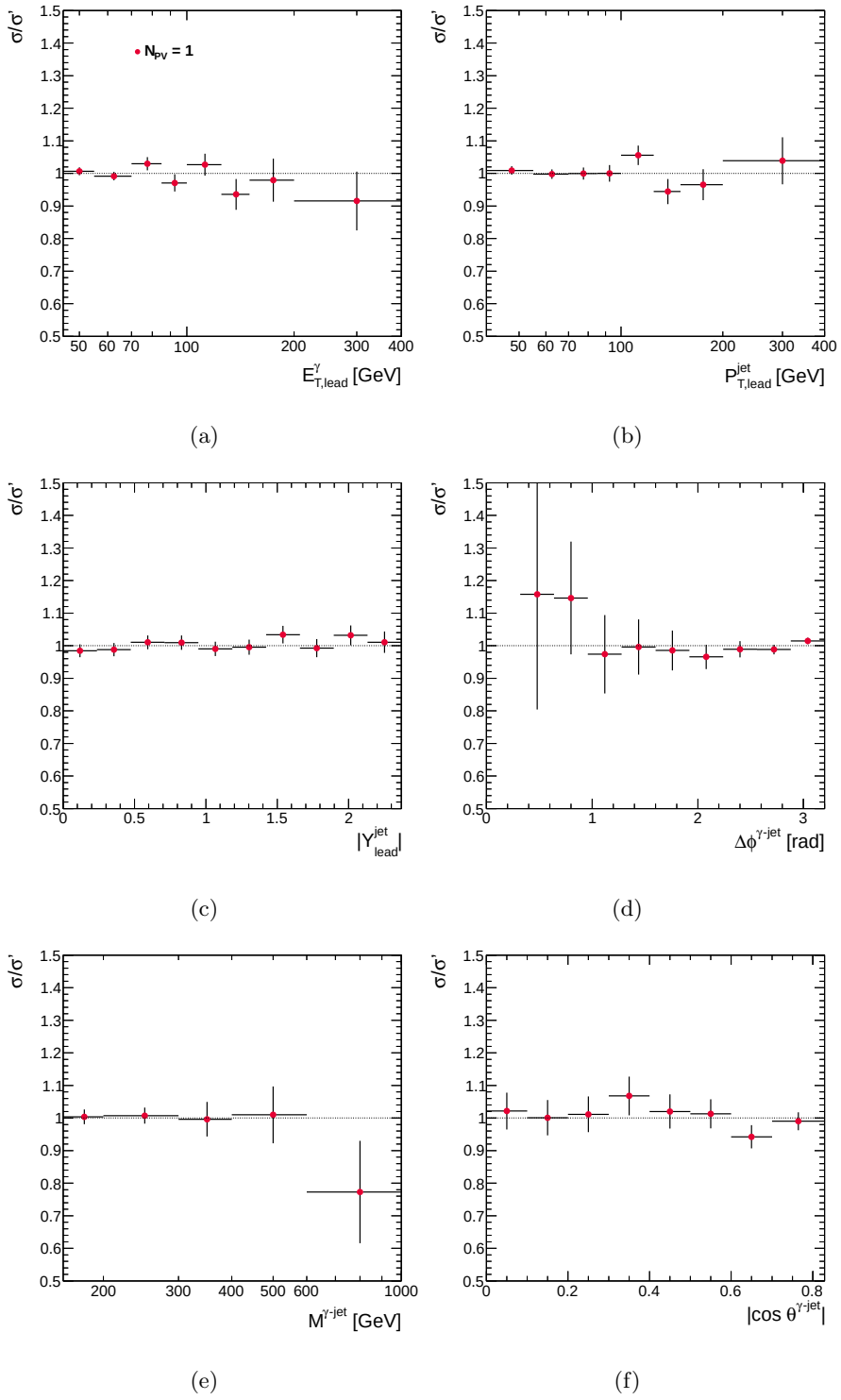

Figure 9.25: Effect of restricting the number of primary-vertex to one in the differential cross sections as functions of (a) $E^{\gamma}_{T,\mathrm{lead}}$, (b) $P^{\mathrm{jet}}_{T,\mathrm{lead}}$, (c) $|Y^{\mathrm{jet}}_{\mathrm{lead}}|$, (d) $\Delta\phi^{\gamma-\mathrm{jet}}$, (e) $M^{\gamma-\mathrm{jet}}$ and (f) $|\cos\,\theta^{\gamma-\mathrm{jet}}|$.

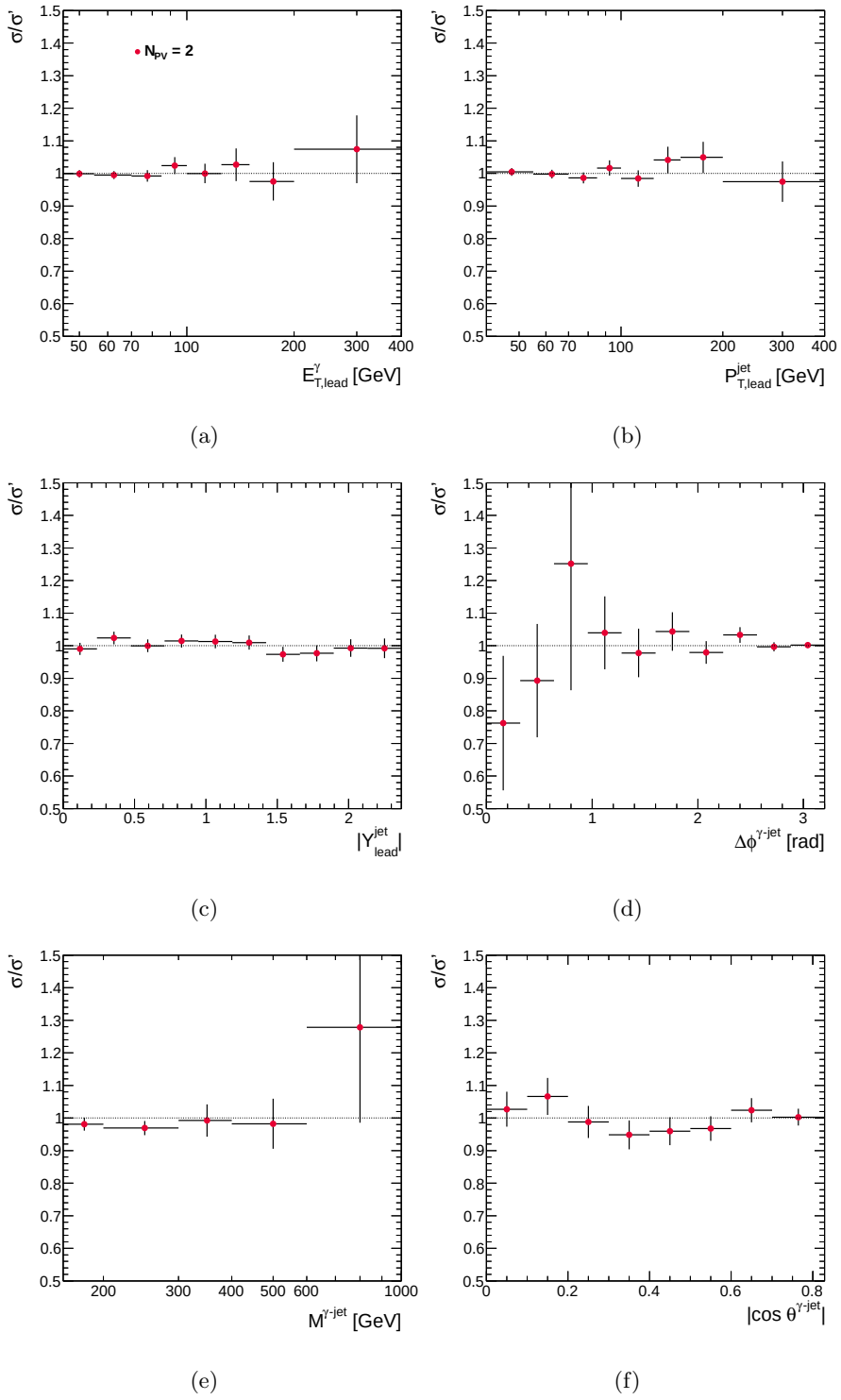

Figure 9.26: Effect of restricting the number of primary-vertex to two in the differential cross sections as functions of (a) $E^{\gamma}_{T,\mathrm{lead}}$, (b) $P^{\mathrm{jet}}_{T,\mathrm{lead}}$, (c) $|Y^{\mathrm{jet}}_{\mathrm{lead}}|$, (d) $\Delta\phi^{\gamma-\mathrm{jet}}$, (e) $M^{\gamma-\mathrm{jet}}$ and (f) $|\cos\,\theta^{\gamma-\mathrm{jet}}|$.

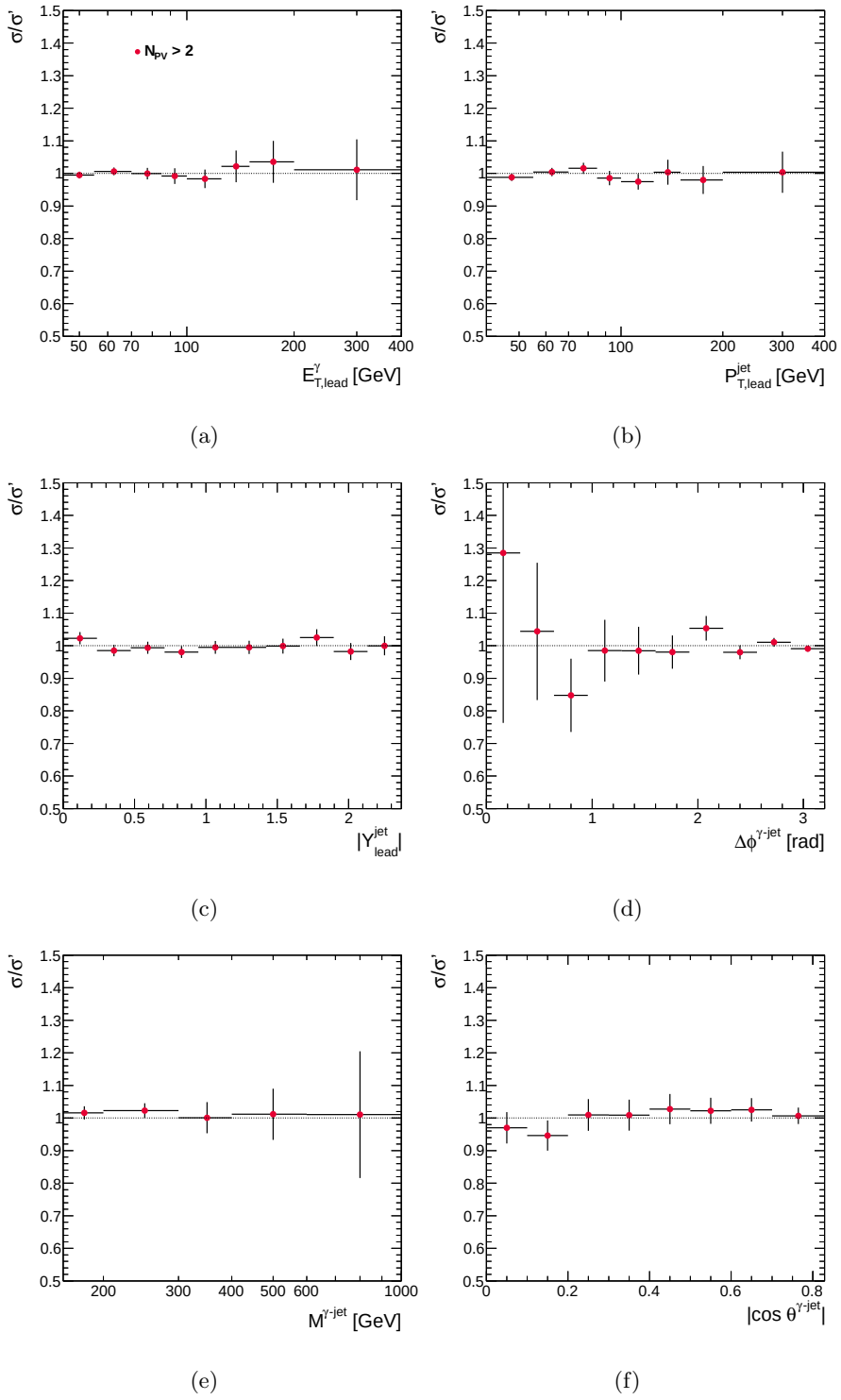

(a) (b) (c) (d) (e) (f)

Figure 9.27: Effect of restricting the number of primary-vertex to three or more in the differential cross sections as functions of (a) $E^{\gamma}_{T,\mathrm{lead}}$, (b) $P^{\mathrm{jet}}_{T,\mathrm{lead}}$, (c) $|Y^{\mathrm{jet}}_{\mathrm{lead}}|$, (d) $\Delta\phi^{\gamma-\mathrm{jet}}$, (e) $M^{\gamma-\mathrm{jet}}$ and (f) $|\cos\,\theta^{\gamma-\mathrm{jet}}|$.

9.2.2 Pile-up effects: jet vertex fraction

The jet vertex fraction (JVF) is a method that allows the identification and selection of jets originating from the hardest-scatter interaction through the use of tracking and vertexing information. By combining tracks and their primary vertices with calorimeter jets, a discriminant for jets which come from pile-up collisions is defined. The JVF discriminator, which rejects pile-up jets or jets with a high contamination of particles from pile-up vertices, is defined as the sum of the p_T of all tracks matched to the jet and originating from a given vertex, divided by the sum of the p_T of all tracks matched to the jet [101]. For a single jet, jet_i, the JVF with respect to the vertex vtx_j in the event is written as

$$\text{JVF}(\text{jet}_i, \text{vtx}_j) = \frac{\sum_k p_T(\text{trk}_k^{\text{jet}_i}, \text{vtx}_j)}{\sum_n \sum_l p_T(\text{trk}_l^{\text{jet}_i}, \text{vtx}_n)}, \tag{9.3}$$

where jet i has a fraction $\text{JVF}(i, j)$ of its total matched-track momentum originating in vertex j (see Fig. 9.28). Calorimeter jets which fall outside of the fiducial tracking region or which have not been matched to tracks are assigned the value JVF =-1.

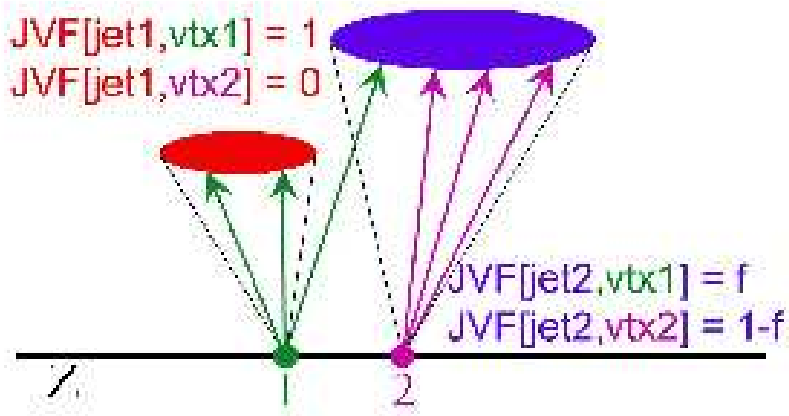

Figure 9.28: Definition of the JVF discriminator.

Figure 9.29 shows the jet multiplicity distributions for $t\bar{t}$ events with pile-up ($< N_{\text{PV}} > = 2.3$). A flat distribution is recovered when jets with tracking information are required to have $|\text{JVF}| \geq 0.75$ compared to that with no selection applied. These results clearly highlight the importance of the JVF discriminator to reduce the pile-up jets.

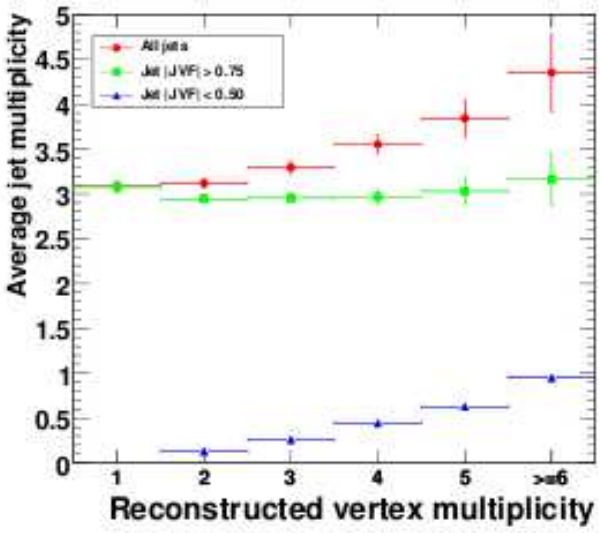

Figure 9.29: Jet multiplicity for MC generated $t\bar{t}$ events as a function of reconstructed primary-vertex multiplicity with (circles) and without (squares) a cut on JVF ($|\text{JVF}| > 0.75$). Jet selection using a requirement on JVF recovers the expected constant hardest-scatter jet multiplicity for $t\bar{t}$ events. Jets were reconstructed with the anti-k_T algorithm with R=0.4, passing $p_T > 10$ GeV and $|\eta_{\text{jet}}| \leq 2$.

The JVF distribution in data and MC is shown in Fig. 9.30. After reweighting the primary-vertex distribution in the MC, the simulation of PYTHIA gives a good description of the data.

To estimate the remaining effect of the pile-up, the whole analysis was repeated after accepting only those events in data and MC with $|\text{JVF}| > 0.75$. Figure 9.31 shows the effect with respect to the nominal analysis for the six observables. The overall effect is smaller than 1%, except in the tail of the $\Delta\phi^{\gamma-\text{jet}}$ distribution.

9.2.3 Primary-vertex and track requirements

The nominal selection includes the requirement of a reconstructed primary vertex, with at least five associated tracks and consistent with the average beam-spot position. These requirements were cross checked by using the signal MC.

The requirements of at least five tracks associated to the primary vertex was relaxed to only three associated tracks. The effect was that 0.08% more events were selected in the signal MC.

The requirement of a reconstructed primary vertex was removed completely from the selection criteria. This requirement was imposed to estimate the influence of the inefficiency of the primary-vertex reconstructing algorithm in the selected sample. The effect was that 0.15% more events were selected in the signal MC. This requirement was also cross checked at the hadron level; a total of 0.1% of the events are lost in the signal due to this requirement.

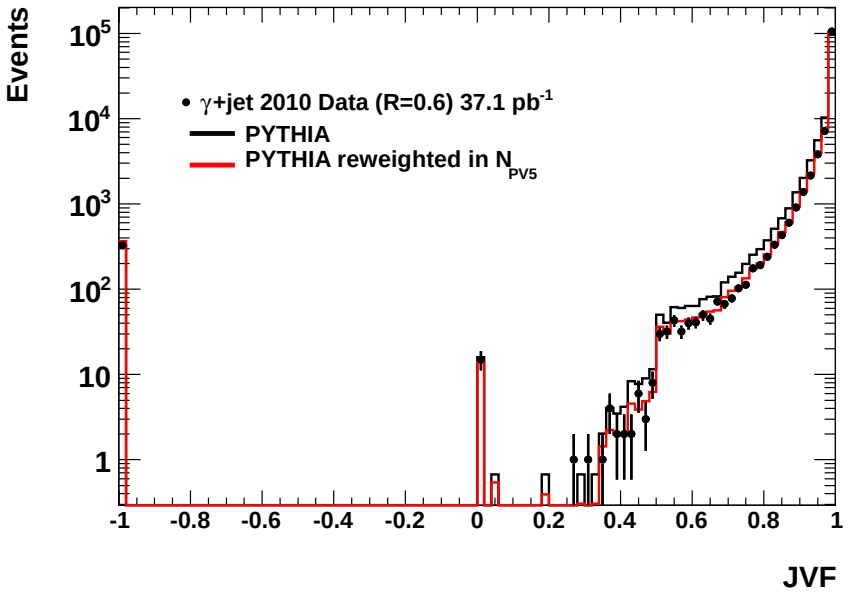

Figure 9.30: The measured JVF distribution (dots). For comparison, the MC simulations of the signal from PYTHIA (histograms) before and after primary-vertex reweighting are also included. The MC distributions are normalised to the total number of data events.

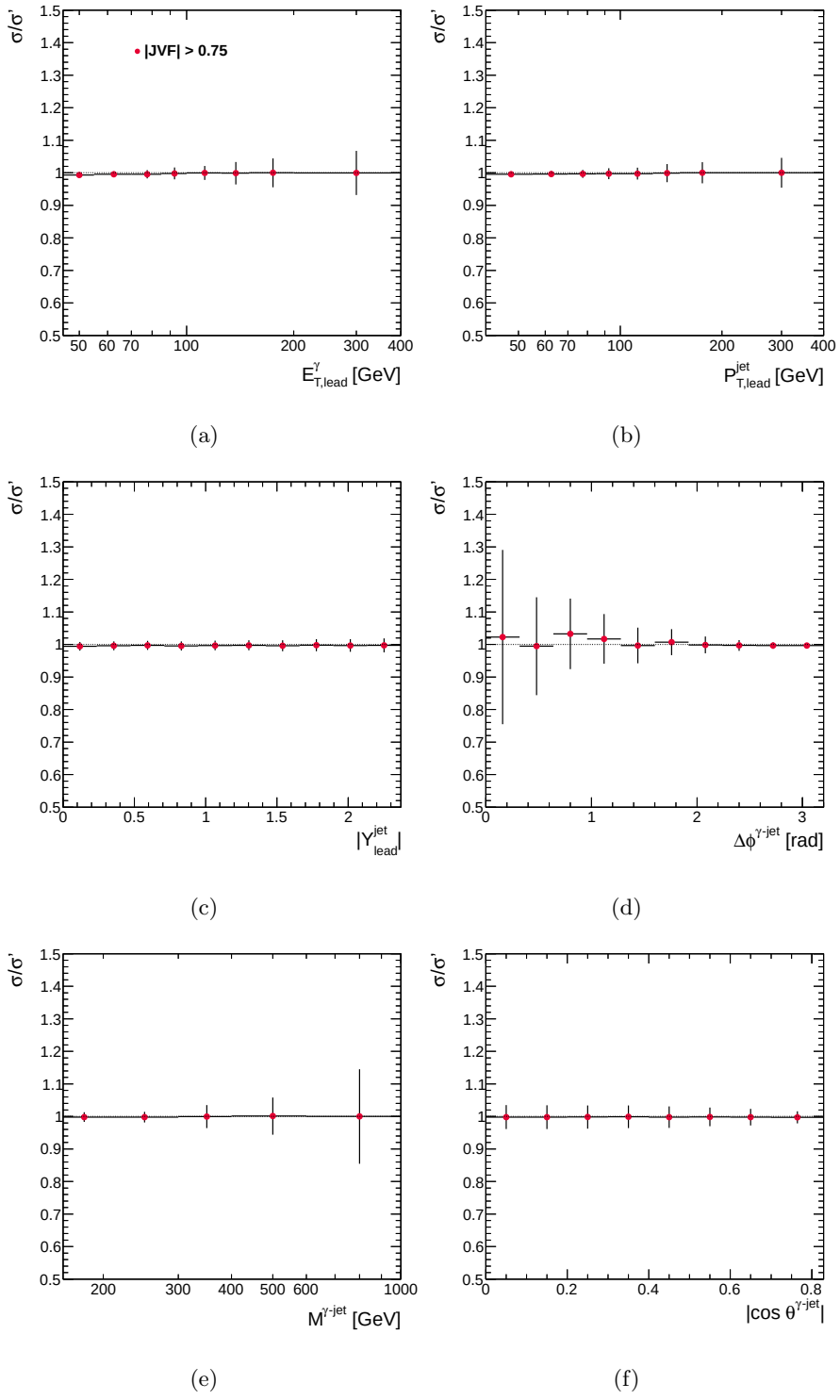

(a) (b) (c) (d) (e) (f)

Figure 9.31: Effect of the cut on JVF in the differential cross sections as functions of (a) $E^{\gamma}_{T,\mathrm{lead}}$, (b) $P^{\mathrm{jet}}_{T,\mathrm{lead}}$, (c) $|Y^{\mathrm{jet}}_{\mathrm{lead}}|$, (d) $\Delta\phi^{\gamma-\mathrm{jet}}$, (e) $M^{\gamma-\mathrm{jet}}$ and (f) $|\cos\,\theta^{\gamma-\mathrm{jet}}|$.

Chapter 10

Theoretical uncertainties

Perturbative QCD cross sections calculated at NLO are affected by uncertainties arising from:

- the residual scale dependence of the cross sections due to the truncation of the series at NLO (higher-order uncertainty);
- the PDF uncertainties derived from the global PDF fits;
- the uncertainty in the value of $\alpha_s(M_Z)$ used in the cross-section calculations;
- the uncertainty due to the modelling of the hadronisation and underlying event.

The estimation of these uncertainties is described in detail in this chapter.

10.1 Higher-order uncertainty

The theoretical predictions must be independent of the μ_R, μ_F and μ_f scales if all perturvative orders were summed up. Therefore, the dependence of the calculations on variations of the scale shows their sensitivity to the absent higher orders. The uncertainty of the higher-order predictions was estimated by repeating the calculations with values of μ_R, μ_F and μ_f scaled by factors 0.5 and 2. Figure 10.1 shows the relative difference on NLO QCD calculations due to these variations.

To estimate the uncertainty of the calculations due to higher orders, the three scales were either varied simultaneously, individually or by fixing one and varying the other two. In this last case, the condition $0.5 \leq \mu_A/\mu_B \leq 2$ was imposed, where $A, B = R, F, f$ and $A \neq B$. The final uncertainty was taken as the envelope of all the 14 possible variations (see Fig 10.2).

10.2 PDF uncertainty

The uncertainty on the NLO QCD calculations due to those on the proton PDFs was estimated by repeating the calculations using the 44 additional sets from the CTEQ6.6 error analysis. The CTEQ6.6 error analysis estimates the PDF uncertainties using the method proposed by J. Pumplin, D. Stump, Wu-Ki Tung et al (PST) [102].

10.2.1 PST method

The PST method is based on the diagonalisation of the matrix of second derivatives of the χ^2 function (the Hessian matrix) near its minimum at χ^2_0. Since χ^2 is approximately parabolic near its minimum χ^2_0, hypersurfaces of constant χ^2 are hyperellipses in the space of the original n PDF parameters a_i that parametrize the x-dependence of the PDFs at the input scale Q_0. By an appropriate change of coordinates $a_i \to z_i,\ i = 1 \cdots n$, where z_i corresponds to the eigenvectors of the hessian matrix, the hyperellipses can be transformed into hyperspheres.

Then, for each eigenvector, there are two displacements from z_i (in the positive and negative directions along the vector), denoted as z_i^+ and z_i^- for the ith eigenvector. At these points, $\chi^2 = \chi^2_0 + T^2$, where T is a parameter called the tolerance. Any set with $\chi^2 - \chi^2_0 < T^2$ is considered an acceptable fit to the global data set. In particular, the $2 \times n$ PDF sets $z_i^\pm$, which are called the eigenvector basis sets, span the parameter space in the neighborhood of the minimum.

The PDF uncertainty for an observable O is the maximal change in O as a function of the variables z_i varied within the tolerance hypersphere. The PST method estimates the variation of O as

$$\delta O = \sqrt{\sum_{i=1}^{n} \delta O_i^2},\ \text{where } \delta O_i \equiv \frac{\partial O}{\partial z_i} \approx \frac{O(z_i^+) - O(z_i^-)}{2}. \tag{10.1}$$

The PDF error in Eq. 10.1 is a combination of $2 \times n$ cross sections, each of which is known with some uncertainty due to the Monte Carlo integration. The maximal

variations of O in the positive and negative directions are estimated by

$$\delta O^{+} = \sqrt{\sum_{i=1}^{n} [\max(O(z_i^{+}) - O(z_i^{0}), O(z_i^{-}) - O(z_i^{0}), 0)]^2} \text{ and} \tag{10.2}$$

$$\delta O^{-} = \sqrt{\sum_{i=1}^{n} [\max(O(z_i^{0}) - O(z_i^{+}), O(z_i^{0}) - O(z_i^{-}), 0)]^2}. \tag{10.3}$$

10.2.2 PDF uncertainty results

By using Eq. 10.2 and the $2 \times n = 44$ additional sets from the CTEQ6.6 PDFs, the systematic uncertainty due to those on the proton PDFs was calculated and it is shown in Fig. 10.3.

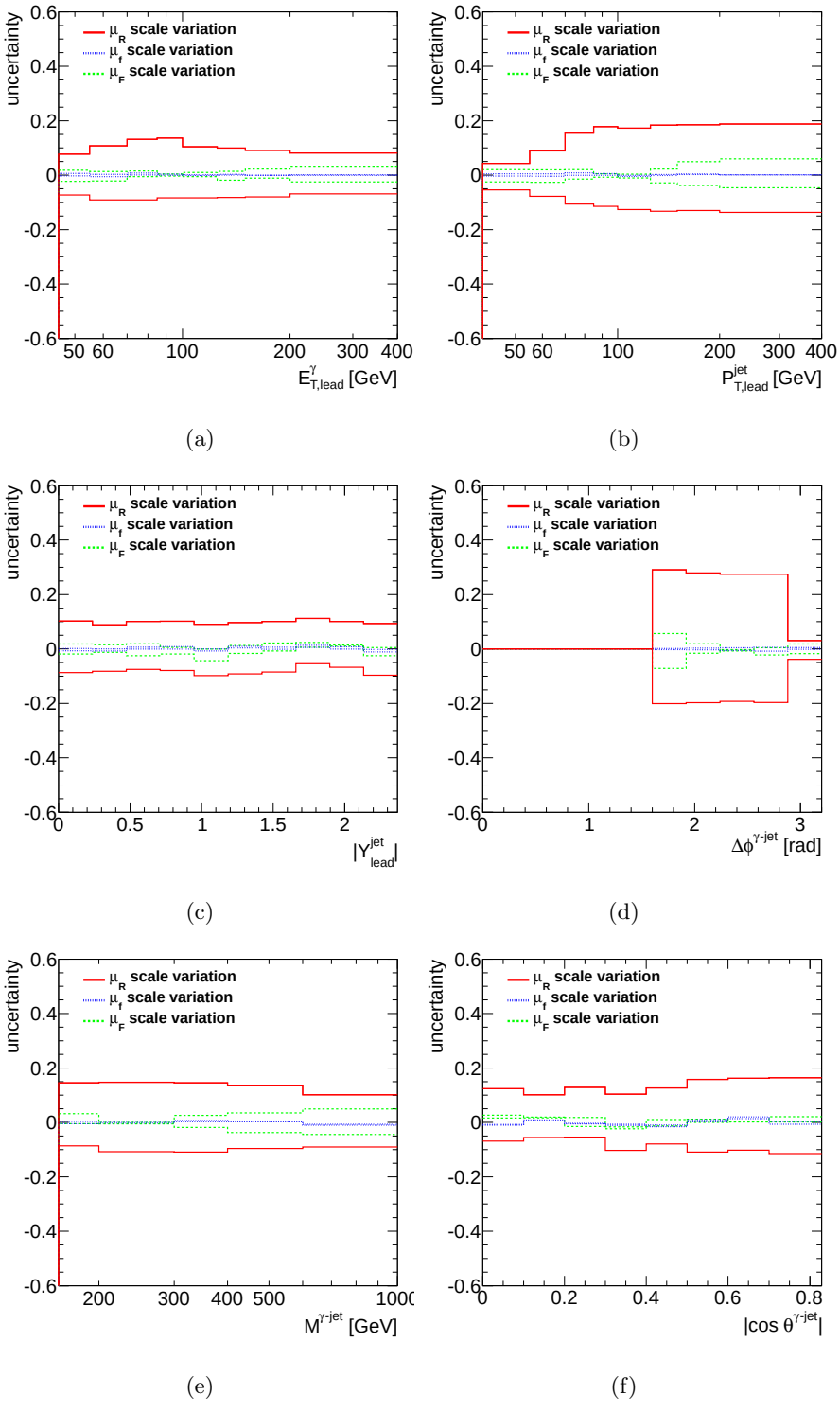

Figure 10.1: Relative difference due to variations of the μ_R, μ_F and μ_f scales for the differential cross sections as functions of (a) $E^{\gamma}_{T,\mathrm{lead}}$, (b) $P^{\mathrm{jet}}_{T,\mathrm{lead}}$, (c) $|Y^{\mathrm{jet}}_{\mathrm{lead}}|$, (d) $\Delta\phi^{\gamma-\mathrm{jet}}$, (e) $M^{\gamma-\mathrm{jet}}$ and (f) $|\cos\,\theta^{\gamma-\mathrm{jet}}|$.

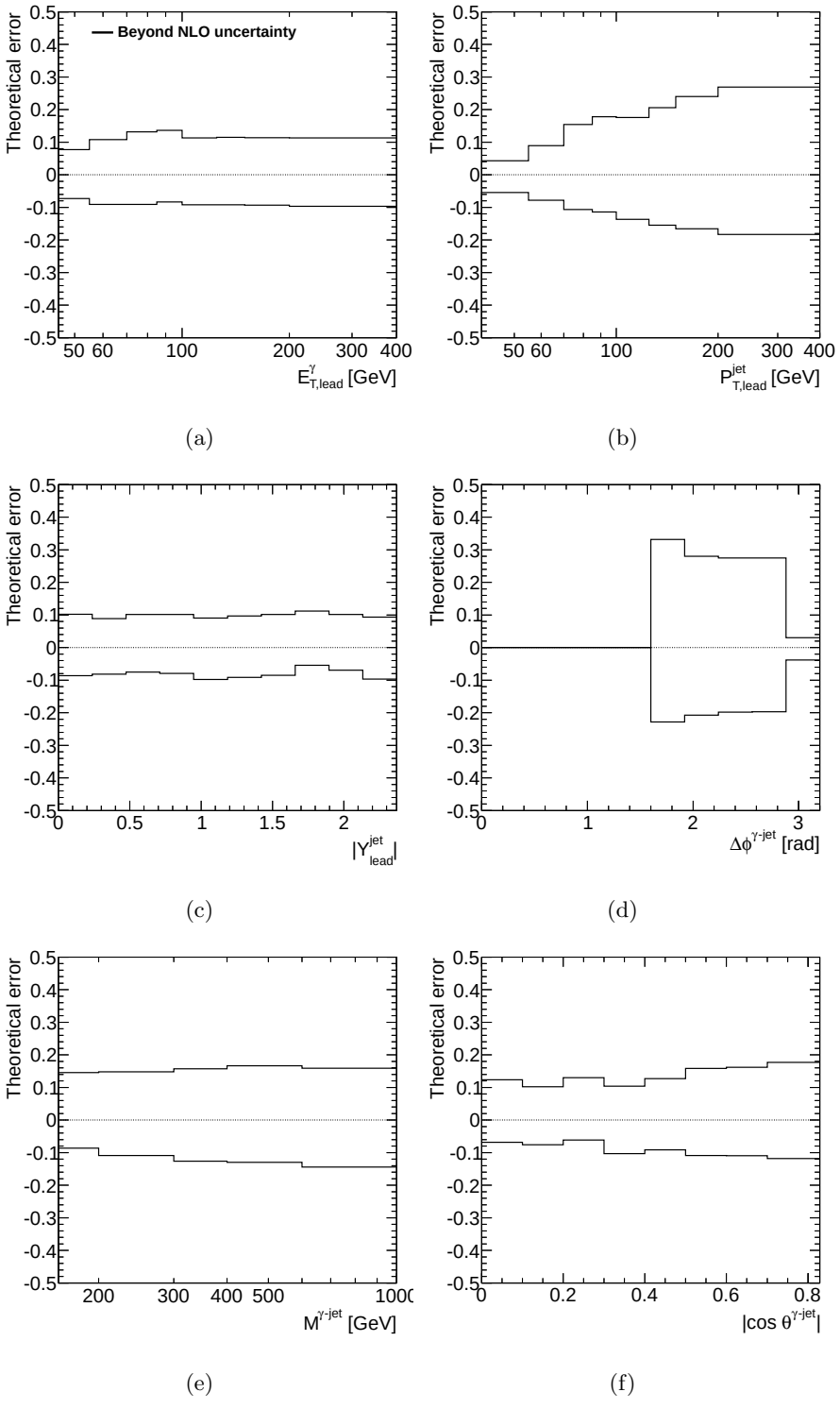

Figure 10.2: Relative uncertainty on the NLO QCD calculations due to the missing higher orders for the differential cross sections as functions of (a) $E^{\gamma}_{T,\mathrm{lead}}$, (b) $P^{\mathrm{jet}}_{T,\mathrm{lead}}$, (c) $|Y^{\mathrm{jet}}_{\mathrm{lead}}|$, (d) $\Delta\phi^{\gamma-\mathrm{jet}}$, (e) $M^{\gamma-\mathrm{jet}}$ and (f) $|\cos\,\theta^{\gamma-\mathrm{jet}}|$.

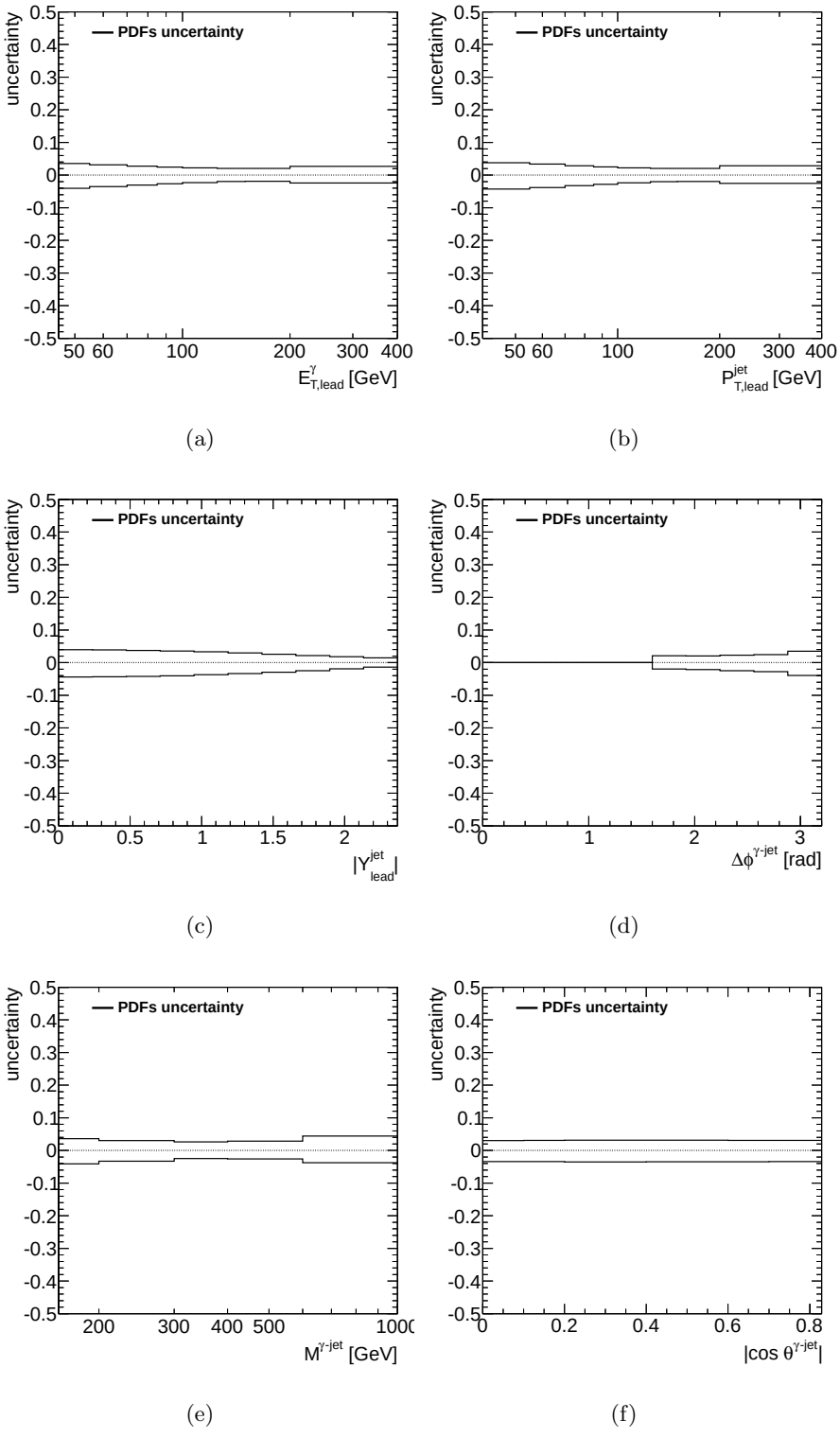

Figure 10.3: Relative uncertainty on the NLO QCD calculations due to those on the proton PDFs for the differential cross sections as functions of (a) $E^{\gamma}_{T,\mathrm{lead}}$, (b) $P^{\mathrm{jet}}_{T,\mathrm{lead}}$, (c) $|Y^{\mathrm{jet}}_{\mathrm{lead}}|$, (d) $\Delta\phi^{\gamma-\mathrm{jet}}$, (e) $M^{\gamma-\mathrm{jet}}$, (f) $|\cos\,\theta^{\gamma-\mathrm{jet}}|$.

10.3 α_s uncertainty

The strong coupling α_s is a basic parameter that enters in the PDF global fitting procedure.

As with the PDF parametrisation, a decision must be taken on how to evaluate the scale dependence of the running coupling constant $\alpha_s(Q)$ and provide a value of α_s at some scale Q' as a boundary condition. Both choices contribute additional uncertainties to the determination of the PDFs. The scale dependence of $\alpha_s(Q)$ is not uniquely determined, but estimated from the NLO approximation of the renormalisation group (RG) equation for $\alpha_s(Q)$:

$$Q\frac{d\alpha_s}{dQ} = -\frac{\beta_0}{2\pi}\alpha_s^2 - \frac{\beta_1}{8\pi^2}\alpha_s^3 + O(\alpha_s^4) , \tag{10.4}$$

where $\beta_0 = 11 - (2/3)n_f$ and $\beta_1 = 102 - (38/3)n_f$. In NLO perturbation theory, terms of order α_s^4 are neglected.

There are different solutions [102] to Eq. 10.4, formally equivalent in the NLO approximation, but differing in higher orders of perturbation theory. Studies have shown that the associated uncertainty, coming from the approximation for the Q dependence of $\alpha_s(Q)$, is small compared to other sources of the PDF uncertainty [103].

The differential equation 10.4 requires an initial value, the conventional choice is the value of $\alpha_s(Q)$ at the Z boson mass, $Q = M_Z$; it is a natural choice, since M_Z is know quite precisely.

The value of $\alpha_s(M_Z)$ could be determined from a global PDF analysis. However, the resulting determination turns out to have a relatively large uncertainty: the scattering processes included have limited accuracy for measuring $\alpha_s(M_Z)$, because they depend on the PDFs, which are themselves affected by an uncertainty.

The 2009 world-average value of α_s based on eight different measurement techniques [104] is given by

$$\alpha_s(M_Z) = 0.1184 \pm 0.0007. \tag{10.5}$$

Traditionally, the CTEQ group presents the *best-fit* PDFs and their parametrisation uncertainties for a constant value of $\alpha_s(M_Z)$ =0.118 close to its latest world-average central value [42]. Separately, the uncertainty in the PDFs induced by the uncertainty in $\alpha_s(M_Z)$ is assessed, by producing a few *alternative PDF fits* for a range of values of $\alpha_s(M_Z)$ around the central $\alpha_s(M_Z)$ value [103] (i.e CTEQ6.6AS).

For the analysis presented here, the CTEQ6.6AS PDFs set was used to determine the uncertainty on the NLO QCD calculations due to that on $\alpha_s(M_Z)$. The CETQ6.6AS analysis uses the same input data and methods as the CTEQ6.6 study and presents a new $\alpha_s(M_Z)$ series of PDFs, based on the 2009 world-average value of $\alpha_s(M_Z) = 0.118$ and four additional PDF sets extracted for $0.116 \leq \alpha_s \leq 0.120$. The uncertainty was then estimated by repeating the calculations using the two additional sets of proton PDFs presented in CETQ6.6AS, for which $\alpha_s(M_Z) = 0.116$ and $\alpha_s(M_Z) = 0.120$ was assumed, respectively, in the fits and correspond approximately to a 90% CL uncertainty.

Due to the correlation between the proton PDFs and the value of α_s, the most complete method to evaluate the combined PDF+α_s uncertainty in the global fit is to vary the theoretical value of $\alpha_s(M_Z)$ as an additional fitting parameter, while *including* the world-average value of $\alpha_s(M_Z)$ with its experimental uncertainty as a precise experimental constraint on $\alpha_s(M_Z)$, in combination with the rest of the hadronic data. The uncertainty from α_s can then be deduced by the Hessian techniques (PST method) as the uncertainty in the PDF parameter. It has been shown that this method is equivalent to the one used in the present analysis [105].

Figure 10.4 shows the α_s uncertainty for the photon plus jet theoretical cross sections in the kinematic region of the measurements as functions of each observable.

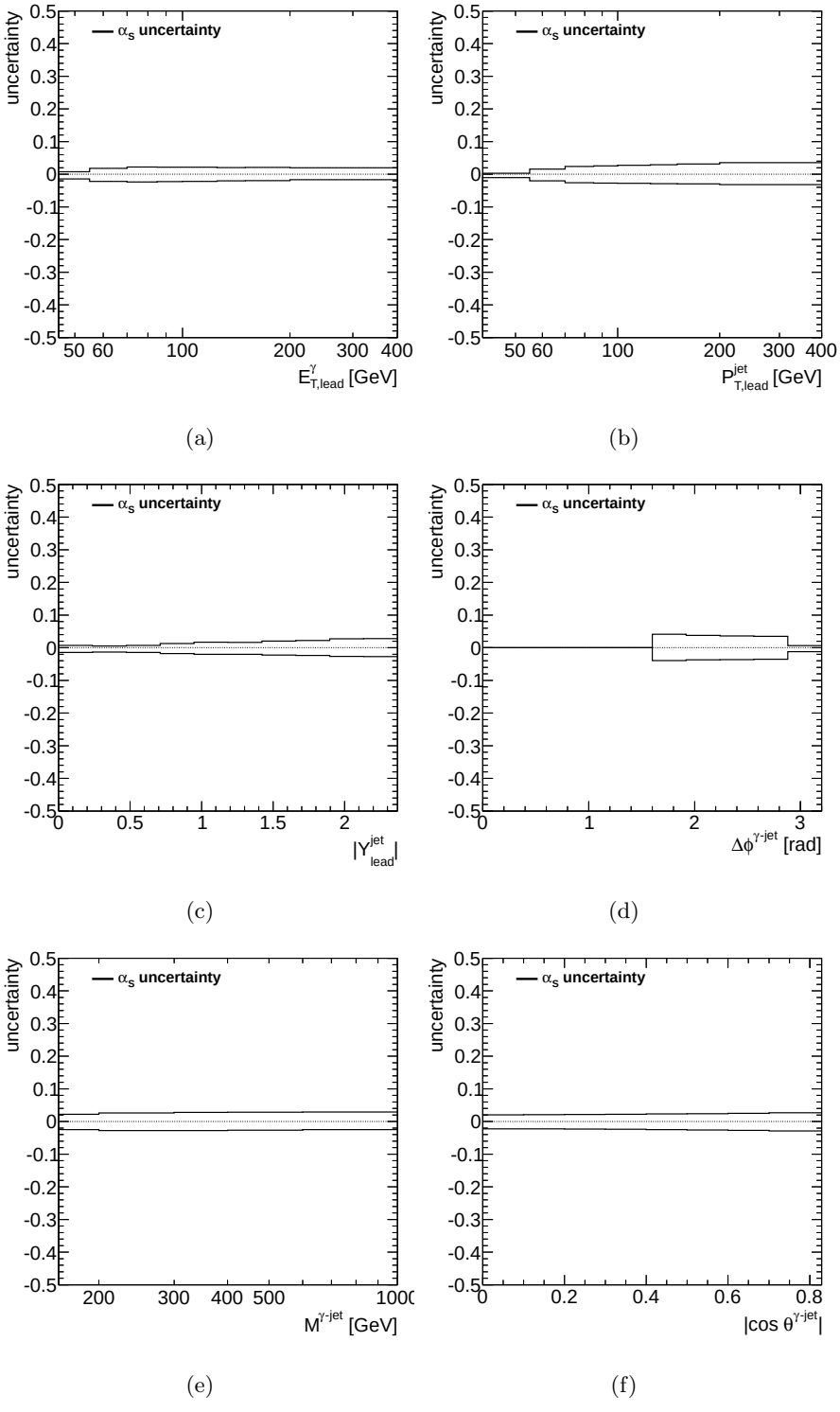

(a) (b) (c) (d) (e) (f)

Figure 10.4: Relative uncertainty on the NLO QCD calculations due to that on the value of $\alpha_s(M_Z)$ for the differential cross sections as functions of (a) $E^{\gamma}_{T,\mathrm{lead}}$, (b) $P^{\mathrm{jet}}_{T,\mathrm{lead}}$, (c) $|Y^{\mathrm{jet}}_{\mathrm{lead}}|$, (d) $\Delta\phi^{\gamma-\mathrm{jet}}$, (e) $M^{\gamma-\mathrm{jet}}$ and (f) $|\cos\,\theta^{\gamma-\mathrm{jet}}|$.

10.4 Hadronisation+UE uncertainty

The NLO QCD calculations were corrected for the effects of underlying event and hadronisation with a multiplicative correction factor C_{NLO} (see Chapter 4). Therefore, the uncertainties due to the modelling of the underlying event and hadronisation will give rise to an uncertainty in the C_{NLO} correction factors.

The C_{NLO} correction factor was calculated from the average of the predictions from PYTHIA and HERWIG. Different prescriptions for simulating the QCD partonic cascade are used by PYTHIA and HERWIG, just as they used different models to simulate the underlying event and the hadronisation. The uncertainty due to such effects was estimated by making the difference of the factors C_{NLO} based on PYTHIA or HERWIG from their average.

Figure 10.5 shows the hadronisation+UE uncertainty for the photon plus jet theoretical cross sections in the kinematic region of the measurements as functions of each observable.

10.5 Total theoretical uncertainty

The total theoretical uncertainty was obtained by adding in quadrature the individual uncertainties listed in previous sections. The dominant theoretical uncertainty is that arising from the terms beyond NLO.

The total theoretical uncertainty is approximately constant as a functions of $E_{T,\mathrm{lead}}^{\gamma}$, $|Y_{\mathrm{lead}}^{\mathrm{jet}}|$, $\Delta\phi^{\gamma-\mathrm{jet}}$, $M^{\gamma-\mathrm{jet}}$ and $|\cos\theta^{\gamma-\mathrm{jet}}|$. It has a value $\sim \pm 10\%$ as functions of the $E_{T,\mathrm{lead}}^{\gamma}$ and $|Y_{\mathrm{lead}}^{\mathrm{jet}}|$, and $\sim \pm 15\%$ as a functions of $M^{\gamma-\mathrm{jet}}$ and $|\cos\theta^{\gamma-\mathrm{jet}}|$. The total theoretical uncertainty increases as $P_{T,\mathrm{lead}}^{\mathrm{jet}}$ increases and takes values between $\pm 6\%$ $(^{+26\%}_{-19\%})$ for low (high) $P_{T,\mathrm{lead}}^{\mathrm{jet}}$.

Figure 10.6 presents the total theoretical uncertainty for the differential cross section as a function of each observable. The uncertainty on the NLO calculation for $d\sigma/d\Delta\phi^{\gamma-\mathrm{jet}}$ is relatively small for $\Delta\phi^{\gamma-\mathrm{jet}} \approx \pi$ and large everywhere else. The reason for such behaviour is that the NLO calculation accounts only for the first non-zero contribution in the region $\Delta\phi^{\gamma-\mathrm{jet}} < \pi$: at LO there is only one final-state parton and $\Delta\phi^{\gamma-\mathrm{jet}} = \pi$; at NLO there are at most two final-state partons and the values of $\Delta\phi^{\gamma-\mathrm{jet}}$ are restricted to be in the range between $\pi/2$ and π.

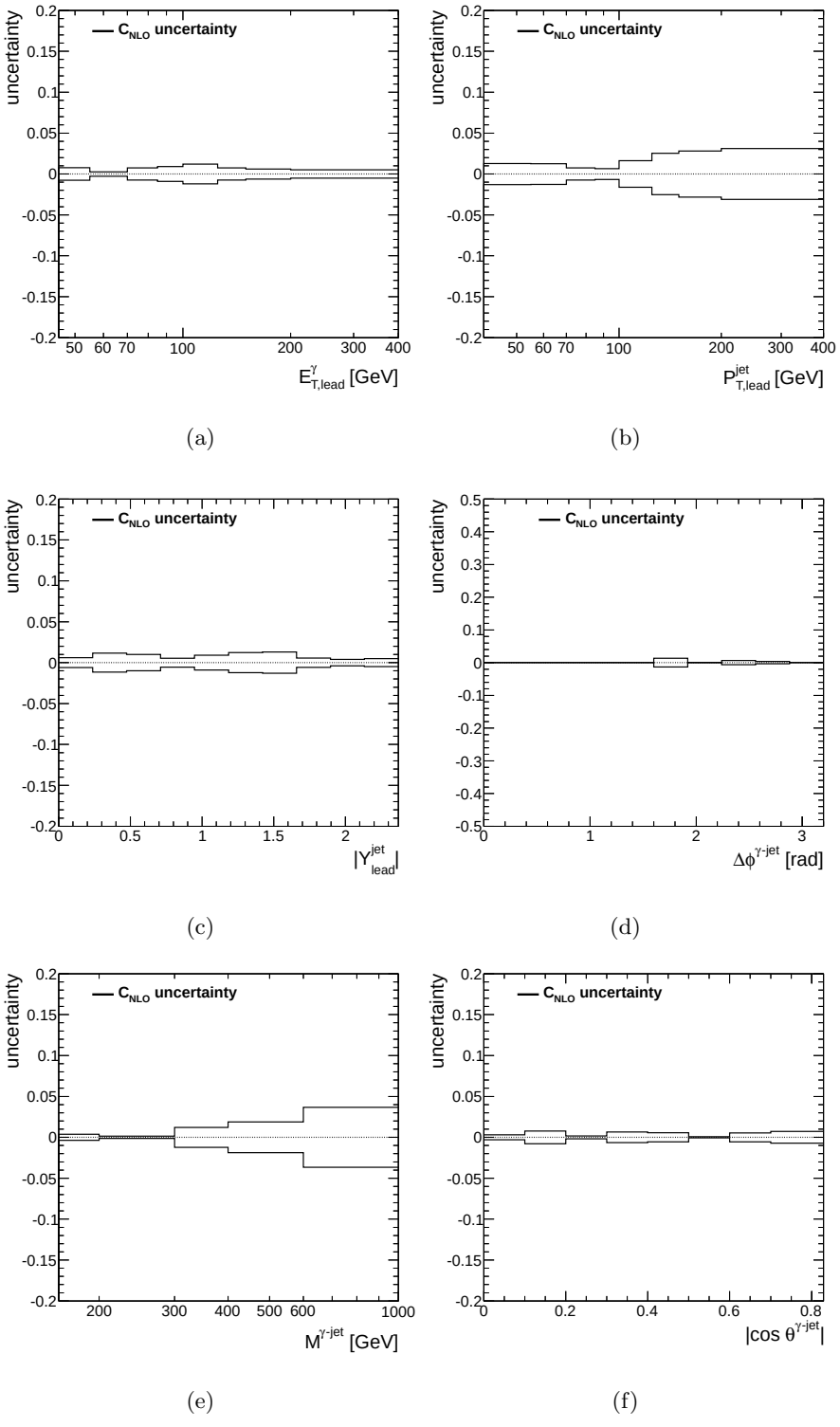

(a) (b)

(c) (d)

(e) (f)

Figure 10.5: Relative uncertainty on the NLO QCD calculations due to that on the modelling of the UE+hadronisation for the differential cross sections as functions of (a) $E^{\gamma}_{T,\mathrm{lead}}$, (b) $P^{\mathrm{jet}}_{T,\mathrm{lead}}$, (c) $|Y^{\mathrm{jet}}_{\mathrm{lead}}|$, (d) $\Delta\phi^{\gamma-\mathrm{jet}}$, (e) $M^{\gamma-\mathrm{jet}}$ and (f) $|\cos\,\theta^{\gamma-\mathrm{jet}}|$.

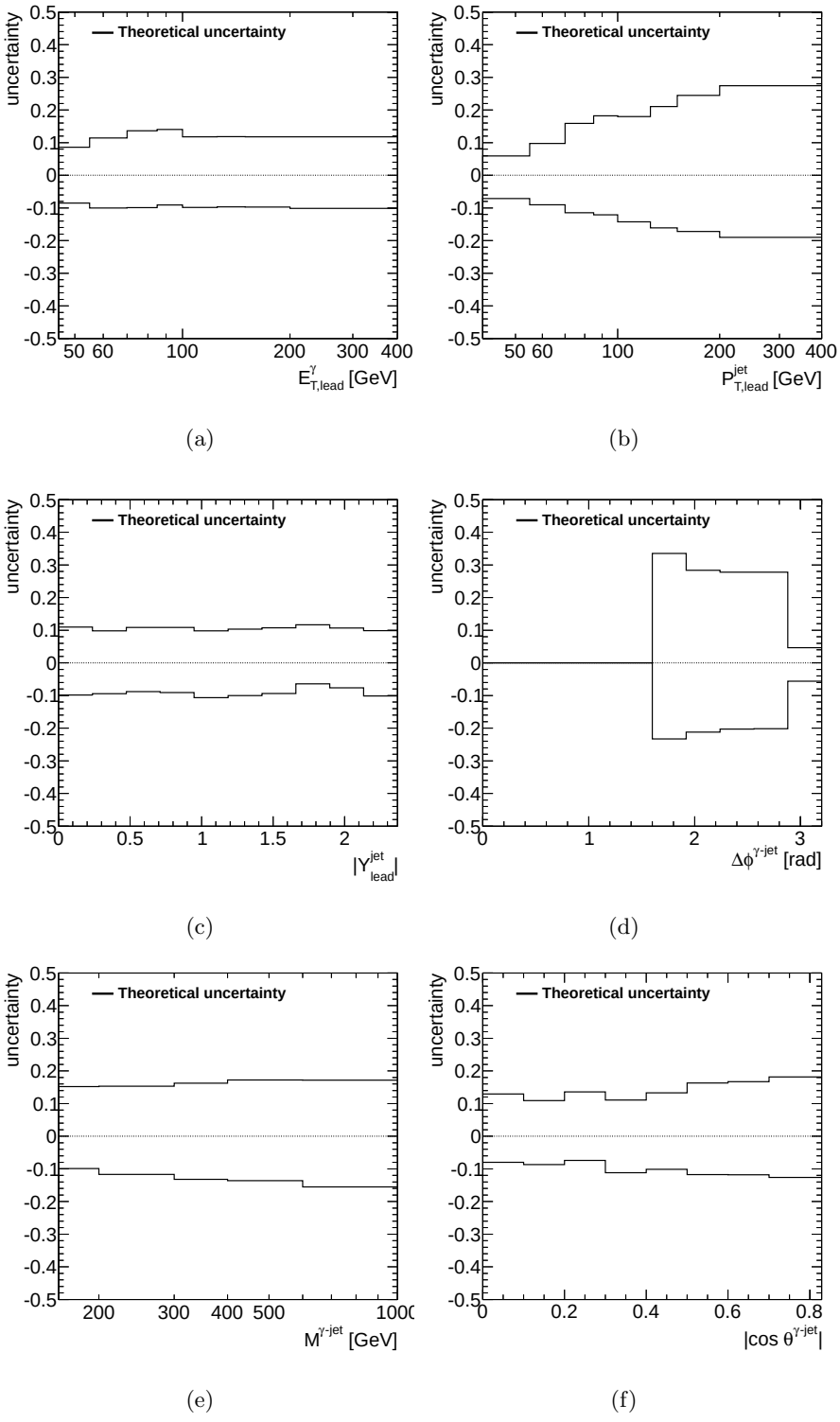

Figure 10.6: Relative total theoretical uncertainty for the differential cross sections as functions of (a) $E^{\gamma}_{T,\mathrm{lead}}$, (b) $P^{\mathrm{jet}}_{T,\mathrm{lead}}$, (c) $|Y^{\mathrm{jet}}_{\mathrm{lead}}|$, (d) $\Delta\phi^{\gamma-\mathrm{jet}}$, (e) $M^{\gamma-\mathrm{jet}}$ and (f) $|\cos\theta^{\gamma-\mathrm{jet}}|$.

Chapter 11

Results

Differential cross sections for isolated photons in association with a jet were measured in proton-proton collisions, $pp \to \gamma$ + jet$+X$ at $\sqrt{s} = 7$ TeV, in the kinematic region given by $E^{\gamma}_{T,\mathrm{lead}} > 45$ GeV and $|\eta^{\gamma}_{\mathrm{lead}}| < 2.37$ (excluding the region of $1.37 < |\eta^{\gamma}_{\mathrm{lead}}| < 1.52$) and isolation $E^{\mathrm{iso}}_{T} < 4$ GeV. The jets were reconstructed using the anti-k_T jet algorithm with $R = 0.6$. The isolated photon plus jet differential cross sections as functions of $E^{\gamma}_{T,\mathrm{lead}}$, $P^{\mathrm{jet}}_{T,\mathrm{lead}}$, $|Y^{\mathrm{jet}}_{\mathrm{lead}}|$ and $\Delta\phi^{\gamma-\mathrm{jet}}$ were measured for the leading jet with $P^{\mathrm{jet}}_{T,\mathrm{lead}} > 40$ GeV, $|Y^{\mathrm{jet}}_{\mathrm{lead}}| < 2.37$ and $\Delta R^{\gamma-\mathrm{jet}} > 1$. The measurements of the $d\sigma/dM^{\gamma-\mathrm{jet}}$ and $d\sigma/d|\cos\theta^{\gamma-\mathrm{jet}}|$ cross sections were performed with the additional selection criteria $|\eta^{\gamma}_{\mathrm{lead}} + Y^{\mathrm{jet}}_{\mathrm{lead}}| < 2.37$, $|\cos\theta^{\gamma-\mathrm{jet}}| < 0.83$ and $M^{\gamma-\mathrm{jet}} > 161$ GeV.

The measured differential cross sections are presented in Figs. 11.1 to 11.6. The measured $d\sigma/dE^{\gamma}_{T,\mathrm{lead}}$ and $d\sigma/dP^{\mathrm{jet}}_{T,\mathrm{lead}}$ fall by over three orders of magnitude in the measured range. The measured $d\sigma/d|Y^{\mathrm{jet}}_{\mathrm{lead}}|$ and $d\sigma/d\Delta\phi^{\gamma-\mathrm{jet}}$ display a maximum at $|Y^{\mathrm{jet}}_{\mathrm{lead}}| \approx 0$ and $\Delta\phi^{\gamma-\mathrm{jet}} \approx \pi$, respectively. The measured $d\sigma/dM^{\gamma-\mathrm{jet}}$ ($d\sigma/d|\cos\theta^{\gamma-\mathrm{jet}}|$) decreases (increases) as $M^{\gamma-\mathrm{jet}}$ ($|\cos\theta^{\gamma-\mathrm{jet}}|$) increases. The values of the differential cross sections as functions of $E^{\gamma}_{T,\mathrm{lead}}$, $P^{\mathrm{jet}}_{T,\mathrm{lead}}$, $|Y^{\mathrm{jet}}_{\mathrm{lead}}|$, $\Delta\phi^{\gamma-\mathrm{jet}}$, $M^{\gamma-\mathrm{jet}}$ and $|\cos\theta^{\gamma-\mathrm{jet}}|$ are shown in Tables 11.1 to 11.6.

The predictions of the NLO QCD calculations from the JETPHOX program described in Chapter 3 and corrected for hadronisation and underlying-event effects are compared to the data in Figs. 11.1 to 11.6. The predictions give a good descriptions of the $E^{\gamma}_{T,\mathrm{lead}}$ and $P^{\mathrm{jet}}_{T,\mathrm{lead}}$ measured cross sections. The shape and normalisation of the measured cross section as a function of $|Y^{\mathrm{jet}}_{\mathrm{lead}}|$ is described well by the calculation in the whole measured range. The NLO QCD calculation fails to describe the measured $\Delta\phi^{\gamma-\mathrm{jet}}$ distribution, as expected due to the fact that in the NLO QCD calculation the photon and the leading jet cannot be in the same hemisphere in the

transverse plane, i.e. $\Delta\phi^{\gamma-\text{jet}}$ is necessarily larger than $\pi/2$. The predictions give a good description of the $M^{\gamma-\text{jet}}$ and $|\cos\,\theta^{\gamma-\text{jet}}|$ measured cross sections.

All these comparisons validate the description of the dynamics of isolated-photon plus jet production in pp collisions at $O(\alpha\alpha_s^2)$. The NLO QCD calculations based on the MSTW2008nlo proton PDF sets are also shown in Figs. 11.1 to 11.6. The predictions based on the two PDF sets are very similar.

For completeness, the predictions of the leading-logarithm parton-shower MC models of PYTHIA and HERWIG are compared to the measurements in Figs. 11.7 and 11.8, respectively. The predictions of PYTHIA and HERWIG describe the shape of the measured $d\sigma/dE_{T,\text{lead}}^{\gamma}$.The predictions of PYTHIA and HERWIG describe the shape of the measured $d\sigma/dP_{T,\text{lead}}^{\text{jet}}$ for $P_{T,\text{lead}}^{\text{jet}} \lesssim 100$ GeV. The predictions of PYTHIA and HERWIG describe the shape of the measured $d\sigma/d|Y_{\text{lead}}^{\text{jet}}|$. The prediction of PYTHIA describes the shape of the $d\sigma/d\Delta\phi^{\gamma-\text{jet}}$, but HERWIG fails to describe the data. The predictions of PYTHIA and HERWIG describe the shape of the measured $d\sigma/dM^{\gamma-\text{jet}}$. Both PYTHIA and HERWIG fail to describe adequately the measured $d\sigma/d|\cos\,\theta^{\gamma-\text{jet}}|$. The comparison of the predictions of PYTHIA and HERWIG normalised to the data are shown in Figs. 11.9 and 11.10, respectively.

To gain insight into the interpretation of the results, the LO calculations of the direct-photon and fragmentation contributions to the cross sections as well as their sum are useful. As it was shown earlier (see Chapter 3), the ratio LO/NLO does not show a strong dependence with $E_{T,\text{lead}}^{\gamma}$, $|Y_{\text{lead}}^{\text{jet}}|$ and $M^{\gamma-\text{jet}}$; on the other hand, this ratio exhibits a strong dependence with $P_{T,\text{lead}}^{\text{jet}}$ and $|\cos\,\theta^{\gamma-\text{jet}}|$. The LO and NLO QCD calculations were compared in Fig 3.17. The fragmentation contribution is observed to decrease as a function of $E_{T,\text{lead}}^{\gamma}$, $P_{T,\text{lead}}^{\text{jet}}$ and $M^{\gamma-\text{jet}}$ and is approximately constant as a function of $|Y_{\text{lead}}^{\text{jet}}|$. However, it increases as a function of $|\cos\,\theta^{\gamma-\text{jet}}|$ from 2% up to 16%. Therefore, the regions at low $E_{T,\text{lead}}^{\gamma}$, $P_{T,\text{lead}}^{\text{jet}}$ and $M^{\gamma-\text{jet}}$ as well as at large $|\cos\,\theta^{\gamma-\text{jet}}|$ are expected to be particularly sensitive to the fragmentation contribution.

The shapes of the differential cross sections for the direct-photon and fragmentation contributions at LO QCD were compared in 3.18. The major difference is observed in the differential cross section as a function of $|\cos\,\theta^{\gamma-\text{jet}}|$ (see Fig. 3.18(f)), with the contribution from fragmentation showing a steeper increase as $|\cos\,\theta^{\gamma-\text{jet}}| \rightarrow 1$ than that of direct-photon processes. This different behaviour is due to the different spin of the exchanged particle dominating each of the processes: a quark in

the case of direct-photon processes and a gluon in the case of fragmentation processes. Therefore, the distribution in $|\cos\,\theta^{\gamma-\mathrm{jet}}|$ is particularly useful to study the dynamics underlying the hard process and the relative contributions of direct-photon and fragmentation processes. The good description of the measured cross section $d\sigma/d|\cos\,\theta^{\gamma-\mathrm{jet}}|$ by the NLO QCD calculations and the fact that the shape of the NLO QCD calculations is much closer to that of the direct-photon processes than that of fragmentation, demonstrates that the dominant contribution comes from direct-photon processes and in agreement with the assumption that the exchanged particle is a quark.

The integrated cross section was calculated for the phase-space regions of the measurements using two different methods. One method was based on the simple counting of events and the second method was based on integrating the differential cross sections. Both methods give compatible results; however, the second method was deemed to be the most reliable since in that case, the background subtraction was done bin-by-bin so it takes better into account the dependence of the observables on the purity of the sample. Figures 11.11 and 11.12 show the results together with the NLO QCD predictions. The measured and predicted integrated cross sections in the phase-space region given by $E^{\gamma}_{T,\mathrm{lead}} > 45$ GeV and $|\eta^{\gamma}_{\mathrm{lead}}| < 2.37$ (excluding the region of $1.37 < |\eta^{\gamma}_{\mathrm{lead}}| < 1.52$) and isolation $E^{\mathrm{iso}}_{T} < 4$ GeV, for jets reconstructed using the anti-k_T jet algorithm with $R = 0.6$ and the leading jet with $P^{\mathrm{jet}}_{T,\mathrm{lead}} > 40$ GeV, $|Y^{\mathrm{jet}}_{\mathrm{lead}}| < 2.37$ and $\Delta R^{\gamma-\mathrm{jet}} > 1$ are

$$\sigma_{\mathrm{meas}} = 3897 \pm 14(\mathrm{stat})^{+403}_{-363}(\mathrm{syst})\mathrm{pb} \tag{11.1}$$

$$\sigma_{\mathrm{NLO}} = 4040^{+422}_{-369}(\text{th unc})\mathrm{pb} \tag{11.2}$$

The measured and predicted integrated cross section with the additional restrictions in the phase space of $|\eta^{\gamma}_{\mathrm{lead}} + Y^{\mathrm{jet}}_{\mathrm{lead}}| < 2.37$, $|\cos\,\theta^{\gamma-\mathrm{jet}}| < 0.83$ and $M^{\gamma-\mathrm{jet}} > 161$ GeV are

$$\sigma_{\mathrm{meas}} = 813 \pm 6(\mathrm{stat})^{+79}_{-77}(\mathrm{syst})\mathrm{pb} \tag{11.3}$$

$$\sigma_{\mathrm{NLO}} = 795^{+120}_{-85}(\text{th unc})\mathrm{pb} \tag{11.4}$$

In both cases, there is a very good agreement between data and theory.

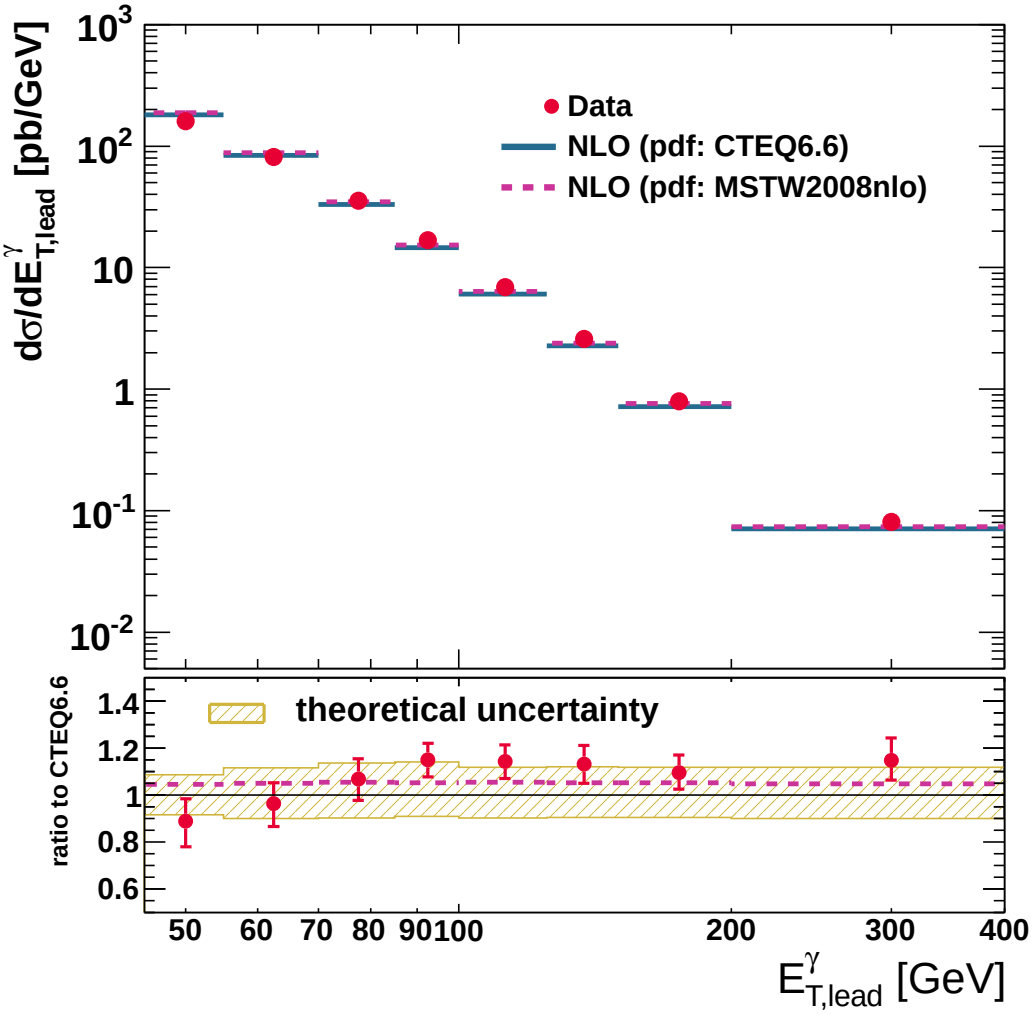

Figure 11.1: The measured differential cross-section for isolated-photon plus jet production (dots) as a function of $E^{\gamma}_{T,\mathrm{lead}}$. The NLO QCD calculations from JETPHOX corrected for hadronisation+UE effects based on the CTEQ6.6 (solid histogram) and the MSTW2008nlo (dashed histogram) PDFs are also shown. The lower part of the figure shows the ratio between the measured cross section and the NLO QCD calculation based on the CTEQ6.6 PDFs (dots); the ratio of the calculation based on MSTW2008nlo to that based on CTEQ6.6 is shown as a dashed line. The error bars represent the statistical and systematic uncertainties added in quadrature and the hatched band displays the theoretical uncertainty.

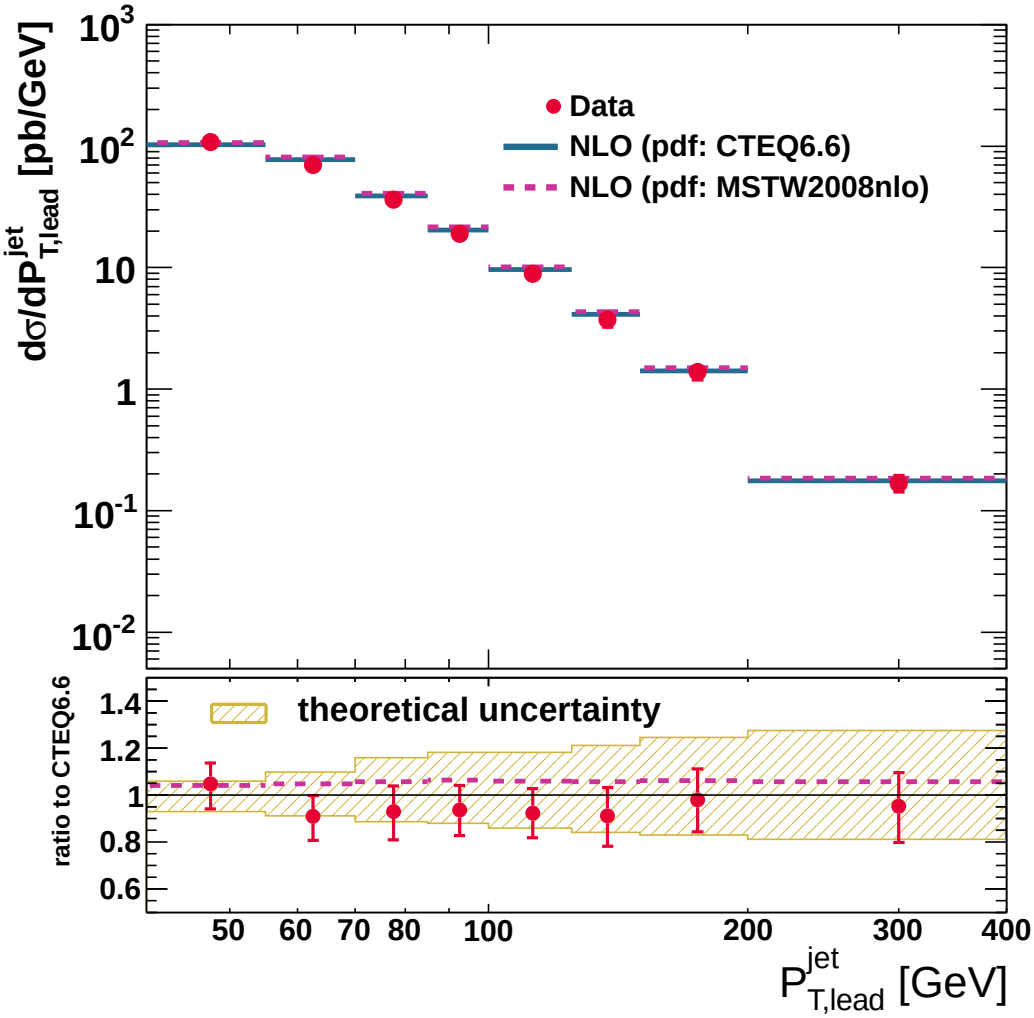

Figure 11.2: The measured differential cross-section for isolated-photon plus jet production (dots) as a function of $P_{T,\mathrm{lead}}^{\mathrm{jet}}$. The NLO QCD calculations from JETPHOX corrected for hadronisation+UE effects based on the CTEQ6.6 (solid histogram) and the MSTW2008nlo (dashed histogram) PDFs are also shown. The lower part of the figure shows the ratio between the measured cross section and the NLO QCD calculation based on the CTEQ6.6 PDFs (dots); the ratio of the calculation based on MSTW2008nlo to that based on CTEQ6.6 is shown as a dashed line. The error bars represent the statistical and systematic uncertainties added in quadrature and the hatched band displays the theoretical uncertainty.

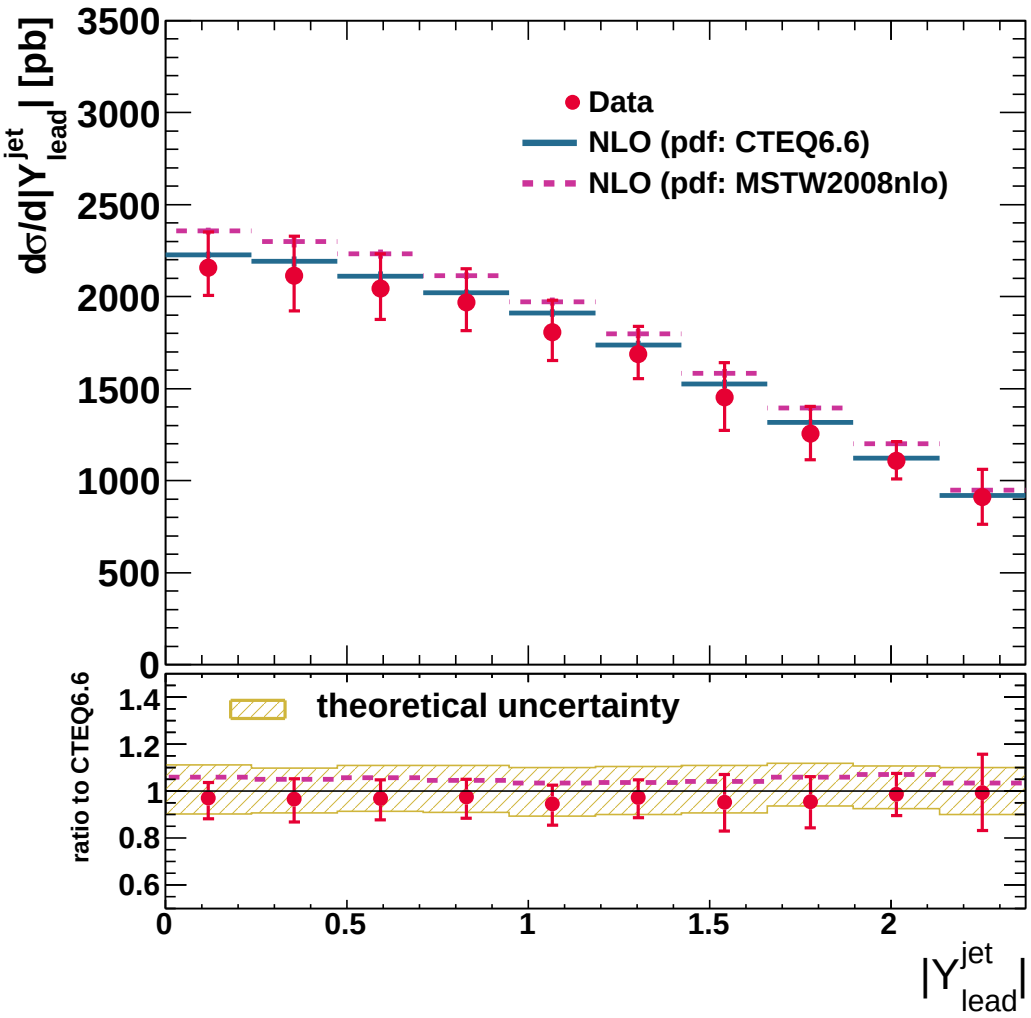

Figure 11.3: The measured differential cross-section for isolated-photon plus jet production (dots) as a function of $|Y^{\rm jet}_{\rm lead}|$. The NLO QCD calculations from JETPHOX corrected for hadronisation+UE effects based on the CTEQ6.6 (solid histogram) and the MSTW2008nlo (dashed histogram) PDFs are also shown. The lower part of the figure shows the ratio between the measured cross section and the NLO QCD calculation based on the CTEQ6.6 PDFs (dots); the ratio of the calculation based on MSTW2008nlo to that based on CTEQ6.6 is shown as a dashed line. The error bars represent the statistical and systematic uncertainties added in quadrature and the hatched band displays the theoretical uncertainty.

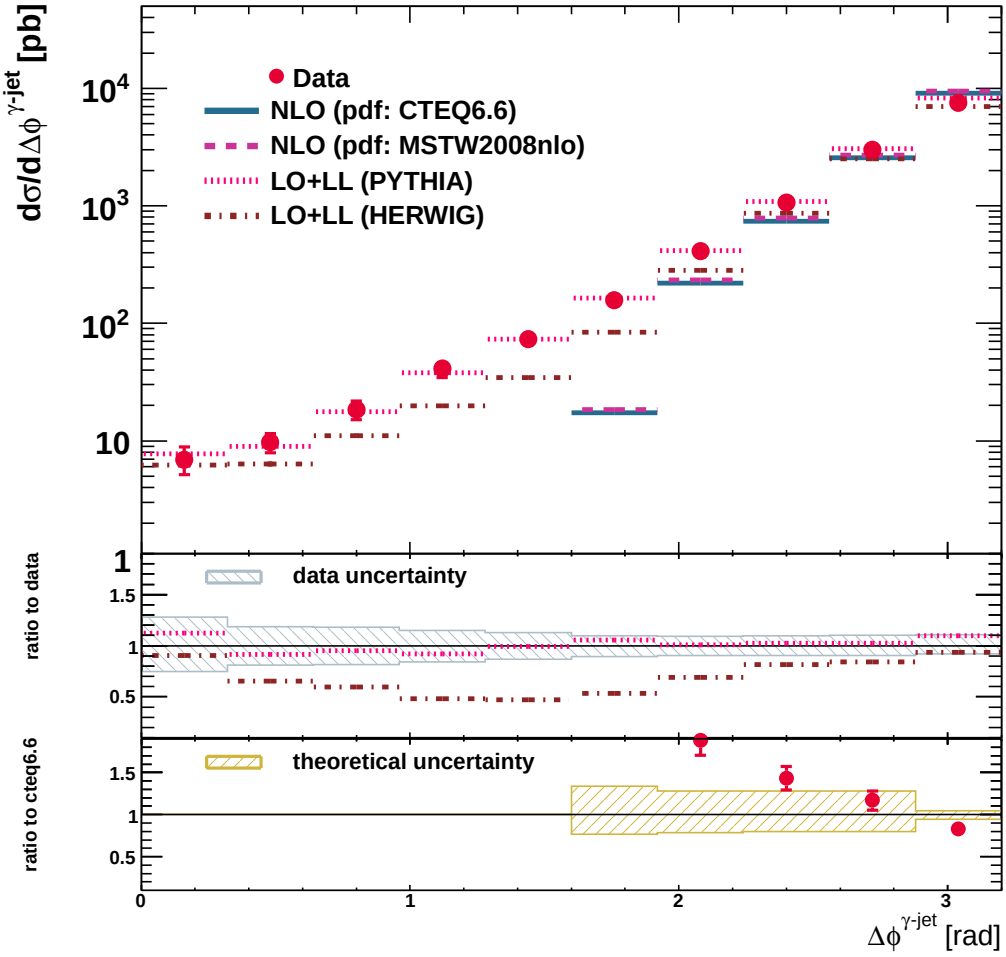

Figure 11.4: The measured differential cross-section for isolated-photon plus jet production (dots) as a function of $\Delta\phi^{\gamma-\mathrm{jet}}$. The NLO QCD calculations from JETPHOX corrected for hadronisation+UE effects based on the CTEQ6.6 (solid histogram) and the MSTW2008nlo (dashed histogram) PDFs are also shown. The predictions from the leading-logarithm parton-shower models of PYTHIA (dotted histogram) and HERWIG (dot-dashed histogram) are also included. The middle part of the figure shows the ratio of these MC predictions to the data; the hatched band displays the data uncertainty. Other details as in the caption to 11.3.

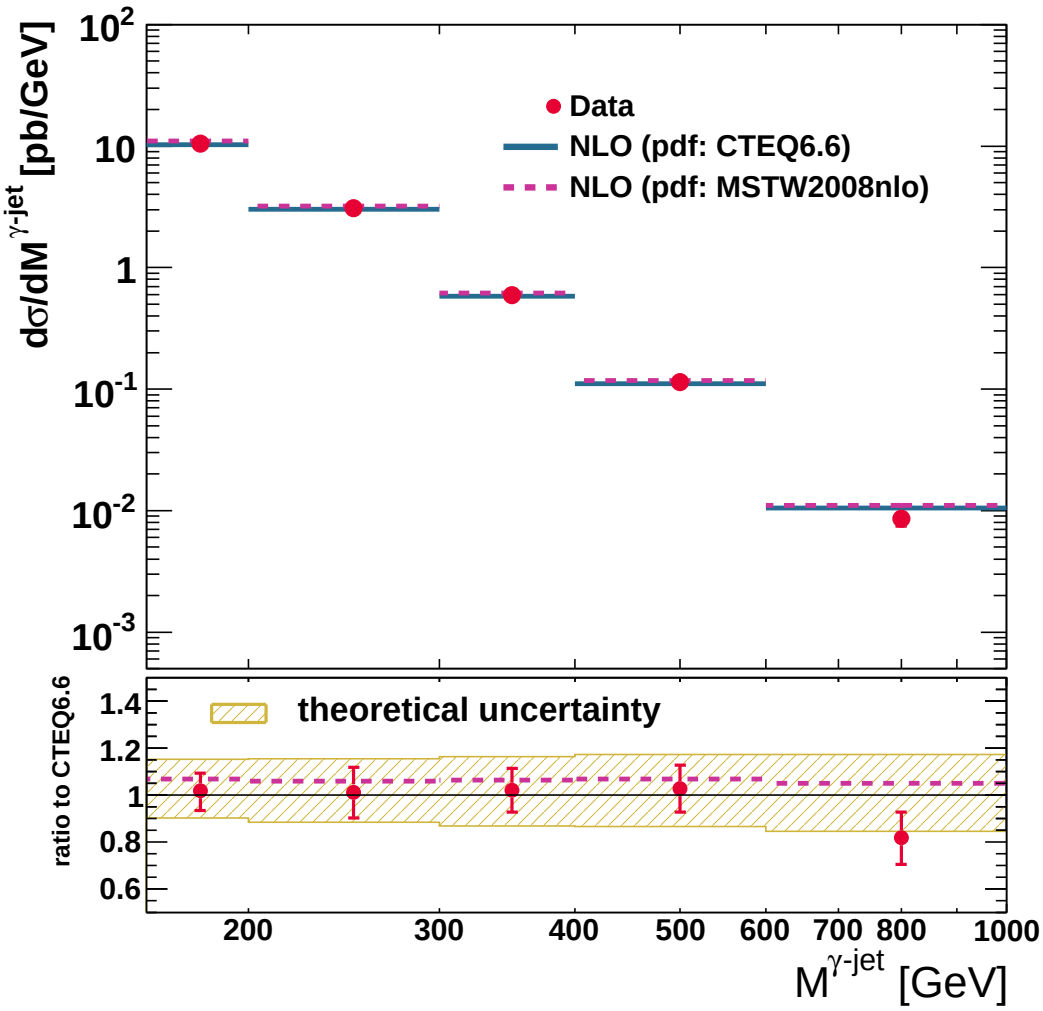

Figure 11.5: The measured differential cross-section for isolated-photon plus jet production (dots) as a function of $M^{\gamma-\mathrm{jet}}$. The NLO QCD calculations from JETPHOX corrected for hadronisation+UE effects based on the CTEQ6.6 (solid histogram) and the MSTW2008nlo (dashed histogram) PDFs are also shown. The lower part of the figure shows the ratio between the measured cross section and the NLO QCD calculation based on the CTEQ6.6 PDFs (dots); the ratio of the calculation based on MSTW2008nlo to that based on CTEQ6.6 is shown as a dashed line. The error bars represent the statistical and systematic uncertainties added in quadrature and the hatched band displays the theoretical uncertainty.

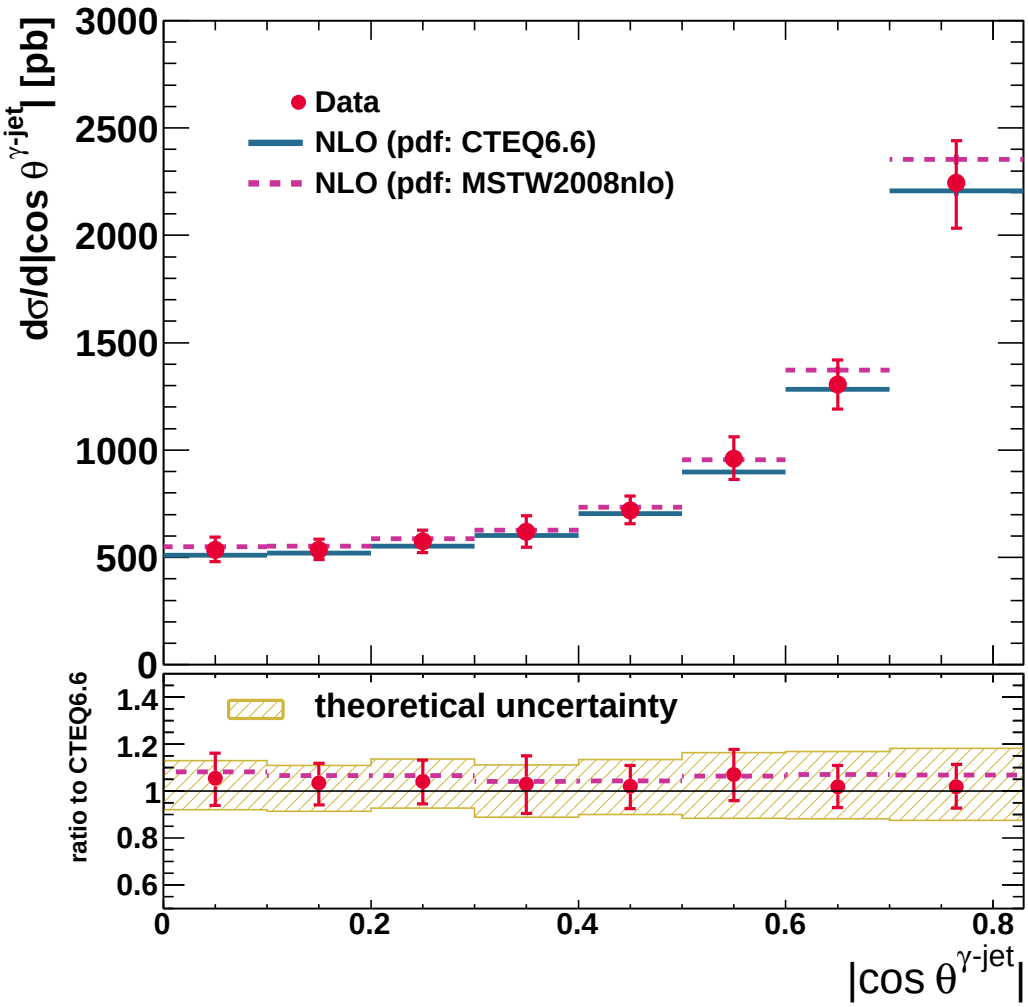

Figure 11.6: The measured differential cross-section for isolated-photon plus jet production (dots) as a function of $|\cos\,\theta^{\gamma-\mathrm{jet}}|$. The NLO QCD calculations from JETPHOX corrected for hadronisation+UE effects based on the CTEQ6.6 (solid histogram) and the MSTW2008nlo (dashed histogram) PDFs are also shown. The lower part of the figure shows the ratio between the measured cross section and the NLO QCD calculation based on the CTEQ6.6 PDFs (dots); the ratio of the calculation based on MSTW2008nlo to that based on CTEQ6.6 is shown as a dashed line. The error bars represent the statistical and systematic uncertainties added in quadrature and the hatched band displays the theoretical uncertainty.

$E^{\gamma}_{T,\mathrm{lead}}$ bin GeV	$d\sigma/dE^{\gamma}_{T,\mathrm{lead}}$ (pb/GeV)	δ_{stat}	δ_{syst}	C_{NLO}
45-55	160.17	± 0.90	$^{+19.48}_{-16.98}$	0.97
55-70	81.09	± 0.50	$^{+8.07}_{-7.32}$	0.96
70-85	35.39	± 0.32	$^{+2.87}_{-2.78}$	0.94
85-100	16.75	± 0.21	$^{+1.01}_{-0.97}$	0.92
100-125	6.89	± 0.10	$^{+0.41}_{-0.40}$	0.92
125-150	2.579	± 0.063	$^{+0.170}_{-0.163}$	0.92
150-200	0.790	± 0.025	$^{+0.044}_{-0.046}$	0.90
200-400	0.0811	± 0.0039	$^{+0.0043}_{-0.0054}$	0.91

Table 11.1: The measured differential cross-section $d\sigma/dE^{\gamma}_{T,\mathrm{lead}}$ for isolated-photon plus jet production. The statistical (δ_{stat}) and systematic (δ_{sys}) uncertainties are shown separately. The corrections for hadronisation and underlying-event effects to be applied to the parton-level NLO QCD calculations (C_{NLO}) are shown in the last column.

$P_{T,\mathrm{lead}}^{\mathrm{jet}}$ bin GeV	$d\sigma/dP_{T,\mathrm{lead}}^{\mathrm{jet}}$ (pb/GeV)	δ_{stat}	δ_{syst}	C_{NLO}
40-55	107.62	± 0.65	$^{+10.83}_{-9.01}$	0.96
55-70	70.13	± 0.47	$^{+7.68}_{-6.73}$	0.98
70-85	36.08	± 0.31	$^{+4.56}_{-4.18}$	0.96
85-100	19.00	± 0.22	$^{+2.18}_{-2.13}$	0.94
100-125	8.86	± 0.11	$^{+1.00}_{-0.97}$	0.91
125-150	3.740	± 0.073	$^{+0.518}_{-0.494}$	0.89
150-200	1.379	± 0.031	$^{+0.187}_{-0.183}$	0.86
200-400	0.1671	± 0.0052	$^{+0.0266}_{-0.0242}$	0.85

Table 11.2: The measured differential cross-section $d\sigma/dP_{T,\mathrm{lead}}^{\mathrm{jet}}$ for isolated-photon plus jet production. The statistical (δ_{stat}) and systematic (δ_{sys}) uncertainties are shown separately. The corrections for hadronisation and underlying-event effects to be applied to the parton-level NLO QCD calculations (C_{NLO}) are shown in the last column.

$\lvert Y^{\text{jet}}_{\text{lead}}\rvert$ bin	$d\sigma/d\lvert Y^{\text{jet}}_{\text{lead}}\rvert$ (pb)	δ_{stat}	δ_{syst}	C_{NLO}
$0.000 - 0.237$	2158	± 20	$^{+190}_{-145}$	0.96
$0.237 - 0.474$	2113	± 20	$^{+211}_{-186}$	0.96
$0.474 - 0.711$	2043	± 20	$^{+186}_{-161}$	0.95
$0.711 - 0.948$	1968	± 20	$^{+177}_{-148}$	0.96
$0.948 - 1.185$	1806	± 19	$^{+170}_{-147}$	0.96
$1.185 - 1.422$	1687	± 18	$^{+146}_{-127}$	0.96
$1.422 - 1.659$	1452	± 17	$^{+187}_{-176}$	0.96
$1.659 - 1.896$	1256	± 16	$^{+144}_{-139}$	0.96
$1.896 - 2.133$	1108	± 15	$^{+100}_{-97}$	0.96
$2.133 - 2.370$	912	± 14	$^{+147}_{-148}$	0.95

Table 11.3: The measured differential cross-section $d\sigma/d\lvert Y^{\text{jet}}_{\text{lead}}\rvert$ for isolated-photon plus jet production. The statistical (δ_{stat}) and systematic (δ_{sys}) uncertainties are shown separately. The corrections for hadronisation and underlying-event effects to be applied to the parton-level NLO QCD calculations (C_{NLO}) are shown in the last column.

$\Delta\phi^{\gamma-\text{jet}}$ bin (rad)	$d\sigma/d\Delta\phi^{\gamma-\text{jet}}$ (pb)	δ_{stat}	δ_{syst}	C_{NLO}
$0.00 - 0.32$	6.9	± 1.1	$^{+1.6}_{-1.3}$	–
$0.32 - 0.64$	9.8	± 1.1	$^{+1.4}_{-1.5}$	–
$0.64 - 0.96$	18.5	± 1.3	$^{+3.0}_{-3.1}$	–
$0.96 - 1.28$	41.1	± 2.2	$^{+5.8}_{-6.1}$	–
$1.28 - 1.60$	73.7	± 2.9	$^{+9.0}_{-9.5}$	–
$1.60 - 1.92$	156.5	± 4.4	$^{+14.7}_{-15.7}$	0.91
$1.92 - 2.24$	411.9	± 7.9	$^{+37.7}_{-38.0}$	0.96
$2.24 - 2.56$	1064	± 12	$^{+103}_{-101}$	0.95
$2.56 - 2.88$	2985	± 21	$^{+299}_{-280}$	0.96
$2.88 - 3.14$	7519	± 34	$^{+800}_{-621}$	0.95

Table 11.4: The measured differential cross-section $d\sigma/d\Delta\phi^{\gamma-\text{jet}}$ for isolated-photon plus jet production. The statistical (δ_{stat}) and systematic (δ_{sys}) uncertainties are shown separately. The corrections for hadronisation and underlying-event effects to be applied to the parton-level NLO QCD calculations (C_{NLO}) are shown in the last column.

$M^{\gamma-\text{jet}}$ bin GeV	$d\sigma/dM^{\gamma-\text{jet}}$ (pb/GeV)	δ_{stat}	δ_{syst}	C_{NLO}
$161-200$	10.46	± 0.11	$^{+0.83}_{-0.75}$	0.97
$200-300$	3.070	± 0.034	$^{+0.325}_{-0.315}$	0.95
$300-400$	0.594	± 0.015	$^{+0.052}_{-0.051}$	0.92
$400-600$	0.1137	± 0.0045	$^{+0.0098}_{-0.0098}$	0.91
$600-1000$	0.00857	± 0.00085	$^{+0.00080}_{-0.00076}$	0.91

Table 11.5: The measured differential cross-section $d\sigma/dM^{\gamma-\text{jet}}$ for isolated-photon plus jet production. The statistical (δ_{stat}) and systematic (δ_{sys}) uncertainties are shown separately. The corrections for hadronisation and underlying-event effects to be applied to the parton-level NLO QCD calculations (C_{NLO}) are shown in the last column.

$\lvert\cos\,\theta^{\gamma-\mathrm{jet}}\rvert$ bin	$d\sigma/d\lvert\cos\,\theta^{\gamma-\mathrm{jet}}\rvert$ (pb)	δ_{stat}	δ_{syst}	C_{NLO}
$0.00-0.10$	536	±14	$^{+56}_{-52}$	0.94
$0.10-0.20$	536	±14	$^{+45}_{-41}$	0.94
$0.20-0.30$	574	±15	$^{+49}_{-47}$	0.94
$0.30-0.40$	619	±15	$^{+73}_{-70}$	0.93
$0.40-0.50$	718	±17	$^{+64}_{-59}$	0.94
$0.50-0.60$	960	±19	$^{+97}_{-93}$	0.94
$0.60-0.70$	1306	±23	$^{+108}_{-112}$	0.97
$0.70-0.83$	2243	±29	$^{+191}_{-205}$	0.97

Table 11.6: The measured differential cross-section $d\sigma/d\lvert\cos\,\theta^{\gamma-\mathrm{jet}}\rvert$ for isolated-photon plus jet production. The statistical (δ_{stat}) and systematic (δ_{sys}) uncertainties are shown separately. The corrections for hadronisation and underlying-event effects to be applied to the parton-level NLO QCD calculations (C_{NLO}) are shown in the last column.

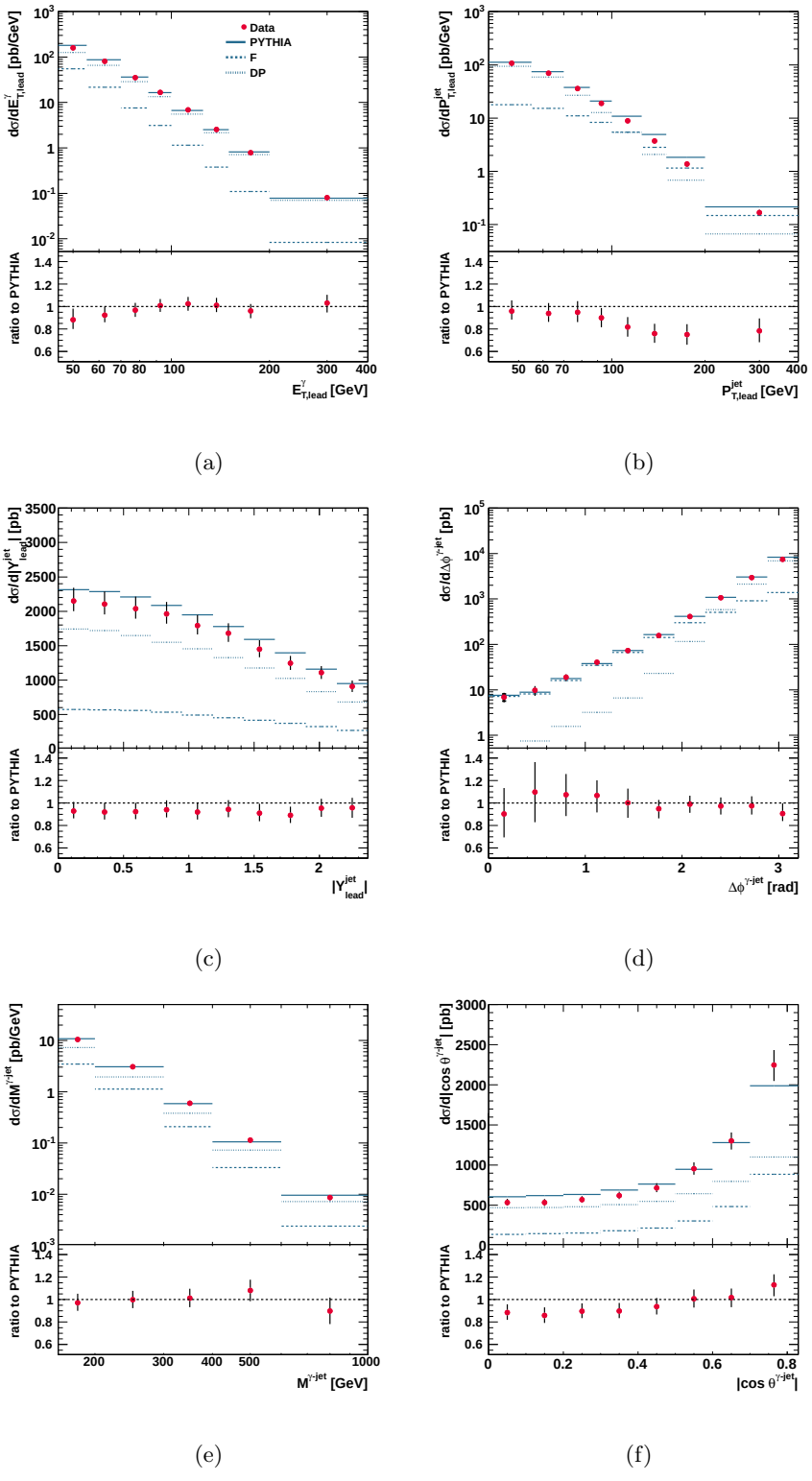

Figure 11.7: The measured differential cross-sections for isolated photon plus jet production (dots) as functions of (a) $E^{\gamma}_{T,\mathrm{lead}}$, (b) $P^{\mathrm{jet}}_{T,\mathrm{lead}}$, (c) $|Y^{\mathrm{jet}}_{\mathrm{lead}}|$, (d) $\Delta\phi^{\gamma-\mathrm{jet}}$, (e) $M^{\gamma-\mathrm{jet}}$ and (f) $|\cos\,\theta^{\gamma-\mathrm{jet}}|$. The calculations from PYTHIA MC for the direct-photon (dotted histogram) and fragmentation (dashed histogram) components as well as their their sum (solid histogram) are also shown. The lower parts of the figures show the ratio between the measured cross sections and the full PYTHIA MC calculation (dots). In all figures, the inner error bars represent the statistical uncertainties; the outer error bars show the statistical and systematic uncertainties added in quadrature.

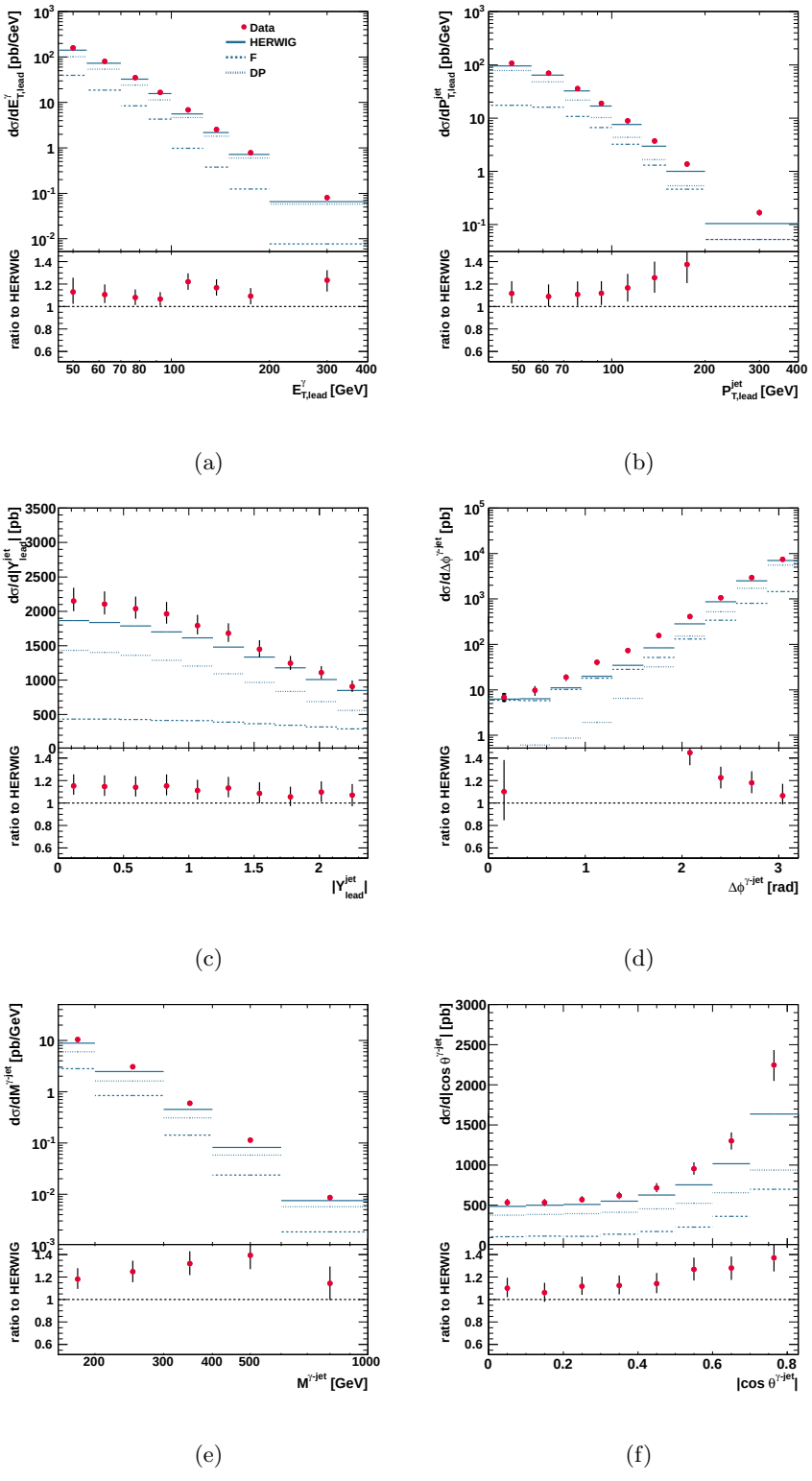

Figure 11.8: The measured differential cross-sections for isolated photon plus jet production (dots) as functions a) $E^{\gamma}_{T,\mathrm{lead}}$, (b) $P^{\mathrm{jet}}_{T,\mathrm{lead}}$, (c) $|Y^{\mathrm{jet}}_{\mathrm{lead}}|$, (d) $\Delta\phi^{\gamma-\mathrm{jet}}$, (e) $M^{\gamma-\mathrm{jet}}$ and (f) $|\cos\,\theta^{\gamma-\mathrm{jet}}|$. The calculations from HERWIG MC for the direct-photon (dotted histogram) and fragmentation (dashed histogram) components as well as their sum (solid histogram) are also shown. The lower parts of the figures show the ratio between the measured cross sections and the full HERWIG MC calculation (dots). In all figures, the inner error bars represent the statistical uncertainties; the outer error bars show the statistical and systematic uncertainties added in quadrature.

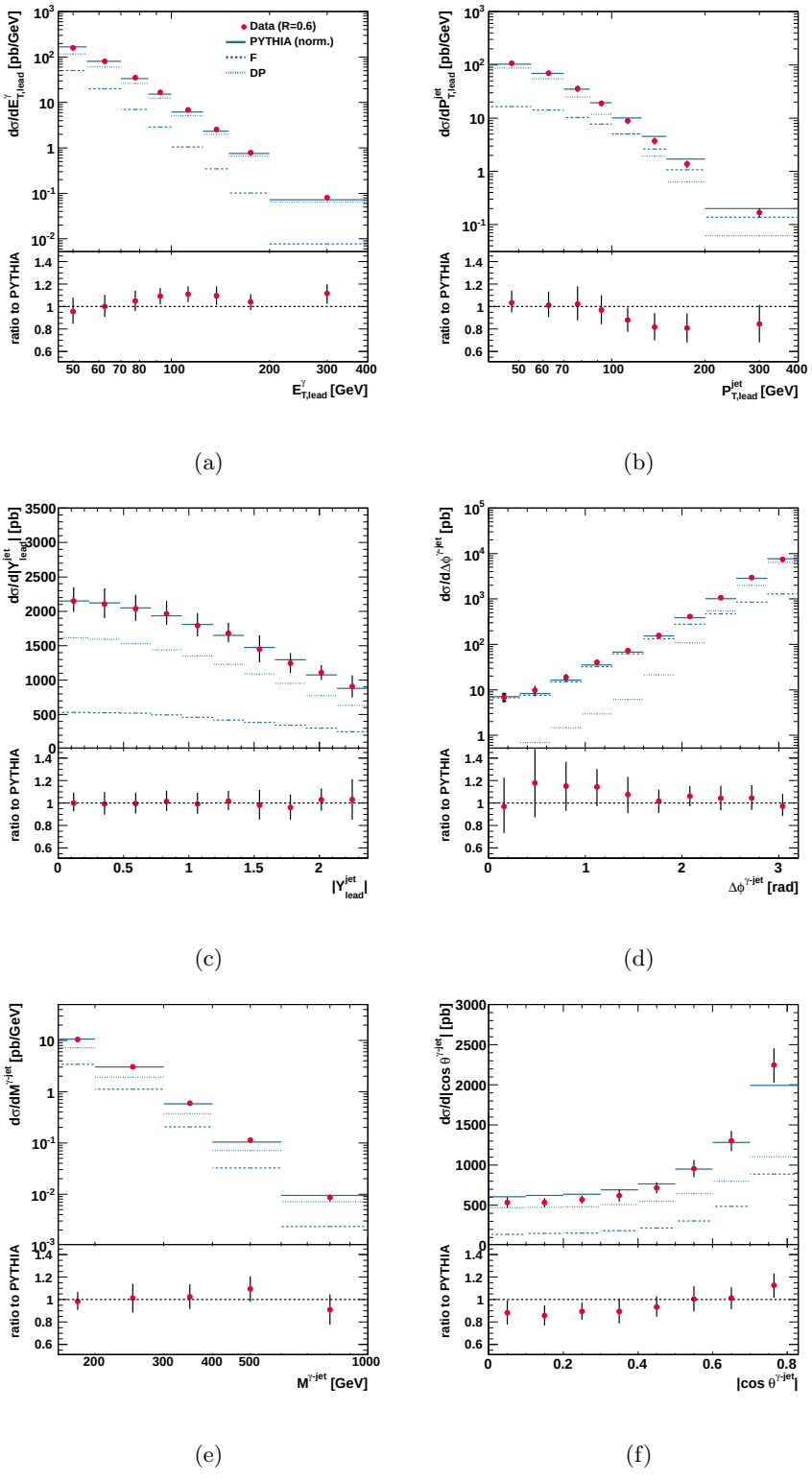

Figure 11.9: The measured differential cross-sections for isolated photon plus jet production (dots) as functions (a) $E^{\gamma}_{T,\mathrm{lead}}$, (b) $P^{\mathrm{jet}}_{T,\mathrm{lead}}$, (c) $|Y^{\mathrm{jet}}_{\mathrm{lead}}|$, (d) $\Delta\phi^{\gamma-\mathrm{jet}}$, (e) $M^{\gamma-\mathrm{jet}}$ and (f) $|\cos\,\theta^{\gamma-\mathrm{jet}}|$. The calculations from PYTHIA MC for the direct-photon (dotted histogram) and fragmentation (dashed histogram) components as well as their sum (solid histogram; normalised to the data) are also shown. The lower parts of the figures show the ratio between the measured cross sections and the full PYTHIA MC calculation (dots). In all figures, the inner error bars represent the statistical uncertainties; the outer error bars show the statistical and systematic uncertainties added in quadrature.

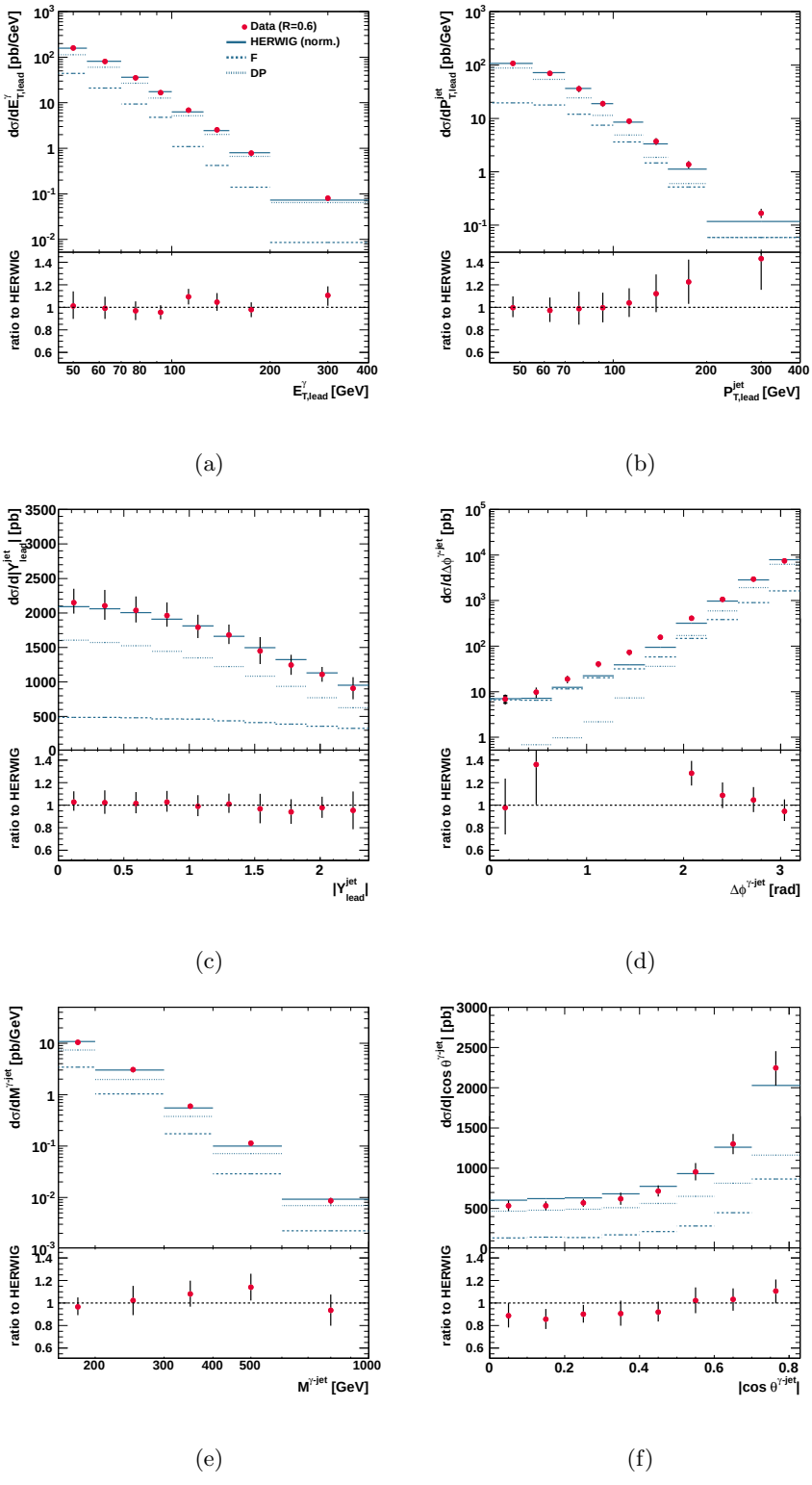

Figure 11.10: The measured differential cross-sections for isolated photon plus jet production (dots) as functions (a) $E^{\gamma}_{T,\mathrm{lead}}$, (b) $P^{\mathrm{jet}}_{T,\mathrm{lead}}$, (c) $|Y^{\mathrm{jet}}_{\mathrm{lead}}|$, (d) $\Delta\phi^{\gamma-\mathrm{jet}}$, (e) $M^{\gamma-\mathrm{jet}}$ and (f) $|\cos\,\theta^{\gamma-\mathrm{jet}}|$. The calculations from HERWIG MC for the direct-photon (dotted histogram) and fragmentation (dashed histogram) components as well as their sum (solid histogram; normalised to the data) are also shown. The lower parts of the figures show the ratio between the measured cross sections and the full HERWIG MC calculation (dots). In all figures, the inner error bars represent the statistical uncertainties; the outer error bars show the statistical and systematic uncertainties added in quadrature.

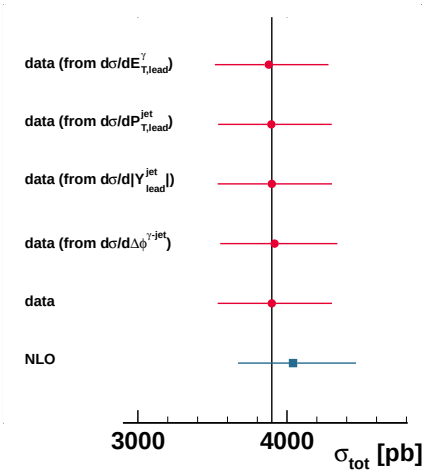

Figure 11.11: Measured integrated cross-sections in the phase space of the differential cross sections as functions of $E^{\gamma}_{T,\mathrm{lead}}$, $P^{\mathrm{jet}}_{T,\mathrm{lead}}$, $|Y^{\mathrm{jet}}_{\mathrm{lead}}|$ and $\Delta\phi^{\gamma-\mathrm{jet}}$ (dots). The second dot from the botton is the result from the event-counting method. The other dots represent the result from the integration of the differential cross sections. The squares represent the NLO QCD predictions. The horizontal error bars display the total experimental (red) and theoretical (blue) uncertainties, respectively.

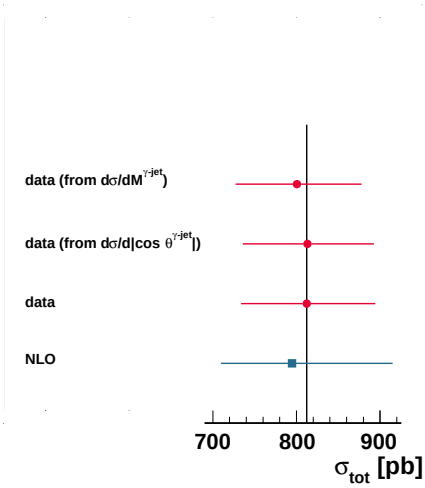

Figure 11.12: Measured integrated cross-sections in the phase space of the differential cross sections as functions of $M^{\gamma-\mathrm{jet}}$ and $|\cos\,\theta^{\gamma-\mathrm{jet}}|$ (dots). The second dot from the botton is the result from the event-counting method. The other dots represent the result from the integration of the differential cross sections. The squares represent the NLO QCD predictions. The horizontal error bars display the total experimental (red) and theoretical (blue) uncertainties, respectively.

Chapter 12

Summary and conclusions

The production of isolated prompt photons in association with jets has been studied in pp collisions at a centre-of-mass energy of 7 TeV with the ATLAS detector at the LHC. The sample of events used corresponds to an integrated luminosity of 37.1 pb^{-1} and was collected during the 2010 data-taking period. The data sample has been used to study the kinematical characteristics as well as the dynamics of the process $pp \to \gamma + \text{jet} + \text{X}$.

The events have been characterised in terms of the leading photon properties such as its transverse momentum ($E^{\gamma}_{T,\text{lead}}$), pseudorapidity ($\eta^{\gamma}_{\text{lead}}$) and azimuthal angle ($\phi^{\gamma}_{\text{lead}}$). Photons have been required to be isolated by imposing an upper cut on the total transverse energy, excluding that of the photon, in a cone of radius 0.4 in the $\eta - \phi$ plane around the photon direction (E^{iso}_{T}). The identification and reconstruction of photons using the Liquid Argon calorimeter of ATLAS has been described in detail as well as its energy-scale and energy-resolution calibrations.

Jets have been defined using the anti-k_T algorithm with the radius parameter $R = 0.6$. The features of this jet algorithm, which provides an optimal performance in the harsh environment of pp collisions at LHC energies, have been described in detail. The leading jet, i.e. that with the highest transverse momentum, has been selected for further study of its kinematical properties, namely its transverse momentum ($P^{\text{jet}}_{T,\text{lead}}$), rapidity ($Y^{\text{jet}}_{\text{lead}}$) and azimuthal angle ($\phi^{\text{jet}}_{\text{lead}}$). The reconstruction of jets using the calorimeters of ATLAS in terms of the so-called topological clusters together with a detailed description of the jet-energy calibration and its associated uncertainties have been discussed.

A sample of events has been selected to perform measurements of differential cross sections as functions of the most relevant kinematical and dynamical vari-

ables. To achieve the best precision of the measurements in terms of the systematic experimental uncertainties and, at the same time, allowing an exploration of the underlying physical phenomena in as a wide range as possible, relatively large thresholds on the transverse momenta of the leading photon and jet have been imposed. Specifically, the leading photon has been required to have $E^{\gamma}_{T,\mathrm{lead}} > 45$ GeV, $|\eta^{\gamma}_{\mathrm{lead}}| < 2.37$ (excluding the region $1.37 < |\eta^{\gamma}_{\mathrm{lead}}| < 1.52$) and $E^{\mathrm{iso}}_{T} < 4$ GeV. The leading jet should fulfill the conditions $P^{\mathrm{jet}}_{T,\mathrm{lead}} > 40$ GeV and $|Y^{\mathrm{jet}}_{\mathrm{lead}}| < 2.37$ as well as that of being relatively far from the leading photon in the $\eta - \phi$ plane, $\Delta R^{\gamma-\mathrm{jet}} = \sqrt{(\eta^{\gamma}_{\mathrm{lead}} - \eta^{\mathrm{jet}}_{\mathrm{lead}})^2 + (\phi^{\gamma}_{\mathrm{lead}} - \phi^{\mathrm{jet}}_{\mathrm{lead}})^2} > 1$.

The selected sample of events, though enriched in genuine isolated prompt photons, still contains some contamination from the decays of hadrons such as π^0's and η's. The removal of this background through simulations of the corresponding processes is not reliable enough and necessitates a data-driven method. For this purpose, a method based on sidebands in the two-dimensional plane spanned by the variable E^{iso}_{T} and a discrete variable which encapsulates the shower-shape properties of the photon has been used. Background-enriched regions in that plane have helped to estimate the background contribution into the signal region using data alone. This method has been complemented with estimates of the contribution of genuine isolated prompt photons (signal leakage fractions) to the background-enriched regions to improve the determination of the genuine signal. As a result, the purity of the sample has been determined as a function of every observable under consideration and found to be above $\approx 90\%$.

Monte Carlo simulations of events in hadron-hadron collisions have been described in detail; starting with the hard scattering of two-body partonic systems, through the inclusion of parton shower, hadronisation, the underlying event and pile-up, and ending with a detailed simulation of the detector, trigger and reconstruction. The multi-purpose Monte Carlo generators PYTHIA and HERWIG have been used for some of the steps enumerated above. Signal events were generated using direct-photon processes ($qg \to q\gamma$ and $q\bar{q} \to g\gamma$) and photon bremmsstrahlung in QCD dijet events. The resulting samples of events have been used for several purposes: (a) the determination of the leakage signal fractions used in the background subtraction; (b) the study of the performance of the reconstruction of the kinematical variables; (c) the evaluation of efficiencies and acceptance corrections to obtain the measurements of differential cross sections as well as (d) some of the associated uncertainties. A comparison between the distributions of kinematical variables in data and simulations has shown, in general, a reasonable agreement.

However, in some cases the level of agreement has not been good enough and a method has been devised to improve the description of the data by the simulations; this has been achieved by fitting the relative contributions of the direct-photon and photon-bremmsstrahlung components in the simulations to the data. The resulting description of the data distributions by both PYTHIA and HERWIG simulations has been found to be satisfactory and validate the use of these samples to evaluate the efficiencies and acceptance corrections.

Measurements have been presented of the differential cross sections as functions of the kinematical variables characterising the leading photon and jet, $E_{T,\mathrm{lead}}^{\gamma}$, $P_{T,\mathrm{lead}}^{\mathrm{jet}}$ and $|Y_{\mathrm{lead}}^{\mathrm{jet}}|$. Furthermore, the dynamics of isolated prompt-photon production in association with a jet has been studied in terms of correlation variables between the leading photon and jet: (a) the azimuthal separation $\Delta\phi^{\gamma-\mathrm{jet}}$; (b) the invariant mass of the photon-jet system $M^{\gamma-\mathrm{jet}}$ and (c) the variable $|\cos\ \theta^{\gamma-\mathrm{jet}}| = \tanh(\frac{|Y_{\mathrm{lead}}^{\mathrm{jet}}-\eta_{\mathrm{lead}}^{\gamma}|}{2})$. The variable $\theta^{\gamma-\mathrm{jet}}$ coincides with the scattering angle in the centre-of-mass system for the case of $2 \to 2$ collinear massless parton-parton scattering. The relevance of such variable lies in the fact that its distribution is sensitive to the spin of the exchanged particle: the differential cross section behaves as $(1 - |\cos\ \theta^{\gamma-\mathrm{jet}}|)^{P}$ as $|\cos\ \theta^{\gamma-\mathrm{jet}}| \to 1$ with $P = -2$ ($P = -1$) for processes dominated by t-channel gluon (quark) exchange. The measurements have been performed in the kinematic region of the selected sample mentioned earlier. For the measurements of the differential cross sections as functions of $M^{\gamma-\mathrm{jet}}$ and $|\cos\ \theta^{\gamma-\mathrm{jet}}|$, the phase-space region has been further restricted to $|Y_{\mathrm{lead}}^{\mathrm{jet}} + \eta_{\mathrm{lead}}^{\gamma}| < 2.37$, $|\cos\ \theta^{\gamma-\mathrm{jet}}| < 0.83$ and $M^{\gamma-\mathrm{jet}} > 161$ GeV to avoid the biases introduced by the transverse momenta and angular cuts on the leading photon and jet.

A detailed study of the systematic uncertainties affecting the measurements has been performed. The major sources of systematic uncertainty are the detector material in the simulation, the model dependence in the signal leakage fractions, the photon energy scale, the jet energy scale and the luminosity determination. The total systematic uncertainty is $\approx 10\%$. These studies have been supplemented by cross checks of the influence of pile-up and of the primary vertex requirement.

The measurements of the differential cross sections have been confronted with next-to-leading (NLO) QCD calculations corrected for hadronisation and underlying-event effects. The ingredients of such calculations have been described in detail. The NLO QCD calculations for isolated prompt-photon production have been made with the JETPHOX program including direct-photon and fragmentation contributions.

A thorough study of the theoretical uncertainties has been made including the effects of terms beyond NLO, the uncertainties on the proton parton distribution functions (PDFs), the uncertainty on the strong coupling constant α_s and the uncertainty due to the modelling of the QCD cascade, hadronisation and underlying event. The dominant uncertainty is that arising from terms beyond NLO for all observables studied. The total theoretical uncertainty is $\approx 10\%$ (15%) for the differential cross sections as functions of $E_{T,\mathrm{lead}}^{\gamma}$ and $|Y_{\mathrm{lead}}^{\mathrm{jet}}|$ ($M^{\gamma-\mathrm{jet}}$ and $|\cos\,\theta^{\gamma-\mathrm{jet}}|$). The dependence of the predictions on the proton PDFs has been studied by comparing the calculations using different sets of proton PDFs such as CTEQ6.6, MSTW2008nlo and CT10. Furthermore, to facilitate the interpretation of the results, leading-order (LO) calculations have been made separately for direct-photon and fragmentation processes. The LO fragmentation contribution is observed to decrease as a function of $E_{T,\mathrm{lead}}^{\gamma}$, $P_{T,\mathrm{lead}}^{\mathrm{jet}}$ and $M^{\gamma-\mathrm{jet}}$ and is approximately constant as a function of $|Y_{\mathrm{lead}}^{\mathrm{jet}}|$. However, it increases as a function of $|\cos\,\theta^{\gamma-\mathrm{jet}}|$ from 2% up to 16%. The shapes of the differential cross sections for the direct-photon and fragmentation contributions at LO QCD have been compared. The major difference has been observed in the differential cross section as a function of $|\cos\,\theta^{\gamma-\mathrm{jet}}|$, with the contribution from fragmentation showing a steeper increase as $|\cos\,\theta^{\gamma-\mathrm{jet}}| \to 1$ than that of direct-photon processes. This different behaviour is due to the different spin of the exchanged particle dominating each of the processes: a quark in the case of direct-photon processes and a gluon in the case of fragmentation processes. Therefore, the distribution in $|\cos\,\theta^{\gamma-\mathrm{jet}}|$ is particularly useful to study the dynamics underlying the hard process and the relative contributions of direct-photon and fragmentation processes.

Regions of phase space have been identified which are particularly sensitive to the contribution from fragmentation, namely at low $E_{T,\mathrm{lead}}^{\gamma}$, $P_{T,\mathrm{lead}}^{\mathrm{jet}}$ and $M^{\gamma-\mathrm{jet}}$ as well as at large $|\cos\,\theta^{\gamma-\mathrm{jet}}|$. As a result, the measurements presented here can be used to tune the relative contributions of direct-photon and fragmentation processes in the description of isolated prompt-photon production by the Monte Carlo models.

The NLO QCD calculations corrected for hadronisation and underlying-event effects give a reasonably good description of the measured cross sections both in shape and magnitude. These comparisons validate the description of the dynamics of isolated prompt photon plus jet production in pp collisions at LHC energies by perturbative QCD at $\mathrm{O}(\alpha\alpha_s^2)$. In particular, the measured dependence with $|\cos\,\theta^{\gamma-\mathrm{jet}}|$ is consistent with the dominance of direct-photon processes and in agreement with the expectation that in the hard process a quark is being exchanged.

Chapter 13

Resumen en castellano

La producción de fotones aislados en asociación con jets en colisiones pp a energías en el centro de masa de 7 TeV ha sido estudiada con el detector ATLAS en el LHC. La muestra de eventos empleada corresponde a los datos recogidos durante el año 2010, que en términos de luminosidad es equivalente a 37.1 pb^{-1}. Esta muestra de datos ha sido usada para estudiar las características cinemáticas y dinámicas del proceso $pp \to \gamma + \text{jet} + \text{X}$.

Los eventos han sido caracterizados en términos de las propiedades del fotón con mayor momento transverso (fotón puntero) tales como: su momento transverso ($E^{\gamma}_{T,\text{lead}}$), pseudorapidez ($\eta^{\gamma}_{\text{lead}}$) y ángulo acimutal ($\phi^{\gamma}_{\text{lead}}$). Se ha requerido que los fotones estén aislados. Para ello, se ha impuesto un corte en la energía transversa total, excluyendo la del propio fotón, calculada dentro de un cono de radio 0.4 centrado en la dirección del fotón en el plano $\eta - \phi$ (E^{iso}_{T}). La identificación y reconstrucción de los fotones usando el calorímetro de argón líquido del detector ATLAS ha sido descrita en detalle así como la calibración de la escala y de la resolución en energía.

Los jets han sido definidos usando el algoritmo de reconstrucción anti-k_T con parámetro $R = 0.6$. Los aspectos de este algoritmo de reconstrucción de jets, que presenta un buen funcionamiento en el complicado estado final de las colisiones pp a las energías del LHC, han sido explicados en detalle. El jet con mayor momento transverso ha sido seleccionado para un estudio más detallado de sus propiedades cinemáticas tales como, su momento transverso ($P^{\text{jet}}_{T,\text{lead}}$), rapidez ($Y^{\text{jet}}_{\text{lead}}$) y ángulo acimutal ($\phi^{\text{jet}}_{\text{lead}}$). También se ha discutido la reconstrucción de jets en términos de los llamados conglomerados topológicos que están formados a partir de celdas del calorímetro de ATLAS, así como la calibración de la escala de energía de los jets y las incertidumbres asociadas.

Se ha seleccionado una muestra de eventos para llevar a cabo medidas de las secciones eficaces diferenciales en función de las variables cinemáticas y dinámicas más relevantes. Se han impuesto cortes relativamente grandes en el momento transverso del fotón y del jet punteros para poder llevar a cabo medidas precisas en términos de las incertidumbres experimentales y, al mismo tiempo, poder explorar los fenomenos físicos subyacentes producidos en el mayor rango posible del espacio de fases. Específicamente, el fotón puntero tiene que cumplir $E^{\gamma}_{T,\mathrm{lead}} > 45$ GeV, $|\eta^{\gamma}_{\mathrm{lead}}| < 2.37$ (excluyendo la región $1.37 < |\eta^{\gamma}_{\mathrm{lead}}| < 1.52$) y $E^{\mathrm{iso}}_{T} < 4$ GeV. El jet puntero debe cumplir que $P^{\mathrm{jet}}_{T,\mathrm{lead}} > 40$ GeV y $|Y^{\mathrm{jet}}_{\mathrm{lead}}| < 2.37$ y, además, estar lo suficientemente alejado del fotón en el plano $\eta-\phi$, en particular, $\Delta R^{\gamma-\mathrm{jet}} = \sqrt{(\eta^{\gamma}_{\mathrm{lead}} - \eta^{\mathrm{jet}}_{\mathrm{lead}})^2 + (\phi^{\gamma}_{\mathrm{lead}} - \phi^{\mathrm{jet}}_{\mathrm{lead}})^2} > 1$.

La muestra de eventos seleccionada, que debido a los cortes realizados consiste en su mayoría de fotones aislados, aún contiene contaminación de eventos en los que hadrones tales como π^0 y η han dejado una señal parecida a la de un fotón aislado. A este tipo de contaminación se le denomina fondo. No es muy preciso quitar este fondo de los datos usando simulaciones que reproduzcan eventos de este tipo. De ahí que se haya usado un método basado en los propios datos para extraer la contribución de este fondo. Este método consiste en dividir el plano bidimensional formado por la variable de aislamiento y una variable discreta que recoge las propiedades de la cascada electromagnética del fotón, en cuatro regiones. Una de esas cuatro regiones corresponde a la zona de medida de la señal, mientras que las tres restantes son zonas en las que abunda el fondo. En este método es posible conocer la cantidad de fondo en la zona de medida de la señal, a partir de la cantidad de fondo en las tres regiones restantes. Este método ha sido complementado estimando la posible cantidad de señal en las zonas enriquecidas por el fondo para mejorar la estimación de la señal en la zona de medida. Como resultado, la pureza de la señal ha sido determinada en función de cada una de las variables bajo estudio y su valor está por encima de aproximadamente 90%.

Las simulaciones Monte Carlo de eventos en colisiones hadrón-hadrón han sido descritas en detalle; empezando por la interacción dura entre los dos partones, la introducción de la cascada partónica, hadronización, eventos subyacentes y terminando con una simulación detallada del detector, trigger y reconstrucción. Los programas Monte Carlo PYTHIA y HERWIG han sido usados para algunos de los pasos mencionados anteriormente. Los eventos de señal fueron generados usando procesos de producción directa de fotones ($qg \to q\gamma$ y $q\bar{q} \to g\gamma$) y procesos de producción de eventos con dos jets en los que los fotones son radiados por los partones del estado

final (fragmentación). Las muestras de eventos resultantes han sido usadas para los siguientes propósitos: (a) determinación de la fracción de la señal en las zonas enriquecidas por el fondo para la determinación de la pureza de la señal; (b) el estudio de la calidad de la reconstrucción de las variables cinemáticas; (c) la evaluación de las eficiencias y de los factores de corrección por aceptancia para obtener las medidas de las secciones eficaces diferenciales así como (d) las incertidumbres asociadas. Se ha comprobado que las distribuciones de las variables cinemáticas predichas por la simulación concuerdan, en general, con las obtenidas en los datos. Sin embargo, en algunos casos el nivel de concordancia no es lo suficientemente bueno por lo que ha sido ideado un método para mejorar la descripción de los datos por la simulación; este método consiste en ajustar a los datos las contribuciones relativas en la simulación de las componentes de los eventos de producción directa de fotones y de los eventos de fragmentación. La descripción de los datos por parte de los modelos PYTHIA y HERWIG resultante de este ajuste se ha encontrado satisfactoria y por lo tanto valida el uso de estas simulaciones para evaluar las eficiencias y los factores de corrección por aceptancia.

Se han presentado medidas de las secciones eficaces diferenciales en función de las variables cinemáticas que caracterizan al fotón y jet punteros, tales como, $E^{\gamma}_{T,\mathrm{lead}}$, $P^{\mathrm{jet}}_{T,\mathrm{lead}}$ y $|Y^{\mathrm{jet}}_{\mathrm{lead}}|$. Además, la dinámica de la producción de un fotón en asociación con un jet ha sido estudiada en términos de variables que los correlacionan, tales como: (a) la separación acimutal $\Delta\phi^{\gamma-\mathrm{jet}}$; (b) la masa invariante del sistema fotón-jet $M^{\gamma-\mathrm{jet}}$ y (c) la variable $|\cos\ \theta^{\gamma-\mathrm{jet}}| = \tanh(\frac{|Y^{\mathrm{jet}}_{\mathrm{lead}}-\eta^{\gamma}_{\mathrm{lead}}|}{2})$. La variable $\theta^{\gamma-\mathrm{jet}}$ coincide con el ángulo de dispersión en el sistema centro de masa para el caso de dispersión colineal de dos partones sin masa. La relevancia de esta variable reside en el hecho de que su distribución es sensible al espín de la partícula intercambiada: la sección eficaz diferencial se comporta como $(1-|\cos\ \theta^{\gamma-\mathrm{jet}}|)^P$ cuando $|\cos\ \theta^{\gamma-\mathrm{jet}}| \to 1$ con $P=-2$ ($P=-1$) para procesos en los que un gluón (quark) es intercambiado en el canal t. Las medidas han sido llevadas a cabo en la región cinemática de la muestra seleccionada comentada anteriormente. Para las medidas de la sección eficaz diferencial en función de $M^{\gamma-\mathrm{jet}}$ y $|\cos\ \theta^{\gamma-\mathrm{jet}}|$, la región del espacio de fases se ha restringido a $|Y^{\mathrm{jet}}_{\mathrm{lead}}+\eta^{\gamma}_{\mathrm{lead}}| < 2.37$, $|\cos\ \theta^{\gamma-\mathrm{jet}}| < 0.83$ y $M^{\gamma-\mathrm{jet}} > 161$ GeV. Está restricción se ha llevado a cabo para evitar el sesgo introducido por las restricciones a los valores del momento transverso y de la rapidez en el fotón y el jet.

Por otro lado, se ha realizado una estimación detallada de las incertidumbres sistemáticas que afectan las medidas llevadas a cabo. La mayores fuentes de incertidumbre sistemática son debidas a la simulación de la cantidad de material del

detector, estimación de la señal en las zonas de fondo, la escala de energía del fotón, la escala de energía del jet y la determinación de la luminosidad. La incertidumbre sistemática total es aproximadamente del 10%. Estos estudios han sido complementados con comprobaciones de la influencia en los resultados del "pile-up" y del requisito en el vértice primario de la colisión.

Una vez obtenidas las medidas de las secciones eficaces diferenciales, éstas han sido comparadas con predicciones teóricas de QCD al segundo orden en teoría de perturbaciones (NLO), corregidas previamente por los efectos de la hadronización y del evento subyacente. Los ingredientes de tales cálculos teóricos se han descrito en detalle. Los cálculos de NLO QCD han sido realizados usando el programa JETPHOX incluyendo la contribución de producción directa de fotones y la producción de fotones por fragmentación. Un concienzudo estudio de las incertidumbres teóricas ha sido realizado incluyendo los efectos de términos de orden superior en teoría de perturbaciones, incertidumbres en las distribuciones partónicas del protón (PDF), la incertidumbre en la constante de acoplo fuerte α_s e incertidumbres debidas al modelo de simulación de la cascada partónica, hadronización y el evento subyacente. La incertidumbre dominante en todas las distribuciones es debida a los efectos de términos de orden superior. La incertidumbre teórica total es aproximadamente del 10% (15%) para las secciones eficaces en función de $E_{T,\mathrm{lead}}^{\gamma}$ y $|Y_{\mathrm{lead}}^{\mathrm{jet}}|$ ($M^{\gamma-\mathrm{jet}}$ y $|\cos\,\theta^{\gamma-\mathrm{jet}}|$). La dependencia en las predicciones teóricas debida a las funciones de distribución partónicas del protón ha sido estudiada comparando el resultado de los cálculos usando diferentes conjuntos de funciones de distribución partónicas, tales como CTEQ6.6, MSTW2008nlo y CT10. Además, para facilitar la interpretación de los resultados, se han llevado a cabo cálculos a primer orden en teoría de perturbaciones separadamente para los procesos de producción directa de fotones y para los procesos de producción de fotones por fragmentación. La contribución de los procesos de producción de fotones por medio de la fragmentación decrece como función de $E_{T,\mathrm{lead}}^{\gamma}$, $P_{T,\mathrm{lead}}^{\mathrm{jet}}$ y $M^{\gamma-\mathrm{jet}}$ y es aproximadamente constante como función de $|Y_{\mathrm{lead}}^{\mathrm{jet}}|$. Sin embargo, crece como función de $|\cos\,\theta^{\gamma-\mathrm{jet}}|$ desde un 2% hasta un 16%. También ha sido comparada la forma de las secciones eficaces diferenciales predichas a primer orden en teoría de perturbaciones para los procesos de producción directa de fotones y los procesos de producción de fotones por fragmentación. La mayor diferencia entre ambos se encuentra en la sección eficaz diferencial como función de $|\cos\,\theta^{\gamma-\mathrm{jet}}|$, en la que la contribución de la fragmentación muestra un crecimiento más pronunciado a medida que $|\cos\,\theta^{\gamma-\mathrm{jet}}| \to 1$. Esta diferencia en comportamientos es debida a la diferencia en el espín de la partícula intercambiada en los procesos dominantes para cada contribución: un quark en el caso de los procesos de producción directa de fotones y un gluón en el caso de los procesos de fragmentación. Por lo tanto, la

distribución de $|\cos\ \theta^{\gamma-\mathrm{jet}}|$ es particularmente útil para el estudio de la dinámica subyacente en el proceso duro y de las contribuciones relativas de las componentes de los procesos de producción directa y de fragmentación.

A partir de los resultados teóricos obtenidos a primer orden en teoría de perturbaciones se ha demostrado que las regiones del espacio de fases particularmente sensibles a la contribución de la fragmentación son para valores bajos de $E_{T,\mathrm{lead}}^{\gamma}$, $P_{T,\mathrm{lead}}^{\mathrm{jet}}$ y $M^{\gamma-\mathrm{jet}}$ así como para valores grandes de $|\cos\ \theta^{\gamma-\mathrm{jet}}|$. Como resultado, las medidas aquí presentadas pueden usarse para ajustar de manera más precisa la contribución relativa de las componentes de producción directa y de fragmentación en la descripción de la producción de fotones aislados dada por los programas Monte Carlo.

Para concluir, es de notar, que los cálculos teóricos al segundo orden en teoría de perturbaciones tras ser corregidos por los efectos de la hadronización y del evento subyacente proporcionan una buena descripción de las secciones eficaces medidas tanto en forma como en magnitud. Esta comparación da validez a la descripción perturbativa basada en QCD al orden $\mathrm{O}(\alpha\alpha_s^2)$ de la dinámica de la producción de un fotón aislado en asociación con un jet en las colisiones *pp* a las energías del LHC. En particular, la dependencia de la medida como función de $|\cos\ \theta^{\gamma-\mathrm{jet}}|$ es consistente con el hecho de que la contribución debida a la producción directa de fotones domina así como con la predicción de que en el proceso duro se está intercambiando un quark.

Bibliography

[1] T. Pietrycki and A. Szczurek, *Photon-jet correlations in pp and $p\bar{p}$ collisions.* Phys. Rev. **D 76** (2007) 034003;
Z. Belghobsi et al., *Photon-jet correlations and constraints on fragmentation functions.* Phys. Rev. **D 79** (2009) 114024.

[2] ATLAS collaboration, G. Aad et al., *Measurement of the inclusive isolated prompt photon cross section in pp collisions at $\sqrt{s} = 7$ TeV with the ATLAS detector.* Phys. Rev. **D 83** (2011) 052005.

[3] ATLAS collaboration, G. Aad et al., *Measurement of the inclusive isolated prompt photon cross-section in pp collisions at $\sqrt{s} = 7$ TeV using 35 pb^{-1} of ATLAS data.* Phys. Lett. **B 706** (2011) 150.

[4] J. Cantero et al., *Measurement of the production cross section of an isolated photon associated with jets in proton-proton collisions at $\sqrt{s} = 7$ TeV with the ATLAS detector.* ATL-COM-PHYS-2011-870.

[5] M. Cacciari, G.P. Salam and G. Soyez, *The anti-k_t jet clustering algorithm.* JHEP **0804** (2008) 063.

[6] The LHC STUDY GROUP collaboration, *LHC - the Large Hadron Collider accelerator project,* CERN-AC-93-03.

[7] The LHC STUDY GROUP collaboration, *LHC - the Large Hadron Collider conceptual design,* CERN-AC-95-03.

[8] O.S. Brning et al. *The LHC design report v.1: the LHC Main Ring,* CERN-2004-003-V-1; *The LHC design report v.2: the LHC Infrastructure and General Services,* CERN-2004-003-V-2; *The LHC design report v.3: the LHC Injector Chain,* CERN-2004-003-V-3.

[9] ATLAS Collaboration, *The ATLAS Experiment at the CERN Large Hadron Collider.* JINST **3** (2008) S08003, pp. 53-110.

[10] ATLAS Collaboration, *The ATLAS Experiment at the CERN Large Hadron Collider.* JINST **3** (2008) S08003, pp. 110-164.

[11] ATLAS Collaboration, *The ATLAS Experiment at the CERN Large Hadron Collider.* JINST **3** (2008) S08003, pp. 164-210.

[12] ATLAS Collaboration, *The ATLAS Experiment at the CERN Large Hadron Collider.* JINST **3** (2008) S08003, pp. 218-256.

[13] R.P. Feynman, *Photon-Hadron interactions.* Benjamin, Reading, MA, 1972.

[14] J.C. Collins, D.E. Soper and G. Sterman, *Factorization of Hard Processes in QCD.* Adv. Ser. Direct. High Energy Phys. 5 (1988) 1 [hep-ph/0409313v1].

[15] Yu. L. Dokshitzer, V.A Khoze, A.H. Mueller and S.I. Troyan, *Basic of Perturbative QCD.* Ed. J. Tran Thanh Van, Edditions Frontires, Gif-sur-Yvette, 1991.

[16] M. Gell-Mann and E.P. Rosenbaum, *Elementary Particles*, Scientific American, July 1957, pp. 72-86.

[17] H1 and ZEUS collaborations, H1-prelim-11-143 and ZEUS-prel-11-010.

[18] J.C. Collins, *Renormalization*, Cambridge Univertisty Press, Cambridge, 1984.

[19] C.G. Callan Jr., *Broken scale invariance in scalar field theory.* Phys. Rev. **D 2** (1970) 1541; K. Symanzik, *Small distance behavior in field theory and power counting.* Comm. Math. Phys. **18** (1970) 227.

[20] S. Bethke and P. Zerwas, *Weak strong interaction: The asymptotic freedom of quarks.* Physik J. **3N12** (2004) 31;
C. Glasman, *Precision measurements of α_s at HERA*, Proceedings of the XIII International Workshop on Deep Inelastic Scattering, Madison, Wisconsin, USA, April 2005; W. Smith ed., AIP Conference Proceedings Vol. 792 (2005), pp 689-692 [hep-ex/0506035].

[21] S. Moch and A. Vogt, *Higher-order soft corrections to lepton pair and Higgs boson production.* Phys. Lett. **B 631** (2005) 48;
R.V. Harlander and W.B. Kilgore, *Next-to-next-to-leading order Higgs production at hadron colliders.* Phys. Rev. Lett. **88** (2002) 201801 [hep-ph/0201206];
C. Anastasiou and K. Melnikov, *Higgs boson production at hadron colliders in NNLO QCD.* Nucl. Phys. **B 646** (2002) 220 [hep-ph/0207004];
V. Ravindran, J. Smith and W.L. van Neerven, *NNLO corrections to the total cross-section for Higgs boson production in hadron hadron collisions.* Nucl. Phys. **B 665** (2003) 325 [hep-ph/0302135].

[22] G. Altarelli and G. Parisi, *Asymptotic Freedom in Parton Language.* Nucl. Phys. **B 126** (1997) 298.

[23] Yu.L. Dokshitzer, *Calculation of the Structure Functions for Deep Inelastic Scattering and e^+e^- Annihilation by Perturbation Theory in Quantum Chromodynamics.* Sov. Phys. JETP **46** (1977) 641.

[24] V.N. Gribov and L.N. Lipatov, *Deep inelastic ep scattering in perturbation theory.* Sov. J. Nucl. Phys. **15** (1972) 438.

[25] R.K. Ellis et al. *Factorization and the parton model in QCD.* Phys. Lett. **B 78** (1978) 281.

[26] P. Aurenche, R.Baier, M. Fontannaz and D. Schiff, *Prompt Photon Production at Large p_T Scheme Invariant QCD Predictions and Comparison with Experiment.* Nucl. Phys. **B 297** (1988) 661;
L.E. Gordon and W. Vogelsang, *Polarized and unpolarized isolated prompt photon production beyond the leading order.* Phys. Rev. **D 50** (1994) 1901.

[27] F. Aversa, P. Chiappetta, M. Greco and J.Ph. Guillet, *Higher Order Corrections to QCD Jets.* Phys. Lett. **B 210** (1988) 225; *Higher Order Corrections To QCD Jets: Gluon-gluon Processes.*

Phys. Lett. **B 211** (1988) 465; *QCD Corrections to Parton-Parton Scattering Processes.* Nucl. Phys. **B 327** (1989) 105.

[28] E.L. Berger and J. Qiu, *Calculations of prompt photon production in QCD.* Phys. Rev. **D 44** (1991) 2002.

[29] E.L Berger, X.F. Guo and J. Qiu, *Breakdown of conventional factorization for isolated photon cross-sections.* Phys. Rev. Lett. **76** (1996) 2234; *Isolated prompt photon production in hadronic final states of e^+e^- annihilation.* Phys. Rev. **D 54** (1996) 5470.

[30] P. Aurenche, M. Fontannaz, J.P. Guillet, A. Kotikov and E. Pilon, *Is factorization for isolated photon cross-sections broken?* Phys. Rev. **D 55** (1997) 1124.

[31] S. Catani, M. Fontannaz and E. Pilon, *Factorization and soft gluon divergences in isolated photon cross-sections.* Phys. Rev. **D 58** (1998) 094025.

[32] S. Catani et al., *Cross section of isolated prompt photons in hadron-hadron collisions.* JHEP **0205** (2002) 028 [hep-ph/0204023].

[33] F. Aversa, P. Chiappetta, M. Greco and J.Ph. Guillet, *QCD Corrections to Parton-Parton Scattering Processes.* Nucl. Phys. **B 327** (1989) 105;
P.Aurenche, P. Chiappetta, M. Fontannaz, J.Ph. Guillet and E. Pilon, *Next-to-leading order bremsstrahlung contribution to prompt photon production.* Nucl. Phys **B 399** (1993) 34.

[34] S. Catani, Y.L. Dokshitzer, M.H. Seymour and B.R. Webber, *Longitudinally invariant K_t clustering algorithms for hadron hadron collisions.* Nucl. Phys. **B 406** (1993) 187 and references therein; S.D. Ellis and D.E. Soper, *Successive combination jet algorithm for hadron collision.* Phys. Rev. **D 48** (1993) 3160.

[35] M. Cacciari, G.P. Salam and G. Soyez, *The anti-k_t jet clustering algorithm.* JHEP **0804** (2008) 063.

[36] M. Cacciari, G.P. Salam and G. Soyez, *A practical seedless infrared-safe cone jet algorithm.* JHEP **0705** (2007) 086.

[37] M. Cacciari, G.P. Salam and G. Soyez, *The catchment area of jets.* JHEP **0804** (2008) 005.

[38] M. Cacciari, G.P. Salam and G. Soyez, http://fastjet.fr;
M. Cacciari, G.P. Salam and G. Soyez, *FastJet User Manual.* Eur. Phys. J. **C 72** (2012) 1896 [arXiv:1111.6097];
M. Cacciari and G.P. Salam, *Dispelling the N^3 myth for the k_t jet-finder.* Phys. Lett. **B 641** (2006) 57 [hep-ph/0512210].

[39] Y.L. Dokshitzer, G.D. Leder, S. Moretti and B.R. Webber, *Better jet clustering algorithms.* JHEP **9708** (1997) 001.

[40] M.Furman, *Study of a nonleading QCD correction to hadron calorimeter reactions.* Nucl. Phys. **B 197** (1982) 413;
W.T. Giele and E.W.N. Glover, *Higher order corrections to jet cross-sections in e^+e^- annihilation.* Phys. Rev. **D 46** (1992) 1980;
W.T. Giele, E.W.N. Glover and D.A. Kosower, *Higher order corrections to jet cross-sections in hadron colliders.* Nucl. Phys. **B 403** (1993) 633.

[41] R.K. Ellis, D.A. Ross and A.E. Terrano, *The perturbative calculation of jet structure in e^+e^- annihilation.* Nucl. Phys. **B 178** (1981) 421;
Z. Kunszt and D.E. Soper, *Calculation of jet cross-section in hadron collision at order $O(\alpha_s^3)$.* Phys. Rev. **D 46** (1992) 192;
S. Frixione, Z. Kunszt and A. Signer, *Three jet cross-sections to next-to-leading order.* Nucl. Phys. **B 467** (1996) 399;
S. Catani and M.H. Seymour, *The dipole formalism for the calculation of QCD jet cross-sections at next-to-leading order.* Phys. Lett. **B 378** (1996) 287;
S. Catani and M.H. Seymour, *A general algorithm for calculating jet cross-sections in NLO QCD.* Nucl. Phys. **B 485** (1997) 291. Erratum in Nucl. Phys. **B 510** (1998) 503.

[42] P. Nadolsky et al., *Implications of cteq global analysis for collider observables.* Phys. Rev. **D 78** (2008) 013004.

[43] L. Bourhis et al., *Next-to-leading order determination of fragmentation functions.* Eur. Phys. J. **C 19** (2001) 89.

[44] A.D. Martin, W.J. Stirling, R.S. Thorne, G. Watt, *Uncertainties on α_s in global PDF analyses and implications for predicted hadronic cross sections.* Eur. Phys. J. **C 64** (2009) 653.

[45] H.-L. Lai et al., *New parton distributions for collider physics.* Phys. Rev. **D 82** (2010) 074024.

[46] T. Sjoestrand et al.*High-energy physics event generation with PYTHIA 6.1.* Com. Phys. Comm **135** (2001) 238.

[47] G. Corcella et al. *HERWIG 6: An Event generator for hadron emission reactions with interfering gluons (including supersymmetric processes).* JHEP **0101** (2001) 010.

[48] B. Andersson et al., *Parton fragmentation and string dynamics.* Phys. Rep. **97** (1983) 31.

[49] B.R. Webber, *A QCD model for jet fragmentation including soft gluon interference.* Nucl. Phys. **B 238** (1984) 492.

[50] T. Sjoestrand et al., *High-energy-physics event generation with PYTHIA 6.1.* Comp. Phys. Comm **135** (2001) 238.

[51] G. Corcella et al., *HERWIG 6: An Event generator for hadron emission reactions with interfering gluons (including supersymmetric processes).* JHEP **0101** (2001) 010.

[52] A. Sherstnev and R.S. Thorne, *Parton distributions for LO generators.* Eur. Phys. J. **C 55** (2008) 553.

[53] J.M. Butterworth, J.R. Forshaw and M.H. Seymour, *Multiparton interactions in photonproduction at HERA.* Z. Phys. **C 72** (1996) 637.

[54] ATLAS Collaboration, *Charged particle multiplicites in pp interactions at $\sqrt{s}$ =0.9 and 7 TeV in a diffractive limited phase-space measured with the ATLAS detector at the LHC and new PYTHIA 6 tune.* ATLAS-CONF-2010-031.

[55] ATLAS Collaboration, *Measurement of the production cross section of an isolated photon associated with jets in proton-proton collisions at $\sqrt{s}$ = 7 TeV with the ATLAS detector* Phys. Rev. **D 85** (2012) 092014.

[56] J. Cantero et al. *Measurement of the production cross section of an isolated photon associated with jets in proton-proton collisions at $\sqrt{s}$ = 7 TeV with the ATLAS detector.* ATL-COM-PHYS-2011-870.

[57] M. Cacciari, G.P. Salam and S. Sapeta, *On the characterisation of the underlying event.* JHEP **1004** (2010) 065.

[58] Ya.I. Azimov, Yu.L. Dokshitzer, V.A. Khoze and S.I. Troyan, *Similarity of Parton and Hadron Spectra in QCD Jets.* Z. Phys. **C 27** (1985) 65.

[59] Ya.I. Azimov, Yu.L. Dokshitzer, V.A. Khoze and S.I. Troyan, *Humpbacked QCD Plateau in Hadron Spectra.* Z. Phys. **C 31** (1986) 213.

[60] S. Agostinelli et al., *Geant4 - a simulation toolkit.* Nucl. Instrum. Meth. **A 506** (2003) 250.

[61] ATLAS Collaboration, *Expected Performance of the ATLAS Experiment, Detector, Trigger and Physics.* CERN-OPEN-2008-020 (2008), arXiv:0901.0512 [hep-ex].

[62] *ATLAS detector and physics performance: Technical Design Report, 1.* Technical Design Report ATLAS. CERN, Geneva, 1999.

[63] ATLAS Collaboration, G. Aad et al., *Expected Performance of the ATLAS Experiment - Detector, Trigger and Physics.* CERN-OPEN-2008-020 (2008), arXiv:0901.0512 [hep-ex].

[64] ATLAS Collaboration, *Electron and photon reconstruction and identification in ATLAS: expected performance at high energy and results at 900 GeV.* ATLAS-CONF-2010-005 (2010).

[65] ATLAS Collaboration, *Expected electron performance in the ATLAS experiment.* ATL-PHYS-PUB-2011-006 (2010).

[66] ATLAS Collaboration, G. Aad et al., *Expected Performance of the ATLAS Experiment, Detector, Trigger and Physics: Reconstruction of photon conversions.* CERN-OPEN-2008-020, Geneva (2008), 112-140.

[67] ATLAS Collaboration, *Reconstruction and Identification of Photons* in *Expected Performance of the ATLAS Experiment: Detector, Trigger and Physics.* pp. 94-111. CERN, Geneva, 2008, CERN-OPEN-2008-020, arXiv:0901.0512 [hep-ex].

[68] ATLAS Collaboration, *ATLAS detector and physics performance: Technical Design Report, Vol. 1.* Technical Design Report ATLAS. CERN, Geneva, 1999.

[69] B. Aubert et al., *Performance of the ATLAS electromagnetic calorimeter end-cap module 0.* Nucl. Instrum. Meth. **A 500** (2003) 178.

[70] B. Aubert et al., *Performance of the ATLAS electromagnetic calorimeter barrel module 0.* Nucl. Instrum. Meth. **A 500** (2003) 202.

[71] Particle Data Group Collaboration, K. Nakamura et al. *Review of particle physics.* J. Phys. **G 37** (2010) 075021.

[72] M. Agustoni et al., *Electron energy scale in-situ calibration and performance.* ATLAS-COM-PHYS-2011-263.

[73] D. Banfi et al., *Cell response equalization of the ATLAS electronic calorimeter without the direct knowledge of the ionization signals.* J. Instrum **1** (2006) P08001.

[74] C. Collard et al., *Prediction of signal amplitude and shape for the ATLAS electromagnetic calorimeter.* ATL-LARG-PUB-2007-010.

[75] H. Abreu et al., *Performance of the electronic readout of the ATLAS liquid argon calorimeters.* JINST **5** (2010) P09003.

[76] J. Colas et al., *Response Uniformity of the ATLAS Liquid Argon Electromagnetic Calorimeter.* Nucl. Instrum. Meth. **A 582** (2007) 429.

[77] ATLAS Collaboration, *Jet Reconstruction Performance* in *Expected Performance of the ATLAS Experiment: Detector, Trigger and Physics.* CERN, Geneva, 2008, CERN-OPEN-2008-020, arXiv:0901.0512 [hep-ex].

[78] ATLAS Collaboration, *ATLAS Detector and Physics Performance Technical Design Report.* Preprint CERN/LHCC 99-14/15, 1999.

[79] ATLAS Collaboration, *Properties of jets and inputs to jet reconstruction and calibration with the ATLAS detector using proton-proton collisions at* $\sqrt{s}$ *= 7 TeV.* ATLAS-CONF-2010-053, CERN, Geneva, June, 2010.

[80] ATLAS Collaboration, *In-situ jet energy scale and jet shape corrections for multiple interactions in the first ATLAS data at the LHC.* ATLAS-CONF-2011-030, CERN, Geneva, February, 2010.

[81] ATLAS Collaboration, *ATLAS Calorimeter Response to Single Isolated Hadrons and Estimation of the Calorimeter Jet Scale Uncertainty.* ATLAS-CONF-2011-028, CERN, Geneva, March, 2011.

[82] E. Khramov et al., *Study of the response of the hadronic barrel calorimeter in the ATLAS combined test-beam to pions of energies from 20-GeV to 350-GeV for beam impact points from 0.2 to 0.65.* ATL-TILECAL-PUB-2009-007, CERN, Geneva, Apr, 2009.

[83] ATLAS Collaboration, *Jet energy scale and its systematic uncertainty for jets produced in proton-proton collisions at* $\sqrt{s}$ *= 7 TeV and measured with the ATLAS detector.* ATLAS-CONF-2010-056, CERN, Geneva, July, 2010.

[84] ATLAS Collaboration, *Mapping the material in the ATLAS Inner Detector using secondary hadronic interactions in* $\sqrt{s}$ *= 7 TeV collisions.* ATLAS-CONF-2010-058, CERN, Geneva, July, 2010.

[85] ATLAS Collaboration, *Study of the Material Budget in the ATLAS Inner Detector with* K^0_S *decays in collision data at* $\sqrt{s}$ *= 900 GeV.* ATLAS-CONF-2010-019, CERN, Geneva, July, 2010.

[86] ATLAS Collaboration, *Probing the material in front of the ATLAS electromagnetic calorimeter with energy flow from* $\sqrt{s}$ *= 7 TeV minimum bias events.* ATLAS-CONF-2010-037, CERN, Geneva, July, 2010.

[87] P. Z. Skands, *Tuning Monte Carlo Generators: The Perugia Tunes.* Phys. Rev. **D 82** (2010) 074018 [arXiv:1005.3457].

[88] ATLAS Collaboration, *In-situ pseudorapidity intercalibration for evaluation of jet energy scale uncertainty using dijet events in proton-proton collisions at* $\sqrt{s}$ *= 7 TeV.* ATLAS-CONF-2011-014, CERN, Geneva, February, 2011.

[89] ATLAS Collaboration,*In-situ jet energy scale and jet shape corrections for multiple interactions in the first ATLAS data at the LHC.* ATLAS-CONF-2011-030, CERN, Geneva, February, 2010.

[90] ATLAS Collaboration, G. Aad et al., *Jet energy measurement with the ATLAS detector in proton-proton collisions at* $\sqrt{s} = 7$ *TeV.* Preprint arXiv:1112.6426, 2011.

[91] ATLAS Collaboration, *Updated Luminosity Determination in pp Collisions at* $\sqrt{7}$ *TeV using the ATLAS Detector.* ATLAS-CONF-2011-011.

[92] ATLAS Collaboration, *Measurement of the inclusive isolated prompt photon cross section in pp collisions at* $\sqrt{s} = 7$ *TeV with the ATLAS detector using 35* pb^{-1}. ATL-COM-PHYS-2011-058.

[93] ATLAS Collaboration, G. Aad. et al., *Measurement of the inclusive isolated prompt photon cross section in pp collisions at* $\sqrt{s} = 7$ *TeV with the ATLAS detector.* Phys. Rev. **D 83** (2011) 052005.

[94] ATLAS Collaboration, *Measurement of the inclusive isolated prompt photon cross section in pp collisions at* $\sqrt{s} = 7$ *TeV with the ATLAS detector using 35* pb^{-1}. ATL-COM-PHYS-2011-058.

[95] Tim Adye, in *Proceedings of the PHYSTAT 2011 Workshop on Statistical Issues Related to Discovery Claims in Search Experiments and Unfolding*, CERN, Geneva, Switzerland, 17-20 January 2011, edited by H.B. Prosper and L. Lyons, CERN-2011-006, pp. 313-318.

[96] G. D'Agostini, *A multidimensional unfolding method based on Bayes' theorem.* Nucl. Instum. Meth. **A 362** (1995) 487.

[97] G. D'Agostini, *Improved iterative Bayesian unfolding.* Preprint arXiv:1010.0632, 2010.

[98] H. Abreu et al. *Measurement of the inclusive isolated prompt photon cross section in pp collisions at* $\sqrt{s} = 7$ *TeV with the ATLAS detector using 35* pb^{-1}. ATL-COM-PHYS-2011-645.

[99] ATLAS Collaboration, G. Aad et al., *Measurement of inclusive jet and dijet cross sections in proton-proton collisions at 7 TeV centre-of-mass energy with the ATLAS detector.* Eur. Phys. J. **C 71** (2011) 1512.

[100] S. van der Meer, *Calibration of the effective beam height in the ISR.* CERN-ISR-PO-68-31 (1968).

[101] D. Miller, A. Schwartzman and D. Su, *Pile-up jet energy scale corrections using the jet-vertex fraction method.* ATL-PHYS-INT-2009-090.

[102] D. Stump et al., *Uncertainties of predictions from parton distribution functions. 1. The Lagrange multiplier method.* Phys. Rev. **D 65** (2001) 014012; J. Pumplin et al., *Uncertainties of predictions from parton distribution functions. 2. The Hessian method.* Phys. Rev. **D 65** (2001) 014013.

[103] J. Pumplin, A. Belyaev, J. Huston, D. Stump and W.-K. Tung, *Parton distributions and the strong coupling: CTEQ6AB PDFs.* JHEP **0602** (2006) 032.

[104] S. Bethke, *The 2009 World Average of* α_s. Eur. Phys. J. **C 64** (2009) 689.

[105] H.-L. Lai et al., *Uncertainty induced by QCD coupling in the CTEQ global analysis of parton distributions.* Phys. Rev. **D 82** (2010) 054021.

Acknowledgements

El concluir este trabajo no es más que el final de un apartado más de mi vida. Para llegar hasta aquí he tenido que superar varias etapas, lo cual no habría sido posible sin la ayuda de mi familia. Por eso y por más tengo mucho que agradecerles. A mi ama, que sin su trabajo y apoyo no habría podido aprobar esos exámenes interminables de sociales. A mi aita, trabajador incansable donde los haya y siempre dispuesto a echarme una mano. A mi hermano Kepa. Él tiene buena parte de culpa de mi pasión por las matemáticas y la física, así como de otras muchas facetas concernientes a mi personalidad. A mi hermana Silvia, la cual siempre ha sido un ejemplo de esfuerzo. A mis aitites, por el enorme cariño que me distéis durante vuestra vida. Si no os hubiera conocido seguramente sería una persona muy distinta de la que soy ahora. A Laura por lo muchísimo que me ayudo en mis inicios en Ginebra, sin ella todo hubiera resultado mucho más difícil y sin embargo, gracias a su compañía, se convirtió en algo bonito y divertido.

Por otro lado, la realización de esta tesis no es desde luego un mérito exclusivamente mío. Me siento en el deber de compartirla con Claudia y Juan. Posiblemente, con otros directores habría podido acabar una tesis, pero desde luego no me sentiría más satisfecho y más realizado de lo que me siento ahora. Los conocimientos y la metodología de trabajo que me han transmitido es algo de lo que me siento enormemente orgulloso. Por eso, y por lo apacible y agradable que habéis hecho esta etapa de mi vida, os doy las gracias.

Quisiera agradacer también a Michel, mi compañero de piso, su enorme amabilidad, a mis amigos barakaldo-zorrotzanos su amistad, a mis amigos de Madrid y a toda la gente que he conocido en Ginebra su compañía. En general, agradecerles a todos, los grandes buenos momentos que me han hecho pasar, ¡gracias!.

Para concluir, quiero confesar que además de la ciencia, el fútbol es otra de mis pasiones. Jugar al fútbol es algo que me hace sentir muy feliz y que me ha ayudado a desahogarme en los momentos en los que lo necesitaba. Es por eso, por lo que aprovecho para dar las gracias a todos los miembros de Pelotazos F.C. por hacerme pasar tantos buenos momentos dentro y fuera de la cancha, ¡sois bakanes!. Y como no, también agradecer a mis compañeros de Zapata F.C., el hacerme sentir parte de un gran equipo y sobre todo, el haberme recordado jugando a su lado, lo bonito que es el fútbol. ¡Gracias compañeros!.